

**3D Topological Reconstruction in JUNO
applied to GeV events**

**3D Topologische Rekonstruktion in JUNO
angewendet auf GeV-Events**

Dissertation
zur Erlangung des Doktorgrades
an der Fakultät für Mathematik, Informatik und Naturwissenschaften
Fachbereich Physik
der Universität Hamburg

vorgelegt von
David J. Meyhöfer

Hamburg
2020

Gutachter/innen der Dissertation:	Prof. Dr. Caren Hagner Dr. Björn Wonsak
Zusammensetzung der Prüfungskommission:	Prof. Dr. Caren Hagner Prof. Dr. Dieter Horns Dr. Belina von Krosigk Prof. Dr. Gudrid Moortgat-Pick Dr. Björn Wonsak
Vorsitzende/r der Prüfungskommission:	Prof. Dr. Dieter Horns
Datum der Disputation:	19. Februar 2021
Vorsitzender Fach-Promotionsausschusses PHYSIK:	Prof. Dr. Günter Hans Walter Sigl
Leiter des Fachbereichs PHYSIK:	Prof. Dr. Wolfgang Hansen
Dekan der Fakultät MIN:	Prof. Dr. Heinrich Graener
Document identifier:	urn:nbn:de:gbv:18-ediss-93047

Abstract

In recent years unsegmented liquid scintillator detectors have demonstrated to be an excellent tool for neutrino physics. Typically, these detector types investigate low energy neutrino interactions, in the MeV range. An example for this is the Jiangmen Underground Neutrino Observatory (JUNO) detector, which is currently under construction and will start taking data in 2021. It will be filled with 20 kt liquid scintillator and measure reactor $\bar{\nu}_e$ from two nuclear power plants that each are ~ 53 km away from the detector. Their signal is of importance for the determination of the neutrino mass ordering. Additionally, JUNO will determine the solar oscillation parameters θ_{12} and Δm_{21}^2 with unprecedented precision. To achieve this an excellent energy resolution and an effective background reduction is of the essence. A main background are the isotope ${}^9\text{Li}$ and ${}^8\text{He}$, which are constantly generated during showering muon events. Therefore, an accurate muon reconstruction and the determination of energy deposition along muon tracks is essential.

During this thesis, a cosmogenic simulation was developed to evaluate the impact of more rigorous muon veto strategies. With it the spatial distribution of the isotopes ${}^9\text{Li}$ and ${}^8\text{He}$ was explored. By testing different veto approaches which do assume shower detectability, it could be determined that up to 12.8 % more total active volume is deemed to be reachable for JUNO. This prompts the development of reconstruction methods that can determine shower positions.

The Topological Track Reconstruction (TTR) is one approach that has been further developed as part of this work. It has the option of determining shower positions along muon tracks, but is not fast enough to be used during live measurement. Hence, a second topological reconstruction approach was developed. The Quadratic Reconstruction (QR) uses a similar concept as the TTR, but is much faster, because it is only executed along a muon track instead of the whole detector. With this, it is possible to determine shower positions with an accuracy of $\sigma = 35$ cm for more than 80 % of showers, which deposit more than 400 MeV. With the explored veto strategies, it is probably possible to measure 10 % more signal in JUNO. Additionally, the reconstruction approaches can also be adapted by other unsegmented liquid scintillator detector experiments to improve their veto strategies.

Zusammenfassung

In den letzten Jahren haben unsegmentierte Flüssigszintillator-Detektoren bewiesen, dass sie gut geeignet für Neutrinophysik sind. Diese Art von Detektor untersucht hauptsächlich niedrig energetische Neutrino Interaktionen im MeV-Bereich. Ein Beispiel dafür ist der Jiangmen Underground Neutrino Observatory (JUNO) Detektor, welcher momentan gebaut wird und dessen Datennahme in 2021 beginnt. Er wird mit 20 kt Flüssigszintillator gefüllt sein und Reaktor- $\bar{\nu}_e$ messen. Diese gehen von zwei Kernkraftwerken aus, welche jeweils ~ 53 km vom Detektor entfernt sind. Ihr Signal ist wichtig für die Bestimmung der Neutrinomassenordnung. Außerdem wird JUNO die solaren Oszillationsparameter θ_{12} und Δm_{21}^2 mit nie zuvor da gewesener Präzision messen. Dafür ist eine exzellente Energieauflösung und eine effektive Hintergrundunterdrückung wichtig. Ein Haupthintergrundsignal geht von den Isotopen ${}^9\text{Li}$ und ${}^8\text{He}$ aus, welche während schauernden Muonen erzeugt werden. Deswegen ist es essenziell eine akkurate Muonrekonstruktion zu entwickeln, die auch Energiedepositionen entlang der Muonspuren bestimmen kann.

Während dieser Arbeit wurde eine Kosmogenen-Simulation entwickelt, welche benutzt wurde um stringenter Muonvetos zu evaluieren. Damit wurde die räumliche Verteilung der Isotope ${}^9\text{Li}$ und ${}^8\text{He}$ studiert. Dabei ist herausgekommen, dass bis zu 12.8 % mehr totales aktives Volumen in JUNO erreicht werden kann. Dies wurde durch das Testen verschiedener Vetoansätze ermittelt und setzt die Möglichkeit der Schauererkennung voraus. Daher ist es wichtig Rekonstruktionsansätze zu finden, welche dieses können.

Während dieser Arbeit wurde die Topological Track Reconstruction (TTR) weiter entwickelt. Sie bietet die Möglichkeit Schauer entlang der Muonspuren zu identifizieren, ist jedoch nicht schnell genug um sie während der Messung anzuwenden. Von daher wurde ein zweiter Ansatz entwickelt. Die Quadratic Reconstruction (QR) benutzt ein Konzept, welches vergleichbar mit der TTR ist. Sie ist jedoch wesentlich schneller, weil sie nur entlang der Muonspur angewendet wird. Mit der QR ist es möglich Schauerpositionen mit einer Genauigkeit von $\sigma = 35$ cm zu finden. Diese gelingt für mehr als 80 % der Schauer, wenn diese mehr als 400 MeV deponieren. Mit den getesteten Vetostrategien ist es vermutlich möglich 10 % mehr Signal in JUNO zu messen. Desweiteren, können diese Rekonstruktionsstrategien auch für andere unsegmentierte Flüssigszintillator-Detektoren benutzt werden, was zur Verbesserung derer Vetostrategien benutzt werden kann.

Contents

Introduction	1
1 Neutrino physics	5
1.1 Neutrino in the Standard Model	5
1.2 Neutrino flavor oscillations	7
1.2.1 In vacuum	8
1.2.2 In matter	10
1.3 Mixing matrix	12
1.4 Status of neutrino physics	16
1.4.1 Neutrino mass ordering	16
1.4.2 Leptonic CP violation	17
1.4.3 Dirac or Majorana	18
1.4.4 Sterile neutrinos	18
2 Liquid scintillator detectors	21
2.1 General layout	22
2.2 Information journey	22
2.2.1 Initial interactions	22
2.2.2 Light Emission	25
2.2.3 Propagation	28
2.2.4 Detection	30
2.2.5 Readout electronics & Data acquisition	34
3 The JUNO Experiment	35
3.1 JUNO Detector	35
3.1.1 Design	36
3.1.2 Detector layout	36
3.1.3 Scintillator	37
3.1.4 Optical modules	38
3.2 JUNO physics goals	40
3.2.1 Neutrino mass ordering	40
3.2.2 Precision measurement of neutrino parameters	46

3.2.3	Additional goals	48
4	Cosmogenics Simulation	55
4.1	Detector layout	55
4.2	Simulated cosmogenic physics	57
4.3	Simulated events & results	60
4.4	JUNO muon veto assessment	67
4.4.1	Preliminary official veto strategy	67
4.4.2	Possible improvements	69
4.4.3	Custom veto creation	71
4.4.4	Conclusion	76
5	Simulation	79
5.1	Official JUNO simulation	79
5.1.1	Layout	79
5.1.2	Reality vs. Simulation	85
5.1.3	Simulation output & extension	87
5.2	Simulated data used for reconstruction	91
6	Topological Track Reconstruction	95
6.1	3D Topological Reconstruction	95
6.1.1	<i>Basic idea</i>	96
6.2	Iteration process	99
6.3	Further development	100
6.3.1	Robustness & versatility	102
6.3.2	Acceleration	105
6.4	Summary & Outlook	109
7	Quadratic Reconstruction	111
7.1	The <i>basic idea</i> as a quadratic equation	111
7.2	Quadratic Reconstruction concept	113
8	Results of the Quadratic Reconstruction	115
8.1	Data structure representation	115
8.2	Realism & robustness	119
8.3	Quantitative analysis	122
8.4	Multi muon bundle events	127
8.5	Reconstruction comparison & synergy	131
8.6	Summary	133
9	Conclusion and Summary	135

A Addition to the Cosmogenics Simulation	139
List of Figures	143
List of Tables	147
List of abbreviations and acronyms	149
Bibliography	151

Introduction

The neutrino, a particle that does not fit completely into the Standard Model of particle physics, has properties that hint for physics beyond and with these could open a window into the next frontier of particle physics. This particle holds information to many important questions, like the unification of the forces of nature and could contribute to the matter-antimatter asymmetry, which would explain why anything even exists in this universe. Due to a very low interaction rate, large detectors with low background are needed to measure it. Therefore, it is still of high interest for particle physics today.

Many neutrino experiments are dedicated to the measurement of neutrino parameters and to draw a conclusion to these fundamental questions, a complete picture of the neutrino is necessary. One of these experiments is the Jiangmen Underground Neutrino Observatory (JUNO), which is a large unsegmented liquid scintillator experiment and is currently under construction. The main objective is to answer the neutrino mass ordering problem. Additionally, JUNO will also determine neutrino parameters, such as θ_{12} and Δm_{21}^2 with unprecedented precision. These goals are of utmost importance for the verification of the unitarity of the neutrino mixing matrix and for the prospect of neutrinoless double beta decay experiments. None unitarity could provide evidence for additional neutrino flavors and the neutrinoless double beta decay would answer the question if the neutrino is its own antiparticle.

JUNO is currently being built about 650 m underground, near Jiangmen, China. It is designed as a 20 kt liquid scintillator experiment with a very high energy resolution of $3\% / \sqrt{E[\text{MeV}]}$ and will measure reactor $\bar{\nu}_e$. This resolution is required to resolve the fine structure of their energy spectrum, which is introduced by neutrino oscillation. The two main goals set by JUNO's physics program can be fulfilled with this measurement. The reactor $\bar{\nu}_e$ are the signal, whereas the main background comes from long-lived isotopes ${}^9\text{Li}$ and ${}^8\text{He}$. The decay of these isotopes can mimic the reactor $\bar{\nu}_e$ signal. Additionally, these isotopes are constantly introduced by showering high energy muons passing the detector, at a muon event rate of about 4.1 ± 0.9 Hz [1]. Without a proper muon tracking and an efficient veto strategy, a 100% dead time of the detector is quite possible. State of the art muon tracking algorithms for liquid scintillator experiments use likelihood methods to reconstruct muon tracks and can identify shower occurrence [2, 3]. The topological reconstruction efforts discussed in this work do not use hypotheses to restrict the muon track direction. In addition to the identification of showering muons, also the location of showers along the muon track can be determine. Instead of vetoing the whole

muon track, this enables one to only veto regions around showers, which mainly is the origin of harmful isotopes. In turn, less dead volume is produced and in the same time more statistics from the relevant signal can be obtained. Additionally, it will be possible to measure production rates and spacial distributions of these harmful isotopes in muon showers.

During the course of this work two topological reconstruction approaches will be discussed: The Topological Track Reconstruction (TTR) and the Quadratic Reconstruction (QR). Development of the TTR has already been going on before the start of this work [4]. The TTR was further improved during this work with a focus on muons with an energy in the GeV regime, especially in terms of robustness, applicability and reduction of reconstruction time. At its core, this approach utilizes mainly geometry and time information. With this and the photon hit time information it is possible to infer an emission probability for this photon, when a reference position and time along the muon track is known and the muon is approximately moving with the speed of light along straight line through the detector. Of course, this requires careful consideration of the detector geometry and optical model. A probability density distribution for each photon can be calculated to map out the event topology, which enables the reconstruction of energy deposition along a muon track. In stark contrast to the commonly used likelihood methods, the TTR does not use a hypothesis, to which a likelihood method would fit parameters such as track direction and energy. This prevents the introduction of errors by the hypothesis and enables a more detailed energy deposition reconstruction. The QR was entirely developed during this work and is basically a revamp of the TTR. The same *basic idea* with geometry and time information is used, but by restricting the reconstruction to the muon track it is possible to drastically reduce the needed reconstruction time. This is also a motivation for the development of the QR. For JUNO, one can currently only verify the performance of these reconstructions with simulations, this can be followed up with real data, once JUNO is actively taking data. Additionally, both topological reconstruction approaches can be applied to any unsegmented liquid scintillator experiment, such as Daya Bay [5], RENO [6] and SNO [7], which in turn will enhance their muon vetos.

In the following, the structure of this work is further elaborated. At the beginning of this work the relevant neutrino physics is discussed in chapter 1. At first, there is the brief history of neutrino physics, followed by a discussion about the neutrino in the Standard Model of particle physics. Subsequently, the case of neutrino oscillation is recapped, with a focus on the solar neutrino problem. Furthermore, the different neutrino parameters in their context of the mixing matrix are discussed and involved neutrino experiments are mentioned. This chapter closes with open questions and the status of neutrino physics at time of writing.

Because the reconstruction approaches used during this work are applicable to any unsegmented liquid scintillator experiment, a general layout of these types of detectors is solicited in chapter 2. Additionally, it is explained how event information travels through such a detector and what distortions this information may face. This is especially important to evaluate what needs to be taken into account for a reconstruction process.

During chapter 3 the JUNO experiment is further introduced. The operation range, detector layout and its components are presented, which mostly follow from the planned $3\% / \sqrt{E\text{MeV}}$ energy resolution. Furthermore, JUNO's physics program will be discussed with a focus on neutrino mass ordering and the precision measurement of the neutrino parameters relevant for JUNO. In particular the aspect of background introduced by high energy muons will be highlighted and in this context the potential background reduction, possible with the topological reconstruction approach, is motivated.

To be able to evaluate what impact a topological reconstruction for high energy muons may have on the experiment, a cosmogenic simulation was developed and analyzed during this work. The simulation is described at the beginning of chapter 4, followed by its results. The chapter closes with an assessment of the JUNO veto strategy for muons in the context of improvements possible with a topological reconstruction approach.

The TTR and the QR use muon events, which are simulated with the official JUNO simulation. Therefore it is necessary to discuss this simulation as well. This is done in chapter 5, which starts with an overview of the layout and physics simulated and then focuses on the differences between simulation and reality. This highlights the differences and shortcomings of simulation data in comparison to experimentally obtained data. It is also discussed how the simulation was altered to enable the comparison between simulated truth and the results of the reconstruction. Finally, chapter 5 is closing with an overview of the simulation sample that was used for reconstructions.

The name giving reconstruction approach is discussed in chapter 6, where the initial development status of the TTR is documented. It starts with an explanation of how this reconstruction mathematically works and how an iterative process can be used to further enhance results. After that, the further development of this approach during this work is discussed, with a focus on improvements in robustness, applicability and reconstruction time reduction. The chapter is concluding with a summary and suggestions for future development.

Based on the experience and ideas of the TTR, the QR approach was developed during this work. The main motivation for this approach is a drastic reduction in reconstruction time. In the beginning of chapter 7 it is explained how the basic concept can achieve this mathematically. Subsequently, it is discussed how this concept can be used to create a full track reconstruction, with the possibility of determining energy deposition along muon tracks.

In chapter 8 the QR is applied to simulated events from the JUNO detector. First, it will be explained how the results can be compared to the simulated event truth, then complications are introduced to reflect more realistic events. After that, the results of a quantitative analysis are discussed to evaluate the performance of the QR approach for single muon tracks. The reconstruction of muon bundle events may also be possible and how the algorithm would perform in this case was also analyzed in this chapter. Furthermore, it is possible to improve the results of the TTR by preselecting light information with the QR and an example of this is can be see at the end of chapter 8. The chapter closes with a summary of the QR results.

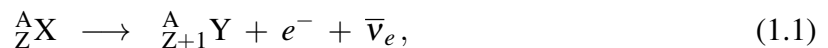
This work closes with a summary of the most important points for the topological reconstruc-

tion approach, in chapter 9. Furthermore, it is discussed what improvements are possible and how to move forward with the development of these approaches.

Chapter 1

Neutrino physics

The concept of the neutrino was an attempt to save energy conservation for the β -decay. Originally the β -decay was expected to have a fixed kinetic energy for electron and nucleus, because it was expected to be a 2 body problem. By turning β -decay into a 3 body problem it is possible to explain the measured continuous kinetic energy distribution. The modern β^- -decay



was published in a paper by Enrico Fermi in 1934 [8], this illustrated the theory of β -decay under the assumption that the neutrino exists.

The experimental discovery was carried out in the 1950s and used the β^- -decay in nuclear reactors. This is a source with high neutrino flux. Clyde L. Cowan and Frederick Reines set up a 300 liter liquid scintillator experiment, which was looking for the reaction



The results were inconclusive, due to the small target mass and lack of decent background shielding. The upgraded experiment with 4000 liters of liquid scintillator provided a clear neutrino signal, which was awarded with the Nobel Prize in 1995 [9], for the detection of the neutrino.

In continuation of this chapter it is discussed how the neutrino fits into the Standard Model of particle physics, then neutrino flavor oscillations will be elaborated based on the history of the solar neutrino problem. After this, there will be more details about the neutrino mixing parameters and the chapter will conclude with a summary about neutrino physics today.

1.1 Neutrino in the Standard Model

The Standard Model (SM) of particle physics uses gauge symmetry and quantum field theory to describe three of the four fundamental forces: The electromagnetic, strong and weak interactions, but not gravitational force. It does this with very few assumptions: symmetries, causality,

quantum theory and relativity. The number of free parameters is quite large with 26 and there are hints for physics beyond the SM. No significant deviations between predictions and measurements had been found, until neutrino oscillation was observed. An outline of the particles and gauge bosons of the SM can be seen in figure 1.1. The neutrinos have spin 1/2 and can be

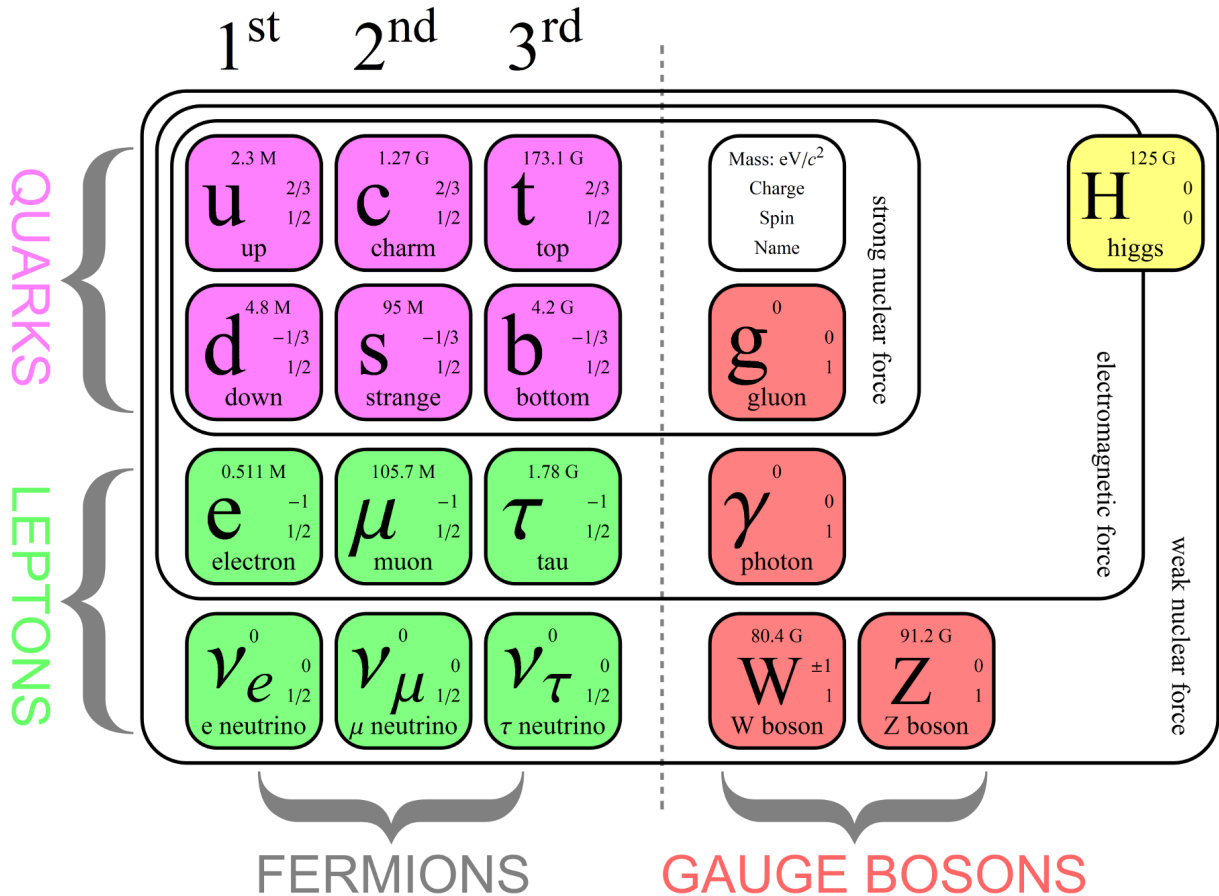


Figure 1.1: Outline of the classical Standard Model with no neutrino mass. It outlines the elementary particles, but the antiparticles are not indicated for Quarks and Leptons. Quarks are shown in purple and leptones are marked in green. The gauge bosons are colored red and the higgs is yellow. Adapted from [10]

seen in light green in the bottom left, below their leptonic counter partners. They are fermions in the SM, have no electric charge, no color charge and no mass in the classical SM without extensions. The 3 neutrino flavors ν_e , ν_μ and ν_τ only interact weakly with the possible channels of charged current (CC) via the W^\pm boson and neutral current (NC) via the Z boson. Even though, it was believed that neutrinos are massless [11], neutrino flavor oscillation has been observed and an explanation can be given with none zero neutrino masses. Nevertheless, the SM is in agreement with most experiments, because most of them consider ultra relativistic neutrinos, which suppresses the expected difference between neutrinos with and without mass.

1.2 Neutrino flavor oscillations

In analogy to the mixing in the quark sector it is also possible to have mixing in the lepton sector. Neutrino oscillation has been observed by multiple experiments. The first evidence arose with the Homestake experiment [12]. Raymond Davis Jr. and John Bahcall wanted to measure electron neutrinos, originating from the Sun, which have been predicted as a byproduct of the nuclear fusion processes in the Sun. Only one third of the theoretically predicted neutrino capture rate turned up in the experiment. This led to the so-called solar neutrino problem. The Super-Kamiokande Observatory observed about 47% of the expected electron neutrino flux in 1998 [13], but is also sensitive to other neutrino flavors. The SNO experiment is a heavy water Cherenkov detector and is sensitive to the three types of neutrinos. Their measurement in 2001 is consistent with an admixture of $1/3 \nu_e$ to $2/3 \nu_{\mu/\tau}$ [14]. A solution to the solar neutrino problem can be given, when one assumes that the originally produced electron neutrinos change flavor along the way and end up in a composition of $\sim 35\% \nu_e$ to $\sim 65\% \nu_{\mu/\tau}$. This composition was confirmed again by SNO in 2002.

The flavor change can be explained with neutrino oscillation, which was predicted by Bruno Pontecorvo [15]. The conditions for this are that neutrinos are produced in a flavor state, which is a coherent mixture of mass eigenstates. The initial phase difference of mass eigenstates is fixed for each flavor. This phase difference enables certain interference effects between the mass eigenstates. The reason why a pure neutrino flavor can contain mass eigenstate contributions from other flavors and is still pure, is because these other contributions have an opposite phase and cancel each other out at time of creation. As an example the electron flavor neutrino states as a combination of mass eigenstates can be seen in figure 1.2 (a). The ν_e and ν_a are a combi-

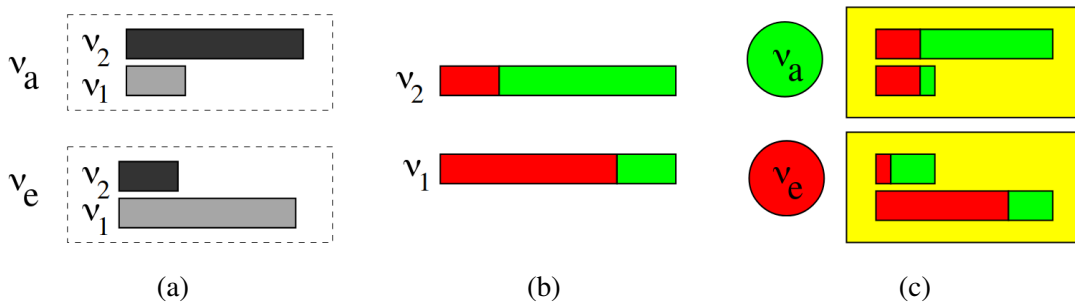


Figure 1.2: Neutrino flavor mixing. In (a) the ν_e and ν_a as a combination of mass eigenstates ν_1 and ν_2 . The box length is normalized to 1. (b) is the flavor composition of the mass eigenstates. In red electron flavor and in green non-electron flavor. In (c) one can see the portraits of the electron and non-electron neutrino as a combination of (b) inserted into (a). [16]

nation of mass eigenstates ν_1 and ν_2 and the corresponding length of the boxes represents the probability to find this mass eigenstate in this flavor state. The flavor composition of the mass eigenstates is given in 1.2 (b). The probability to find the electron and non-electron neutrino in a given mass states is indicated by the color red and green. Now, by putting (b) the flavor

composition of the mass eigenstates into (a) the combination of mass eigenstates that make up a neutrino flavor, one can see that the non-electron neutrino components are contributing the same amount in the electron neutrino. Vice versa, the electron neutrino components are contributing the same amount in the non-electron neutrino state. This is represented in figure 1.2 (c). With the addition that these contributions have opposite phase one can apprehend that no non-electron contributions are left in the initial electron neutrino state and also no electron neutrino contributions are left in the non-electron neutrino state. During propagation this phase difference changes and the cancellation disappears. Therefore, other flavor components can emerge and different neutrino flavors can be observed. This mechanism is called neutrino oscillation [16].

1.2.1 In vacuum

For neutrino oscillation in vacuum the neutrino mass eigenstates are the eigenstates of the Hamiltonian. This gives the dynamic propagation the following properties:

- The mixture of mass eigenstates is determined at the production point and does not change, which means the mass eigenstates propagate independently.
- The portray in figure 1.2 (c) does not change during propagation.
- The relative phase of eigenstates increases monotonously.

The difference in mass of the mass eigenstates results in different phase velocities

$$\Delta v_{\text{phase}} \approx \frac{\Delta m_{ij}^2}{2E}, \quad (1.3)$$

where $\Delta m_{ij}^2 \equiv m_i^2 - m_j^2$ and m_i is the mass of mass eigenstate ν_i . The phase difference change is $\Delta\phi = \Delta v_{\text{phase}} t$. This enables a periodic process, which returns to its initial state when $\Delta\phi = 2\pi$ and has the largest chance of observing a different flavor at $\Delta\phi = \pi$. The oscillation length l_ν is

$$l_\nu = \frac{2\pi}{v_{\text{phase}}} = \frac{4\pi E}{\Delta m^2}. \quad (1.4)$$

As an example for flavor survival probability in vacuum, a plane wave approximation is given, without taking production, detection and 3 dimensional propagation into account. The time dependent neutrino flavor transition probability for the general case of n arbitrary orthogonal eigenstates is stated. Therefore, a flavor eigenstate $|\nu_\alpha\rangle$ is connected to mass eigenstates $|\nu_i\rangle$ with the unitary matrix U by

$$|\nu_\alpha\rangle = \sum_i U_{\alpha i} |\nu_i\rangle, \quad (1.5)$$

where $|\nu_i\rangle = \sum_\alpha U_{\alpha i}^* |\nu_\alpha\rangle$. Let there be a finite number of n flavor eigenstates $\langle \nu_\beta | \nu_\alpha \rangle = \delta_{\alpha\beta}$ and mass eigenstates $\langle \nu_j | \nu_i \rangle = \delta_{ij}$ defined.

Due to the unitary properties of U we also have,

$$U^\dagger U = 1 \text{ , therefore } \sum_i U_{\alpha i} U_{\beta i}^* = \delta_{\alpha\beta} \text{ , } \sum_i U_{\alpha i} U_{\beta j}^* = \delta_{ij} \text{ ,} \quad (1.6)$$

but to enable oscillation this can not be the unit matrix. The time dependency of mass eigenstates $|v_i\rangle$ is

$$|v_i(t)\rangle = e^{-iE_i t} |v_i\rangle . \quad (1.7)$$

Using this and applying (1.7) to the flavor eigenstate (1.5), one gets

$$|v(t)\rangle = \sum_i U_{\alpha i} e^{-iE_i t} |v_i\rangle . \quad (1.8)$$

This is a representation of the time development for a flavor eigenstate, which started pure at a time $t = 0$. The time dependent transition amplitude $A_{\alpha\rightarrow\beta}(t)$ can be defined as

$$A_{\alpha\rightarrow\beta}(t) \equiv \langle v_\beta | v(t) \rangle = \sum_i U_{\alpha i} U_{\beta i}^* e^{-iE_i t} . \quad (1.9)$$

The energy-momentum relation will be used in the next step and is stated as

$$E_i = \sqrt{p^2 + m_i^2} \approx p + \frac{m_i^2}{2p} \approx E + \frac{m_i^2}{2E} . \quad (1.10)$$

Equation (1.10) can be used with the transition amplitude (1.9), if $p \gg m_i$ and $E \approx p$. This is a valid assumption for relativistic neutrinos. Inserting (1.10) into (1.9) one obtains

$$A_{\alpha\rightarrow\beta}(t) = \sum_i U_{\alpha i} U_{\beta i}^* \exp\left(-i \frac{m_i^2}{2E} L\right) = A_{\alpha\rightarrow\beta}(L) , \quad (1.11)$$

where $L = t$, which is the distance from the neutrino source where v_α was created to the point of v_β detection. Then the survival probability $P_{\alpha\rightarrow\beta}(t)$ can be obtained from the transition amplitude (1.11) as follows

$$\begin{aligned} P_{\alpha\rightarrow\beta}(t) &= |A_{\alpha\rightarrow\beta}(t)|^2 \\ &= \sum_{i,j} U_{\alpha i} U_{\alpha j}^* U_{\beta i}^* U_{\beta j} e^{-i(E_i - E_j)t} \\ &= \sum_i |U_{\alpha i} U_{\beta i}^*|^2 + 2\Re \sum_{j>i} U_{\alpha i} U_{\alpha j}^* U_{\beta i}^* U_{\beta j} \exp\left(-i \frac{\Delta m_{ij}^2}{2E} L\right) . \end{aligned} \quad (1.12)$$

In this form of equation (1.12) one can see, that the neutrino oscillation is sensitive to Δm_{ij}^2 . Hence, one cannot obtain the direct neutrino masses in this way. Apart from the lightest neutrino, this also means that neutrinos need to have a mass different from zero to enable oscillation and a lower bound for the neutrino mass can be given, which is about 50 meV [17].

By assuming CP invariance the survival probability (1.12) for neutrino flavor transition can be rewritten in to a simpler way, as

$$P_{\alpha \rightarrow \beta}(t) = \delta_{\alpha\beta} - 4 \sum_{j>i} U_{\alpha i} U_{\alpha j} U_{\beta i} U_{\beta j} \sin^2 \left(-i \frac{\Delta m_{ij}^2}{4E} L \right). \quad (1.13)$$

1.2.2 In matter

Even though neutrino oscillation is realised in vacuum, it is not the dominating contribution for the solar neutrino problem. Due to the size of the Sun it is not enough to consider oscillations in vacuum. Matter effects modify the oscillation and the large angle Mikheyev-Smirnov-Wolfenstein (MSW) effect is contributing the most to the solar neutrino conversion. Common matter is comprised of electrons, neutrons and protons. Neutrinos can interact with particles in common matter, which changes the pattern of neutrino oscillation.

The incoherent elastic and quasi-elastic scattering where the initial neutrino gets changed during the process (meaning the coherence between neutrino states gets destroyed) is negligible, because it basically does not happen. This is due to a small cross section and hence, a large mean free path length, which is about 10^{10} km even while traversing matter as dense as 150 g/cm^3 , which is the approximate density in the center of the Sun, while the radius of the Sun is only 6.96×10^5 km.

The main contribution of matter effects on the neutrino oscillation are driven by coherent elastic forward scattering. This introduces a phase change in the order of π after the traversed length of about 10000 km, which is much smaller than the mean free path [18].

For solar neutrinos, which are produced as ν_e 's in the core region, we can consider the propagation from ν_e to ν_x , where ν_x is a superposition of ν_μ and ν_τ . The effects of usual matter are important for the electron neutrino flavor ratio, because only this part has the potential of charged current scattering on electrons. This can be described as a potential V_e, V_x

$$V = V_e - V_x = \sqrt{2} G_F n_e, \quad (1.14)$$

where n_e is the electron number density and G_F is the Fermi coupling constant. Comparable to the oscillation in vacuum, this adds to the phase difference in the neutrino system as: $\Delta\phi_{\text{matter}} \equiv (V_e - V_x)t$ and again after $\Delta\phi_{\text{matter}} = 2\pi$ repeats periodically. This gives the oscillation length in matter with constant density as

$$l_0 \equiv \frac{2\pi}{V_e - V_x} = \frac{\sqrt{2}\pi}{G_F n_e} \quad (1.15)$$

The MSW effect describes the neutrino oscillation in matter with changing density, where the number density of electrons changes with time. This means the Hamiltonian also depends on time, which enables the mixing angle to change over the course of propagation and transitions between the mass eigenstates are also possible. However, if the changes in density are slow enough, the mass eigenstate transitions can be neglected. This so called adiabatic condition

leaves 2 degrees of freedom:

- Depending on the density, the flavors of the neutrino eigenstates change, which is determined by $\theta_m(t)$.
- Similar to the vacuum oscillations, the phase difference increases, but the rate depends on the changes in density over time.

Therefore, the MSW effect is a combination of the changes in flavor mixing of the neutrino eigenstates and the phase change, which is the reason for the oscillation effect during the adiabatic conversion [16].

The transition probability $P_{\alpha \rightarrow \beta}$ in matter for a two-flavor case is given by

$$P_{\alpha \rightarrow \beta}(\theta_m, m_m, L) = \sin^2(2\theta_m) \sin^2\left(\frac{\Delta m_m^2}{4E} L\right), \quad (1.16)$$

where the parameters θ_m and Δm_m^2 are affected by the matter. They are connected to their vacuum counterpart via

$$\sin^2(2\theta_m) = \frac{\sin^2(2\theta)}{\left(\frac{A}{\Delta m^2} - \cos^2(2\theta)\right)^2 + \sin^2(2\theta)} \quad (1.17)$$

and

$$\Delta m_m^2 = \Delta m^2 \sqrt{\left(\frac{A}{\Delta m^2} - \cos^2(2\theta)\right)^2 + \sin^2(2\theta)}. \quad (1.18)$$

This implies that θ_m and Δm_m^2 change with the density, because A depends on the matter density. Additionally, an energy dependent resonance condition can be deduced from the shape of $\sin^2(2\theta)$, which is

$$A_R = \frac{\Delta m^2 \cos^2(2\theta)}{2E\sqrt{2}G_F}. \quad (1.19)$$

Using this one can take a look at figure 1.3, where the survival probability $P_{e \rightarrow e}(E)$ for solar electron neutrinos depending on their energy is given.

- For neutrino energies greater than 10 MeV the adiabatic conversion with small oscillation effects are valid and it behaves like equation (1.16).
- At an energy range between 2 MeV to 10 MeV the oscillation effects are significant. At 2 MeV is the resonance region.
- Below 1 MeV the sun is basically transparent for the neutrinos and the vacuum oscillation with small matter corrections dominate.

The flow of this graph is also the reason why the sign for m_{21}^2 is known to be positive, which will be relevant for the discussion of the neutrino mass ordering, later in section 1.4.1.

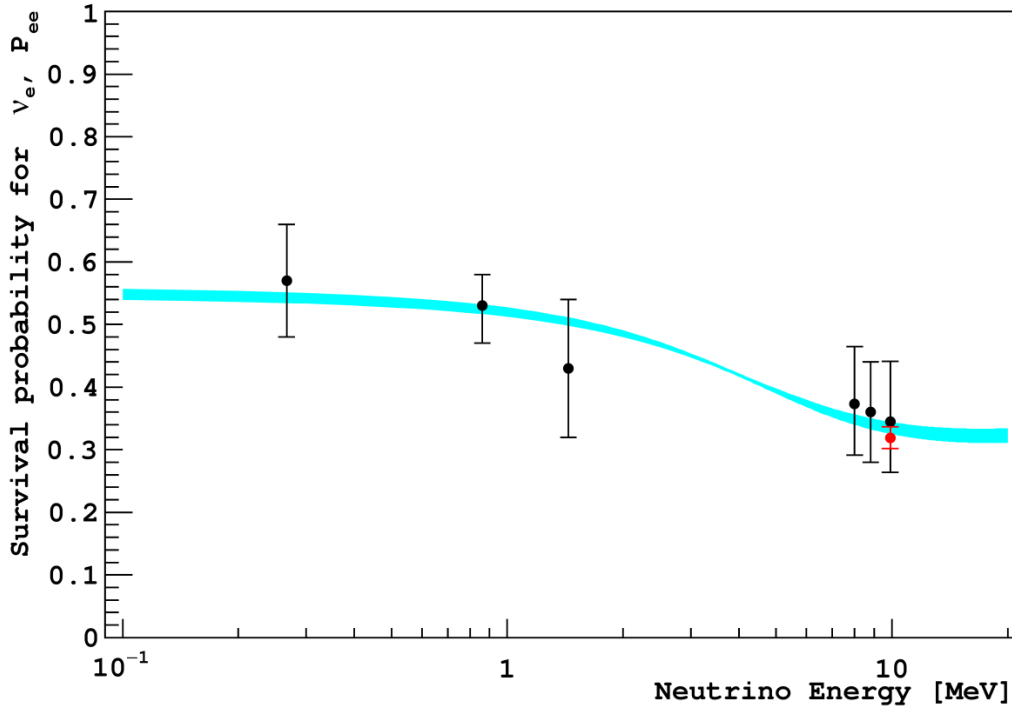


Figure 1.3: Survival probability $P_{e \rightarrow e}(E)$ for electron neutrinos. The light blue band is the survival probability $P_{e \rightarrow e}(E)$ based on predictions made by the LMA MSW effect. The flux is based on the Standard Solar Model. Additionally, the black points indicate Borexino neutrino data and the Red point is combined Super Kamiokande and SNO data. Taken from [19].

As finishing thoughts on the matter effects: The large mixing MSW effect can resolve the solar neutrino problem. The electron density in the sun satisfies the adiabatic condition for all important energies. Hence, the original electron neutrinos, produced in the core, undergo adiabatic conversion and travel a few thousand oscillation length inside the sun. During the transition from the sun to the Earth the coherence of the neutrino state is lost. Hence, incoherent mass eigenstates arrive at the Earth and the ν_e ratio can partially be restored with oscillations in the matter of the Earth. The KamLAND results are in good agreement with the predictions made by the large mixing MSW effect [20].

1.3 Mixing matrix

For three flavor neutrino oscillation the unitary matrix U becomes a 3×3 matrix, which is called Pontecorvo–Maki–Nakagawa–Sakata (PMNS) matrix. The PMNS matrix describes the superposition of mass eigenstates for each flavor eigenstate. It is commonly accepted that there are 3 neutrino flavors e, μ and τ , which are an orthonormal basis for the neutrino in the Standard Model. In the same way an eigenbasis of 3 mass eigenstates ν_1, ν_2 and ν_3 can be defined. Then the PMNS matrix $U_{\alpha i}$ holds the information on how much mass eigenstate i is in flavor α .

With this, the 3 neutrino flavors can be perceived as the combination of mass eigenstates in the following way:

$$\begin{pmatrix} \nu_e \\ \nu_\mu \\ \nu_\tau \end{pmatrix} = \begin{pmatrix} U_{e1} & U_{e2} & U_{e3} \\ U_{\mu1} & U_{\mu2} & U_{\mu3} \\ U_{\tau1} & U_{\tau2} & U_{\tau3} \end{pmatrix} \begin{pmatrix} \nu_1 \\ \nu_2 \\ \nu_3 \end{pmatrix}. \quad (1.20)$$

The PMNS matrix U_{PMNS} has free parameters, which need to be fixed to fully describe neutrino oscillation. A first part is the reduction of free parameters, which is done by requiring unitarity and on the other hand the restriction to 3 neutrino flavors. A factorisation of this matrix is

$$U_{PMNS} = \underbrace{\begin{pmatrix} 1 & 0 & 0 \\ 0 & c_{23} & s_{23} \\ 0 & -s_{23} & c_{23} \end{pmatrix}}_{\text{atmospheric}} \underbrace{\begin{pmatrix} c_{13} & 0 & s_{13} e^{-i\delta_{CP}} \\ 0 & 1 & 0 \\ -s_{13} e^{i\delta_{CP}} & 0 & c_{13} \end{pmatrix}}_{\text{reactor}} \underbrace{\begin{pmatrix} c_{12} & s_{12} & 0 \\ -s_{12} & c_{12} & 0 \\ 0 & 0 & 1 \end{pmatrix}}_{\text{solar}} \quad (1.21)$$

$$= \begin{pmatrix} c_{12}c_{13} & s_{12}c_{13} & s_{13}e^{-i\delta_{CP}} \\ -s_{12}c_{23} - c_{12}s_{23}s_{13}e^{i\delta_{CP}} & c_{12}c_{23} - s_{12}s_{23}s_{13}e^{i\delta_{CP}} & s_{23}c_{13} \\ s_{12}s_{23} - c_{12}s_{23}s_{13}e^{i\delta_{CP}} & -c_{12}s_{23} - s_{12}c_{23}s_{13}e^{i\delta_{CP}} & c_{23}c_{13} \end{pmatrix} \quad (1.22)$$

where $c_{ij} = \cos(\theta_{ij})$, $s_{ij} = \sin(\theta_{ij})$ and δ_{CP} is the CP violating phase. θ_{ij} are the mixing angles with indices $0 < i, j \leq 3$. If neutrinos are Majorana particles, two extra complex phases are needed, which is omitted for simplicity, but will be further discussed in section 1.4.3. The U_{PMNS} matrix is similar to the CKM matrix, but due to the rare interactions of neutrinos it is more difficult to determine the coefficients of the PMNS matrix. The U_{PMNS} matrix can be factorized in 3 different sectors: The atmospheric, reactor and solar sector. Neutrinos that originate from these sectors can be used to determine the coefficients of the PMNS matrix. Additionally, accelerator experiments contribute as well, mostly to the atmospheric sector and for historic reasons it is still called that. The following paragraphs will discuss the contributions of these sectors in more detail. The numbers that are of interest for the 3 flavor neutrino oscillation are summarized in table 1.1, which states the global fit data with Super Kamiokande atmospheric data in 2020.

Atmospheric Some experiments in this sector are Super Kamikande [22] and IceCube, with its addition of DeepCore [23]. Furthermore, contributing accelerator experiments are MINOS [24], T2K [25] and Nova [26]. This sector is mainly occupied with the determination of θ_{23} and Δm_{32}^2 but most experiments are actively measuring multiple neutrino parameters.

Atmospheric neutrinos are created from cosmic rays, which are mainly protons, that hit the atmosphere of the earth. This does not happen directly, instead most of the neutrinos are pro-

Table 1.1: Oscillation parameters for 3 flavor neutrino mixing, from nu-fit July 2020, global analysis with Super Kamiokande atmospheric data. Similar results are obtained for each ordering, with the exception for Δm_{3l}^2 . Additionally it is to note that $\Delta m_{3l}^2 = \Delta m_{31}^2 > 0$ for NO and $\Delta m_{3l}^2 = \Delta m_{32}^2 < 0$ for IO. [21]

	Normal Ordering (best fit)		Inverted Ordering ($\Delta\chi^2 = 2.7$)	
	bf $\pm 1\sigma$	3σ range	bf $\pm 1\sigma$	3σ range
$\sin^2\theta_{12}$	$0.304^{+0.012}_{-0.012}$	$0.269 \rightarrow 0.343$	$0.304^{+0.013}_{-0.012}$	$0.269 \rightarrow 0.343$
$\theta_{12}/^\circ$	$33.44^{+0.77}_{-0.74}$	$31.27 \rightarrow 35.86$	$33.45^{+0.78}_{-0.75}$	$31.27 \rightarrow 35.87$
$\sin^2\theta_{23}$	$0.573^{+0.016}_{-0.020}$	$0.415 \rightarrow 0.616$	$0.575^{+0.016}_{-0.019}$	$0.419 \rightarrow 0.617$
$\theta_{23}/^\circ$	$49.2^{+0.9}_{-1.2}$	$40.1 \rightarrow 51.7$	$49.3^{+0.9}_{-1.1}$	$40.3 \rightarrow 51.8$
$\sin^2\theta_{13}$	$0.02219^{+0.00062}_{-0.00063}$	$0.02032 \rightarrow 0.02410$	$0.02238^{+0.00063}_{-0.00062}$	$0.02052 \rightarrow 0.02428$
$\theta_{13}/^\circ$	$8.57^{+0.12}_{-0.12}$	$8.20 \rightarrow 8.93$	$8.60^{+0.12}_{-0.12}$	$8.24 \rightarrow 8.96$
$\delta_{CP}/^\circ$	197^{+27}_{-24}	$120 \rightarrow 369$	282^{+26}_{-30}	$193 \rightarrow 352$
$\frac{\Delta m_{21}^2}{10^{-5}\text{eV}^2}$	$7.42^{+0.21}_{-0.20}$	$6.82 \rightarrow 8.04$	$7.42^{+0.21}_{-0.20}$	$6.82 \rightarrow 8.04$
$\frac{\Delta m_{3l}^2}{10^{-3}\text{eV}^2}$	$+2.517^{+0.026}_{-0.028}$	$+2.435 \rightarrow +2.598$	$-2.498^{+0.028}_{-0.028}$	$-2.581 \rightarrow -2.414$

duced by the decay of Kaons and π -mesons, which mostly decay as follows:

$$\pi^+, K^+ \rightarrow \mu^+ + \nu_\mu \quad \text{and} \quad \pi^-, K^- \rightarrow \mu^- + \bar{\nu}_\mu. \quad (1.23)$$

Additionally the muons further decay, which produces neutrinos as well:

$$\mu^+ \rightarrow e^+ + \nu_e + \bar{\nu}_\mu \quad \text{and} \quad \mu^- \rightarrow e^- + \bar{\nu}_e + \nu_\mu. \quad (1.24)$$

The Kaons and π -mesons are produced by cosmic rays, which are to about 87% protons. A problem with atmospheric neutrinos is the large uncertainty of the production point. This in turn leads to large uncertainties for θ_{23} and Δm_{32}^2 . Therefore, more and more neutrino beam experiments joined the task of determining these parameters. The production via accelerators is similar to the production of atmospheric neutrinos, but the production point is well known. Neutrinos that are produced via an accelerator are made by bombarding a target with protons, which again produce Kaons and π -mesons.

The sign of Δm_{32}^2 could not be determined so far. This is the reason for the so called mass ordering problem, which will be further discussed in section 1.4.1.

Reactor Some reactor neutrino experiments are KamLAND [27], Double-Chooz [28], Daya Bay [29] and RENO [6]. These experiments use reactor $\bar{\nu}_e$ and measure the smallest mixing angle θ_{13} . This is also of importance for the determination of the CP-violating phase δ_{CP} , which will be further discussed in section 1.4.2.

A nuclear reactor is a point source with a high flux of $\bar{\nu}_e$, which are created during the β^- -

decay of radioactive material inside the reactor. The main detection channel is usually via the so called Inverse Beta Decay (IBD), which is not actually the inversion of the beta decay but instead

$$\bar{\nu}_e + p \rightarrow e^+ + n. \quad (1.25)$$

The follow up neutron capture and positron annihilation have discrete time and energy signals, which can be used to drastically reduce backgrounds. This will be further discussed in section 3.2.1.

An additional option to measure θ_{13} is given by long baseline experiments, but due to the success of reactor experiments the efforts of such experiments are more focused on the determination of the CP-violating phase δ_{CP} .

Solar For the solar sector some important experiments are Homestake [12], Gallex [30], SAGE [31], Super Kamikande [32], SNO [7] and Borexino [33]. Focus of their research is the determination of θ_{12} and Δm_{21}^2 , which is possible with electron neutrinos from the sun. These are produced during the fusion of protons, which takes place in the two major mechanisms of pp-chain and the CNO-cycle and create exclusively electron neutrinos. These mechanisms are part of the Standard Solar Model (SSM), which can be tested with these neutrinos as well. The flux and energy distribution of the solar neutrinos depends on where in the mechanisms the neutrino was produced and they are given specific names depending on the production partner. For example the highest flux of solar neutrinos stems from the so called pp neutrinos, which are produced at the beginning of the pp-chain, via

$$p + p \rightarrow {}^2\text{H} + e^+ + \nu_e. \quad (1.26)$$

The initial experiments before the solar neutrino problem used the ν_e -induced beta decay form ${}^{37}\text{Cl}$ and ${}^{71}\text{Ga}$. Especially for the solar neutrino problem it was important to be sensitive to as many neutrino flavors as possible. Therefore the focus shifted to detection mechanisms, which are sensitive to all flavors. For example Super Kamikande used elastic scattering (ES) via the neutral current interaction of

$$\nu_x + e^- \rightarrow \nu_x + e^-, \quad (1.27)$$

which is sensitive to all flavors of solar neutrinos.

It is possible to observe θ_{12} and Δm_{21}^2 with solar neutrinos, because the conversion to other neutrino flavors highly depends on these parameters. If the SSM is correct, the value of θ_{12} can be obtained by the shape of the survival probability $P_{e \rightarrow e}(E)$ curve, which can be seen in figure 1.3. Then Δm_{21}^2 depends on the position of the transition region around 2 MeV and upturn in the same curve. The measurement of the transition region has yet to be done, hence the restriction of Δm_{21}^2 by solar neutrinos is still pretty loose.

1.4 Status of neutrino physics

The status of neutrino physics in 2020 is that only a few open questions remain. The main questions in this field are:

- Which mass ordering (MO) is realized?
- What is the value of the complex phase δ_{CP} ?
- Are neutrinos Dirac or Majorana particles?
- Do sterile neutrinos exist?

This will be discussed in more detail in the next sections.

1.4.1 Neutrino mass ordering

The absolute mass for each of the three neutrinos is currently unknown, but the squared mass differences are accessible through neutrino oscillation. This enables one to order the neutrino mass states. A squared mass difference is defined as $\Delta m_{ij}^2 = m_i^2 - m_j^2$, but to order them one needs to know the sign for the squared mass difference. The sign of m_{21}^2 is positive, which is known from measuring matter effects on solar neutrinos (see sec. 1.2.2), but so far the sign for Δm_{32}^2 could not be constrained by the current generation of experiments. This opens the possibility for two neutrino mass orderings. One option is the normal ordering (NO) $m_1 < m_2 < m_3$ and the other option is the inverse ordering (IO) $m_3 < m_1 < m_2$. A sketch for both mass ordering possibilities is shown in figure 1.4. Because δ_{CP} is not well constrained the full

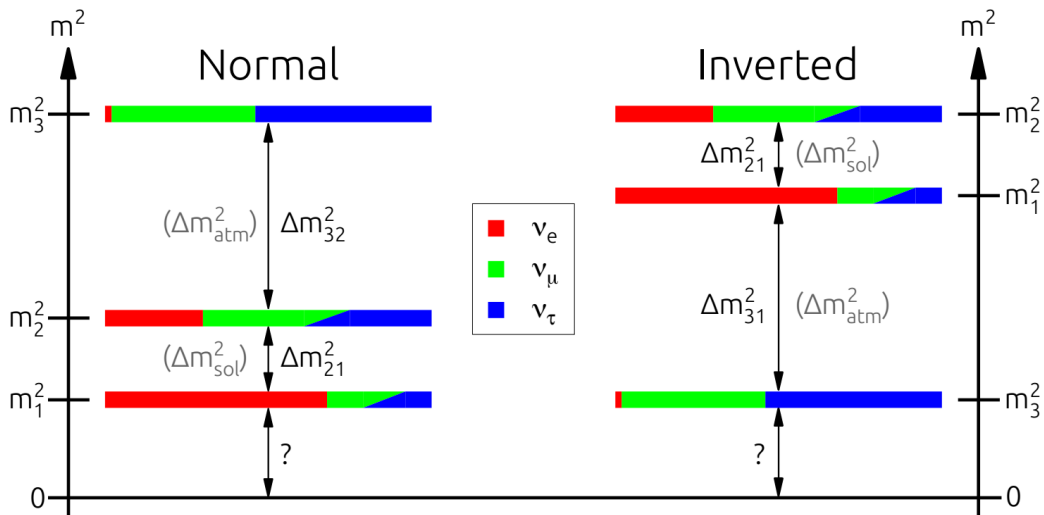


Figure 1.4: Diagram showing the possible realization of neutrino mass ordering, with NO on the left and IO on the right. The mixing of mass eigenstates is represented by the different coloring and the diagonal division represents the uncertainty from the unknown phase δ_{CP} . This diagram is taken from [34].

range from 0 to 2π is represented by the diagonal line between ν_μ and ν_τ .

The impact of determining the neutrino MO can be summarized as follows:

- The MO helps to define the scope of neutrinoless double beta decay experiments, because observing this decay is greatly enhanced if the IO is realized [35].
- The determination of the MO enhances the significance of measurements for the CP-violating phase [36].
- It is an important parameter for testing of supernova models [37].
- Depending on the MO, the neutrino mass scale (i.e., $\sum m_\nu$) can be determined in cosmology with either 1σ for IO or 4σ for NO [36].
- The MO is a crucial parameter when one tries to understand the origin of neutrino mixing and masses [38].
- It will help to determine θ_{23} , if it is different from $\pi/4$, it could be smaller $\pi/4$ or larger than $\pi/4$ [36].

The recent global nu-fit from July 2020 suggests that previous hints for the neutrino MO have significantly decreased. The NO is now favored by only 1.6σ and combined with the Super Kamikande atmospheric data reaches 2.7σ for NO [21].

1.4.2 Leptonic CP violation

As already mentioned the Charge Parity (CP) violation is a hot topic in neutrino physics. It can contribute to the question: Why do we exist? In other words: Why is there more matter than antimatter in the universe? This question is formally known as the matter-antimatter asymmetry problem. At the beginning of the universe matter and antimatter should have been created in equal amounts, but the universe we experience right now has more matter than antimatter. In 1967 A. Sakharov came up with a solution to this problem, which requires three parts:

- Baryon number violation
- CP-symmetry violation
- The rate of the reaction that drives the asymmetry must be less than the expansion rate of the universe.

There are other solutions to this problem, for example that we are in a region of the universe where matter dominates and outside the observable universe could be regions that are antimatter dominated or the solution that our universe has a mirror anti-universe, which would restore the symmetry. These hypothesis are difficult to explore experimentally and CP violation has already been found in the quark sector (namely K and B-mesons) [39]. To allow for CP violation in the neutrino sector, the CP violation phase δ_{CP} can be introduced into the PMNS-matrix. To

accurately measure this phase all other mixing parameters are required, which is why only loose constraints are in place for δ_{CP} , at time of writing. Nevertheless, measuring a δ_{CP} different from 0 or π would contribute to the solution of the matter-antimatter asymmetry problem.

For normal ordering the best fit value for δ_{CP} is 195° [21]. This is close to the CP conserving value of 180° , which is allowed with 0.6σ without Super Kamiokande atmospheric data. In case the IO should be realised, δ_{CP} is close to the maximum of CP violation and CP conservation then is rejected with 3σ [21].

1.4.3 Dirac or Majorana

Neutrinos are Dirac particles if the total lepton number L is conserved. This means neutrinos and antineutrinos have the same mass (CPT), but different lepton numbers $L(\nu) = -L(\bar{\nu})$. In case neutrinos are Majorana particles there is no conserved lepton number, which means there is no quantum number to distinguish between neutrino and antineutrino [40]. Hence, they are the same particle.

Due to neutrino oscillation it is widely accepted that neutrinos have mass. A mechanism how this mass may be obtained can be given with the Higgs mechanism [41], which requires lepton number conservation. However, the neutrino masses are very small compared to other masses in the SM. Therefore, it may be the case that neutrinos are indeed massless in the SM, but obtain mass through a mechanism beyond the SM. One of the most economical explanations can be given, if one assumes only left-handed flavor neutrino fields exist and the lepton number is not conserved [40].

One way to test for the Majorana case is given by the neutrinoless double beta decay ($0\nu\beta\beta$). Because in the Majorana case the neutrino is its own anti-particle it should be possible that there is a double beta decay, where no neutrinos are released.

$$(A, Z) \rightarrow (A, Z + 2) + e^- + e^-, \quad (1.28)$$

would be the decay mode. Current generation experiments like GERDA [42], KamLAND-Zen [43], EXO-200 [44], CUORE [45] and CUPID-0 [46] have not measured this decay so far and therefore can only provide a lower limit for the decay half time and their respective elements used for the $0\nu\beta\beta$ decay, which is around 10^{25} years [40].

When it is determined that neutrinos are either Dirac or Majorana particles many theoretical models are excluded and the remaining ones will shed light on the origin of small neutrino masses. An overview of neutrino mass models is given in [47].

1.4.4 Sterile neutrinos

Additionally to the 3 known neutrino flavors ν_e , ν_μ and ν_τ it may be possible that other neutrinos exist. These are the so called sterile neutrinos, because they do not interact via the weak force. Experimentally additional non-sterile neutrinos are unfavored, because the decay width of the

Z^0 boson confirms the number of neutrino flavors to be $N_\nu = 2.984 \pm 0.008$ [19] for neutrinos with a mass below half of the Z^0 bosons mass. Heavy sterile neutrinos may exist if neutrinos are Majorana particles. This would favor the existence of heavy (GeV range) right-handed neutrinos via the see-saw mechanism [48].

A hint for sterile neutrinos is given by anomalies which appeared in short baseline reactor neutrino experiments like NEOS [49] and Daya Bay [5], beamline experiments such as LSND [50] and MiniBooNE [51] and solar neutrino experiments GALLEX and SAGE, which both use gallium [52]. Another hint for additional neutrino flavors would be non-unitarity of the PMNS matrix. This would require a precise measurement of all involved parameters, which has not been reached yet.

Chapter 2

Liquid scintillator detectors

How to chart the unknown depth of the neutrino parameter sea? Well, a reasonable approach can be unsegmented liquid scintillator detectors. Current examples like Borexino [53] and KamLand [54] have proven the feasibility for much larger experiments. Much higher statistics will be reached by JUNO, which will enable us to determine the realized neutrino mass ordering. Additionally, it will reach unprecedented precision for the measurement of neutrino parameters.

Why this type of detector? Building such a detector is one way to be able to perform low energy neutrino measurements. Typically the target of such a detector is dense and large to make neutrino interactions more frequent. The intrinsic features of scintillator can achieve an energy threshold in the keV range, which is much lower than the MeV range of similarly designed Cherenkov detectors. It is also possible to determine the energy of an event with great precision due to the scintillators almost perfect linear response in the low energy range. This is important when measuring reactor neutrinos for the mass ordering problem. There is the option for solid or liquid scintillator. Solid scintillator would mean segmentation into blocks, because the creation of scintillator crystals in the size of a large detector target is not feasible. Segmenting would mean a lot of instrumentation and many surfaces, which would introduce a lot of radioactivity. Furthermore, liquid scintillator handling, cleaning and filling is simple compared to creating radiopure solid scintillator blocks and stacking them. Segmenting a detector is possible and can restrict the location of an event in a much more significant way, but would make the building process and instrumentation more complex. The event location and topology can also be determined in unsegmented detector types, which can be enabled by the reconstructions discussed in chapter 6 and 7. Therefore, unsegmented large liquid scintillator detectors are an excellent choice for low energy neutrino physics.

The next section will describe the general layout of large unsegmented liquid scintillator detectors followed by a description of its inner workings. This is accomplished by following information on its journey through the detector.

2.1 General layout

What makes a liquid scintillator detector work? In principle, a large unsegmented liquid scintillator detector is just that: A large volume of liquid scintillator, acting as a target. This is contained in some sort of enclosure, like a tank. Normally, it has the shape of a sphere or cylinder. During an event scintillation light near the ultra violet spectrum will be emitted from the target and for any reconstruction efforts to succeed, this has to be detected. To be able to see the light emitted from the target region, wavelength sifters should be added to the scintillator and there has to be some sort of photo sensors, either inside the tank or outside. If the photo sensors are outside, the enclosure has to be transparent for the respective wavelength to pass through. A simplistic detector like this would already work.

Some additional requirements are needed to further enhance the detector signal and lower backgrounds. To understand what counts as background it is of the utmost importance to consider the physics involved. This starts from the first interaction inside the target until the read-out electronics is reached. Photo sensors must be shielded from any unwanted interference that could distort the information from the event light. Also, radioactive contaminations of materials outside the detector and components inside the detector itself should be reduced. This means high radiopurity of detector components and especially the liquid scintillator is of the essence. Sealing and shielding against the outside of the detector should be added as well. Some particles will enter the detector regardless of how thick the shielding is, for example atmospheric muons. If this is something the detector should not measure, it should be located deep underground, because rock is basically the cheapest form of shielding and even if this does not stop all particles from entering the detector it can help to reduce their flux to a tolerable level.

2.2 Information journey

In general, the event information we are looking at, in this type of detector, starts as a particle interaction inside the scintillator target. Then light is produced, which can travel through the detector to a photo sensor, where it is turned into an electronic signal and subsequently saved. Therefore, this section will further go into detail of the initial interactions relevant, then how the light is produced and what can happen to the photon information while it is traversing the detector. The chapter will conclude with the information distortion during its detection and saving.

2.2.1 Initial interactions

There are several types of interactions possible, depending on the particle, energy and target. For neutrinos, these are the weak interactions. Because this detector can only measure charged particles, neutrinos can not be measured directly. Instead of this, the charged particles produced during an interaction with the detector target will be measured. The energy deposition E , per

unit length x , can be determined, which is usually described with the Bethe-Bloch formula (2.1), for charged particles between $0.1 \lesssim \beta\gamma \lesssim 1000$:

$$\left\langle -\frac{dE}{dx} \right\rangle = Kz^2 \frac{Z}{A} \frac{1}{\beta^2} \left[\frac{1}{2} \ln \frac{2m_e c^2 \beta^2 \gamma^2 W_{max}}{I^2} - \beta^2 - \frac{\delta(\beta\gamma)}{2} \right]. \quad (2.1)$$

The maximum energy transfer is given by

$$W_{max} = \frac{2m_e c^2 \beta^2 \gamma^2}{1 + 2\gamma m_e / M + (m_e / M)^2}.$$

Table 2.1: The variables used in the *Bethe-Bloch-equation* (2.1). [19]

Symbol	Definition	Symbol	Definition
A	Atomic mass of absorber	M	Incident particle mass
β	v/c	m_e	Electron mass
c	speed of light in vacuum	N_A	Avogadro constant
$\delta(\beta\gamma)$	Density effect correction to ionization energy loss	r_e	Classical electron radius: $e^2/4\pi\epsilon_0 m_e c^2$
ϵ_0	Vacuum permittivity	v	Speed of particle
γ	Lorentz factor	W	Energy transfer to an electron in a single collision
I	Mean excitation energy	Z	Atomic number of absorber
K	$4\pi N_A r_e^2 m_e c^2$	z	Charge number of incident particle

When $\beta\gamma$ reaches more than 1000, radiative losses start to contribute significantly and later dominate. These radiative losses are mainly bremsstrahlung and the energy loss due to bremsstrahlung can be given as

$$\left\langle -\frac{dE}{dx} \right\rangle = 4\alpha N_A \frac{Z^2}{A} z^2 \left[\frac{e^2}{4\pi\epsilon_0 m c^2} \right]^2 E \ln \frac{183}{Z^{1/3}}. \quad (2.2)$$

But the energy loss description by Bethe-Bloch and bremsstrahlung is independent of traversed thickness. Therefore, for high energies in materials with the density of scintillator and a thickness of up to a few centimeters the most probable energy loss should be used. This is due to statistical fluctuations in energy loss. In the experimental case, with limited detector thickness, it is very rare that energy transfers happen that reach all the way up to the maximum energy transfer W_{max} at several GeV. Given enough thickness and statistics, these high energy transfers are expected and would shift the mean of the energy loss to the tail of the distribution. This means for experiments with limited thickness the mean of the energy loss distribution largely fluctuates for high transfer energies and the tail of the distribution has low statistics, which also makes the measured mean energy transfer very sensitive to cuts. In this case the most probable

energy loss should be used instead, which is given by

$$\Delta_p = \xi \left[\ln \frac{2m_e c^2 \beta^2 \gamma^2}{I} + \ln \frac{\xi}{I} + j - \beta^2 - \delta(\beta\gamma) \right], \quad (2.3)$$

with $\xi = (K/2)\langle Z/A \rangle z^2 (x/\beta^2)$ MeV, where the detector has a thickness x in g cm^{-2} , and $j = 0.2$ [19]. For an experiment with muons, in the GeV range, traversing a scintillator of about 0.64 cm the most probable energy loss will rise slightly beyond the minimum ionization energy and after that will basically stay constant [19].

These energy depositions are only applicable for charged particles and this also means neutral particles can not be measured directly. One of the particles that can be measured indirectly is the gamma. They are electromagnetic entities and hence can interact with the target material, in the way of photoelectric effect, Compton scattering and pair production. These interaction release charged particles, which can be measured. The difference to other interactions that release charged particles from none charged particles is that, these electromagnetic interactions always happen and are very well understood, which makes it sufficiently simple to draw conclusions from them about the incident particle. The cross section of these different effects in carbon for an energy range between 10 eV and 100 GeV can be seen in figure 2.1. For low energies the

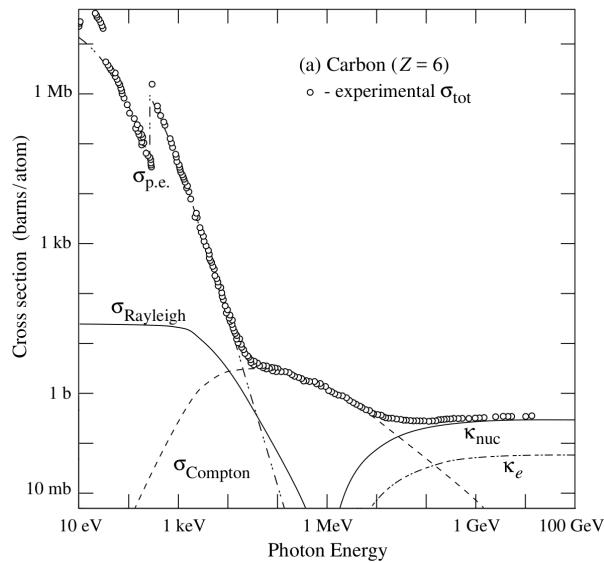


Figure 2.1: Cross section for gamma energy range between 10 eV to 100 GeV . $\sigma_{p.e.}$ is the cross section for the photoelectric effect. σ_{Rayleigh} denotes the contribution of Rayleigh scattering and σ_{Compton} is for Compton scattering. κ marks the pair production for the nucleon field and electron field [19].

photoelectric effect dominates. The transition region between 100 keV to 10 MeV is dominated by the Compton effect and at higher energies the pair production within the electron fields as well as the nuclear fields contributes the most.

Other neutral particles can only be detected by their secondary products if they interact. For example the neutron can be captured by a hydrogen nucleus after it thermalised and a 2.2 MeV gamma will be released that can be detected again.

2.2.2 Light Emission

The light in this type of detector is essentially the messenger that holds the information to event reconstruction. This next few paragraphs will focus on the journey of the scintillation light, to highlight information distribution and the time scales these events play out on. The timing and photon interactions are especially interesting for the reconstruction approaches discussed later in chapters 6 and 7.

Two types of light production mechanisms are of interest for this kind of detector. The more prominent and name giving one is scintillation and the second one is the Cherenkov mechanism. There are other types of radiation¹ that can be detected, but those mainly contribute as background and usually do not hold information usable for reconstruction efforts. Hence, the following paragraphs focus will on firstly scintillation light and secondly Cherenkov light.

Scintillation This process of light production starts when a charged particle deposits energy and elevates an electron in the scintillator molecule to a higher energy state. When this electron falls back to the initial energy level it can produce a photon. When this process takes place in the time scale of a few nanoseconds of radiative lifetime it is called fluorescence and if it takes microseconds it is called Phosphorescence. In organic scintillators this process can take place in molecules with aromaticity, because the π -bonds can freely flip between the 6 carbon atoms in a ring which enables electrons to *freely move about* inside the ring and become delocalized. With great freedom for these electrons comes a great amount of energy state diversity and in turn the proximity between the different energy levels becomes lowered to a point where a passing charged particle can elevate an electron to a higher state. But more importantly the lowered distance between the different energy states can produce light in the UV-range, when an excited electron falls back from an excited energy level. As an example the energy states for an organic scintillator can be seen in the Jablonski diagram figure 2.2. The energy gaps between the π -electron singlet states are distributed in the likeness of $E_{i+1} \simeq E_{i-1} + 1.35 \cdot E_i$ for organic scintillators, up to the ionization energy I_n . Sub-levels of vibrational energy states are indicated by dashed lines, which have a distance of about 0.16 eV. The singlet energy levels S_0 and sub-levels are populated at normal temperatures. Additionally to the singlet states, it is possible to reach excited π -electron triplet states with nonradiative transitions. The direct excitation to the triplet states is forbidden due to spin conservation. However, the triplet state T_1 can be populated by nonradiative transition of a fraction of π -electrons from S_1 . De-excitation from S_1 or T_1 or respective sub-levels can produce photons in the UV-range, but if the scintillator would be composed of only one type of molecule, the light would be self absorbed. To circumvent this, so called wavelength shifters are introduced. As an example a combination of molecules that will be used in JUNO is shown in figure 2.3. Here, the initial main solvent LAB has its wavelength shifted two times until light in the visible range is released. The wavelength shifters are introduced in a much lower concentration of a few g/L, which drastically reduces

¹For example, transition radiation or black-body radiation.

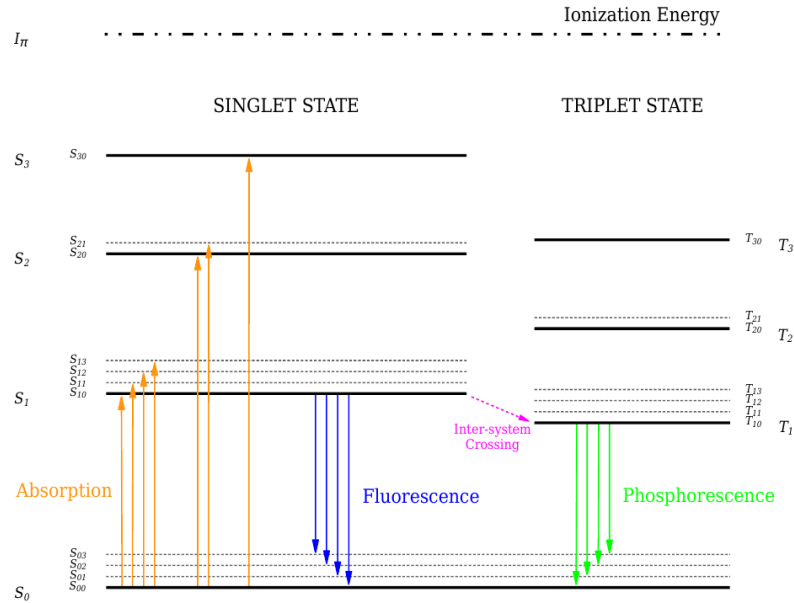


Figure 2.2: Example Jablonski diagram for an organic scintillator. The usual scintillation process takes place by absorption (orange) and subsequent fluorescence (blue) or phosphorescence (green) from a triplet state. Different possible energy states are indicated by lines in black. Whereby the dashed and dotted line at the top indicates the ionisation energy. A nonradiative crossing from single to triplet state is marked in violet. [34]

the self absorption probability. The energy transfer happens through Förster resonance transfer, a nonradiative dipole-dipole coupling process, at distances about 100 times smaller than the involved wavelengths.

The time scales at which this process from energy deposition over shifting until emission plays out is in the nanosecond range. The nonradiative relaxation takes a few picoseconds and the Förster resonance transfer as well as the fluorescence take from a few nanoseconds up to a few hundred nanoseconds. The decay rate is proportional to the population of that exited state. Therefore, the resulting emission times can be described by a combination of exponential functions with weights ω_i and mean lifetimes τ_i .

$$\phi_{em}(t) = \sum_{i=1}^n \frac{\omega_i}{\tau_i} \exp\left(-\frac{t-t_0}{\tau_i}\right), \quad (2.4)$$

where the total of weights needs to be 100 % and t is greater than zero.

Form the example in figure 2.3 one can see that the photon emission from the last wavelength shifter happens, at around 430 nm, in an isotropic way. The light yield of this liquid scintillator mixture is almost linear, which is an important feature for the energy reconstruction of an event and releases about 10 k photons per deposited MeV. Main contribution to nonlinearity is

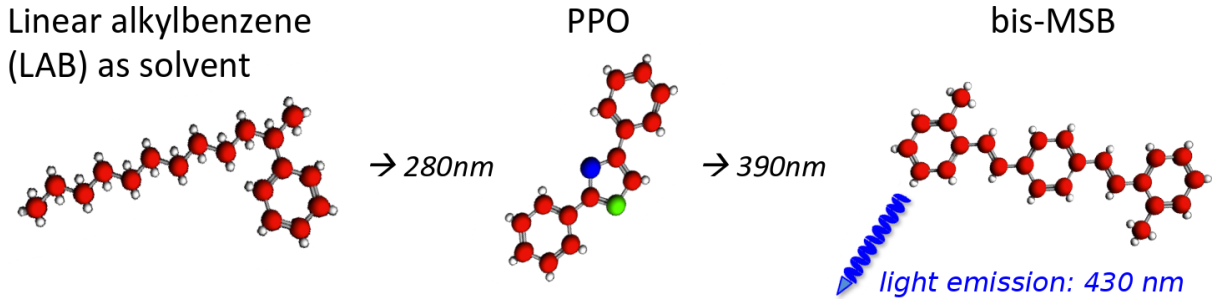


Figure 2.3: Example liquid scintillator mixture, which will be used in JUNO. The main component linear alkylbenzen transfers the energy via nonradiative dipole-dipole coupling to the wavelength shifter PPO, which itself does the same to bis-MSB at which point light around 430 nm is emitted. Addapted from [55]

saturation of available states. The light yield can be described by Birks theory

$$\frac{d\mathcal{L}}{dx} = \mathcal{L}_0 \frac{\frac{dE}{dx}}{1 + k_B \frac{dE}{dx}}. \quad (2.5)$$

Here, k_B needs to be determined experimentally and this also implies that the luminescence \mathcal{L} is particle and energy dependent. By integration over the total length x , the total light emission can be determined.

The Cherenkov mechanism This process can happen while charged particles traverse a dielectric material. The particle needs to move through the material with a speed greater than the phase velocity of light in this medium. Then the electromagnetic field deflection through polarization of the dielectric medium and subsequent relaxation cannot happen fast enough and instead an electromagnetic wave is produced in the visible light range. This light is called Cherenkov radiation and the photons are polarized perpendicular to the particle travel direction. This process is neglectable in terms of energy loss.

The light is emitted under an angle Θ_c that depends on the refractive index of the material as well as the velocity of the particle. For the case that the charged particle moves with a speed close to the speed of light in vacuum, through a material with refractive index $n > 1$, the angle under which the Cherenkov radiation is emitted, can be described by

$$\Theta_c = \text{acos} \frac{1}{\beta n(\epsilon)}, \quad (2.6)$$

where $n(\epsilon)$ considers the dispersion depending on the wavelength in ϵ . The directional information provided by the Cherenkov radiation can be useful when determining the particle direction and can even help with particle identification.

A threshold is implied for the Cherenkov effect, because the velocity needs to be higher than

the local phase velocity of light. It can be described by

$$E_C \geq mc^2 \left[\frac{1}{\sqrt{1 - \frac{1}{n^2}}} - 1 \right], \quad (2.7)$$

where m is the particle mass. Utilizing equation 2.7 it can be determined that the critical energy for muons in scintillator ($n \approx 1.5$) is about 36 MeV and for electrons it is about 210 keV.

The ratio of Cherenkov photons compared to the total light yield depends on the scintillator composition and is in the range of a few percent. The amount of photons emitted per unit length can be determined with [19],

$$\frac{d^2N}{dx d\lambda} = \frac{2\pi\alpha z^2}{\lambda^2} \left(1 - \frac{1}{\beta^2 n^2(\lambda)} \right), \quad (2.8)$$

where α is the fine structure constant and λ is the photon wavelength. The time scale for the emission is basically instantaneous.

The spectrum of the Cherenkov radiation is continuously and mainly emits in near ultraviolet, but for the human eye blue appears to be most prevalent.

2.2.3 Propagation

At this point, one has photons travelling through the detector target with a wavelength mainly around 430 nm. As an example one can assume it travels towards a device capable of photon detection, then the time it will take to reach it can be calculated. The phase velocity is given by:

$$v_p = c/n \quad (2.9)$$

and the group velocity is

$$v_g = \frac{d\omega}{dk} = \frac{c}{n(\omega) + \omega \left(\frac{dn}{d\omega} \right)}, \quad (2.10)$$

where ω is the photons frequency and $k = 2\pi/\lambda$.

Information distortion and loss along the way While a photon is travelling through the detector several things can happen to it. At any point along its path it can be scattered or absorbed. The scattering is mostly caused by Rayleigh or Mie scattering. Both can be described well by just using Lorenz-Mie-Theorie, but the effects can be separated well by their direction of polarisation and scattering distribution. Therefore, they will be discussed separately.

Rayleigh scattering is the elastic scattering of electromagnetic waves on particles, where the particle size is much smaller than the wavelength. The particles can be individual molecules or atoms. The Rayleigh scattering process induces a dipole moment into an electron with instant subsequent emission of a photon with the same energy. In liquid scintillator the scattering cross section is inversely proportional to the fourth power of the wavelength [56]. The scattering

distribution is given by the differential cross section [57], which is proportional to

$$\frac{d\sigma}{d\Omega} \propto \frac{1 + \cos^2\theta}{2}, \quad (2.11)$$

where θ is the angle under which the photon is scattered. One can see that scattering is maximal suppressed for $\theta = \pm 90^\circ$, hence the main scattering direction is forwards and backwards. A photon that has been subject to Rayleigh scattering differs only in its direction of travel. This difference can not be detected by photo sensors and therefore can hurt reconstruction efforts.

Mie scattering occurs for particle sizes larger or equal to the incoming wavelength, where the particle is assumed to be spherical. Hence, these particles are impurities in the liquid scintillator. This scattering is only weakly linked to the wavelength of the photon and also anisotropic. The directional distribution can be complex, depending on the particle, but mostly features a forward boosted distribution [57]. Photons that experienced Mie scattering are also only different in their direction of travel and can hurt reconstruction efforts. On the contrary to Rayleigh scattering, the anisotropy is more complex. Therefore, it is unlikely to obtain useful information from a photon that has undergone Mie scattering, even if this process could be detected.

So called Raman scattering, which describes inelastic scattering can shift the wavelength of a photon through adding or subtracting energy. This basically happens in the same way as Rayleigh scattering, but the difference in energy typically involves vibrational energy from the molecule or atom. The contribution of this effect is about 10^3 to 10^4 times lower than Rayleigh scattering and can be neglected.

Absorption can either transform the photon energy into heat or a new photon can be re-emitted in an isotropic fashion with an additional delay, a new direction and energy. The time scale at which the re-emission happens can be up to few 100 ns. This is especially harmful for the event reconstruction, because this process can not only erase photon information, but also in the case of re-emission produce wrong directional information as well as wrong time and energy information.

Because none of these processes can be accurately detected the information received is reduced by the amount of photons that have undergone scattering or absorption. The information reduction² can be described by equation (2.12), depending on the distance x travelled.

$$I(x) = I_0 \exp\left(-\frac{x}{L}\right), \quad (2.12)$$

where L is the attenuation length and I_0 is the initial amount of information in terms of photons. The attenuation length is a combination of former effects³ and can be further expanded by

$$\frac{1}{L} = \frac{1}{L_{\text{ray}}} + \frac{1}{L_{\text{mie}}} + \frac{1}{L_{\text{abs}}} + \frac{1}{L_{\text{are}}}. \quad (2.13)$$

²It is assumed here that any photon that has undergone any of the scattering or absorption processes holds no usable information afterwards, even though it may be possible to extract information like event energy from a scattered photon or other information remnants like statistical directional distributions.

³Indices correspond to the effects in order of prior sequence of discussion.

It is not necessary to measure the individual contributions, because the total attenuation length can be measured directly with a scintillator sample. By careful composition, selection and treatment of the scintillator it is possible to extend the attenuation length.

Information distortion and loss at boundaries At specific points along the photon path additional distortions are possible. These points are material boundaries, where the photon can be refracted and reflected. In contrast to scattering and absorption effects these are predictable, because they always happen and can only happen at material boundaries.

Reflection in this circumstance is the deflection of a photon under conservation of the incident angle into the reflection angle. Depending on the incident angle and materials involved this can happen with only a part of incoming light or all of it. In general the amount of light reflected is roughly proportional to the incident angle. To predict how likely it is for detected light to be reflected and from where reflected light is entering a photon detector one can generate directional probabilities with a simulation. This needs to be done from the position of the photon detector to consider the correct geometry of other detector parts and their boundaries.

Refraction can happen to the part of the light that is not reflected, when two transparent materials are placed adjacent to each other and they have different refractive indices. The part of the light that is entering a material is called transmission. Without dispersion the angle of deflection can be calculated with:

$$n_1 \cdot \sin(\Theta_1) = n_2 \cdot \sin(\Theta_2), \quad (2.14)$$

where n_1 is the refractive index of the material the photon is coming from and n_2 is the refractive index of the material the photon is entering. The incident angle is given by Θ_1 and Θ_2 is the angle between the new direction and the normalised surface vector pointing inside material the photon is entering. One needs to account for this effect in order to prevent false information processing due to distortion.

2.2.4 Detection

Photons need to be detected and some options will be summarized next. Followed by an explanation how the very process of photon detection can degrade the information conveyed by the photons.

Photon detectors There are several options for photon detection, it is a desirable approach to cover the surface around the target with as much active photon detection electronics as possible. This can enable excellent energy resolution, but may not always be possible, for example due to budget restrictions. Additionally, these photon detectors should be able to preserve the information that is brought to them by the photons as detailed as possible. This means single photon detection capabilities as well as linearity and a high saturation limit are desirable. Common choices include photomultiplier tubes (PMTs), large area picosecond photo detectors

(LAPPDs) or silicone based photomultipliers (SiPMs), which will be selected based on mainly the surface that needs to be covered, the needed detection capabilities and funds available.

Some of the important photon detection characteristics are the ratio of incoming to detected photons, the statistical distribution of detection time and the rate of false photon reports, where the usually used terms are photon detection efficiency (PDE), transit time spread (TTS) and dark count rate. These parameters depend on the type of photon detector used.

The usual option for photon detectors are PMTs. They cover a lot of surface for the amount of money they cost and deliver reasonable sensitivity, linearity and saturation limits. In figure 2.4 a scheme for a dynode PMT can be seen. Photons can enter the PMT through the faceplate.

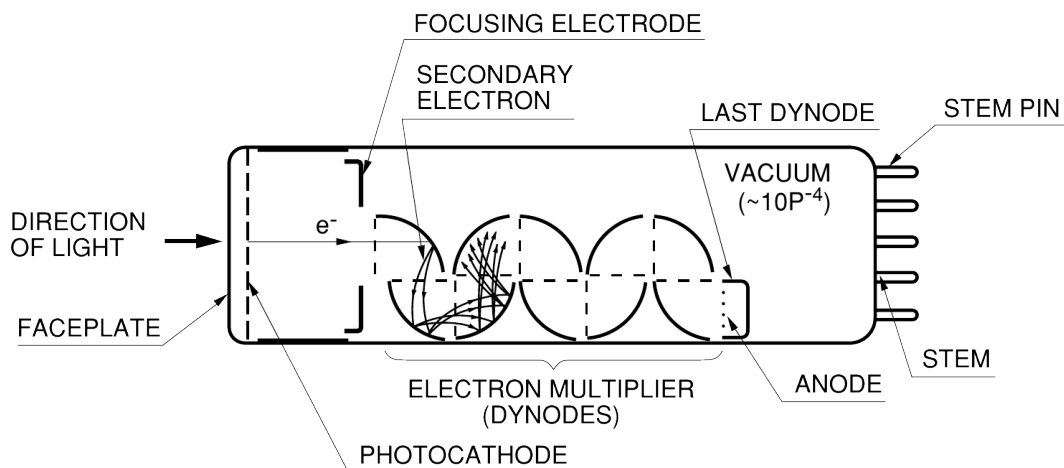


Figure 2.4: This is a basic scheme for a dynode PMT. Photons can be converted into photo electrons at the photocathode. The PE is accelerated towards the dynode structure and an electron cascade is produced. When this reaches the anode, the drop in voltage can be read out. [58].

Behind this is a photocathode, where a photon can be transformed into an photo electron (PE) through the photoelectric effect. This electron is accelerated by the electric field towards the dynode structure. This is where the electron multiplication happens through the development of a cascade. An incoming electron releases additional electrons at each dynode, which are subsequently accelerated towards the next dynode until the anode is reached, at which point the voltage drop is sufficient to be read out.

A similar approach is used by the micro channel plate (MCP) PMT. The structure is pretty much the same with the exception for the electron multiplication system, which is replaced by a MCP. A schematic view of a MCP can be seen in figure 2.5. The plate has a thickness of a few millimeters and is densely perforated by multiple channels with a diameter of about $10\ \mu\text{m}$, which are parallel to each other, but slightly slanted compared to the surface to increase the probability of electron interaction. To avoid electrons passing through without any interaction, multiple plates can be stacked with channels slanting in different directions per plate. The main material of the plate is glass and it is on both sides coated with a thin layer of metal, usually

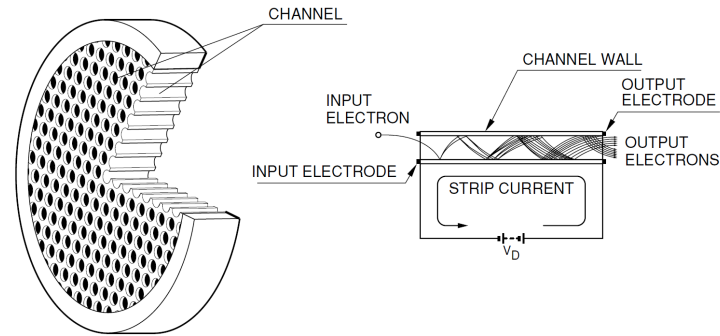


Figure 2.5: Schematic view of micro channel plate on the left. The plate is usually made from a glass and coated on both sides with a thin layer of metal. On the right one can see a channel with an example electron cascade. The size of a micro channel is about $10\ \mu\text{m}$, which motivates its name. [58]

a nickel alloy. This enables one to apply a voltage between the two sides, with a potential in the keV range. A cascade can be triggered by an impinging PE, which releases secondary electrons from the channel wall by striking it.

The size and distance of the photocathode to the dynode structure can be increased to cover larger areas and save costs. The additional cost of more glass and photocathode material is small compared to the cost of the cascade structure. To make this work, the initial PE travels a larger distance towards the multiplication structure, which can have some negative side effects on transit time, dark count rate and PDE.

A different approach can be used, which is the idea behind LAPPDs. Instead of just increasing the size of the photocathode, they also add more micro channels to the MCP to cover larger areas up to $20 \times 20\ \text{cm}^2$. This brings the photocathode back close to the multiplication structure, which negates the former mentioned negative impact and with some clever strip layout of the anodes it is also possible to determine where on the LAPPD a photon hit with a resolution of a few centimeters [59].

The silicone based photo detectors, which can be used for scintillator detectors, are based on Charge-coupled devices (CCDs), but have significantly less dark rate. The basic structure is a p-n-diode with the p-type surface segmented to obtain detailed positional information. To be able to increase the depletion region, the n-type bulk is much thicker as it usually would be for a CCD, this is done to reduce the dark rate. To further reduce this it may be necessary to cool down the whole assembly. This in combination with the depletion of the n-type bulk of free charges by a high electric field, enables the use for single photon detection applications with larger surface areas. Compared to the previously elaborated photon detectors this custom silicone is still very expensive, especially when one wants to cover large areas. The function principle is comparable to an ionization chamber. A charge passing through it creates electron-hole pairs in the depletion zone and this can be detected when a reverse bias is applied, which enables the release of secondary charges due to the acceleration towards the electrodes. This avalanche is not necessarily connected to the amount of light received, but due to the segmentation of the p-type surface it is possible to reach a pixelation in the millimeter range, which makes it

unlikely to hit the same pixel again with the amount of light produced in an unsegmented liquid scintillator detector.

Information distortion and loss by photon detectors For the dynode PMT, MCP PMT and LAPPD the PDE is basically a combination of the ratio of photons that are converted to PE and the ratio of PE that are collected. The chance that a PE enters the multiplication structure and does not produce a cascade is very low. Hence, this effect can be neglected and all PEs that reach it are expected to produce a signal. The collection efficiency for these types of photo detectors depends mostly on the position where on the surface the PE is emitted, but is usually above 90%. This leaves the dominating parameter, which is the conversion ratio of incident photons to PEs, also called quantum efficiency (QE) and this mainly depends on the wavelength of the incident photon. Obviously a high QE at the main wavelength that is emitted from the scintillator is desirable for maximum PDE. Common photocathode materials and their respective QE for different wavelength are stated in reference [58]. High QE for large PMTs can reach more than 35%. LAPPDs have a PDE of around 20% [59]. The PDE of silicone based photon detectors also depends on the wavelength of the incoming photons and can reach more than 50%. The loss of information can be somewhat compensated by weighting the registered photons with the inverse PDE, which becomes more complicated near the saturation limit and impossible after full saturation for a single PMT. Low PDE in very low light conditions can imply complications for event energy reconstruction due to low statistics.

The detection time information will be altered by the function principle of the photo detector as well. For a PMT the time it takes to detect a photon is a combination of the time from transformation into a PE until it reaches the multiplication structure and then the time needed during the cascade. The statistical distribution of these different times create the transit time spread. Of course, larger variety in travel distances result in larger time variations. Therefore, it is no surprise that large PMTs, be it with dynodes or MCPs, have a TTS in the range of a few nanoseconds, while the LAPPD approach shortens the distance between cathode and multiplication structure significantly, which in turn enables an excellent TTS of a few hundred picoseconds [59]. The TTS for SiPMs is also in the picosecond range [60]. In general, shorter TTSs on average result in better preserved timing information.

Not only can photon detectors reduce the amount of available information, but also add wrong information. The dark count is one way to produce wrong information. For large PMTs with high QE this rate is in the range of 2-50 kHz. The usual way for this is the emission of electrons due to heat, which then is subject to the same amplification process as a legitimate PE. As discussed, LAPPDs cover an area of about $20 \times 20 \text{ cm}^2$, but their readout electronics enable extra positional information, which is why the dark count rate stated as 100 Hz/cm^2 under optimal conditions [59]. Dark counts also happen for SiPMs and are highly dependent on temperature, which is why they sometimes need to be cooled to minus tens of degrees Celsius. At below 15°C less than 20 kHz could be achieved [60]. Other possibilities for fake photon information

can be attributed to pre and after-pulses⁴, radioactivity in build materials inside or close to the photon detector and faulty electronics in general.

2.2.5 Readout electronics & Data acquisition

The final step of the information journey is reached, which will discuss event information after it has been detected. After amplification of the photon detector signal it travels through data cables to more sophisticated electronics. A discriminator can be used to impose a threshold on the signal. This will enable one to crudely discriminate between noise and true photon signals. After that there are several options to further treat the signal and depending on the available storage space one can choose to digitize and save the entire temporal evolution of the voltage drop or only the most important information, like the integral and threshold crossing time. Digitization would be performed by a fast analogue to digital converter, which can sample the signal at multiple points during its temporal evolution. The pulse shape of the voltage drop can hold important information about the photons arriving. This is especially true when photons arrive in quick succession. Then the single pulses become superimposed onto each other and it may be necessary to further analyze the full waveform. With the full waveform it should be possible to infer how many photons arrived and maybe even what kind of particles were involved during the event. Unfortunately, it may not always be possible to preserve all information due to data storing constraints. This can be resolved by performing analysis on live analogue data or digitized waveforms, before the information is condensed for storage. This has the additional constraint, that the results need to be obtainable quickly, but this also enables a live monitoring of the detector. If the reconstructions discussed in chapter 6 and 7 should not be able to run as fast as new information comes in, it is also possible to save more details for events that are important for these reconstructions. But full analog waveforms before further processing will probably produce better results than digitized pulse shapes and even less information than that may not be sufficient to reach the goals set for these reconstruction approaches.

⁴These have various origins, for example a pre-pulse may be a PE produced at the dynode instead of the photocathode or an after pulse may originate from ES at the dynode structure.

Chapter 3

The JUNO Experiment

JUNO stands for Jiangmen Underground Neutrino Observatory and is an experiment, which is currently being built near Jiangmen, China. Data taking is planned to start winter 2021. The main focus for the experiment is the neutrino mass ordering, as well as the precision measurements of neutrino parameters. Additionally, it has an extended physics program covering parts of the discussed open questions about neutrinos as well as proton decay and dark matter. For more details take a look at section 3.2 or [36]. The experiment was planned as a follow up of the Daya Bay experiment. Fueled by the large neutrino mixing angle θ_{13} a first paper was published early in 2013 [61], in which the original name is Daya Bay II. Later that year, a first meeting in Kaiping was held, to formulate experimental goals. The idea of an unprecedented 20 kt liquid scintillator experiment took shape, with a planned energy resolution of $3\%/\sqrt{E [\text{MeV}]}$. The international collaboration was established a year later, in August of 2014. The next few years R&D took place and civil construction started in 2015.

This chapter will provide an overview of the planned detector, how it works and focus on parts which are of interest for a topological reconstruction of events in the GeV energy range. The second section will yield an overview of JUNO's physics goals with a focus on the application of the topological reconstruction to improve the physics program results.

3.1 JUNO Detector

Continuing the history in 2016, the production of PMTs and central detector parts started. During the year 2017 and following, PMT testing was performed, the top tracker arrived and PMT potting began. At the time of writing in 2020 the civil construction was ongoing and different parts of the detector were being produced. A few examples would be electronics and the acrylic sphere. Where all these elements are needed, will be discussed in the detector layout. The following section is about the reasoning behind some of the design choices.

3.1.1 Design

JUNO originally should have been built next to Daya Bay, but was ultimately moved to Jiangmen, due to the planned construction of an additional nuclear power plant. At its current location it has a distance of 53 km to both Yangjian and Taishan nuclear power plants, which makes JUNO a medium baseline experiment. JUNO will utilise the inverse beta decay from reactor $\bar{\nu}_e$ to determine the neutrino mass ordering. The experiment is located under a small hill for additional overburden, which was first planned to be about 700 m thick, but due to porous rock and water ingress is now only about 650 m deep. To satisfy the need of high statistics, the detector target size was chosen to be 20 kt of liquid scintillator. Furthermore, an excellent energy resolution of $3\% / \sqrt{E [\text{MeV}]}$ is of the essence, which will be reached with high liquid scintillator transparency, a PMT coverage of about 77 % for the target and extensive calibration. These are the main requirements for the determination of neutrino mass ordering, which also co-insight well with the science goal of the precise measurement of θ_{12} and Δm_{21}^2 .

3.1.2 Detector layout

Following section will describe the JUNO detector layout starting at the center and going outward. As a visual reference a rendered view of the JUNO detector can be seen in Figure 3.1.

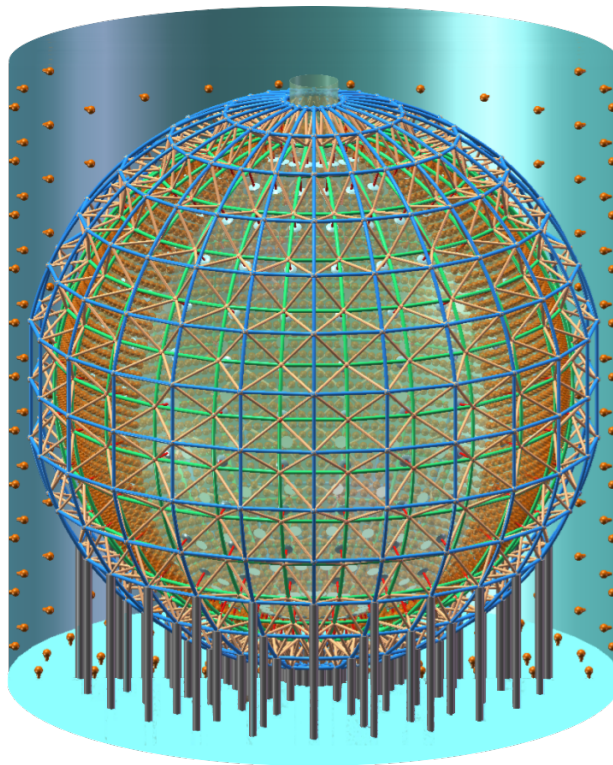


Figure 3.1: A rendering of the JUNO detector, without the top tracker [62]. To enable the view into the central detector, one fourth of the central detector PMTs is not displayed as well as the light blocking tyvek sheets that prevent light leakage between the veto and central detector region.

At the center of the detector is the spherical, 20 kt liquid scintillator target, with a radius of 17.7 m. It is surrounded by an acrylic sphere of about 12 cm thickness. Outside of this is ultra pure water and to counter the buoyancy effects the acrylic sphere is connected to a stainless steel structure via few hundred steel struts. The structure also provides mounting points for about 45000 optical modules and has an inner radius of about 20 m. An optical module is composed of one potted PMT with blast protection and holding structure. There will be 3 kinds of PMTs, 2 types of large 20 inch PMTs and 1 type of small 3.1 inch PMTs. About 18000 large PMTs as well as approximately 25000 small PMTs will look into the central detector. The large PMTs will be arranged in a hexagonal fashion and the small PMTs will fill the spaces in between, for an excellent coverage of $\sim 77\%$. Underwater electronic boxes will be mounted to the steel structure as well, which will contain high voltage (HV) regulation and signal readout systems for the optical modules. All this is part of the so called *central detector*. The rest of the detector continues on the outside of that steel structure. For earth magnetic field shielding the steel structure will have two wires wrapped around it, which will be electrically powered and act as enormous coils. The whole central detector is submerged in a cylinder filled with ultra pure water. The outside of the steel structure and the insides of the cylinder are instrumented with ~ 2400 large PMTs. In combination with the water, this will be used as a veto, utilizing Cherenkov radiation. The cylinder will have a diameter of 43.5 m and a height of 44 m, the water level will go up to 43.5 m. The water reaches from the acrylic sphere to the cylinder walls and can flow through the steel structure, but light is blocked from the central detector by tyvek sheets mounted behind the central detector PMTs. Additionally, the ultra pure water acts as shielding from radiation of the outside rock as well as radioactive impurities from materials inside the detector. On top of the cylinder will be a plastic scintillator strip detector as an additional muon veto, because it is originally from the OPERA experiment it will not cover the whole detector.

3.1.3 Scintillator

To reach JUNO's formidable energy resolution the light yield should be around 10 k photons per MeV. Due to the size of JUNO, the attenuation length needs to be ≥ 20 m to ensure that some light can reach the photo sensors uninterrupted. For the same reason gadolinium will not be added in favour of transparency [36]. With these main constraints, linear alkylbenzene (LAB) was chosen as the main ingredient. To this will be added 2,5-diphenyloxazole (PPO) and 1,4-Bis(2-methylstyryl) benzene (bis-MSB) for wave length shifting. The mixture will contain 2.5 g/l PPO and 3 mg/l bis-MSB, which will shift the wavelength maximum to around 430 nm. The exact mixture can still be subject to change, because the scintillator development is still ongoing. While sourcing this, extra care has to be taken to ensure radiopurity for the detectability of the reactor $\bar{\nu}_e$ signal and especially solar neutrinos. Solar electron neutrinos are detected by elastic neutrino-electron scattering, which does not have a unique handle like the *inverse beta decay*. The limits for this are stated in table 3.1 A dedicated pre-detector, called Online Scintillator Internal Radioactivity Investigation System (OSIRIS) will monitor

Table 3.1: Needed radiopurity in JUNO for the $\bar{\nu}_e$ signal, detected by *inverse beta decay* and solar neutrinos detected by elastic neutrino-electron scattering. [62]

Concentrations [g/g]	$\bar{\nu}_e$ detection	ν_e detection
^{238}U	$\leq 10^{-15}$	$\leq 10^{-17}$
^{232}Th	$\leq 10^{-15}$	$\leq 10^{-17}$
^{40}K	$\leq 10^{-16}$	$\leq 10^{-18}$

the radiopurity during the filling process of JUNO. This enables testing while filling and a cut off in case of abnormal parameter detection.

3.1.4 Optical modules

JUNO will have three different kinds of photomultiplier tubes (PMTs) built into it. This section will go more into detail about these different types and their differences. An optical module in JUNO is composed of following parts:

- One potted PMT
- Passive electromagnetic shielding
- Blast cover

What always will be used is a potted PMT and an acrylic blast cover, that will be held together by a steel encapsulation, which also acts as a blast cover for the back side of the PMT. Water will be able to enter the space between the encapsulation and the PMT through holes added for this purpose. This will ensure a much smaller difference in refractive index than any gas could provide. The blast cover is added to prevent a chain reaction of imploding PMTs. Passive electromagnetic shielding will only be used in the veto and is made from μ -metal. The central detector optical modules are shielded from earth's magnetic field by the active solution of two wires coiled around the central detector. The size and shape of the optical modules will be prescribed by the PMTs and as of time of writing, the final optical module design is still ongoing. As mentioned there are 3 types which will be detailed next.

Large dynode PMTs The 20 inch dynode PMTs are produced by Hamamatsu and about 5000 units will be used for the central detector, which is the classical choice for liquid scintillator as well as water Cherenkov detectors. Their function principle is explained in section 2.2.4. To reach the high energy resolution, JUNO needs to measure as much light as possible and coverage as well as PDE are key parameters to archive this. The PMTs needed to be large, because a smaller amount of large PMTs is cheaper than a large amount of small PMTs. Additionally, a low dark noise rate and especially for the topological reconstruction a small TTS are desirable, which can be fulfilled by this PMT. For the exact parameters check table 3.2.

Large MCP PMTs A new competitor entered the market with the JUNO experiment. Producer of this new candidate is Northern Night Vision Technology (NNVT). About 13000 units of this PMT type are used for the central detector and approximately 2400 for the veto. In stark contrast to the dynode approach, this PMT type utilises a micro channel plate (MCP) for the photon multiplication. The function principle is explained in section 2.2.4. The gain is comparable to the classic dynode system and the time contribution to the TTS during the cascade is in the range of a few hundred pico seconds. But for a high PDE every spot on the photo cathode surface has to be able to reach the small MCP, which introduces a large spread into the TTS of more than 10 ns. The large MCP PMTS parameters can be compared in table 3.2.

Small dynode PMTs The coverage is further increased by filling the gaps in between the large PMTs with 3.1 inch PMTs. Hence, about 25000 small dynode PMTs of the model XP72B22 have been ordered from Hainan Zhanchuang Photonics (HZC). Even though their contribution is only about 2 % to the total coverage, they still fill an important role. They are essential for the calibration of the large PMTs, because about 98 % of the small PMTs will receive only a single PE during reactor $\bar{\nu}_e$ events. This will help to correct nonlinearity and radial detector nonuniformity effects for large PMTs, that will receive between ten to a few hundred PEs during the same event. Parameters are again stated in table 3.2.

Table 3.2: JUNO PMT parameter comparison table. [63]

PMT type	Large dynode	Large MCP	Small dynode
Amount	~ 5000	~ 13000	~ 25000
Size	20 inch	20 inch	3.1 inch
Vendor	Hamamatsu	NNVT	HZC
Model	R12860 HQE	N.A.	XP72B22
PDE(420 nm)	24 % - 35 %	24 % - 35 %	22 % - 27 %
Dark-noise	< 50 kHz	< 100 kHz	< 1.8 kHz

3.2 JUNO physics goals

JUNO has a rich physics program, focusing on many different aspects of neutrino physics. The main goals are the determination of neutrino mass ordering and a precision measurement of neutrino parameters, in particular θ_{12} and Δm_{21}^2 . Some additional points for JUNO's physics program are Supernova neutrinos, DSNB, solar neutrinos, atmospheric neutrinos and Geoneutrinos. Also the proton decay can be analysed, which is the main non-neutrino related topic. Additionally JUNO will be able to probe some exotic physics, like dark matter and non-standard interactions. This section will follow the same structure, that is already used in [36].

3.2.1 Neutrino mass ordering

An open question in neutrino physics is focused on the neutrino mass ordering [64], which will answer the question whether the third neutrino mass eigenstate is lighter or heavier than the other two. This was already discussed in section 1.4.1 and one can take a look at figure 1.4, where the normal mass ordering refers to ν_3 being heavier and inverted ordering means ν_3 is lighter than ν_2 and ν_1 . Due to the relatively large mixing angle θ_{13} it is possible to resolve the mass ordering with neutrino oscillation. There are several options ranging from medium baseline reactor over long-baseline accelerator to atmospheric neutrino oscillation experiments. As established, JUNO is a medium baseline reactor $\bar{\nu}_e$ experiment and analyses the oscillation of Δm_{21}^2 , Δm_{31}^2 and Δm_{32}^2 .

Now, what do these squared mass differences mean and why do we care? Δm_{32}^2 is just defined as $m_3^2 - m_2^2$, but since neutrinos are so light and only interact via gravitation and the weak force, it is not a simple task to measure their masses directly. Nevertheless, there are experiments attempting a direct neutrino mass eigenstate measurement, see for example KATRIN [65]. Not knowing the neutrino mass is one thing, but at least knowing the mass ordering of the neutrino generations is desirable. Hence, we turn back to the squared mass differences, because they can offer almost a complete solution. We have access to squared mass differences through neutrino oscillation, but there is one unknown sign, which defines the neutrino mass ordering question and can be summarized with the following relations:

$$\begin{aligned}
 \Delta m_{31}^2 &= \Delta m_{32}^2 + \Delta m_{21}^2 \\
 \text{NO: } |\Delta m_{31}^2| &= |\Delta m_{32}^2| + |\Delta m_{21}^2| \\
 \text{IO: } |\Delta m_{31}^2| &= |\Delta m_{32}^2| - |\Delta m_{21}^2|.
 \end{aligned}
 \tag{3.1}$$

In the case of normal ordering (NO) a *plus* is needed and for inverted ordering (IO) one needs to subtract [66]. From the equations (3.1) it is possible to determine the mass ordering when $|\Delta m_{31}^2|$ and $|\Delta m_{32}^2|$ have been measured, but in reality this is difficult, because the difference between them is only $\sim 3\%$. Therefore, this also yields one of the requirements for JUNO: The 3% energy resolution per $\sqrt{E \text{ MeV}}$.

The method JUNO will use to determine the mass ordering is based on measuring the reactor $\bar{\nu}_e$ L/E spectrum [66] and exploiting the phase difference in the oscillation fine structure for NO compared to IO. To enhance this difference in the spectrum it can be Fourier transformed, which can reveal the realized mass ordering. A description, how the neutrino flux spectrum at JUNO is determined, will follow next.

The expected flux spectrum $F(L/E)$, that can be measured at JUNO, can be factorized as follows:

$$F(L/E) = \phi(E) \sigma(E) P_{ee}(L/E) , \quad (3.2)$$

where $\phi(E)$ is the expected flux of $\bar{\nu}_e$ from the reactor, $\sigma(E)$ is the cross section, which determines how many neutrinos can be detected and $P_{ee}(L/E)$ is the survival probability of $\bar{\nu}_e$ due to neutrino oscillation.

The flux the reactor is emitting largely depends on the power, with which it is driven and the fuel used at the time. The isotopes that are contributing about 99.7% to thermal power and production of reactor $\bar{\nu}_e$, are ^{235}U , ^{238}U , ^{239}Pu and ^{241}Pu [36]. An approximation of this is given in [66] and can be written as follows:

$$\phi(E) = 0.58 \exp(0.870 - 0.160E - 0.0910E^2) \quad (3.3)$$

$$+ 0.30 \exp(0.896 - 0.239E - 0.0981E^2) \quad (3.4)$$

$$+ 0.07 \exp(0.976 - 0.162E - 0.0790E^2)$$

$$+ 0.05 \exp(0.793 - 0.080E - 0.1085E^2) .$$

This is used for the spectra in figure 3.6, but for the real experiment this is not enough. A fine structure similar to the anticipated oscillation spectrum is expected and could corrupt the measurement [67]. Hence, it was determined that a near detector is needed, which will be built ~ 30 m away from one of the Taishan reactor cores. The name of the near detector is Taishan Antineutrino Observatory (TAO) [68, 69] and it will be used to determine the correct reactor $\bar{\nu}_e$ flux for JUNO.

The interaction rate of $\bar{\nu}_e$ with the protons in the scintillator can be described by the corresponding cross section. For the spectra in figure 3.6 the following formula, taken from [34], has been used:

$$\sigma(E) = 9.61 \cdot 10^{-44} (E - 1.29 \text{ MeV})^2 \text{ cm}^2 \text{ MeV}^{-2} . \quad (3.5)$$

Finally, the survival probability of $\bar{\nu}_e$ is given by equation (3.6) and is the only part of equation (3.2) that depends on the baseline length. When developing the neutrino oscillation formula it usually will be expanded by time evolution. Distance instead of time can be applied, because

the time needed to reach the detector is fixed by the distance travelled for relativistic neutrinos.

$$\begin{aligned}
 P_{ee}(L/E) &= 1 - P_{21} - P_{31} - P_{32} \\
 P_{21} &= \cos^4(\theta_{13}) \sin^2(2\theta_{12}) \sin^2(\Delta_{21}) \\
 P_{31} &= \cos^4(\theta_{12}) \sin^2(2\theta_{13}) \sin^2(\Delta_{31}) \\
 P_{32} &= \cos^4(\theta_{12}) \sin^2(2\theta_{13}) \sin^2(\Delta_{32}),
 \end{aligned} \tag{3.6}$$

is the electron neutrino survival probability, with $\Delta_{ij} = \frac{\Delta m_{ij}^2 L}{4E}$ and θ_{ij} the neutrino mixing angle. The oscillation is dominated by the $1 - P_{21}$ term, but P_{31} and P_{32} are the oscillation terms sensitive to neutrino mass ordering. Utilising equation (3.2) the expected reactor $\bar{\nu}_e$ flux at JUNO can be calculated, which can be seen in figure 3.6.

For the spectrum the global best fit neutrino parameters from [19] were used, as well as the

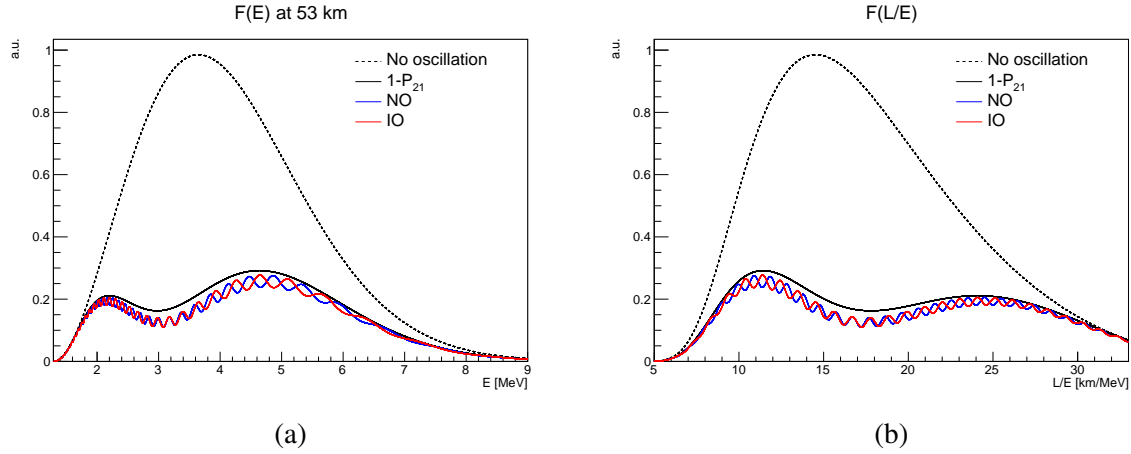


Figure 3.2: Reactor anti-neutrino spectrum at JUNO. For a fixed baseline of 53 km in (a) and in L/E space in (b). The dashed black line is the spectrum without oscillation and the solid black line uses only the first term of $1 - P_{12}$. The spectrum in red would be measured if NO is realized and the blue line is the spectrum if IO is realized.

assumption that there will be about 1.5×10^{33} protons in the JUNO target. The cross section for the *Inverse Beta Decay* and an approximation of $\phi(E)$ is given in [66]. The baseline of JUNO has a perfect distance, because the fine structure for both possible mass orderings is opposed for energies with the largest expected statistics. This should make the identification of the realized mass ordering simpler. From this spectrum one can already deduce which mass ordering is realized, but to create a clearer picture this can be further analyzed. The oscillations have a frequency and this can be inspected with a Fourier transformation. This can be done with sine and cosine Fourier transformation:

$$FST(\omega) = \int_{t_{\min}}^{t_{\max}} F(t) \sin(\omega t) dt \tag{3.7}$$

$$FCT(\omega) = \int_{t_{\min}}^{t_{\max}} F(t) \cos(\omega t) dt. \tag{3.8}$$

The oscillation frequency is proportional to Δm_{ij}^2 . When applying FST and FCT to the different terms of equation 3.6, symmetry breaking features are visible in the Fourier transformation that can be analyzed. When quantifying this features into parameters an enhanced representation can be deduced, where NO and IO are clearly separated [66]. This should be possible with a baseline around 60 km and for a mixing angle $\sin^2(2\theta_{13}) > 0.005$.

The expected neutrino flux spectrum was explored and with it information on the neutrino oscillation and reactor spectrum has been discussed. But how does JUNO measure neutrinos exactly? In short: the main neutrino signal measured in the JUNO detector is the *Inverse Beta Decay* and of course it is not free from backgrounds. Hence, the following sub section will focus on the reactor $\bar{\nu}_e$ signal and possible backgrounds. Especially, the energy regime of a few hundred GeV will be discussed, since this is part of the reconstruction explored in this thesis. For the exploration of the low energy regime with the topological reconstruction one can look into [63].

Reactor $\bar{\nu}_e$ signal in JUNO The signal is the so called *Inverse Beta Decay* (IBD). It is used as the main detection channel in JUNO. It is not actually the inversion of the beta decay, but instead an $\bar{\nu}_e$ that weakly interacts with a proton to create a neutron and positron, which can be seen in Figure 3.3. The products of this interaction, a positron and a neutron, each create a distinctive

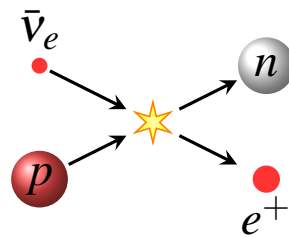


Figure 3.3: A simple case of an $\bar{\nu}_e$ interaction is shown here. This one is referred to as *Inverse Beta Decay*. A reactor $\bar{\nu}_e$ hits a proton from a hydrogen atom, which for example could be part of a scintillator molecule. Through the weak interaction the proton and neutrino are turned into a neutron and a positron.

energy signal. During this event the first signal is from the energy deposition during ionisation. After a few nanoseconds the signal with a distinctive energy is generated, by the annihilation of the positron with an electron, from the scintillator, which is shown in Figure 3.4. Two gamma-rays with 511 keV each are emitted. This is the so called prompt signal, it serves as a start point to look for the second distinctive signal. Meanwhile, the neutron scatters inside the detector until it is thermalized and after $\sim 200\mu\text{s}$ the second signal is emitted, from the neutron capture (Figure 3.5). The delayed signal originates from excited deuterium, which is created by the neutron capture and releases a gamma of 2.2 MeV. The time and energy pattern as well as the location of these signals make it simple to identify $\bar{\nu}_e$ interactions in JUNO and hence, greatly suppress backgrounds. Additionally, there are also variations in these interactions that can broaden and change this behaviour. For example, neutron scattering and the annihilation

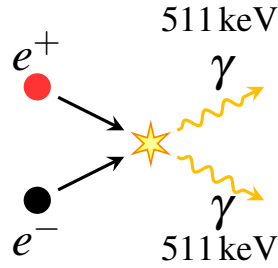


Figure 3.4: A positron from the *Invers Beta Decay* annihilates with an electron from the hull of an atom in the scintillator. Two gammas are released, each with the energy of 511 keV. Before that, there is also the possibility for positronium, which just delays the annihilation.

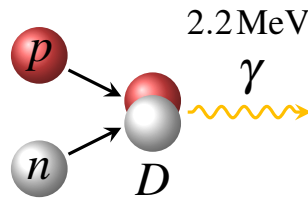


Figure 3.5: A neutron capture, where a hydrogen atom from the scintillator becomes deuterium. The created deuteron is in an excited state and releases a gamma of 2.2 MeV.

time of the positron can vary. In case of direct annihilation there is no time delay. If positronium is created, an unstable exotic atom made from an electron and a positron, there are two more cases. When para-positronium is created (total spin 0), the maximum delay is only ~ 125 ps. But if ortho-positronium is created (total spin 1), the delay can be up to ~ 142 ns. Additionally, at any time the ortho-positronium can be destroyed, by a spin flip or a pick-off. The preliminary IBD selection criteria for energy, time and location are:

- Prompt signal between 0.7 MeV and 12 MeV
- Delayed signal between 1.9 MeV and 2.5 MeV
- Time between them < 1.0 ms
- Distance between them < 1.5 m

The variations in this pattern open up the possibility for other signals to be falsely identified as an IBD event. This could impact JUNO's capability of recording the oscillation spectrum. Hence, we will take a look into the possible background for the IBD now.

Background The main backgrounds for the IBD are accidental background, cosmogenics, fast neutrons and α capture by ^{13}C . Additional selection criteria can reduce some of these backgrounds. There will be a fiducial volume cut to 17 m target radius, which will help to control accidentals and α capture by ^{13}C events. Muons need to be reconstructed well, to reduce cosmogenics and fast neutron backgrounds. The expected efficiency of the selection criteria can

be seen in table 3.3 . While determining the oscillation spectrum, the Geoneutrinos are actually

Table 3.3: JUNO selection cuts for reactor $\bar{\nu}_e$ spectrum measurement, with signal and background as expected events per day. [36]

Selection	IBD eff.	IBD	Geo-vs	Accidental	${}^9\text{Li}$ & ${}^8\text{He}$	Fast n	$\alpha+{}^{13}\text{C}$
No cuts	100 %	83	1.5	$\sim 5.7 \times 10^4$	84	-	-
Volume cut	91.7 %	76	1.4	410	77	0.1	0.05
Energy cut	97.8 %	73	1.3		71		
Time cut	99.1 %				1.1		
Vertex cut	98.7 %				0.9		
Muon veto	83 %	60	1.1	0.9	1.6		
Combined	73 %	60	3.8				

contributing as background and when just looking for the IBD, it can not be reduced, but the amount is only about 1.5 events per day.

The accidental background creates a dual signal like the IBD. It is composed of a signal from radioactivity in combination with a signal from cosmogenic isotopes, spallation neutrons or radioactivity again. The volume cut is so effective, because most radioactivity comes from the rock surrounding the detector and components used outside the target. The muon reconstruction can help to reduce the contribution of accidental background when it contains a signal from cosmogenic isotopes.

Cosmogenic isotopes are created by spallation, from muons passing through the detector. The isotopes can contribute to the background, if their decay chain has a beta decay followed by a neutron release, because this can mimic the IBD pattern. Especially ${}^9\text{Li}$ and ${}^8\text{He}$ have been identified as such candidates. In figure 3.6 the decay chains and branching ratios for ${}^9\text{Li}$ and ${}^8\text{He}$, that contain such a decay mode, can be seen. Because the muon creates the cosmogenic isotopes, they are connected to the muon in time and space. This is a major reason for the development a muon reconstruction, because it can reduce the contribution of cosmogenic background significantly. The isotope distribution, lateral to the muon track, roughly follows an exponential function. Hence, the preliminary approach for a muon veto in JUNO consists of a veto volume in the shape of a cylinder around a muon track. The overall distribution will be further explored with a simulation in this thesis and different veto volume approaches will be discussed in chapter 4 . This helps to determine the requirements for a muon reconstruction and boosts its ability to reach the best possible results in terms of veto volume and efficiency.

Fast neutrons are produced by passing muons as well. They can contribute to the background when scattering of a proton with subsequent capture in the LS target. They are dangerous when the muon that produces them cannot be tracked. This can happen when it passed by in the surrounding rock or only touches the water veto and has a short track.

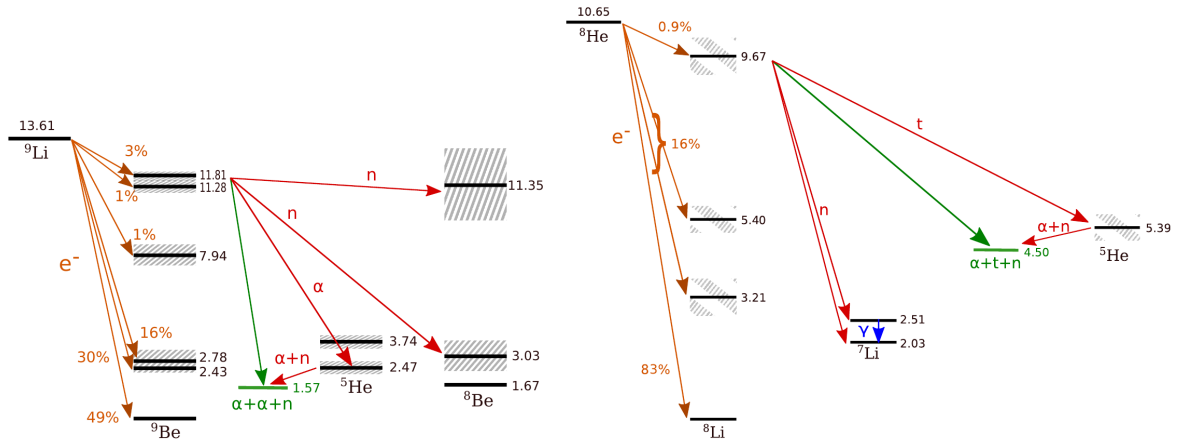
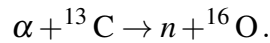


Figure 3.6: Beta decay (orange) and branching ratios for ${}^9\text{Li}$ (left) and ${}^8\text{He}$ (right). All decay modes shown, that are above the lowest energy level, will be followed by a neutron release. For both isotopes only the highest excitation state has the following decays indicated. The energy scale for the excitation states is MeV and green arrows indicate direct three-body break-ups. [70]

The α capture by ${}^{13}\text{C}$ is a special background, that can happen when a alpha particle is captured by ${}^{13}\text{C}$ in the LS. The reaction is as follows:



This can mimic the IBD signal if the neutron is fast enough or the de-excitation of ${}^{16}\text{O}$ creates a gamma. Since the alpha particle is likely to stem from a radioactive decay process, the volume cut is also very efficient in the reduction of this background.

These are the main backgrounds for the oscillation spectrum, but they also apply to other science goals of JUNO, if the IBD is involved.

3.2.2 Precision measurement of neutrino parameters

There are three neutrino parameters, which JUNO will precisely measure. These are θ_{12} , Δm_{21}^2 and $|\Delta m_{ee}^2|$, where $|\Delta m_{ee}^2| = \cos^2\theta_{12}\Delta m_{31}^2 + \sin^2\theta_{12}\Delta m_{32}^2$. Additionally, θ_{13} is accessible to JUNO, but it will not meaningfully improve the results already provided by Daya Bay. Nevertheless, it will be an opportunity to evaluate the Daya Bay results. The other three parameters are extracted from the reactor $\bar{\nu}_e$ spectrum already used to determine the mass ordering. Hence, the planned energy resolution of $3\% \sqrt{E \text{ MeV}}$ and accurate energy resolution $< 1\%$ will come in handy. The precision deemed reachable, compared to the current precision can be seen in table 3.4

Table 3.4: Precision improvement for Δm_{21}^2 , $|\Delta m_{ee}^2|$ and $\sin^2(\theta_{12})$, which is made possible with JUNO. The 1σ uncertainties are started. Precision from a global analysis [71] and feasibility for JUNO measurement calculated in [36].

oscillation parameter	precision today	precision JUNO
Δm_{21}^2	2.4%	0.59%
$ \Delta m_{ee}^2 $	1.9%	0.44%
$\sin^2(\theta_{12})$	4.1%	0.67%

What will we gain from the precise measurement of these parameters? Mainly the precision measurements will be used to test already established theories in neutrino physics. For example:

- The unitarity of the MNSP matrix can be probed and the existence of more lepton generations can be studied.
- The precision measurement of $\sin^2\theta_{12}$ is important to neutrinoless double beta decay experiments [35].
- Also, precision measurement of $\sin^2\theta_{12}$ can help to discriminate between tri-bimaximal mixing models [72].

The measurement of $|\Delta m_{ee}^2|$ combined with a precise measurement of ongoing muon (anti) neutrino disappearance experiments will enable one to probe the mass sum rule:

$$\Delta m_{13}^2 + \Delta m_{21}^2 + \Delta m_{32}^2 \stackrel{?}{=} 0. \quad (3.9)$$

Additionally, it will provide information that increases the sensitivity for the neutrino mass ordering, by quantitative calculations that can be found in [61].

The neutrino parameters can be obtained by fitting the reactor $\bar{\nu}_e$ oscillation spectrum, but the method used in JUNO is still in development. That leaves the precision open for discussion. It is important to consider matter effects, when analyzing the data. They need to be considered for solar neutrino oscillation parameters, since the effects are in the size of 0.5% - 1.0%. To increase the precision of θ_{12} the spectral shape and rate information is used and it is important that the baseline from both reactor locations is very similar to prevent smearing the oscillation pattern. If the baselines were identical for all reactor cores the precision could be significantly increased. The determination of $|\Delta m_{ee}^2|$ can be done with such high precision, because every small oscillation cycle can be treated as a statistically independent measurement. But this also means the energy resolution is very important, because most of the information is stored in the fast oscillation fine structure. Since, the precision measurement of neutrino parameters also relies on the oscillation spectrum all the backgrounds for the IBD apply here as well.

3.2.3 Additional goals

Of course JUNO has more to offer than just neutrino mass ordering and precision measurements of oscillation parameters. Hence, the following paragraphs will be about the auxiliary physics program, which also sometimes contribute to the main goals. The muon reconstruction is important to some of them, especially when cosmogenics are involved, because their position can be better constrained.

Supernova neutrinos There is a lot of information that can be gained by observing a supernova within our galaxy. Not only from measuring the neutrino signal but also the combination with other experiments like gravitational waves or visual observations. For astrophysics this would be a great way to test supernova models, which will answer questions about heavy element production, conditions inside a supernova and the creation rate of black holes compared to neutron stars [73]. For particle physics it could yield neutrino mass boundaries [36], the neutrino mass ordering by comparing event rates of IBD to the elastic neutron-proton scattering channel [74] as well as collective neutrino oscillations or even new physics.

A core-collapse supernova within our galaxy would be a jackpot for almost every astrophysics experiment, from just telescopes, over gravitational waves to neutrino experiments. So far there was only one supernova in recent history, where modern physics could actively measure neutrinos. The probability for JUNO to measure such an event is about 30 % in 10 years, but this number can vary widely depending on the method used to obtain it. There are many different ways to estimate the rate of supernovae in our galaxy. For example by observing supernovae in distant galaxies, the abundance of the radioactive isotope ^{26}Al that is created in core-collapse supernovae or the mentioning rate of such events in history. A supernova has some requirements, when one wants to investigate it with JUNO. It can't be too close and can't be too far. As an example the nearest possible candidate Betelgeuse is only 0.2 kpc away and would generate about 10^7 neutrino events in JUNO. This is a lot of information for the detector to cope with and of course it will be designed in a way to save as much information as possible, but the expected event rate for this is 20 MHz, which will be challenging to handle. Then again too far away would also be unfortunate. A supernova in the Andromeda Galaxy, our closed neighboring galaxy and about 750 kpc away would produce probably 1 neutrino event in JUNO. The assumed distance distribution of core-collapse supernovae remnants has its average at about 10 kpc for our galaxy [75] and is mainly dominated by our location in it as well as the shape and size of our galaxy.

A supernova 10 kpc away would produce about 5000 neutrino events in the IBD-channel. It could be obstructed by dust in the visual range, but pretty much anywhere within our galaxy has the potential for combined observations. The detection channels and expected event rates in JUNO, for a supernova at a distance of 10 kpc, are summarized in table 3.5. One can see that JUNO is sensitive to all neutrino flavors, which enable it to collect the complete supernova neutrino spectrum. But this opens up the possibility of backgrounds additional to the IBD

Table 3.5: Channels and event rates in JUNO for a supernova at a distance of 10 kpc. When no flavor is given in the interaction channel all flavors and anti-flavors are meant. Different average neutrino energies are listed and contributions from all three flavors are summed up, where applicable. Taken from [36].

Channel	Type	Event rate for different $\langle E_\nu \rangle$		
		12 MeV	14 MeV	16 MeV
$\bar{\nu}_e + p \rightarrow e^+ + n$	CC	4.3×10^3	5.0×10^3	5.7×10^3
$\nu + p \rightarrow \nu + p$	NC	0.6×10^3	1.2×10^3	2.0×10^3
$\nu + e \rightarrow \nu + e$	ES	3.6×10^2	3.6×10^2	3.6×10^2
$\nu + {}^{12}\text{C} \rightarrow \nu + {}^{12}\text{C}^*$	NC	1.7×10^2	3.2×10^2	5.2×10^2
$\nu_e + {}^{12}\text{C} \rightarrow e^- + {}^{12}\text{N}$	CC	0.5×10^2	0.9×10^2	1.6×10^2
$\bar{\nu}_e + {}^{12}\text{C} \rightarrow e^+ + {}^{12}\text{B}$	CC	0.6×10^2	1.1×10^2	1.6×10^2

backgrounds. The backgrounds mostly can be controlled due to the high amount of events, that the supernova will generate in JUNO, in the short time of 10 seconds. Due to this short time frame there will be very little other event. The natural radioactivity from the scintillator and surrounding materials will contribute the major portion of the background, but this should be controllable with time, location and fiducial cuts. The cosmogenic backgrounds from muons, should be low as well. In general backgrounds for supernovae are currently under investigation and for more information see [36].

Additionally JUNO will be part of the supernova early warning system (SNEWS), where it will help to coordinate the multi messenger detection efforts.

DSNB Even if there should be no supernova while JUNO active operates, there still is a chance for supernova related physics. It is believed that there is a constant flux of neutrinos from old and far away supernovae. These are neutrinos from the so called diffuse supernova neutrino background (DSNB). So far, none have been detected and this may stay this way, but even than this would greatly improve current limits for the DSNB parameter space.

Detecting diffuse neutrinos from long passed supernovae would be an achievement in itself and a positive test for the models predicting them. With JUNO an analysis of the spectrum will not be possible. Partly because of the reactor $\bar{\nu}_e$ and partly because not enough statistics can be gathered over 10 years. But this would be a motivation for new experiments that could gather enough statistics for a full spectrum analysis and would answer questions about the core collapse, failed SNe, black hole formation, neutrino propagation and flavor conversion.

In principle all the same neutrino detection channels as for the supernova section can be used (see table 3.5), but the event rate in this case is much lower and therefore more backgrounds apply. The main detection channel in JUNO is the IBD and the flux is currently expected to be about one per $20\text{cm}^2\text{s}$. This implies a lower energy limit by the reactor $\bar{\nu}_e$ of about 11 MeV

where the DSNs cannot be detected. Cosmogenic isotopes can be neglected, because their energy spectrum ends below 11 MeV. The expected DSNB event rate for this channel is 1.5 to 2.9 per year. For charged current neutrino interactions the backgrounds can be tagged based on Michel electrons and final state muon identification, by pulse shape analysis. Neutral current neutrino interactions can be mistake for IBD events [76], but pulse shape analysis may enable a retrieval of this observation window [77]. Depending on what the mean energy for the DSNB is, the expected detection significance over 10 years reaches from 2.3σ for $\langle E_{\bar{\nu}_e} \rangle = 12$ MeV up to 5.5σ for $\langle E_{\bar{\nu}_e} \rangle = 21$ MeV (5 % background uncertainty) [36]. In general the studies for the DSNB analysis are still ongoing.

Solar neutrinos This field of neutrino physics is historically very important, because it gave rise to the solar neutrino problem, which led to the discovery of neutrino flavor oscillation. Since then there have been other scintillator experiments, like KamLAND and Borexino that have observed solar neutrinos. JUNO has some unique advantages, for example the unprecedented target size and energy resolution, but also the disadvantage of less overburden compared to other detectors.

The signal of solar neutrinos in JUNO has room for improvement and the topological reconstruction approach may be the missing puzzle piece. Nevertheless, with the chance to study solar neutrinos this will yield a great opportunity for solar and neutrino physics. First of all JUNO could test the results of other detectors and contribute to the statistics. The standard solar model could be probed and the metallicity problem could be investigated, with the measurement of ${}^7\text{B}$ and ${}^8\text{B}$ solar neutrinos. Furthermore, neutrino oscillation and the MSW-effect could be tested, because the solar neutrinos traverse a great deal of matter before they reach the surface of the sun. Additionally, the CNO-cycle could be further constrained.

The detection channel for all flavors will be via elastic neutrino electron scattering:

$$\nu + e^- \rightarrow \nu + e^-,$$

which unfortunately yields almost no direction information [78] and has no unique signal handle like the IBD. The signal will be just a flash of light and basically looks like any beta or gamma decay. This opens up the possibility for backgrounds to swallow the signal. Hence, high radiopurity is of the essence when one wants to observe solar neutrinos. But contaminations are not the only source of radioactive decays. There are also cosmogenics that are being generated constantly from muons passing through the target. A combined plot for signal and backgrounds can be seen in figure 3.7. One can see the expected signal and background mix as the black line for the *ideal* radiopurity case in JUNO (see radiopurity table 3.1). Hence, it may be possible to detect ${}^7\text{B}$ solar neutrinos as well as pp-neutrinos. There are some cosmogenics in this plot. With the muon reconstruction developed during this thesis, it may be possible to constrain the location of cosmogenic decays and veto these areas. With the identification of ${}^{11}\text{C}$ it may even be possible to measure the pep-neutrino signal in the region of 1.2 MeV, but this

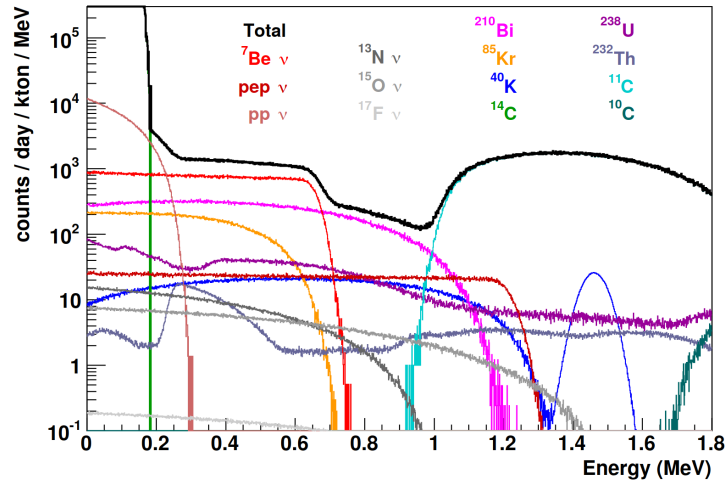


Figure 3.7: The expected energy spectra in JUNO for the solar neutrino case, with ideal background conditions added. [36].

may be to unfeasible due to the long life time of several minutes. The other solar neutrinos are unfortunately deeply buried in background. This also drives the story for the detection efforts of ^8B solar neutrinos. It is possible to detect them with the low energy threshold of JUNO, but again backgrounds may be a showstopper. Here, cosmogenics are the main background, which can be seen in the figure 3.8. Not only the muon reconstruction but also particle identification

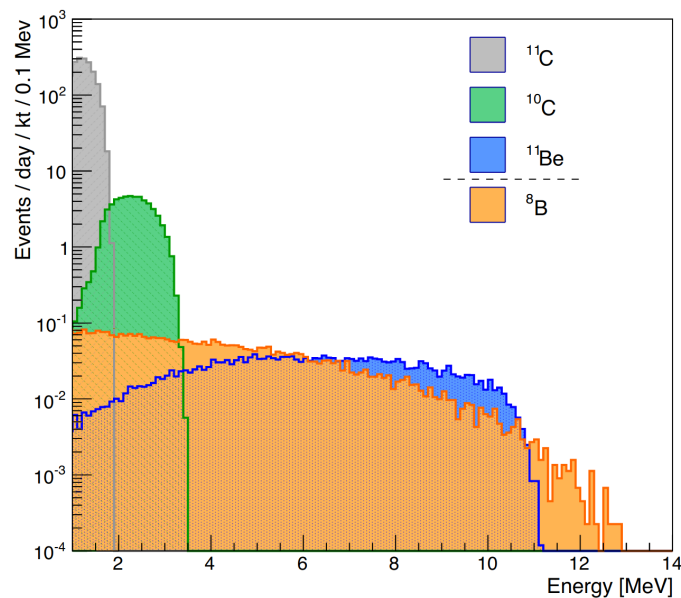


Figure 3.8: The energy neutrino spectrum for ^8B neutrinos, with backgrounds. [36].

could be used to control the cosmogenic background. Particle identification in the MeV regime was performed with the reconstruction approach utilized in this thesis and the results can be seen in [63].

Atmospheric neutrinos So called atmospheric neutrinos are generated by high energy particles, that hit the upper atmosphere. Hence, they come from all over the world, in a wide range

of baselines from 15 to 13000 km and energies of 0.1 GeV up to 10 TeV. The generation is dominated by the production of muon neutrinos. The contribution of atmospheric neutrinos lies in determination of MO and CP violation. The additional determination of MO with atmospheric neutrinos is complementary to the reactor $\bar{\nu}_e$ results for JUNO and it is expected to reach a sensitivity of 0.9σ in 10 years from atmospheric neutrinos alone. It will also be attempted to measure θ_{23} and Dirac CP violation phase δ with atmospheric neutrinos.

In general, atmospheric neutrinos will be tracked by the created muon in CC and NC interactions and classified by the muon track properties into four categories, with the labels fully contained, partially contained, ν_μ -like and $\bar{\nu}_\mu$ -like. When a muon neutrino interacts within the JUNO target and a muon is produced it can be tracked and one can infer the direction of the incoming neutrino. The topological reconstruction can be used, not only for the muon tracking, but also additional particle identification of pions and positrons maybe possible [63]. The direction information is also important when applying the MSW-effect, which needs to be considered for the determination of the MO with atmospheric neutrinos. This should enable JUNO to reach a sensitivity of 0.9σ in 10 years. On the contrary to this, the direction information is not crucial to the investigation of the Dirac CP violation phase δ , because low energy neutrinos will contribute the most to this analysis. The identification of muon or electron flavor as well as neutrino to antineutrino can be done with the triple coincidence of prompt muon production, Michel electron from muon decay and decay of daughter nuclei. The daughter nuclei ^{12}B and ^{12}N can help with the identification of neutrino and antineutrino, because of different lifetimes and Q-values. Particle identification and reconstruction in the 100 to 300 MeV region is still ongoing and the backgrounds are not well determined yet.

There is also a synergy effect, for combining JUNOs analysis of the reactor $\bar{\nu}_e$ spectrum, with results from other atmospheric neutrinos experiments. The atmospheric neutrinos will contribute to the rejection of a wrong MO assumption. This would enable one to determine the MO in less than 2.5 years with more than 5σ significance. The proposed combined analysis can be found in [79].

Geoneutrinos Radioactive material inside the earth decays and emits neutrinos. These so called geoneutrinos will be measured by JUNO and provide the opportunity to look into our home planet without the need of a borehole. This is significant because everything we know about earth's composition is from the surface as well as seismic studies and geoneutrinos yield material information from regions deeper than humanity can drill.

From the investigation of geoneutrinos one can settle the discussion on earth's primordial power budget versus power from radioactive sources. And knowledge can be gained about the history of earth's formation and thermal evolution. In combination with surface studies, the local crust composition can be explored and model predictions can be tested. Additionally, it may be possible to look into a tectonic fold, which is only ~ 1000 kilometres from JUNO, in the south china sea.

JUNO will detect about 300 to 500 geoneutrinos per year, this is much more than other neu-

trino detectors. Geoneutrinos stem mostly from Thorium, Uranium and Potassium, which are expected to make up about 99 % of the initial radioactive isotopes on earth. Of course, this will mainly probe the local geology around the JUNO testing site, but since neutrinos travel mostly uninterrupted through matter it will also have contributions from deeper inside the planet. The main detection channel is again the IBD, with all its backgrounds. Especially one should note that the reactor $\bar{\nu}_e$ counts as background in this study, because they are indistinguishable. To be able to determine the geoneutrino contribution it is implied that the $\bar{\nu}_e$ spectrum needs to be measured with great accuracy. Other than contaminations inside the detector, the cosmogenics play a role here and hence this is another science goal where the topological reconstruction can be helpful.

Sterile neutrinos There is the possibility for neutrinos that do not participate in standard weak interactions, but that can become active neutrinos through flavor oscillation, due to a nonzero mixing angle. Grand Unified Theory (GUT) predicting heavy sterile neutrinos can explain the matter-antimatter asymmetry [80, 81] and light sterile neutrinos in the range of a few keV could be candidates for warm dark matter [82].

JUNOs potential to search for sterile neutrinos in the eV-scale is limited without a near detector, but as mentioned before it was determined that a near detector is necessary will be built [68, 69]. With TAO there will be great opportunities to provide evidence to reinforce or dispute several anomalies in the short baseline sterile neutrino sector. This options would use $\bar{\nu}_e$ and the IBD detection channel. Therefore, it will have the same backgrounds connected to it.

Additionally, there are some ideas to introduce neutrino sources near or in JUNO to basically turn it into a short baseline experiment. But these efforts would most likely be a continuation of the physics program after the main program finished. One could also introduce a short baseline by building a cyclotron near JUNO, positioning a radioactive source next to JUNO or introducing radioactive material into the scintillator.

Nucleon Decays As for any low background experiment, the search for the nucleon decay is an option, because they all contain protons. This is physics beyond the standard model and several GUT models predict the proton decay. Especially SUSY-GUT models prefer the proton decay into a kaon and could be tested with the observation of this event. And even if no proton decay will be measured this would still add statistics to the mean lifetime of a proton and help constrain the current limits, which are $\tau(p \rightarrow \pi^0 e^+) > 1.6 \times 10^{34}$ years [83]. One of the proposed channels for JUNO is the decay of a proton into a kaon:

$$p \rightarrow K^+ + \bar{\nu},$$

which could be detected in JUNO and will be competitive with other detectors like Super-Kamiokande or Dune. The signal would have an energy of 105 MeV from hydrogen, because its a two-body decay and about 25 to 198.8 MeV from carbon. The K^+ has a lifetime of 12.4 ns

and the following signal has five options. In about 84 % the following signal will be again well defined with two-body decays and all decay possibilities contain at least one typical μ^+ to a positron decay with subsequent positron capture. This would display a clear threefold coincidence signal in the detector and makes it possible to reject most backgrounds. One possible background is from atmospheric neutrinos creating a muon, which could be handled by pulse shape discrimination. Nevertheless, muon tagging in the energy range of the proton decay is an important task, that should not be neglected.

Dark Matter The search for dark matter candidates is an ongoing task in physics. There would be a variety of implications for detecting dark matter and this would be especially important for theory development. Many particle physics models could be tested and it would shed light on the visible universe creation itself. In case of no event detection, theoretical particle proposals and more parameter space could be excluded.

A direct measurement of dark matter interaction with the target material is possible. The best candidate for this to happen in JUNO are weakly interacting massive particles (WIMP), with a particle mass around 100 GeV. This interaction would be observed by nucleus recoil. Another possibility to detect dark matter is indirectly, by detecting final-state particles of dark matter annihilation. As an example, this could be a part of the neutrino flux from dark matter annihilation in the sun. The sensitivity for final-state detection is estimated to be around 2σ in 5 years, with the main background of atmospheric neutrinos.

Additional physics beyond the standard model Finally, there is the possibility for nonstandard interactions and effects that could contribute to the measurements. JUNO is sensitive to nonstandard interactions that can effect the neutrino production as well as the neutrino detection. Another could be Lorentz invariance violation, which would be probed by sidereal variation studies of the reactor $\bar{\nu}_e$ spectrum and would manifest in its distortion [84].

Chapter 4

Cosmogenics Simulation

Isotopes like ${}^9\text{Li}$ and ${}^8\text{He}$ can mimic an $\bar{\nu}_e$ signal, as discussed in the section 3.2.1. It is a goal of the topological reconstruction approaches to provide more confined vetos for events containing these. Hence, one has to look into the production and kinematics of the connected processes. Unfortunately, there is very little experimental data for these production channels. The mainly cited experimental study about monoenergetic muon induced production of ${}^9\text{Li}$ and ${}^8\text{He}$ was performed during NA54 at SPS [85] in 1999. Thereby, the positional distribution of these isotopes during their production processes was not studied. Fortunately, there are some recent developments on ${}^9\text{Li}$ and ${}^8\text{He}$ measurements for liquid scintillator detectors, as well as simulation efforts. A paper from the Double Chooz Collaboration was published in 2018 [70]. It describes their results and a rough description on their custom simulation efforts, but no actual code was published. The JUNO simulation has recently been updated to treat the branching ratios and kinematic of ${}^9\text{Li}$ and ${}^8\text{He}$ itself correctly. Actually, the same person who was involved with the Double Chooz paper and the updating efforts for the JUNO simulation, C. Jollet, undertook the development of a public Geant4 update to make the code available for the whole community [86]. During this thesis a Geant4 simulation was created, by which the spatial distributions of ${}^9\text{Li}$ and ${}^8\text{He}$ can be examined. This is essential for the development of veto strategies and due to the focus on only ${}^9\text{Li}$ and ${}^8\text{He}$ production, can be performed much faster than the full JUNO simulation. With a back of the envelope calculation it can be determined that the JUNO simulation would take about 2.5 years to produce about 1000 events of ${}^9\text{Li}$ and ${}^8\text{He}$ combined, with the computing resources available during this thesis.

The following sections describe the detector built in Geant4, the physics used and the results produced. The last part of this chapter describes the current veto strategy for JUNO and how it may be improved based on the findings of this isotope production simulation.

4.1 Detector layout

For this simulation a very simple detector was built. Utilising Geant4 version 4.10.5 and creating only a *G4Box*. The detector dimensions are (10.0, 35.4, 10.0)m. A picture of the detector can be seen in figure 4.1. The height of 35.4m was chosen to mimic the diameter of the JUNO

target. From the center to the edge of the detector it is a minimum distance of 5 m. This ensures that events in the center, even with high energetic showers, can be contained within the target. The material is LAB, or to describe it in Geant4 terms the density distribution of atoms

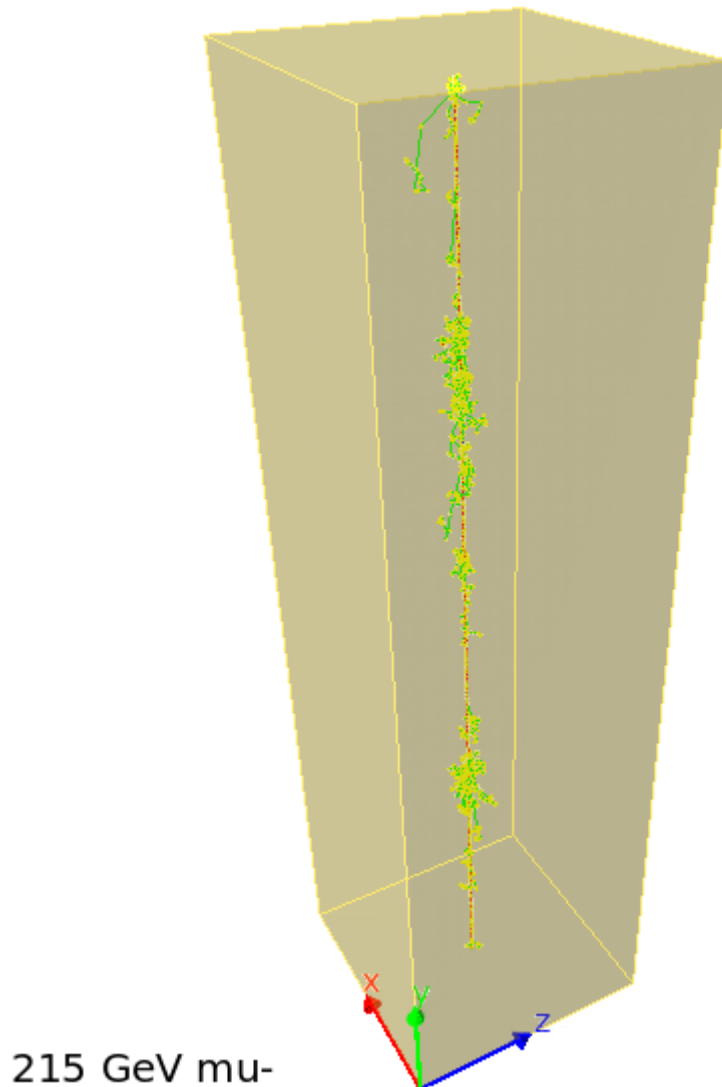


Figure 4.1: A view of the detector for the cosmogenic simulation. It is a cuboid filled with an atom distribution, that resembles LAB. It has a density of 0.859 g cm^{-3} at 20°C . The dimension are (10.0, 35.4, 10.0)m. Also shown in the center is an event of a muon, marked in red, with an energy of 215 GeV. The secondary particles are marked in green and vertices are marked in yellow.

resembling LAB, since this is the usual way to incorporate molecules. The elements and their distribution are listed in table 4.1. The LAB is simulated in a liquid state with a density of 0.859 g cm^{-3} at a temperature of 20°C throughout the detector. These values are taken directly from the JUNO simulation. Hence, this should characterize the JUNO target well enough¹. For more information on the full JUNO simulation read chapter 5. Additionally, the expected

¹Even though light is simulated in the official JUNO simulation, effects like convection and density differences are not considered yet, but may be added in the future.

Table 4.1: The composition of LAB taken from the JUNO simulation and used during the cosmogenic simulation as the target. The top row labels atoms.

	C	H	O	N	S
Z	6	1	8	7	16
A [g/mol]	10.01	1.01	16.00	14.01	32.066
Mass ratio	0.87924	0.1201	0.00034	0.00027	0.00005

variations² in the liquid scintillator state have little to no effect on the high energetic interactions between muon and the atoms in LAB. Differences would become important for the light generation and transportation as well as detection, but no light is considered in this simulation³. No light is simulated, because it is the purpose of this simulation to study the interactions and spatial distribution of the cosmogenic isotopes. This also reduces the amount of calculations a lot, which in turn enables us to generate a significant amount of statistic in a short time. The generated information is gathered during the tracking process and saved in a binary format, since there is no detection elements in this simulation.

4.2 Simulated cosmogenic physics

An important part of a Geant4 simulation is the correct use of physics, which usually come in the form of physics list that are chosen based on the energy ranges and interactions that need to be considered. Results from different lists and list compositions have been produced. As elaborated at the beginning of this chapter there is very little experimental data for this isotope production. To be able to compare yields with Double Chooz results, the production rate, the cross section and yield for ⁹Li were calculated. As will be presented, there are great variations between different lists. It is possible to create own physics processes to approach the real creation modes, but this is outside the scope of this thesis. Especially, since this chapter is only meant to give an idea of positional creation for ⁹Li and ⁸He and the kinematics involved should be good enough in general, even if the branching ratios and creation modes are not very exact for these isotopes.

The cross section can be calculated with:

$$\sigma = \frac{N_c}{N_t \cdot j}, \quad (4.1)$$

where N_c is the number of created ⁹Li and N_t is the number of target particles, which was

²"Variations" here means: Expected changes in temperature or density, due to heat from electronics or the weight of the scintillator itself.

³Scintillation and Cherenkov light do have an impact on the kinematics in reality, but energy conservation is not considered for these types of processes in Geant4.

calculated to be:

$$\begin{aligned}
 N_t &= N_0 \cdot \frac{V_t \cdot \rho_t \cdot {}^{12}C_{\text{ratio}}}{{}^{12}C_{\text{mol}}} \\
 &= 6.022 \times 10^{23} [\text{mol}^{-1}] \cdot \frac{3.47 \times 10^9 [\text{cm}^3] \cdot 0.859 [\text{g}/\text{cm}^3] \cdot 0.879}{12.01 [\text{g}/\text{mol}]} \\
 &= 1.314 \times 10^{32}.
 \end{aligned} \tag{4.2}$$

Here N_0 is the Avogadro constant, V_t is the target volume, ρ_t is the target density, ${}^{12}C_{\text{ratio}}$ is the mass ratio of carbon in LAB and ${}^{12}C_{\text{mol}}$ is the mol number for carbon. The particle current density j is given in formula (4.3), where the rate has been omitted because this is a simulation and it can be set to one per second.

$$j = \frac{N_\mu}{A}, \tag{4.3}$$

with N_μ is the amount of 1×10^6 muons for physics list testing runs and A is the area of $1 \times 10^6 \text{ cm}^2$.

The yield in cm^2/g per muon Y can be inferred via the relation:

$$Y = \frac{\sigma}{m_t}, \tag{4.4}$$

where m_t is the mass of the target atom, in this case ${}^{12}C$ [70]. The results for different lists can be seen in table 4.2. By looking into these pre curated lists it is revealed what they set out to

Table 4.2: Number of ${}^9\text{Li}$ created per 1×10^6 muons, for different physics lists. Additionally, the cross section and yield have been calculated from the amount of created isotopes using formula (4.1) and (4.3). "+ Decay" in the list combination refers to G4DecayPhysics and G4RadioactiveDecayPhysics. For comparison an estimated for JUNO was added from the Double Chooz paper [70].

Physics lists & combination	${}^9\text{Li}$ created	σ [μb]	Y [$\times 10^{-8} \text{ cm}^2/\text{g}$] per muon
QGSP_BERT_HP	242	1.84	9.24
QGS_BIC	294	2.24	11.2
Shielding	506	3.85	19.3
Double Chooz estimate for JUNO [70]	~ 523	~ 3.98	19.96 ± 1.21
QGSP_BERT_HP + Decay	561	4.27	21.4
QGSP_BIC_HP	643	4.89	24.6
QGS_BIC + Decay	746	5.68	28.5

describe and which physics is considered. Most of them are a collection of standard processes, with the addition of a specific model for hadron interactions. All of these lists, in table 4.2, contain G4EmStandardPhysics, G4EmExtraPhysics, G4HadronElasticPhysics, G4StoppingPhysics and G4IonElasticPhysics. Some slight variations, for example G4EmStandardPhysics_option4 instead of G4EmStandardPhysics or the addition of G4IonPhysics, exist. The main differences arise from the specific hadron physics involved, which also give these lists, in table 4.2, their name. The quark-gluon string (QGS) model is for GeV interactions and applied during hadronic

interactions. For lower energies the binary cascade (BIC) model is used, which treats interactions of protons and neutrons below 10 GeV as well as pions below 1.2 GeV. It is also appropriate for the simulation of nucleon and ion interactions. The Bertini cascade (BERT) model is mainly for protons, neutrons, pions and kaons below ~ 10 GeV. HP stands for high precision data and handles mostly neutron elastic and inelastic interactions below 20 MeV. To make use of high precision data one has to additionally load libraries like Geant4 Neutron Data Library (G4NDL) or Japanese Evaluated Neutron Data Library (JENDL). Additional settings used for *NeutronHP* have been set up with G4NDL4.5 and the recommended flags are used:

- G4NEUTRONHP_SKIP_MISSING_ISOTOPES = 1
- G4NEUTRONHP_DO_NOT_ADJUST_FINAL_STATE = 1
- AllowForHeavyElements = 0

When comparing yields in table 4.2 the same lists with additional decay physics will yield more ${}^9\text{Li}$, than without it. It makes no difference for Shielding as well as QGSP_BIC_HP, because they already contain G4RadioactiveDecayPhysics.

For more information on physics lists refer to the Physics Reference Manual [87] and the Book For Application Developers [88], where one can find information about neutron high precision data: "Nuclear models fail (sometimes catastrophically)..." and "It should be noticed that the information available varies from isotope to isotope and can be incomplete or totally missing.". This all indicates and contributes to the fact that this is a simulation and has to be understood as such. There is no guarantee that the results actually play out as predicted. To verify the claims based on this simulation, an experiment would be needed that studies the local distribution of cosmogenics in liquid scintillator. In general, the physics described by these lists has to be taken with a grain of salt, because the interactions that lead to ${}^9\text{Li}$ and ${}^8\text{He}$ are mainly based on models and very few data points, for comparison with these models, exist.

There is a wide range of production differences, but choosing a physics list that creates the expected amount of ${}^9\text{Li}$ does not mean its the correct physics description. Even results from different experiment types do not agree in some parts. As an example the calculated cross section from NA54 at SPS [85] for ${}^9\text{Li} + {}^8\text{He}$ is $2.12 \pm 0.35 \mu\text{b}$ at a muon energy of 190 GeV. The estimated cross section for JUNO, by calculating the value for ${}^9\text{Li}$ from the power law relation deduced in [70], is $\sim 3.98 \mu\text{b}$ at an energy of 215 GeV. There is a clear discrepancy between these results, therefore it is important to investigate the physics involved. By studying the creation of these isotopes, one can not only enhance the vetoes and in turn statistics for JUNO, but also, by later analysing these isotopes in JUNO, deliver results for a wide range of experiments that need to look into the same matter.

For a comparison with JUNO take a look into section 5.1.1. As a short summary, initially JUNO started with QGSP_BERT_HP, later most of the processes relevant to neutrino physics and scintillation have been customised, with respect to existing processes used in the Daya Bay simulation.

The main physics list which was chosen for this cosmogenic simulation is the precured list Shielding. It was chosen since it described the expected production rate for JUNO, but again this does not mean it is correct. The kinematics involved should be described well enough, for the motivation of new veto approaches.

4.3 Simulated events & results

To be able to reason about veto volumes one has to investigate the spatial production of potentially harmful isotopes. The cosmogenic simulation has been developed for this purpose. The amount of muon events simulated is 1×10^8 . The initial direction is (0,-1,0), with the starting point (0,17.0,0) m. Their energy spectrum, in mega electronvolt, is based on the expected distribution in JUNO⁴, but approximated by an exponential fit:

$$N_\mu = \exp((-6.799 \pm 1.547) \times 10^{-3} \cdot E_\mu) \quad (4.5)$$

This can be rearranged to draw a muon energy E_μ from a random flat distribution between (0,1].

$$E_\mu = \frac{\ln(N_\mu)}{-6.799 \times 10^{-3}} \quad (4.6)$$

These 1×10^8 simulated muons respectively yielded 52351 ⁹Li and 8612 ⁸He isotopes. The ⁹Li yield follows the expected amount very well, which might be a hint that a similar base physics list was used. Hence, it may be the case that there is some simulation bias through the Double Chooz paper by utilizing the same basic physics list or the maintenance of the Shielding physics list is so fast that it was already updated with these recent findings. In any case, this is an indication that this simulation might describe reality, but only an experiment can confirm these results.

The simplest approach to veto these isotopes is a cylinder. To determine the radius for this cylinder we can look at the lateral distribution in figure 4.2. From this figure one can see that about 99 % of ⁹Li isotopes can be contained in a cylinder with radius ~ 2.3 m. For ⁸He even a radius of ~ 2.1 m would be sufficient. Now, one could assume that this is energy dependent and the radius could be adjusted based on the energy deposition of showers. In fact, this is not the case, at least for the lateral distance, which can be seen in figure 4.3. Initiating shower particle energy refers to the kinetic energy and mass from the initial particle branching of from the muon that at a later stage lead to the isotope. This can approximate the shower energy, because this is basically the shower energy for the isotope producing part in a shower. In reality, the energy of that particle can not be determined, because no reconstruction in liquid scintillator is able to resolve single particle tracks inside a shower. This definition of energy should enhance any results concerning a connection between the lateral cosmogenic isotope location and initial energy. But one is unable to visually make out any proportionality between energy and lateral

⁴The fit was performed on the muon energy spectrum that can be seen in figure 5.7 from the chapter simulation.

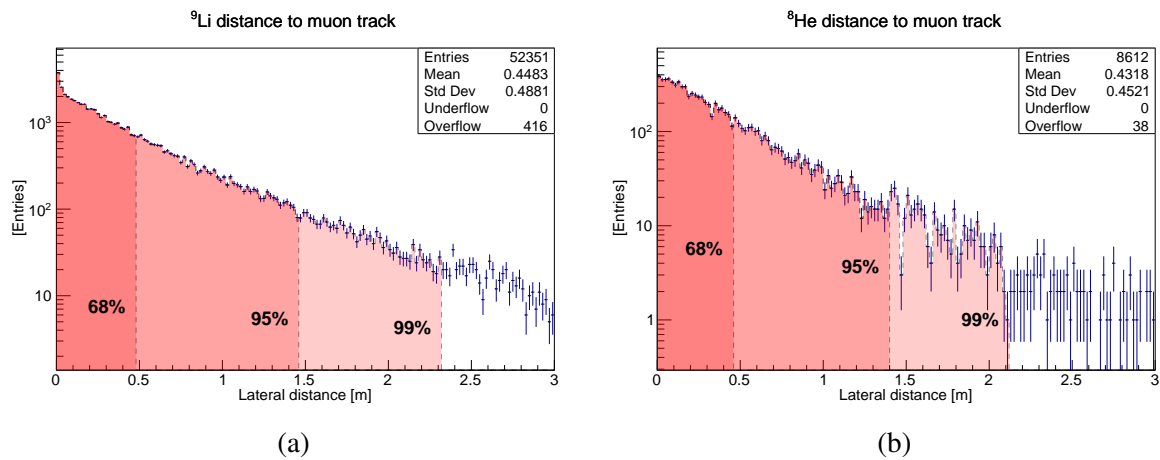


Figure 4.2: (a) The amount of ${}^9\text{Li}$ produced in logarithmic scale, for different lateral distances to the muon track. Filled in shades of red are radii indicating containment of the isotope from 0 to 68 %, 95 % and 99 %. (b) The same for ${}^8\text{He}$, but the number of produced ${}^8\text{He}$ isotopes is only 8512, which is significantly less statistics.

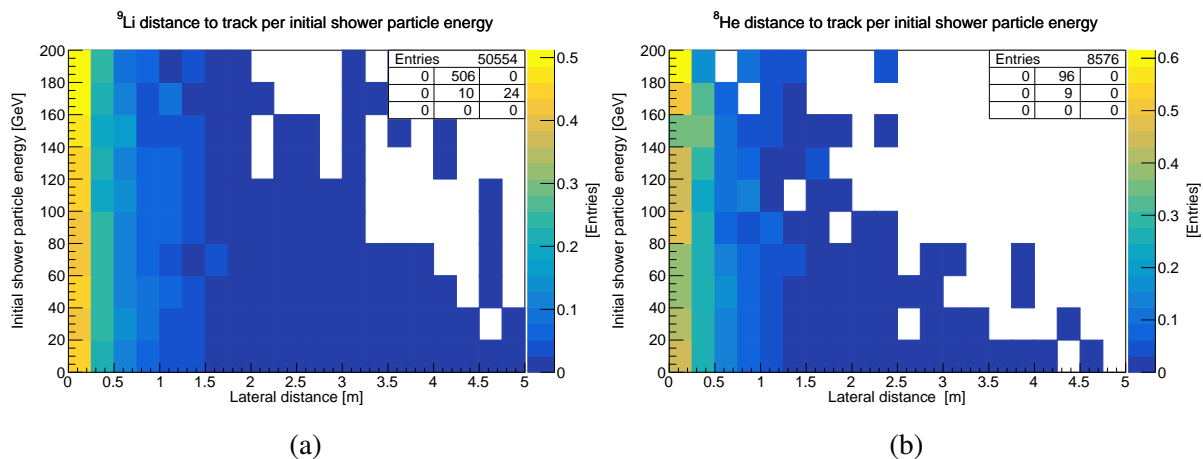


Figure 4.3: (a) The lateral distance of ${}^9\text{Li}$ to the muon track for different energies of the shower initiating particle that lead to the isotope. The sum of every energy range on the y-axis, along x is normalised to 1, so entries are comparable. There are much more low energy entries than high energy entries. (b) The same for ${}^8\text{He}$.

distance. Instead, one could even argue that it is reversed and low energies have a higher probability for larger distances. However, this effect does not seem to be significant.

These results can be compared to a different simulation, described in [89]. It was made for JUNO as well, uses the FLUKA model and also contains information on the lateral isotope distribution. In figure 4.4 on can see the radius that contains 99 % of ^9Li , which is about 3.5 m. The radius containing 99 % of ^9Li in this cosmogenic simulation can be seen in figure 4.2, which is about 2.3 m. This is a discrepancy and maybe a hint that the kinematics involved in hadronic interactions are not well described in Geant4. Nevertheless, the same result of no proportionality between energy and lateral distance has been reproduced in both simulations.

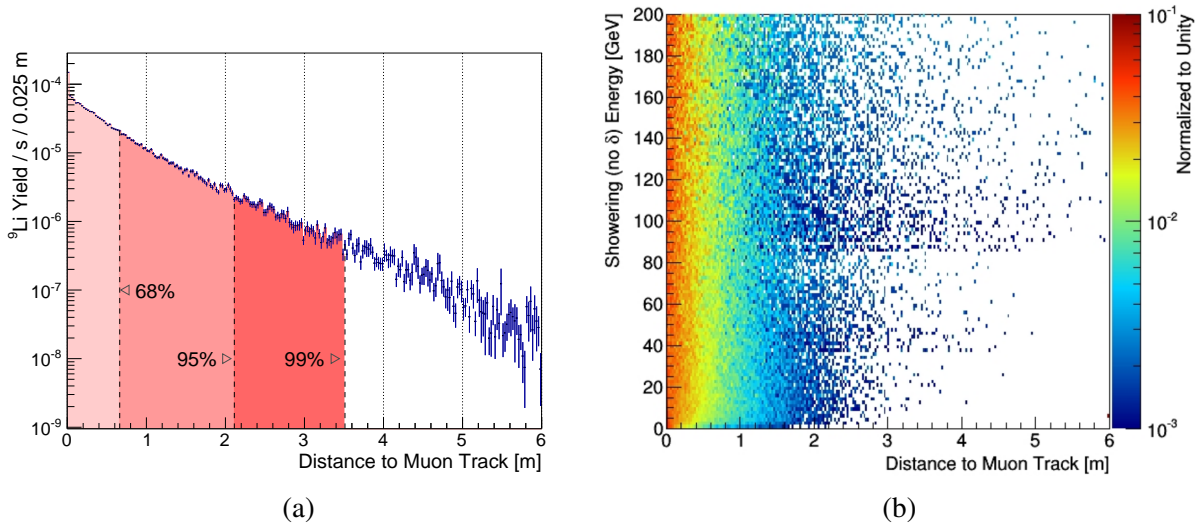


Figure 4.4: (a) The lateral distance of ^9Li to the muon track in a cosmogenic simulation [89], based in FLUKA. (b) Also the lateral distance for ^9Li but different shower energies, normalised for each energy range [89].

When one only considers the lateral distance, it is implied that the topology of a muon event is not of interest for the veto strategy. But by considering of the whole shower kinematics this view can shift. Firstly, a look into the definition that has been used: In figure 4.5 on can see a zoomed in view of a muon shower event in a 2D projection. The trajectory of the muon, is marked by a red line. Almost all secondary particles are visualised by gray lines, except the particles that lead to the creation of the ^9Li isotope, which are marked with black lines. The green line is the distance from where the first particle branched of the main muon track to the creation point of the isotope, which is a combination of lateral and longitudinal distance. Only the point of creation is considered, because the isotope itself travels only a few millimeters and the additional journey, until the delayed signal from respectively ^9Be and ^8Li , is assumed to be negligible. Convection and diffusion is not simulated, but is assumed to be in the range of millimeters due to the short time frame. Therefore, the point of creation for these isotopes is also the point that needs to be considered for a veto. In figure 4.6 a projection can be seen, containing the just established distance from initial shower particle to isotope creation point. From here onwards this is the used definition of distance. The muon direction is from left to

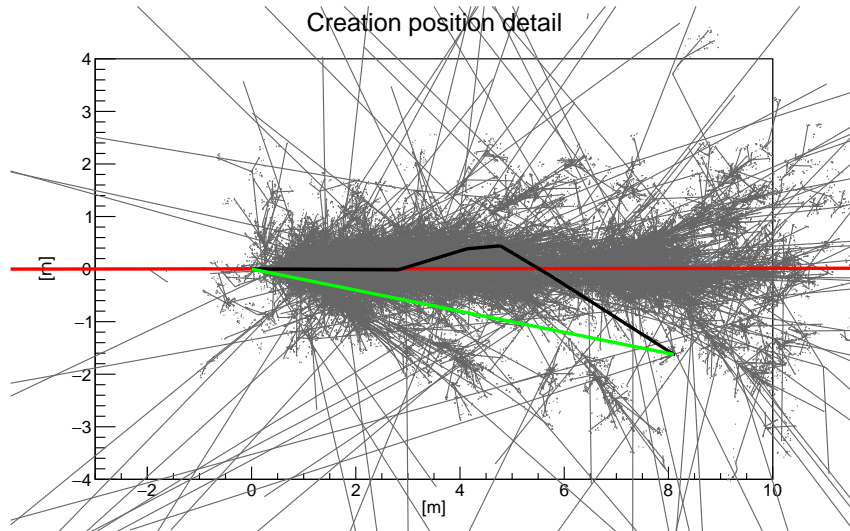


Figure 4.5: Muon shower projection, were a 215 GeV muon is entering from the left. Its path is marked by the red line. All secondary particles are indicated in gray. Marked in black are the particles that let to a ${}^9\text{Li}$ isotope. Starting at the initial interaction of the muon, with a target atom, which produced this shower and ending at the isotope. This distance, marked in green, between the initial interaction and the isotope will be used as a none lateral distance definition.

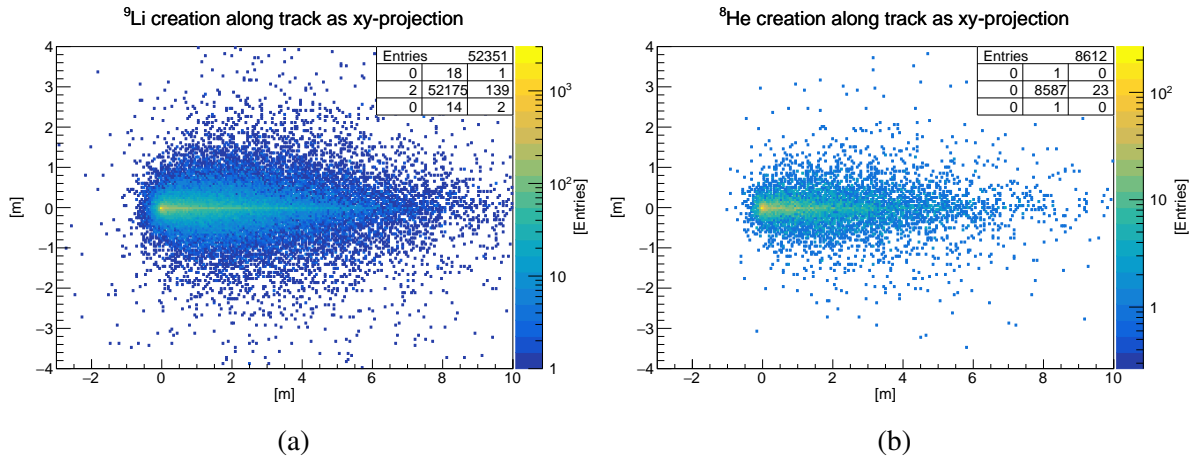


Figure 4.6: (a) The point of isotope creation is projected onto the yx-plane for each ${}^9\text{Li}$, when a shower could be found. The initial shower starting point is at (0, 0) m and this utilises the distance definition from figure 4.5. The shape of isotope creation can be used for veto strategies. (b) The same for ${}^8\text{He}$.

right. At (0,0) m the shower starts and for each created isotope the distance is projected into the yx-plane. The distribution follows a drop like shape, which is to be expected for boosted high energy events. Most of the isotopes are produced directly at the interaction point and roughly taper off in an exponential fashion. This can be used as a starting point for the development of shower vetoes.

As already established, the lateral distance does not depend on the energy, but kinematic does play a role during the longitudinal distribution. In figure 4.7 one can see an accumulation of isotopes depending on shower energy and distance. The distribution look similar for both isotopes.

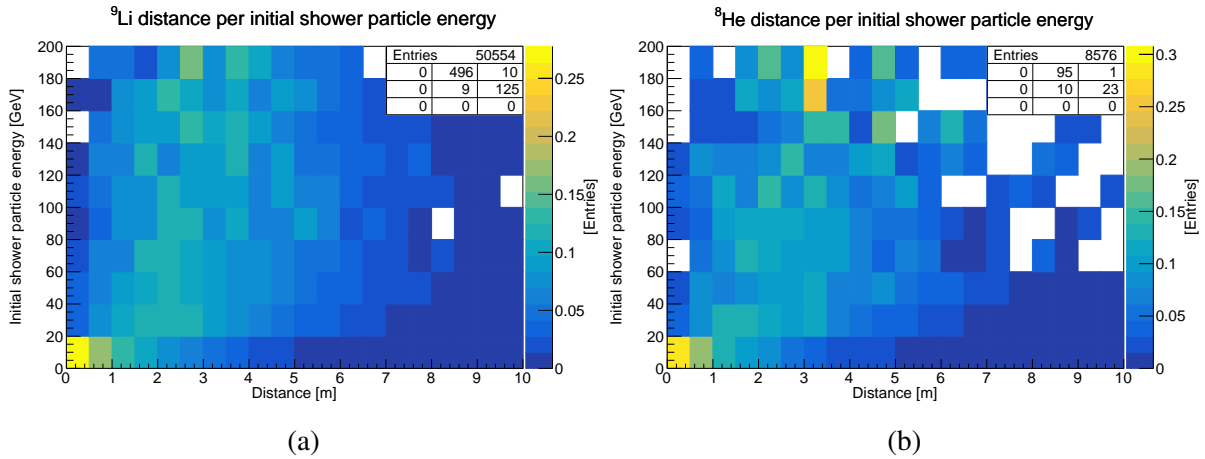


Figure 4.7: (a) ${}^9\text{Li}$ creation distance for different initial shower particle energies. This uses the distance definition from figure 4.5. The initial shower starting particle energy is used to check for a correlation between distance and energy. This particle eventually produces ${}^9\text{Li}$. The bins in this plot are normalised to 1 for each row in x-direction. (b) The same for ${}^8\text{He}$.

The same graph, considering only longitudinal distance, can be found in Appendix A. This is promising, but during the real experiment the initial shower particle energy is unobtainable. To move from here to something obtainable, the actual shower energy has been used in figure 4.8. One can see the distribution persists even after exchanging the shower energy definition. Here

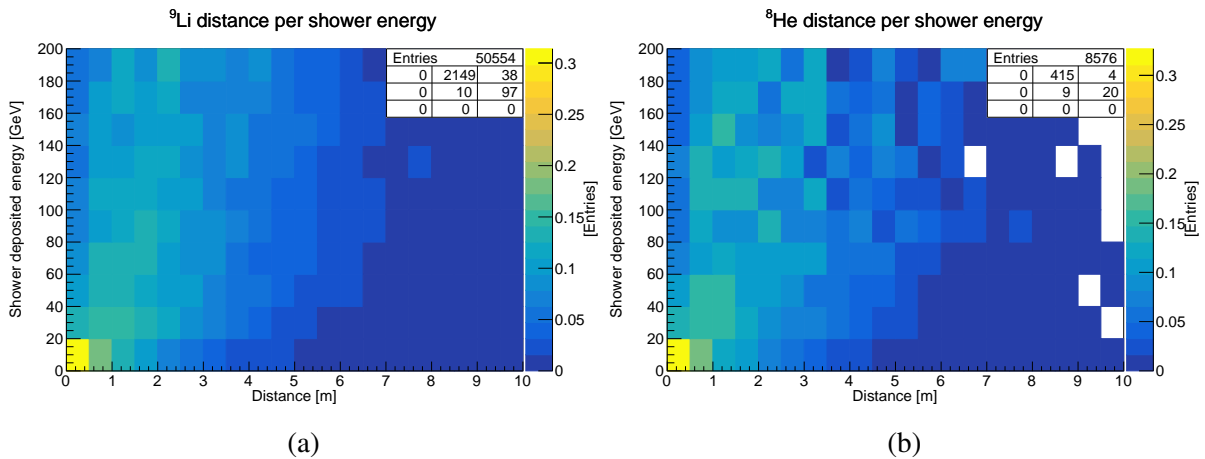


Figure 4.8: (a) ${}^9\text{Li}$ creation distance for different shower energies. This uses the distance definition from figure 4.5. The bins in this plot are normalised to 1 for each row in x-direction. (b) The same for ${}^8\text{He}$.

the total deposited energy of all particle in a shower has been summed up to obtain this result. This definition of shower energy is something that the topological reconstruction approaches in chapter 6 and 7 should be able to reconstruct reliably. But there is an even simpler definition, that yields similar result, which can be seen in figure 4.9. Here, only the shower length has been used, which is the most basic reduction, because this figure already describes the distance of isotope production. This is dominated by the longitudinal distance of the shower expansion. The definition of shower length is set by an energy deposition threshold, which is a pretty ar-

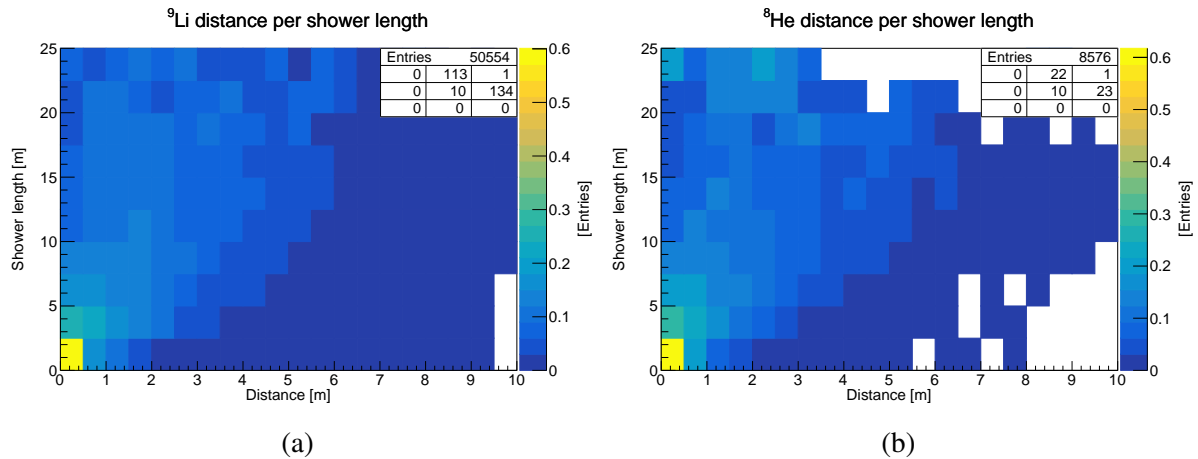


Figure 4.9: (a) ${}^9\text{Li}$ creation distance for different shower lengths. If the shower energy is not obtainable the shower length could be determined by setting a threshold. This plot uses the distance definition from figure 4.5. The bins in this plot are normalised to 1 for each row in x-direction. (b) The same for ${}^8\text{He}$.

bitrary definition. But in principle this should not affect the shower length much, compared to other definitions, because it only introduces a constant systematic error that other definitions will also suffer from. The definition of what defines a shower and its size is not well described in general, because it is actually just a concept that is used to cope with the fact that a shower is simply a lot of particle tracks at a small area. The track density at that area is so high that the tracks are unlikely to be resolve. Hence, the description as a shower is used, to get hold of characteristic parameters and features, which enables one to get some form of description. This brings up another issue, which is finding the starting point of a shower. Particles will move in all directions from the starting point, but they will be boosted in the direction of the initial particle. A threshold can be used to define a beginning of a shower. If neither the starting point nor the beginning can be found, the peak energy depositions along the track could be used, to define a shower position. The distribution of isotope production as a xy-projection has been redone for the shower beginning in figure 4.10 and for the shower maximum peak 4.11. These descriptions for cosmogenic distributions should be reconstructable. It would be cleaner to have the real initial shower starting point to create a more confined veto, but this is probably not obtainable in reality. The isotope distributions from figure 4.6, 4.10 and 4.11 can be used to construct improved vetos. Which of these will create the most desirable veto strategy will be discussed at the end of the next section, but one can already deduce that any of these three approaches will create less dead volume than the default approach of a cylinder.

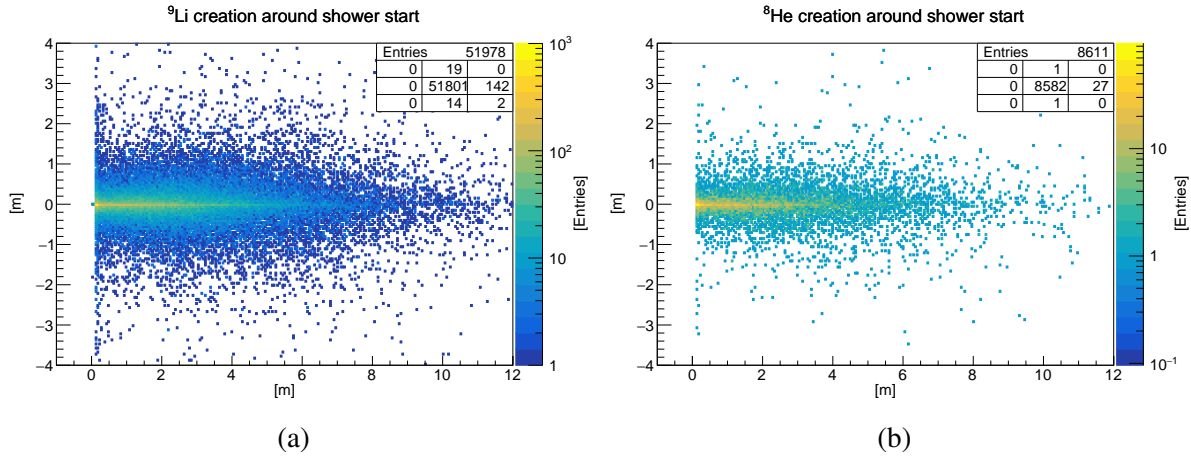


Figure 4.10: (a) The point of isotope creation, projected onto the yx -plain for each ${}^9\text{Li}$, when a shower could be found, depending on the determined shower starting point along the track. The shower threshold was set to be 5 MeV per cm above the muon deposited energy. The shower starting point is at (0,0) m and to this, the relative isotope location is populated. This shape can be used to develop veto strategies. (b) The same for ${}^8\text{He}$.

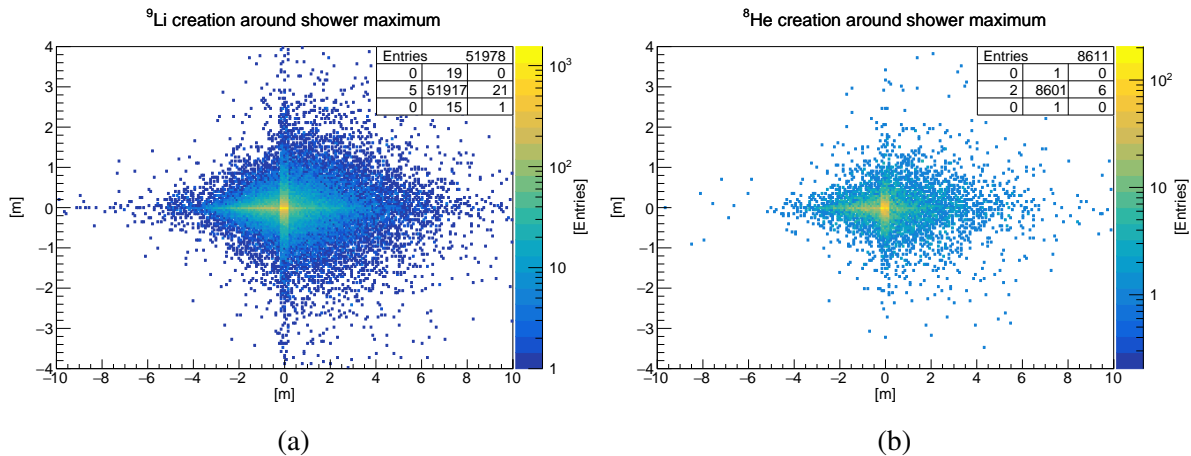


Figure 4.11: (a) The point of isotope creation, projected onto the yx -plain for each ${}^9\text{Li}$, when a shower could be found, depending on the determined shower maximum along the track. The shower maximum is at (0,0) m and to this, the relative isotope location is populated. This shape can be used to develop veto strategies. (b) The same for ${}^8\text{He}$.

4.4 JUNO muon veto assessment

What is the impact of a more confined muon veto for the JUNO experiment? This section will start with a recap of the current JUNO veto strategy. The results from the cosmogenic simulation will be used for veto development. In the final paragraph, custom veto approaches will be tested and the requirements for a muon reconstruction will be gauged.

4.4.1 Preliminary official veto strategy

The criteria for muons in JUNO are stated in Neutrino Physics with JUNO [36]. The background assessment already mentions ${}^9\text{Li}$ and ${}^8\text{He}$ as potentially harmful candidates and has stated the preliminary veto strategy for muons with the following criteria:

- For the muon itself \rightarrow Veto whole detector for 1.5 ms
- If untrackable \rightarrow Veto whole detector extend time to 1.2 s
- If well tracked \rightarrow Veto cylinder around track with radius 3 m for 1.2 s

Additionally, other cosmogenics like ${}^{11}\text{C}$ and ${}^{14}\text{C}$ are also important, especially for solar neutrino physics with JUNO. These have not been the focus of the previously stated simulation, but should in principle behave in a similar way as ${}^9\text{Li}$ and ${}^8\text{He}$. The following states an approximation of the veto effectiveness and the expected dead volume resulting from the criteria above.

The initial veto of the whole detector for 1.5 ms is very short compared to the extension to 1.2 s. Therefore, one can simplify the veto calculation to only consider the 1.2 s long vetos. The calculation including the initial veto of 1.5 ms is stated in appendix A, but basically a similar result is obtained. The simple veto efficiency ϵ_{full} of the full detector for untrackable muons can be given by [89]:

$$\epsilon_{\text{full}} = 1 - e^{-\frac{t}{\tau}}. \quad (4.7)$$

As an example only ${}^9\text{Li}$ is considered. For ${}^9\text{Li}$ the mean decay time τ is ~ 255 ms and the initial veto time $t = 1.2$ s, this results in efficiency $\epsilon_{\text{full}} = 0.991$. To calculate the efficiency for the cylinder one can modify equation (4.7) with the ratio R_r of isotope captured by a cylinder with radius $r=3$ m:

$$\epsilon_{\text{cyl}} = R_r \cdot \left(1 - e^{-\frac{t}{\tau}}\right). \quad (4.8)$$

The ratio $R_{r=3\text{m}}$, of cosmogenics contained inside a cylinder with radius 3 meters, can be obtained from figure 4.2, which states the lateral distribution of cosmogenics. Assuming the lateral distribution from the simulation is kinematically correct, one can take this sample and count how much ${}^9\text{Li}$ is inside a cylinder with radius of 3 meters compared to all ${}^9\text{Li}$ in the sample. Using this, the ratio can be calculated to be:

$$R_{r=3\text{m}} = \frac{52351 - 416}{52351} = 0.992 \pm 0.004 \quad (4.9)$$

This means 99.2 % of ${}^9\text{Li}$ isotopes are inside the cylinder and the error is just the statistical one from the sample size. Therefore, the efficiency of the cylindrical veto is $\epsilon_{\text{cyl}} = 0.983 \pm 0.004$. By utilising the same assumption, as in Neutrino Physics with JUNO [36], that 99% of muons are well tracked. The total efficiency for ${}^9\text{Li}$ is:

$$\epsilon_{\text{total}} = 99\% \epsilon_{\text{cyl}} + 1\% \epsilon_{\text{full}} = 0.983 \pm 0.004. \quad (4.10)$$

The definitions used in the yellow paper for trackability are later defined for showering muons as well as multi muon events. Reconstruction development for bundle muon events is currently ongoing and track reconstruction for showering muons is expected to reach 99 % efficiency. Contributions from these types of events are not negligible. About 20 % of muons are expected to be showering and showering muons produce more than 85 % of these isotopes [1]. Additionally, about 11 % of muon events are estimated to be multi muon events, which will account for ~ 31 % of all muons. Hence, about one third of potentially harmful isotopes [89]. This will not impact the veto efficiency much, but it will increase the dead volume per time.

For the worst case scenario, when multi muon and shower events cannot be tracked, one can calculate the dead time. For this the expected muon rate at JUNO is needed. This information can be found in table 1. from [1]. The event frequency is expected to be 4.1 ± 0.9 Hz and the frequency of only single muons is 3.4 ± 0.7 Hz. Additionally, the frequency of muons striking the detector is 5.4 ± 1.2 Hz, counting each muon, even if they arrive at the same time and only count as one event, because of multi muon events.

For each muon event, at a frequency f_{event} of 4.1 Hz, the detector is dead for 1.5 ms and with a single muon frequency f_{single} of 3.4 Hz this results in ~ 82 % single muon hits, with a shower probability P_{shower} of ~ 20 % for all muon tracks. Assuming showering and multi muon events are not trackable, the trackability T can be calculated with:

$$T = \frac{f_{\text{single}}}{f_{\text{event}}} \cdot (1 - P_{\text{shower}}) \quad (4.11)$$

and results in a T of ~ 66 % of muons that can be tracked. As an interesting side note, these none showering muon events account for < 15 % of the harmful isotopes. Hence, if one would not apply a veto for these events, the dead volume could be reduced significantly, but the signal would be compromised a bit.

The rate of muons that cannot be tracked create the worst case scenario, where on average the whole detector is dead 100 % of the time. The frequency of untracked muons f_{un} would be:

$$f_{\text{un}} = f_{\text{event}} \cdot (1 - T) \quad (4.12)$$

This results in a frequency of $f_{\text{un}} = 1.39$ Hz, which means every ~ 0.72 seconds a untrackable muon event occurs and the veto time of 1.2 s is almost double that. This implies that especially showering muons must be trackable for JUNO, but also muon bundles play an important role.

4.4.2 Possible improvements

The previous results urge one to develop a muon reconstruction that can track shower events as well as multi muon event. What actually changes in a best case scenario? Of course the efficiency could be improved by making veto volume larger and extending the veto time, but for comparability the stated default veto time and efficiency are left as it is. The assumptions for the best case scenario then can be summarized as follows:

1. Showers and high energy deposition can be detected and their position determined.
2. The isotopes are only created in significant amounts at shower locations.
3. Muon bundle events are assumed to be reconstructable.
3. During muon bundle events it is assumed to be possible to determine showers.

These assumptions need to be verified by data, but currently only the comparison to the simulation is possible. The shower detection and muon bundle reconstruction capabilities of the topological reconstruction approach will be discussed later, in chapter 8.

The veto efficiency and dead time can be determined, for the best case scenario, when 100 % trackability would be achieved. This is unrealistic, but can be done as an example for ${}^9\text{Li}$, with the default veto criteria. Then the total ${}^9\text{Li}$ veto efficiency is just the efficiency of the cylindrical veto $\varepsilon_{\text{cyl}} = 0.986 = \varepsilon_{\text{total}}$. For the dead volume one can use the spherical symmetry of JUNOs central detector target and reduce the problem to one dimension. Assuming all muon tracks are straight and the cylindrical veto will traverse the whole detector regardless of muons stopping inside the detector. Then the only parameter that determines the size of the dead volume V is the lateral distance d of the muon track to the detector center and for the simplest case of $d = 0$ m can be given by:

$$V(d = 0) = V_{\text{cyl}}(r, H) + 2 \cdot (V_{\text{cap}}(D, r, h)) = \pi r^2 H + 2 \cdot \frac{\pi h^2}{3} \cdot (3D - h). \quad (4.13)$$

The radius of the cylinder is $r = 3$ m and the height of the cylinder H can be given by:

$$H = 2 \cdot \sqrt{D^2 - r^2}, \quad (4.14)$$

were D is just the maximum possibly distance from the center 17.7 m, which is the target radius of JUNO. The cylinder cap height $h = D - H/2$. With this we can derive $V(0) = 993.66 \text{ m}^3$. The other cases are more complex, hence a numerical solution was used and the result for $V(d > 0)$ can be seen in figure 4.12 (a). The voxel size for the numerical volume determination is 1 cm^3 .

To calculate the average veto volume per muon, $V(d)$ needs to be weighted with the probability density $P(d)$ of a muon hitting at that lateral distance. This can be calculated by:

$$P(d) = \frac{2d}{D^2} \quad (4.15)$$

This is assuming equal distributions of muons in an xy-plane. The veto volume per muon weighted with the probability density can be seen in figure 4.12 (b). The mean volume V_{mean} that a muon will veto is $\sum_{d=0}^D V(d) \cdot P(d) = 647.04 \text{ m}^3$.

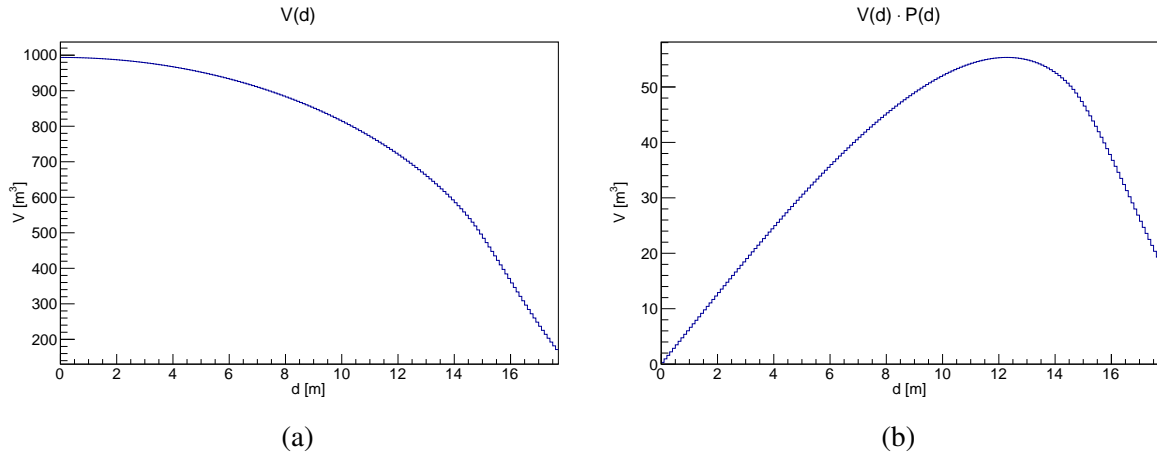


Figure 4.12: (a) Numerical solution for veto volume per muon $V(d)$ depending on distance d to center for the cylinder case. (b) The veto volume per muon weighted with the probability density $P(d)$ of radial hit probability.

Finally, the frequency of muon events needs to be taken into account, since a cylinder per traversing muon is needed. This introduces an error when cylinders are overlapping, but it should be small for muon bundles, since on average the distance for muons in a muon bundle event is around 10 m. But the possibility of already vetoed area being struck by a muon again is possible and probably not negligible. Hence, for the following calculation it is probable that the real world number is even smaller. By considering the total frequency f_{total} of muons striking the detector, which was stated to be $5.4 \pm 1.2 \text{ Hz}$ [1], the average dead volume at any given time V_{dead} can be calculated. In the best case scenario, with default criteria and under the approximation that a veto is never striking another veto, the average dead volume is:

$$V_{\text{dead}} = V_{\text{mean}} \cdot t \cdot f_{\text{total}}, \quad (4.16)$$

which is $V_{\text{dead}} = 4192.82 \text{ m}^3$ with the ^9Li veto time of $t = 1.2 \text{ s}$. Considering the detector target volume $V_{\text{target}} = \frac{4}{3} \pi D^2 = 23228 \text{ m}^3$, the ratio of dead volume is $R_{\text{dead}} = V_{\text{dead}}/V_{\text{target}} = 18.1 \%$. This does not consider the 1.5 ms full detector veto for each muon event. It can be neglected, when comparing different veto strategies, because it is the same for every veto approach.

18.1 % is already much better than 100 % dead, but the ratio of dead volume R_{dead} could be improved even more, by only vetoing showering muons. Of course, that implies the possibility to identify showering muons. Since, the rate of showering muons is expected to be around 20 %, this reduces the frequency f_{total} of muons that need to be vetoed to 20 %. Hence, $R_{\text{dead}} \cdot 20 \% = 3.6 \%$, but this would reduce the veto efficiency to about 83.6 %. To bring it back up, one could veto with a cylinder of smaller radius and catch the isotopes from no showering muons this way.

4.4.3 Custom veto creation

Previous sub-section calculated dead volume for the default cylindrical veto, but this could be further improved by applying a veto made specifically for the positional isotopes distribution. Based on the obtainable parameters from the topological reconstruction it is possible to replace the default cylindrical veto with relatively simple veto shapes, which can be seen in figure 4.13. These shapes are based on the earlier discussed simulation results for the cosmogenic

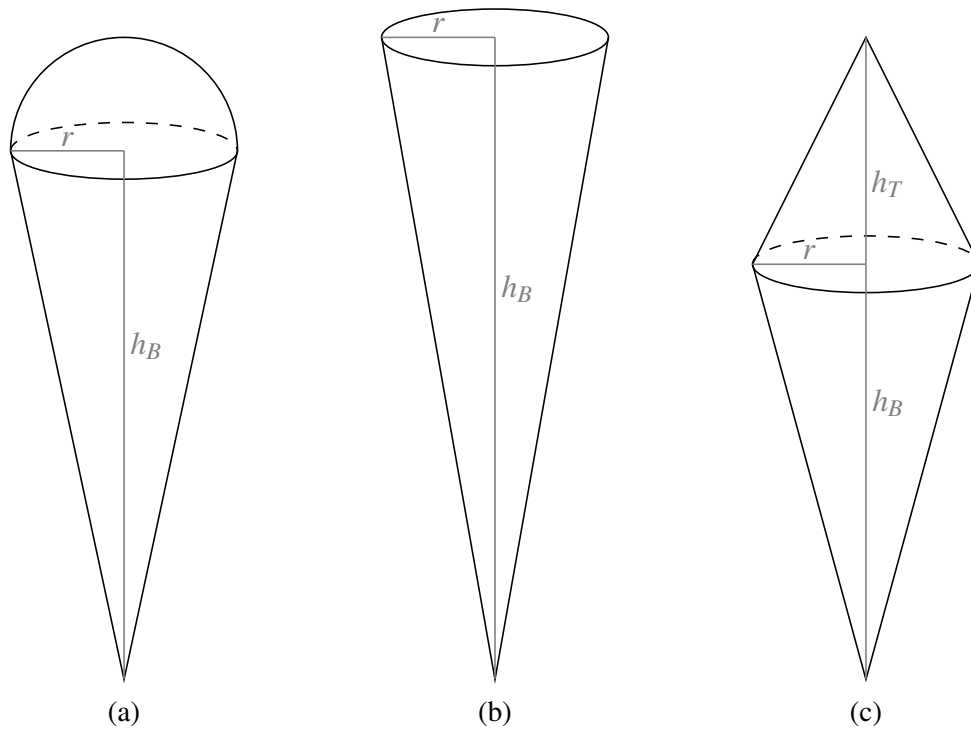


Figure 4.13: Different custom veto approaches, that will be tested for dead volume. For each strategy, a muon is entering from the top and travels along the axis marked h_B . r will be denoted as cone radius, h_T is also called top height and h_B will be referred to as bottom height. A shower is produced and around this, these custom vetoes will be applied. (a) will be referred to as the *ice cone*, (b) will be the *cone* approach and (c) is the *double cone* design.

distributions. All of these assume a muon travelling vertically through the veto and that it produces a shower. These veto shapes are meant to contain most of the cosmogenics, which may be produced during a shower event. If cosmogenics are produced along the track, but no shower can be detected, it is possible to add a cylinder around the track, with a smaller radius. The radius of such a cylinder would need to correspond to the expected transversal distance of a cosmogenic nucleus for the case that no shower was detected. The threshold for a shower depends on the reconstruction and so does the radius connected to it. When comparing these vetoes, the cylinder would apply to all in the same way. Hence, it can be neglected for now.

- (a) The half sphere with cone shape, also called *ice cone*, is based in figure 4.6 and assumes the perfect reconstruction of the point where the initial particle, that lead to the cosmogenic, left the muon track. It is unrealistic to obtain this parameter, but it will be interesting to compare this to the other two options.
- (b) The *cone* is based on figure 4.10 and here the start point of a shower is taken to start the veto. The detectability of a shower depends on the reconstruction and so does the energy threshold where a shower can be detected. For this example the shower threshold is triggered when more than 5 MeV per cm along the track is deposited, which is not counting the energy deposited by the muon itself.
- (c) The *double cone* is used when tracking the maximum of a shower, which should be a point that is relatively simple to obtain for a reconstruction. This shape was chosen based on figure 4.11.

These 3 veto options have a few free parameters. The ones that apply to all are the radius of the cone base r and the total height in track direction h_B , also called bottom height. As a starting point a radius of $r = 3$ m was chosen, for comparability with the cylinder and by eye it can be determined that a total height of 17 m for all three seems reasonable. There are different tail cone length for each veto, which can be seen in table 4.3. With these parameters the proposed veto volumes are well defined. There is a number of possible adjustments for the veto parametrisation, but this should be enough for a simple first approach. It would also be an option to construct even complexer vetoes to describe the cosmogenic distributions more exactly, but the dead volume reduction should be negligible compared to the ones already described and the introduction of more parameters would make the evaluation unnecessarily complex. Additionally, also the ^8He isotopes could be used through out this veto development efforts, but in principle the kinematic distribution is similar to the ^9Li distribution and the low amount of ^8He samples would yield a much greater error. Hence, it is neglected here, but it should produce similar results as the ^9Li .

The efficiencies for these veto volumes can be calculated with data from the cosmogenic simulation and then can be compared. This has been done for total length of 17 m and $r = 3$ m. The results can be seen in table 4.3. For the volume data the same numerical solution was used

Table 4.3: The efficiencies for different veto types, with a radius of 3 m and total height of 17 m. For comparability the length of the cylinder was set to 17 m as well, for volume and efficiency. The statistical error on the efficiency is $1/\sqrt{51838} = \pm 0.004$.

Veto type:	Cylinder	Ice cone	Cone	Double cone
r [m]:	3	3	3	3
h_T [m]:	-	-	-	6
h_B [m]:	-	14	17	11
Volume [m ³]:	647.04	153.95	120.15	132.23
Veto ε for ^9Li :	0.983	0.975	0.972	0.970

as in 4.12, with the addition that an even distribution of showers along the track is assumed. The table already hints, that the volumes are significantly smaller and already reach efficiencies above 97 %. Two parameters are interesting in this analysis, the efficiency and the veto volume. To ensure comparability, the veto time should not be altered and therefore the ratio of isotopes inside the veto is proportional to its efficiency. Furthermore, the efficiency can be set to a fixed value. Then one can evaluate the veto just by examining the dead volume. To hold the custom vetoes up to the same standard as the default cylinder, one can specify that the efficiency must reach the same value as the default approach. As a reminder, the total efficiency of the default cylinder approach is $\epsilon_{\text{total}} = 98.3\%$, for the simulated ${}^9\text{Li}$ sample. A minimization algorithm was developed to determine the smallest volume for a custom veto to enclose 99.2 % of the ${}^9\text{Li}$ isotopes. This means the same total efficiency as for the cylinder is reached. The results can be seen in table 4.4. There are 3 free parameters for each custom veto. All of them have a

Table 4.4: Determination of smallest volume containing 99.2 % of the ${}^9\text{Li}$ isotopes from the cosmogenic sample. Determined by the developed minimisation algorithm, with step size 1 cm. The volume error is dominated by input value variation and the error was determined by fitting a Gaussian distribution to the distribution of results, when varying the minimisation start values. The statistical error on the efficiency is $1/\sqrt{51838} = \pm 0.004$.

Veto type:	Cylinder	Ice cone	Cone	Double cone
r [m]:	3	4.05	4.7	4.61
h_T [m]:	-	-	-	5.3
h_B [m]:	-	11.71	14.3	11.63
Shift [m]:	-	2.86	-0.01	-
Volume [m^3]:	647.0	281.3 ± 2.5	249.6 ± 5.1	298.4 ± 9.2
Veto ϵ for ${}^9\text{Li}$:	0.983	0.983	0.983	0.983

radius and the height of the bottom cone. For the ice cone veto and cone veto the position along the track is also a free parameter and is called shift. The double cone veto has the top cone height as a free parameter, but the shift is fixed to 0. This leaves all custom vetoes with 3 free parameters. The topology of the parameter space is fragment for the needed efficiency of ${}^9\text{Li}$, because of the relatively small sample size of 51838 isotopes. Hence, there are some variations in the results, depending on the starting parameters and there will be smaller volumes containing the needed amount of isotopes. The error on the mean volume is defined here as the sigma of a Gaussian fit, which was performed on a set of minimisation results, generated by varying starting parameters.

The longitudinal isotope travel distance is also dependent on the energy of the shower, which can be deduced from figure 4.7 and 4.8. Each isotope energy⁵ has a longitudinal distance connected to it and intuitively the probability of finding it further along the track is logarithmically proportional to its energy. But only a few isotopes per energy is not enough for this pattern

⁵The energy term here means the kinetic energy of the initial particle, created by the muon, that later lead to the isotope.

to emerge. In an effort to connect some statistical information to the longitudinal isotope distribution, the sample of ^9Li cosmogenics was sorted by energy and separated into batches of about 1000 events. This enables one to have a longitudinal isotope distribution for a given energy. This can be seen in figure 4.14 (a). The respective distance for all ^9Li isotopes has been filled in track direction, for 51 batches sorted by energy. Here, height h is only the longitudinal

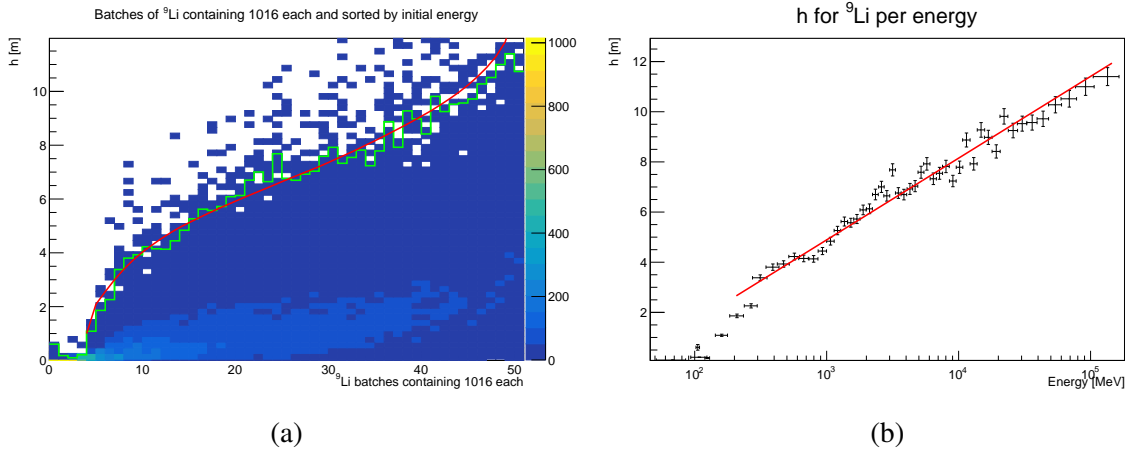


Figure 4.14: (a) Longitudinal ^9Li distance h for 51 batches containing 1016 isotopes each. The green line is marking the limit where 99.2 % of ^9Li are contained below. (b) The same 51 batches with their mean energy on a logarithmic scale on the x-axis and the height h , of the limit that contains 99.2 % of ^9Li , on the y-axis. The fit (4.17) is marked in red for both figures.

distance component from the interaction point to the isotope, from distance definition in figure 4.5. Each batch has a height limit where 99.2 % of isotopes are contained, which is marked by the green line. The mean energy and this height limit for each batch is used to create a data point in figure 4.14 (b). The batches have some variation in the energy range they represent, because there are more isotope samples with low energy compared to the high energy range. This means, there are more batches for smaller energies and they have a smaller energy range attached to them. Hence, the error attached to them is also smaller and in turn the error for higher energy ranges is larger. This is represented by the errors in figure 4.14 (b) and one can see, from the logarithmic scale of the x axis, that there are more data points for lower energies. The distribution of data points in this figure roughly follows a straight line, which enables one to turn this into a useful tool, that can describe the veto bottom height with the initial particle energy. A fit for a logarithmic function has been performed and the result can be seen as the red line in both plots. The fit function result is as follows:

$$h(E) = \log(E \cdot (0.032 \pm 0.003) [\text{MeV}^{-1}]) \cdot (1.42 \pm 0.02) [\text{m}]. \quad (4.17)$$

With this one can reduce the mean veto volume even further, by allowing for individual bottom cone height h_B , based on the initial energy. For this, h_B is comprised of a minimum height plus the additional height described by fit (4.17). The results can be seen in table 4.5. This changes the height individually for every isotope, based on the initial shower particle energy.

Table 4.5: Results of the minimization algorithm after allowing for individual cone length based on the initial energy, with step size 1 cm . The smallest volume containing 99.2 % of the ${}^9\text{Li}$ isotopes from the cosmogenic sample, with the bottom cone height h_B defined as minimum height plus energy based height from fit (4.17). The volume error is dominated by input value variation and is the sigma value of a Gaussian fit to the result distribution. The statistical error on the efficiency is $1/\sqrt{51838} = \pm 0.004$.

Veto type:	Cylinder	Ice cone	Cone	Double cone
r [m]:	3	3.89	4.82	4.21
h_T [m]:	-	-	-	5.67
Minimum h_B [m]:	-	3.87	5.96	5.66
Mean h_B [m]:	-	10.52	12.61	12.31
Shift [m]:	-	2.82	-0.01	-
Volume [m^3]:	647.0	257.3 ± 3.8	236.6 ± 8.0	280.8 ± 8.6
Veto ϵ for ${}^9\text{Li}$:	0.983	0.983	0.983	0.983

For all custom vetoes with energy dependency 4.17 the mean veto volume was reduced by at least 12 m^3 . For the mean veto volume integration, the bottom height h_B is now represented by the mean of all heights for the sample and is composed of the individual height per event from fit 4.17 and an added minimum height. For the isotopes positions tracked by shower start and shower maximum the energy relation seems to break down below 200 MeV. Hence, for initial energies below this, the height h_B is set to 2.5 m plus minimum height. The same minimization algorithm as for table 4.4 was used and all custom vetoes still have 3 free parameters.

As stated before, it is unrealistic to obtain the energy of the initial particle, that later lead to the isotope, because there is no reconstruction for JUNO that can resolve single particle tracks in a shower. But it may be possible to determine the total energy of a shower and a new fit can be determined, that will describe the veto bottom height h_B based on that total shower energy. This has been done and the results are still better than the ones from table 4.4, but worse than table 4.5. This means the results from table 4.5 can be seen as a maximum improvement, with energy dependency. The improvements are not really significant and only free up additional $\sim 0.5\%$ of the detector volume for the case that a shower is detected. Therefore, the shower energy dependent veto results are not stated here. At this point, the dead volume is mainly dominated by the none showering case, which will be discussed in the next paragraph.

Returning to the case of no shower detection and there is very little data for it. For the no shower detection case, the threshold was set to more than 5 MeV per cm over the muon energy. Hence, for the no shower case, this implies low statistics for the determination of a radius for a cylinder. The transversal distribution of ${}^9\text{Li}$ for the no shower case is in the appendix A and has only 551 entries, but as an example one can choose a radius of 1.55 m, which is the distance that can be taken from that figure, for 99 % containment. Then the mean dead volume, for the none shower case, can be determined, which is $V_{\text{none}} = 176 \pm 8 \text{ m}^3$. With this and the mean volume for each custom veto from table 4.4 and 4.5, the dead volume can be calculated with equation

(4.18), which is evolved from equation (4.16).

$$V_{\text{dead}} = t f_{\text{total}} (R_{\text{shower}} \cdot V_{\text{mean}} + (1 - R_{\text{shower}}) \cdot V_{\text{none}}), \quad (4.18)$$

where the ratio of showering muons is $R_{\text{shower}} = 20 \pm 4 \%$, $f_{\text{total}} = 5.4 \pm 1.2 \text{ Hz}$ is the frequency of muons striking the detector and the time the veto is applied is $t = 1.2 \text{ s}$. The results obtained with (4.18), can be seen in table 4.6. The table summarises the dead volume in JUNO

Table 4.6: Dead volume for different custom veto types, with mean volume from table 4.4 and 4.5 using equation (4.16). Additionally, expressed as ratio of dead volume, in percent of a total target volume $V_{\text{target}} = 23228 \text{ m}^3$. The default cylinder is always $r = 3 \text{ m}$ for every muon, but the adaptive cylinder has a $r = 1.55 \text{ m}$ for none showering muons and $r = 3 \text{ m}$ for showering.

Veto type:	Default Cyl.	Adaptive Cyl.	Ice cone	Cone	Double cone
$V_{\text{dead}} \text{ static } h_B [\text{m}^3]:$	4192 ± 931	1751 ± 410	1277 ± 288	1236 ± 278	1300 ± 293
$V_{\text{dead}} h_B(E) [\text{m}^3]:$	-	-	1246 ± 281	1219 ± 274	1256 ± 283
$R_{\text{dead}} \text{ static } h_B [\%]:$	18.1 ± 4.0	7.5 ± 1.8	5.5 ± 1.2	5.3 ± 1.2	5.6 ± 1.3
$R_{\text{dead}} h_B(E) [\%]:$	-	-	5.4 ± 1.2	5.3 ± 1.1	5.4 ± 1.2

for different veto strategies. In the case of the default approach, when a cylinder of 3 m radius is applied for every muon, about 18 % of JUNO is dead at all times. When the default approach is adapted to change the cylinder radius to 1.55 m, if no shower is detected, the dead volume can be reduced to about 7.5 %, without affecting the veto efficiency much. Further improvements are possible with the energy dependent custom veto strategies, though the differences are mainly dominated by the none showering case, which is the same for the 3 custom veto types. Nevertheless, the cone veto can reduce the dead volume by more than 3 times, over the default approach. As reminder, the same assumptions as for the default veto apply, which means overlapping vetoes are not considered. Hence, the real world dead volume may be smaller and this applies to all veto strategies, but overlapping is more likely for larger vetoes.

4.4.4 Conclusion

From table 4.6 one can conclude that a custom veto for muons with a shower would reduce the dead volume roughly 3.5 times. The additional total active volume is about 12.8 %, which means in the same measurement time JUNO could gather about 12.8 % more statistic. Or, in terms of time reduction, JUNO could measure the same confidence level in about 8.72 years, with a custom veto approach, compared to 10 years. The needed prerequisite for a strategy like this, is a reliable muon reconstruction, that can detect showers and reconstruct all muon tracks. A possible candidate will be examined later in this thesis starting from chapter 6 and onwards. The answer to the question, which custom veto approach is the best suited for this task, depends on the reconstruction as well. The precision needed for the ice cone veto is not realistic. Hence, it can probably not be used in a real application. Interestingly, the single cone starting from the

shower beginning has delivered the most promising results, which can probably be attributed to the fact that selecting a shower start already reduces the space where isotopes can spread to and the sphere on top of the ice cone veto impacts veto volume more than naively expected. A complication with this approach is to define the shower start. For this a threshold is needed and depending on the reconstruction capabilities it may actually prove unfeasible to reach the anticipated efficiency, as some isotopes may be generated below the threshold. To counter this there is the option of adding a smaller cylinder for every muon track, which has been explored here as well. This keeps the efficiency high, but introduces more dead volume. When a shower can be detected all custom veto approaches can be used, without the energy dependency $h_B(E)$. With the energy dependency $h_B(E)$ the vetoes for the shower case can be further improved, but the dead volume is mainly dominated by the none showering case, when a cylinder with radius 1.55 m is assumed. The double cone veto still offers a similar improvement as the cone and can already be used when only the shower maximum can be determined, which seems like an achievable goal for reconstruction efforts.

Chapter 5

Simulation

Since, JUNO is still in the process of being build, it is not possible to obtain real data yet. Instead, simulations are used to enable one to work on reconstructions for the detector. In the first section of this chapter, there will be information on the official JUNO simulation and how it describes reality. Later an overview of the simulated data obtained with this simulation will be given.

5.1 Official JUNO simulation

It is part of the so called *Software for Non-collider Physics ExpeRiment* (SNiPER) framework [90]. The framework is written in python and C++ and makes use of multiple libraries. The core physics is described by Geant4¹ [91, 92] and the data structure utilises ROOT [93] to read and store information. The software aims to describe the real JUNO detector as accurately as possible. The following information and generated data describes simulation version J17v1r1.

5.1.1 Layout

The simulation should reflect the real detector as closely as possible, which is not a simple task while the detector is partly still in development. Some parts still have to be measured, like the real behaviour of the liquid scintillator, other parts can only be determined after they are built, for example parameters of PMTs have to be measured, but even then it is not yet determined which PMT will be mounted where. Therefore, the simulation can at best describe the current status, with approximations for the further development. The layout of the detector in simulation version J17v1r1 can be seen in figure 5.1 and 5.2.

Dimensions & numbers The detector simulation is described in this part, starting from the center and going outward. For comparison with the current state of the JUNO experiment and future plans see chapter 3. The central sphere of liquid scintillator has a radius of 17.7 m. The

¹Geometry and tracking (GEANT) a toolkit to simulate the interaction of particles with matter. Its based around MC methods.

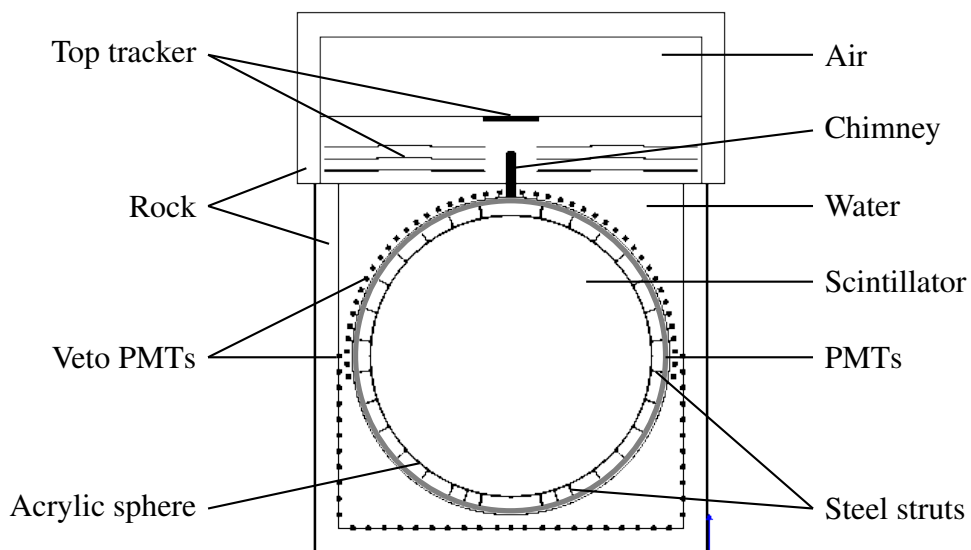


Figure 5.1: An orthogonal cut view of JUNO in the simulation version J17v1r1. The central detector PMTs are added in post as a gray outlined circle. The rest is from the actual simulation implementation. The print is to scale as 1 mm in this figure corresponds to 1 m in the simulated detector. A slice of 1 m thickness was cut out of the middle of the detector.

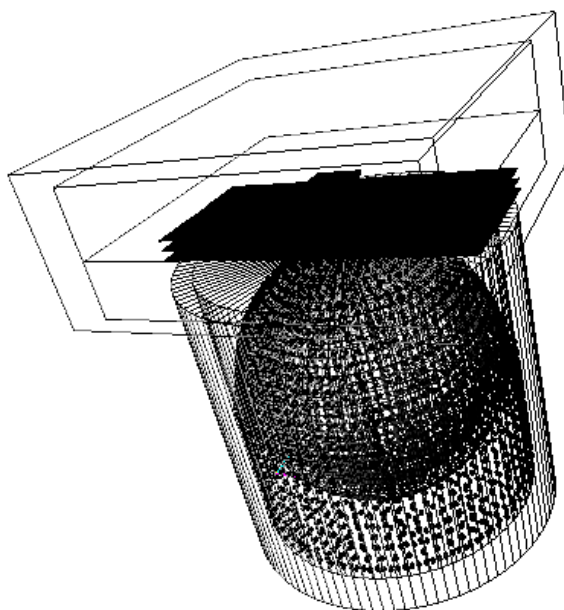


Figure 5.2: A 3D wireframe view of JUNO in the simulation version J17v1r1. Due to the large amount of objects the central detector PMTs are omitted.

detector contains $\sim 23227\text{ m}^3$ of liquid scintillator, which translates to $\sim 20\text{ kT}$ target mass. It is enclosed by an acrylic sphere of 12 cm thickness with an opening at the top, where the acrylic chimney is located. Outside of this sphere is water, which fills up the rest of the lower detector. A steel construction is implemented, with a radius of $\sim 20\text{ m}$, which is connected to the acrylic sphere via steel struts and acrylic fasteners. It also houses all central detector optical modules as well as part of the veto optical modules and tyvek sheets that prevent light from entering and escaping the central detector. The total number of central detector PMTs is 54311. Which can be further subdivide in 36572 PMTs of 3" and 17739 PMTs 20" size. In the simulation the 20" PMTs are characterised as 12670 micro channel plate PMTs and 5069 dynode PMTs. The central detector 20" PMTs are distributed in a hexagonal setup for close-packing of equal spheres and look directly into the target center. The smaller PMTs fill out the space in-between. Some of the potential places for PMTs are not populated to allow for the steel struts to connect to the acrylic sphere. Outside of the steel structure the water in combination with additional 20" PMTs is utilised as a veto. Below the steel structure will be steel beams holding it in place, but these are only implemented in later versions of the simulation, which are currently unverified as of the time of writing this thesis. All this is submerged in water surrounded by a steel cylinder, with an inner height of 43.5 m, an inner radius of 21.75 m and a thickness of 3 mm. On top of this is a cuboid experiment hall with a length and width of 48 m and a height of 18.6 m. It is filled with air and contains the top tracker. The whole detector is encased by Rock with a thickness of 3 m. Finally, this is all within a world box volume of edge length 120 m.

Materials These are implemented as pure, hence there is no chance of random background decay. In the real world materials are always made up of a composition of isotopes that will have some sort of minor decay probability. Some isotopes of atoms used in molecules in the central detector are listed in table 5.1. Adding real compositions of isotopes is possible and

Table 5.1: Isotope definition for the simulation.

	Z	g/mole
Hydrogen	1.0	1.01
Carbon	6.0	12.01
Nitrogen	7.0	14.01
Oxygen	8.0	16.00
Sulfur	16.0	32.066

more realistic, but not desired for the simulation because the created background will interfere with the purity of processes that one is actually interested in studying. To estimate the impact of these decay backgrounds, measurements of the different materials have been carried out and can be added when needed. Furthermore, there are no real molecules in Geant4, instead they are described as a weighted densities of the different atoms that they are made of. The molecule composition of some materials can be seen in table 5.2. During the simulation process the volumes are not filled with anything, instead atoms only come into existence if an interaction with

Table 5.2: Molecule composition for the simulation. Only a few materials used in the central detector are summarized.

	LAB	ACRYL	WATER
Hydrogen	0.1201	0.08055	2.0
Carbon	0.87924	0.59984	
Nitrogen	0.00027		
Oxygen	0.00034	0.31961	1.0
Sulfur	0.00005		

the material requires them and is then calculated based on the weighted distribution from the molecule composition. Other interactions like scattering processes have to be handled by material property tables, which are also part of an material. These physics processes are described during pre-, along- and post-step. Since, the detection principle in JUNO relies on optical transportation processes, material property tables for photons passing the materials have to be set. In figure 5.3 the refractive index and absorption length for the main materials used in the central detector can be seen. In reality the scintillator emits around 300 nm, which then is shifted to around 420nm. During the simulation the spectrum is already in the *past shifted* state. In figure 5.4 one can see the emission spectrum used in the simulation as well as the re-emission from antecedent absorption. Combining the information of these graphs one can approximate how likely it is for photons to be detected. To determine what actually will happen during an interaction of a photon is part of the simulated physics, which will be described next.

Simulation Physics The simulation for JUNO is integrated into the SNI_PER framework and the physics simulation in this framework is done by Geant4. This tool is commonly used for high energy particle physics applications, but can basically be used for anything particle physics related. In the JUNO simulation version J17v1r1, Geant4 version 9.4, patch 4 is used. What physics will be simulated depends on the implementation of the experiment. The relevant particle physics involved can be implemented individually, but in general a base set of processes is defined by so called *Physics Lists*. This has also been done for the JUNO simulation and the base *Physics Lists* are QGSP_BERT_HP and G4EmExtraPhysics. The first list is a combination of the Quark Gluon String model, Bertini cascade model and High Precision data. The QGS model handles high energy GeV hadronic interactions and the BERT model is responsible mainly for protons, neutrons, pions and kaons below ~ 10 GeV. The HP data is valid for elastic and inelastic neutron interactions below 20 MeV. G4EmExtraPhysics treats electromagnetic interactions. For example, neutrino electron processes, gamma conversion into muons and muon pair annihilation. It is also possible to add an implementation of the Cherenkov and scintillation process, but because these are especially important for the JUNO detector, they have been implemented independently by the JUNO collaboration. Daya Bay results have been used to verify the JUNO physics simulation implementation, because the JUNO experiment is closely connected to the Daya Bay experiment and they both use the SNI_PER framework.

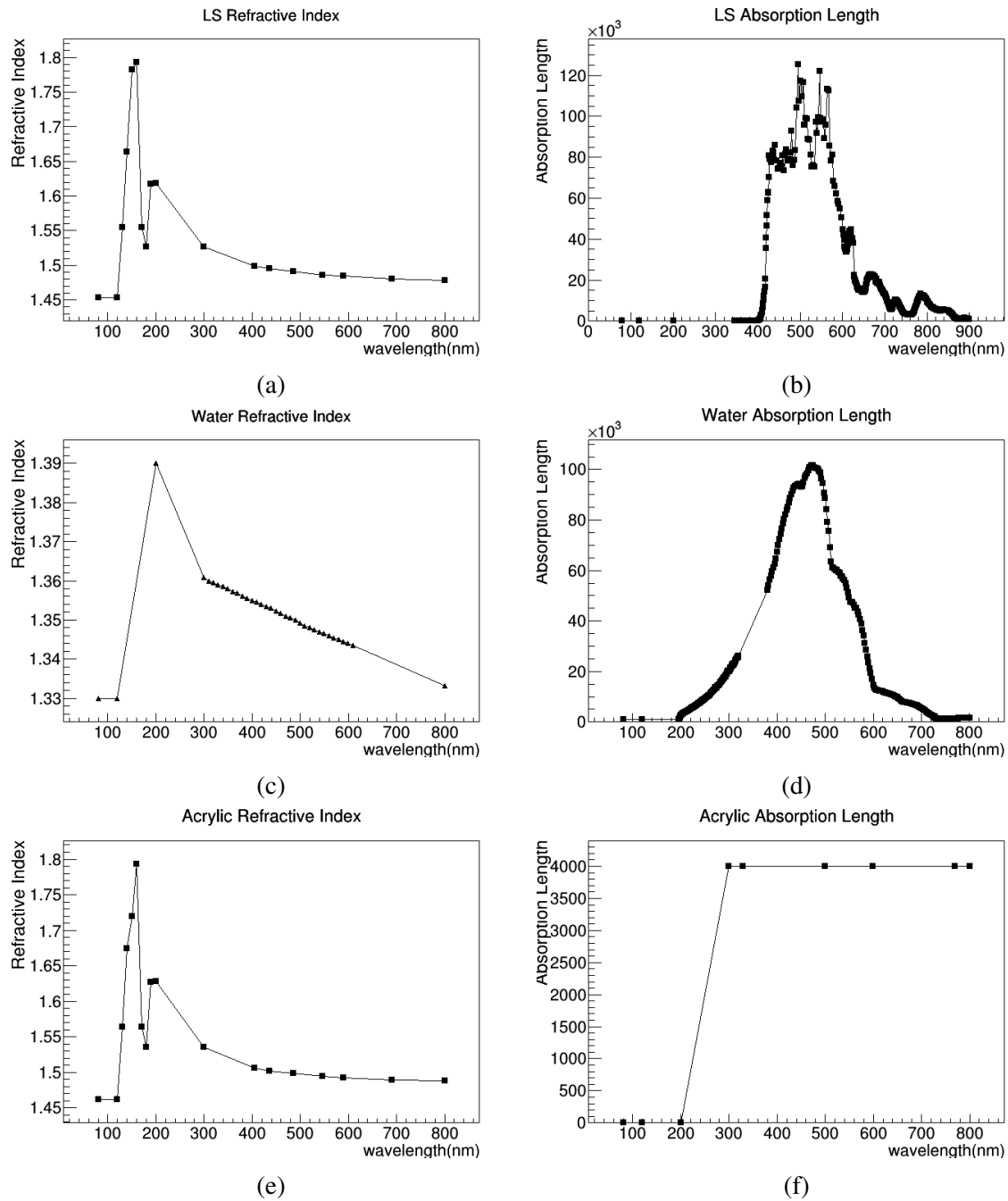


Figure 5.3: The refractive indices (left) and absorption lengths (right) for different materials in the JUNO simulation, depending on the wavelength. (a) & (b) are for liquid scintillator, (c) & (d) are for water and (e) & (f) are for the acrylic sphere construction. [94]

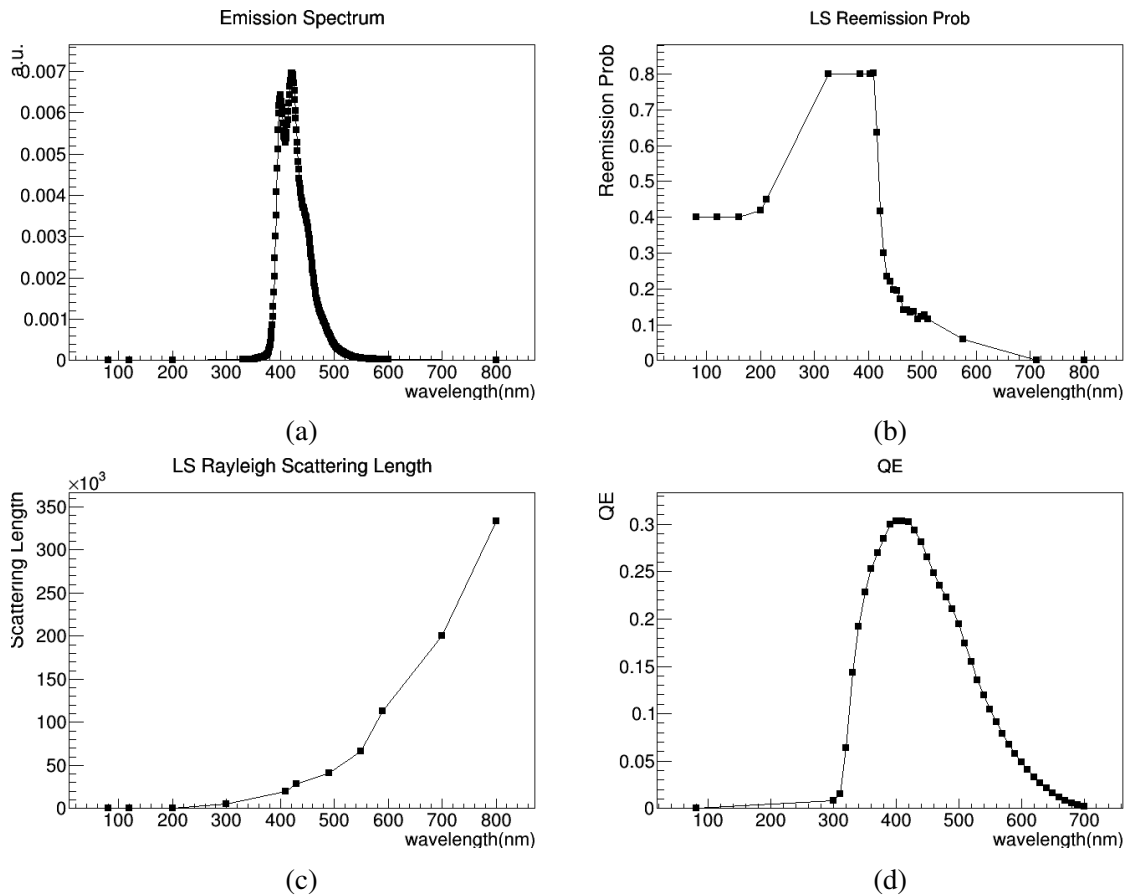


Figure 5.4: (a) is the emission spectrum of the liquidcintilator depending on the wavelength, (b) the re-emission probability depending on the wavelength and (c) the rayleigh scattering length, also depending on the wavelength. In (d) one can see the quantum efficiency of a PMT in the simulation. [94]

5.1.2 Reality vs. Simulation

This subsection will describe the development of a real event compared to a simulated event. This will highlight the impact of simulated data in comparison to real data. As an example we take a muon passing through the detector.

A real muon It could be created high up in the atmosphere, by a cosmogenic interaction and travel in the direction of the detector. Assuming that it will reach JUNO, it will have a high energy of around 209 GeV, since lower energy muons will most likely be absorbed in the rock above the detector. The first time it can be detected is during its journey through the top tracker. Further along it reaches the muon veto and finally the inner detector with the scintillator target. For simplicity it is assumed that there will be no shower and it will straightly exit the detector. On its way out it will pass the muon veto a second time. Focusing on the scintillator target, here the muon will transfer a few percentage of its energy electromagnetically into, not only electron excitations, but also vibrational and rotational excitations. The excitations will be passed to a solute molecule via dipole-dipole interactions, called Förster interactions. An added secondary fluor will, again mostly nonradiative, take over the excitations and finally release the energy in a radiative process. As an example we further focus on one of the released photons and again for simplicity assume it will travel through the scintillator with no further interactions. But this does not necessarily imply a straight path, since variations in the scintillator density, induced by e.g. temperature differences, can warp the trajectory. It then will be refracted at the acrylic-sphere and enter the water pool until it hits an optical module. In this example it will reach the photocathode and will be transformed into an photoelectron. In a PMT it can then initiate an electromagnetic avalanche and become an electrical signal. This will be further processed by the 1-F3-scheme, which is at its core an underwater electronic box. Then this sends the signal via ethernet to a rack with readout electronics to save the information. The described process would be an example for one perfect photon signal detection of a muon passing through the detector. It is important not to underestimate the different processes that are going on during the muon pass through as well. For example there will be radiation entering the detector from the rock around it, caused by the decay of muon induced spallation products or by contamination of the scintillator, which will also produce signals. Even the electronics add to the signal in unwanted ways, for example the PMT can have dark noise or saturation. Most of these effects should be under control and how much each of these effects contribute has been studied extensively or is currently under investigation.

A simulated muon It will be simplified at different points along this journey. The goal is to describe reality with less information without sacrificing too much required final state information. Simplifications are almost always made to save time or complexity. The differences already start at the creation: The start point usually is chosen a few meters above the detector and in some cases even inside the target. For muons the distribution of energies and directions

is predetermined by other simulations and these spectra are used by generators and are called for each different set of start parameters. The simulation consists of mainly three parts.

The first part is the detector simulation. Here, Geant4 will compute most of the endeavor, with a semi-classical approach. The particle is treated in a classical way, but the interactions take quantum mechanical effects into account. Hence, the muon particle is taking steps and each step the interactions with their corresponding probability are considered. A basic implementation of the scintillation process is already predefined in Geant4, but for the official simulation this is replaced by a more sophisticated code. Nevertheless, it is vastly different from reality. After each step, an along step method is called and depending on the material, energy, kind of particle and step length the number and position of emitted scintillation photons is determined. Each photon is emitted with a spectrum weighted randomised direction, time delay and energy. The spectra aim to mimic the scintillator behaviour in its macroscopic effects. After a photon has been emitted through this process it is a new *Track*, which will be put on to a *Stack* to face a similar treatment as the muon before it. After the photon *Track* is picked up again by the Geant4 process it will travel through the detector in steps as well and has the possibility to interact, similar to a real photon, by scattering, absorption, reflection and other processes. As before we will assume no interaction in the scintillator, but in contrast to reality the scintillator is assumed to be perfect, with the same density and same probabilities for interaction throughout the whole target. In general all materials are assumed to be perfect and even without any contamination. Hence, there will be just a straight trajectory until the photon reaches the acrylic-sphere. It will then undergo a transition process at the boundary, which will describe the refraction. In difference to reality the shape of the acrylic-sphere is also assumed to be perfect, which means there is no deformation due to buoyancy or other effects. After going through the water it will finally reach the simulated optical module. Depending on the detection efficiency the hit will be counted or not. The first part of the simulation for this photon ends as soon as the photocathode is hit. For the muon simulation case there is special treatment for any other photons that reach the same photocathode within a certain time frame², just the charge will count up and only the time of the first hit, within the time frame, will be recorded. This is done by the official simulation to reduce the amount of data. The results are saved in a ROOT file. This is the end of the detector simulation part.

The second part is approximating the electronics, which makes it the electronic simulation. It picks up where the detector simulation ended, by reading in the ROOT file. The photon hit time will be shifted by the corresponding TTS spectrum of the PMT and a fixed offset will be added, which emulates the cable length of the optical module. Additionally, dark noise can be simulated. This is proceeded by the calculation of a waveform for all hits in a PMT, which also considers effects like saturation and after pulses. The output is again saved in a ROOT file, which is used during the next part.

The third part of the simulation is the calibration and it is supposed to counter effects that have been introduced during the simulation. It is more of a reconstruction, for example it attempts to

²The time frame is set to 1 ns in the simulations used in this thesis, which is the smallest possible time.

perform a deconvolution of the PMT waveform. Effects like the added offset due to cable length differences are left untouched by this, which is something that needs to be added to calibration in the future. This part of the simulation is still under development and the deconvolution has been proven to be a difficult task. The final result, before any other reconstruction takes place, takes the form of hit times and charges for each optical module. Some kind of calibration will also be performed on real data, once the detector is running. Therefore, this is not strictly part of the simulation, but it is questionable if this exact calibration algorithm will be performed or a completely different algorithm for the 1-F3 scheme is necessary. Hence, this calibration may only remain a part of the simulation.

5.1.3 Simulation output & extension

This subsection describes the output of the simulation and its modification for this thesis. By default the JUNO detector simulation does already provide some information, but additional output is required to evaluate certain aspects of the reconstructions. Two ROOT files are created per run.

The Event-file This is usually named something like *evt-name_energy_vertex_direction.root* and will be used as input for the electronic simulation, which will further process the generated information as described in subsection 5.1.2. In figure 5.5 the file structure can be seen. A

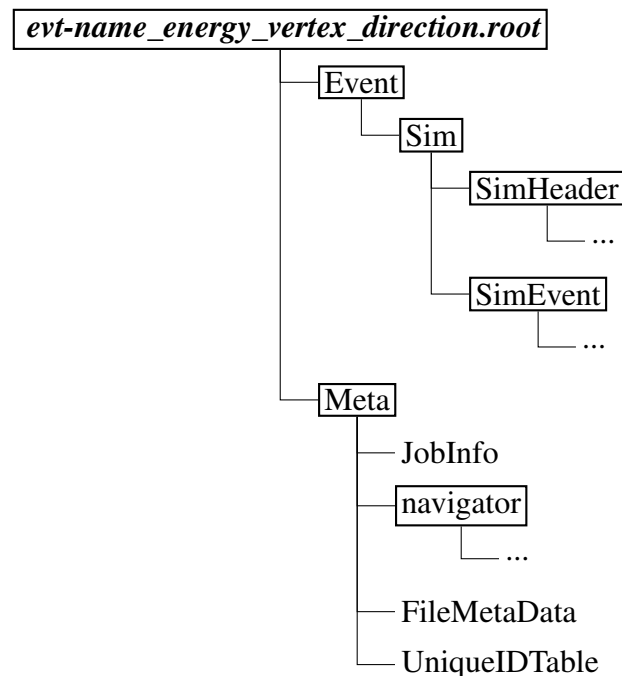


Figure 5.5: The event file structure was not changed to ensure compatibility with the electronic simulation, which uses this as an input. To properly readout information from this file several custom ROOT objects need to be defined. The proper setup is described in quickstart.md section event data model by the JUNO-Soft documentation. Since this file is not directly used by the reconstruction no further elaboration is needed.

correct environment setup is needed to read out information from this file, because it contains ROOT objects and the necessary ROOT dictionaries need to be generated and loaded. Hence, Monte Carlo information was also added to the *User-file* as a simple access point. The *Event-file* is not meant to be altered in any way to ensure compatibility with the electronic simulation and therefore still follows default behaviour.

The User-file The second ROOT file created per run and it is meant to hold useful information for the individual user. The default naming scheme just adds user to the file name as follows *user-evt-name_energy_vertex_direction.root*. The simulation is written in a way that most of the user desirable information can be extracted from the so called *analysis manager*. Depending on the focus of the simulation different analysis managers can be selected for a run. For the simulation of muons the *muon analysis manager* is selected. In figure 5.6 the default structure of the *User-File* can be seen. Additionally, further information had to be extracted during an

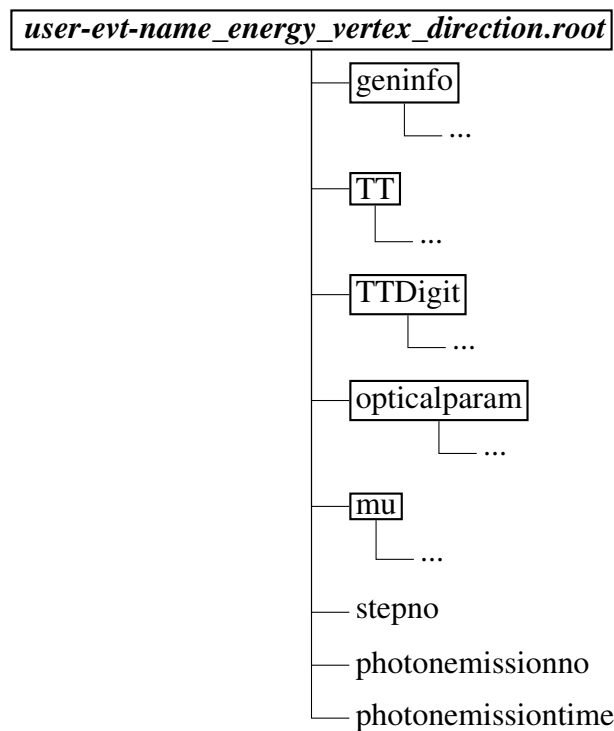


Figure 5.6: The structure of the *User-file*. The *geninfo-tree* contains information from the initial event generation, for example the event ID and primary particle information. The *TT-tree* holds information about the top tracker and interactions with it. *TTDigit* saves the interactions results, in terms of channel charge and times. The *opticalparam-tree* has information on optical effects during a run, in example the absorption length of absorbed photons inside the different materials. Finally, the *mu-tree* tracks information about the muon and additional event information. The none boxed part of this file structure contains histograms, which can give a simple inside about the events. The *stepno* reveals how many steps optical photons needed to end. The *photonemissionno* tracks the photon emission along the muon track and the *photonemissiontime* reveals at which point in time during an event how many photons have been emitted.

event. The extended Monte Carlo truth will be used during analysis in chapter 8. To collect all necessary information, the modifications are mostly contained within the *muon analysis manager*, but also extend into other parts of the detector simulation software. The histograms are filled during a run. Namely the *stepno*, *photonemissionno* and *photonemissiontime*. The step number counting histogram was already part of the default structure and can be used to determine if photons get stuck in infinite reflections, which in best case slows down the simulation and in worst case traps it in an infinite loop. Hence, a stepping count and tracking abort is put into place, which usually triggers after 1000 steps. The photon emission number histogram was added to gain insight into the photon emission along the muon track and can provide a basic shower overview as well as a reference for the reconstruction, which essentially aims to determine exactly the $\frac{dE}{dx}$ structure of an event. Finally, the photon emission time histogram was added to evaluate time cuts and re-emission features. Further needed none histogram information is saved into the *mu-tree*. This tree is called *evt-tree* when selecting the *normal analysis manager*, hence additional event information was added to this tree to be consistent between the *muon* and *normal analysis manager*. In table 5.3 the additional sub structure of the *mu-tree* can be seen. The photon and Monte Carlo event information is collected during the event tracking and then put into formats that can almost already be read by the reconstruction. But a conversion step is kept in between to gain more control over the input for the reconstruction, which enables one to specify for example to only read in non-scattered light. This helps to test and improve different aspects of the reconstruction. The detailed photon path information has to be collected and adjusted during the tracking of photons and only some of them have a Geant4 method which marks the specific propagation effect. Saving the complete trajectory information of each photon is not possible due to the sheer amount of information, when dealing with millions of photons. Hence, reduction to essential defining moments during a photons journey is necessary. The *original emission time* and *original optical photon* flag can be set during the creation of a photon. To identify Cherenkov photons the creation process name can be checked and for the *from gamma* flag the parent particle needs to be a gamma. For absorption, scattering and reflection the photons current process type has to be checked every step. For absorption and scattering it ends there by checking against correct process name, but reflection is harder to identify and can only be spotted by a combination of post- and pre-step material analysis with careful comparisons between steps. This works because the post-step already contains the next material at a geometric boundary and the pre-step has the material the photon is coming from. When a reflection takes place, during the following step at the same position and track ID, the materials flip and the new post-step material is the old pre-step material as well as the new pre-step material being the old post-step material. The *re-emission* flag is set when the parent particle and the particle itself are photons and the creation process is scintillation. These flags had to be implemented into the hit collection to be able to access them at the end of the event. This had an undesirable side effect, because for muons the hit collection is implemented in such a way that it collects and adds up photons during a specific time frame after a photon has hit a PMT. Presumably, this is performed to reduce information, which could cause the RAM to fill

Table 5.3: Information added to the *mu-tree*. The event photon information is a hit collection for each event that can be read out and used with the reconstruction. The detailed photon path options give an insight into the interactions of a photon, during its journey through the detector, which is important for the interpretation of the reconstruction results and improvements. The Monte Carlo information is needed to evaluate the reconstruction results. It was also added to the user file in this structure for simple access without the hassle of root objects. There are more variables in this tree, but these are the ones we will focus on.

	mu-tree-variables	Additional event information detail.
Event photon information.	nPhotons totalPE nPE energy hitTime pmtID PETrackID TrackID	Length of the hit array. Note, PE can be merged. Total number of counted PE for this event. Number of hits (Charge) Optical photon energy. Hit time on a PMT. PMT ID for each hit. Parent track ID this optical photon was emitted from. Track ID for this photon.
Detailed photon path information.	isCerenkov isScattered isReemission isOriginalOP isFromGamma isReflected OriginalOPTime	Flag if photon is Cerenkov light or not. Flag if photon that has been scattered. Flag if photon re-emitted during propagation. Flag if photon is the original photon. No re-emission. Flag if photon that originates from a gamma. Flag if photon has been reflected. Original time the photon was emitted.
Event Monte Carlo information.	MCPdgId MCTimeOfCreation MCEKin MCTrackId MCParentId MCVertexPosition MCEndPosition MCVertexDirection MCCreatorProcess	PDG ID for none photons. Creation time for none photons. Kinetic energy for none photons. Track ID for none photons. Parent ID for none photons. Creation position for none photons. Tracking end for none photons. Initial direction for none photons. Process name that led to the particle creation.
	...	

up and kill the program. For all simulated data this time frame was set to the minimum possible amount of 1 ns, but this also means that only the flags of the time frame starting photon are recorded and all following photons within 1 ns are only shown as charge and their flags assume the properties of the first photon. This is not a problem at lower energies, but around 200 GeV about 85% of photons have more than 1 PE in their time frame. However, this does not effect the reconstruction itself, but instead the capability of input specifications for the reconstruction.

5.2 Simulated data used for reconstruction

Before detailing the data used for this thesis one has to specify which simulation version was used for each data set and during this point in time the latest validated full version is J17v1r1. Only pre-release versions of J18 and J19 have been built. Furthermore, the mixing of simulation results can introduce none trivial inconsistencies. Therefore, the same version was used throughout this thesis, which is version J17v1r1, revision r3057, state 20th of October 2017.

To cope with the information amount and to understand reconstruction behavior³, contained muon events of a few GeV have been simulated, with varying starting points from around 0 to 10m distance from the detector center. The main direction of these events is straight down, though some events with a different angle from this, up to 45 degrees, have been generated as well. These asymmetric events can be used to check the reconstruction against errors, which can be hidden by symmetry effects. Later, the focus was shifted to simulate muon events with the predicted mean energy⁴ of ~ 215 GeV. Which was later adjusted to 209 GeV, since the original construction site position of JUNO was altered by ~ 70 m due to water ingress and rock stability issues. This in-turn lessened the overburden by ~ 50 m and created the newly predicted mean muon energy of 209 GeV. It also had the side effect of a slightly raised muon rate from 3 Hz to 3.7 Hz [94]. Finally, a set of 4000 muon events with the full energy spectrum and directionality as provided by the muon generator of version J17v1r1 has been generated. No existing set could be used, due to the extra Monte Carlo information needed and the simulation of one high energy muon took around 2 hours. Fortunately, extra computing resources enables parallel event simulation. Additionally, these events are simulated as starting at the edge of the Geant4 world volume, this makes them unlikely to hit the central detector, which reduces the 4000 samples to 976 events which are of interest for the reconstruction. The momentum spectrum generated and used by the simulation can be seen in figure 5.7. For these plots the muon generator was set to produce 100k muon starting parameters. The same generator was used for the 4000 sample events. In figure 5.8 the angular distribution can be seen.

This is mainly dominated by two effects. Firstly, there is a smaller solid angle element around the zenith compared to the horizon area, which explains why it starts at 0 and rises. Secondly the distribution of incoming muons has its maximum around the zenith and declines, because

³The topological reconstruction was tested for low energy events and has some issues with event energies greater than ~ 15 GeV.

⁴Only single muon events are considered for the mean muon energy.

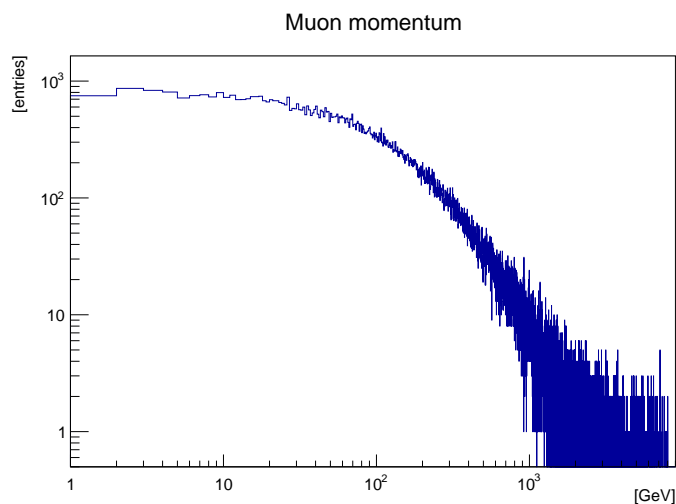


Figure 5.7: Logarithmic style muon momentum energy spectrum, created by the JUNO simulation muon generator and used as input for the Simulation. Generation of 100k muons, which are filled in their respective momentum magnitude.

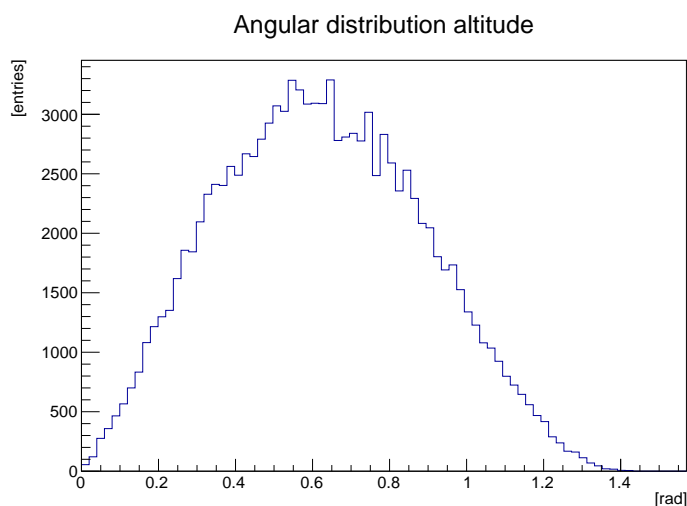


Figure 5.8: Angular altitude distribution for a generated sample of 100k muons, where 0rad is the zenith and $\frac{\pi}{2}$ rad corresponds to the horizon.

these muons are generated high up at the edge of the atmosphere and have to traverse more distance and matter the flatter they are coming in. These two effects create a maximum around 0.6rad for the incoming altitude angle. In figure 5.9 the azimuth angular distribution can be seen. It describes the geologic topological conditions. The numerosness of muons varies

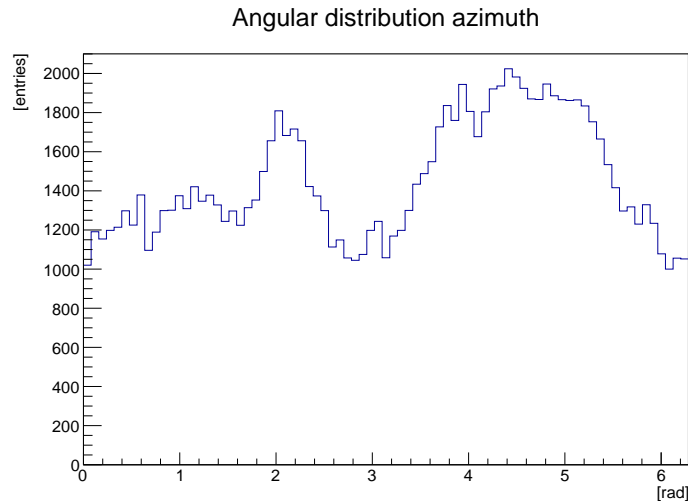


Figure 5.9: Angular azimuth distribution for a generated sample of 100k muons, where 0 and 2π rad is north, $\frac{\pi}{2}$ rad is east, π rad is south and $\frac{3}{2}\pi$ rad is west.

with the overburden in that particular direction, in a way that the amount of muons is inverse proportional to the quantity of overburden traversed in that direction. One can take from that graph that the terrain surrounding JUNO is not flat, but instead flanked by mountains. The muon generator output is based on a combined simulation of the Gaisser formula and MUSIC⁵ takes care of the transportation through the overburden. It is fed with terrain measurements and geological surface measurements as well as successional calculated geological properties for depths that can not be probed.

All these simulations of muon events for the reconstruction have been performed by the detector simulation, but not by the electronic simulation and calibration. As previously discussed in section 5.1.2, the electronic simulation and calibration are meant to be applied together and the calibration is meant to reverse the impact of electronic introduced effects, but these parts of the simulation are not quite finished, because the waveform deconvolution is not satisfying yet. Hence, it is improbable to generate reliable date from the complete software chain. Therefore, the electronic simulation and subsequent calibration are not performed. To approximate the impact of electronics and calibration one can offset hit times with the TTS of the hit PMT. This has been done for later stages of the reconstruction development, at the beginning input without this alteration was chosen to be able to evaluate effects introduced by the reconstruction.

⁵MUon SIMulation Codes (MUSIC) is a tool to calculate muon transportation through rock, water and other materials, to gain information on there expected underground energy spectrum and angular distribution.

Chapter 6

Topological Track Reconstruction

In recent years the typically provided event information for liquid scintillator detectors was extended from only charge information to also provide photon hit time information. With this it was possible to develop likelihood based methods, that can determine more than energy and vertex information for low energy events. A likelihood based approach tests a hypothesis and fits appropriate parameters, such as track direction and energy to it. MiniBooNE was able to reconstruct electrons and muons [95]. In KamLAND the first successful reconstruction of direction and entry point for a through-going muon was performed [96]. These methods for liquid scintillator detectors have proven the potential to extract detailed track information, but they restrain the event to a hypothesis. On the contrary, the topological track reconstruction is a new approach, which enables one to directly determining where the event light is coming from inside the detector. It does that with the recorded temporal photon information.

6.1 3D Topological Reconstruction

It is the goal of the 3D Topological reconstruction to provide a 3-dimensional *image* of the energy deposition of an event. This is done by determining the photon emission inside the detector. Utilizing this data, other algorithms can be used to apprehend information on the event itself and involved kinematics. Therefore, this approach can be applied to multiple topology dependent problems. Such as, finding showers along muon tracks to determine potential cosmogenic backgrounds for the IBD, which was already discussed in chapter 4. Or the discrimination of electrons from positrons and gammas due to small differences in the event topology, which was further explored in [63]. This can dramatically reduce the internal natural radioactive background, as well as ^{10}C and ^{11}C from cosmogenics, for solar neutrino research. It may also be possible to determine low energy particle travel directions from differences in the topology induced by Cherenkov light, which is discussed in [78].

How the determination of the event topology is performed will be discussed in the next section, followed by the use of iterations to further improve results. Then the developments during this thesis for the GeV regime will be laid out, which will have a focus on speed and robustness. In the final section 6.4 the potential future developments are elaborated.

6.1.1 Basic idea

This section will give an introduction to the topological reconstruction algorithm. The first part is about the *basic idea*, necessary assumptions made and event geometry, followed by the utilization of multi photon event information and finishing with additional corrections. Since this approach is applicable to unsegmented liquid scintillator detectors, one can assume a sphere of liquid scintillator surrounded by photo sensors. These can tell us if light arrived, roughly how much and particularly when in time.

The *basic idea* just utilizes geometry and following assumptions about the event development:

- We have the event interaction point, referred to as reference point \vec{r} .
- A start time t_{ref} for this position \vec{r} .
- The main particle approximately follows a straight path.
- The speed of said particle is close to the speed of light in vacuum.

This can be tied to the geometry for an event with one example photon in figure 6.1, which is a visual representation of the *basic idea*. A particle travels inside a detector and induces

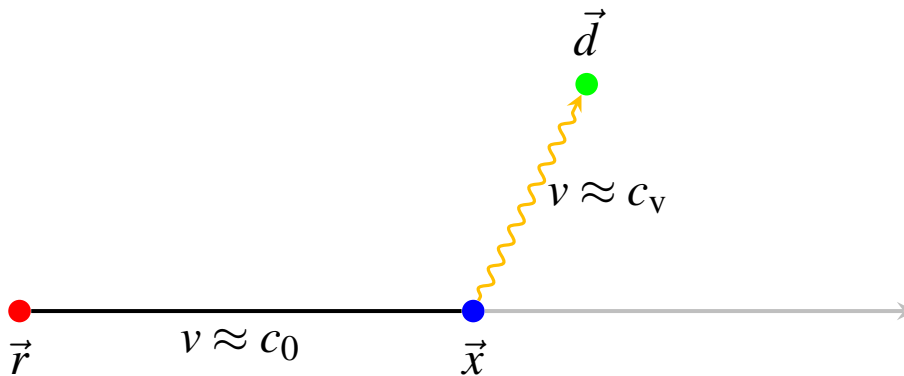


Figure 6.1: Visual representation of the *basic idea*. A particle is assumed to travel along a straight track, with a reference point \vec{r} (red) and induces scintillation passing point \vec{x} (blue). A photon is emitted and in this example it travels through the scintillator until it is detected at point \vec{d} (green) by a PMT.

scintillation of a photon at \vec{x} , which is detected in a PMT at \vec{d} . When the reference point and time is provided by a prior analysis of the event, the time it takes from reference point \vec{r} until a photon is detected at point \vec{d} can be calculated, with

$$t_i(\vec{x}) = t_{\text{ref}} + \frac{|\vec{x} - \vec{r}|}{c_0} + \frac{|\vec{x} - \vec{d}|}{c_v}, \quad (6.1)$$

where c_v is the speed of light in the medium and c_0 is the speed of light in vacuum. This describes the basic signal time t_i for one photon hit during an event, where the left side of the

equation corresponds to the detection time of a photon i , in a PMT at \vec{d} . Now, one can calculate the right side of equation (6.1) for any point \vec{x} . This is only reasonable for points inside the detector, where light can actually come from. Under the aspect of a time wise solution to equation (6.1) one can obtain the same signal time t_i for several points \vec{x} inside the detector. These points in a 3 dimensional space result in an isochronic drop-like surface of equivalent time solutions. Of course, only one of these points may be the actual point \vec{x} , where the photon was emitted from. Certainly, this model is drastically simplified, hence some corrections are necessary.

Since time information is of the essence, one needs to carefully evaluate distortions in this type of information. The first two major points are the distortion from scintillation time delay at point \vec{x} and the TTS of the photo sensor at point \vec{d} . The scintillation time can be described by a combination of exponential decay functions, using equation (2.4) and the TTS σ can be described by a Gaussian distribution. The convolution of these two results in following time distribution

$$D(t_i) = \sum_{c=1}^n \frac{\omega_c}{2\tau_c} \exp \left[\frac{1}{\tau_c} \left((t_i - t_{ref}) + \frac{\sigma^2}{2\tau_c} \right) \right] \cdot \left(1 + \operatorname{erf} \left[\frac{1}{\sigma\sqrt{2}} \left((t_{ref} - t_i) - \frac{\sigma^2}{\tau_c} \right) \right] \right), \quad (6.2)$$

where ω_c is the weight of the component c and τ_c is the mean lifetime of that component. The time distribution can use (6.1) as an input for t_i and subsequently a probability density function can be calculated for the emission probability of points \vec{x} . One can imagine this as sticking the time distribution (6.2) perpendicular on to the isochronic surface of equation (6.1). To help visualize this one can take a look at the projection in figure 6.2 (a).

Additionally to these time distortion effects one has to consider light propagation effects for the photon on its way to the PMT and how likely it is from that position \vec{x} to hit said PMT. The local detection efficiency $E_{\det}(\vec{x})$ considers effects of signal attenuation in the scintillator, the effective PMT area seen from point \vec{x} and angular acceptance, which represents optical properties of the PMT as well as detector geometry. A simple way to determine the local detection efficiency is to measure it inside the real detector by emitting light from a position \vec{x} . This is also possible by analytical calculations, as well as simulations. This leads to equation (6.3)

$$p_i(\vec{x}) = D(t_i(\vec{x})) \cdot E_{\det}(\vec{x}). \quad (6.3)$$

To obtain a probability density function (p.d.f.) of photon emission this has to be calculate for an infinite volume V . This volume V can be reduced to just contain the detector volume v , because the probability of detection is zero outside the detector. The total probability needs to be normalized

$$\iiint_v p_i(\vec{x}) d\vec{x} \stackrel{!}{=} 1, \quad (6.4)$$

because we expect one detected photon to be emitted from somewhere inside the detector. With

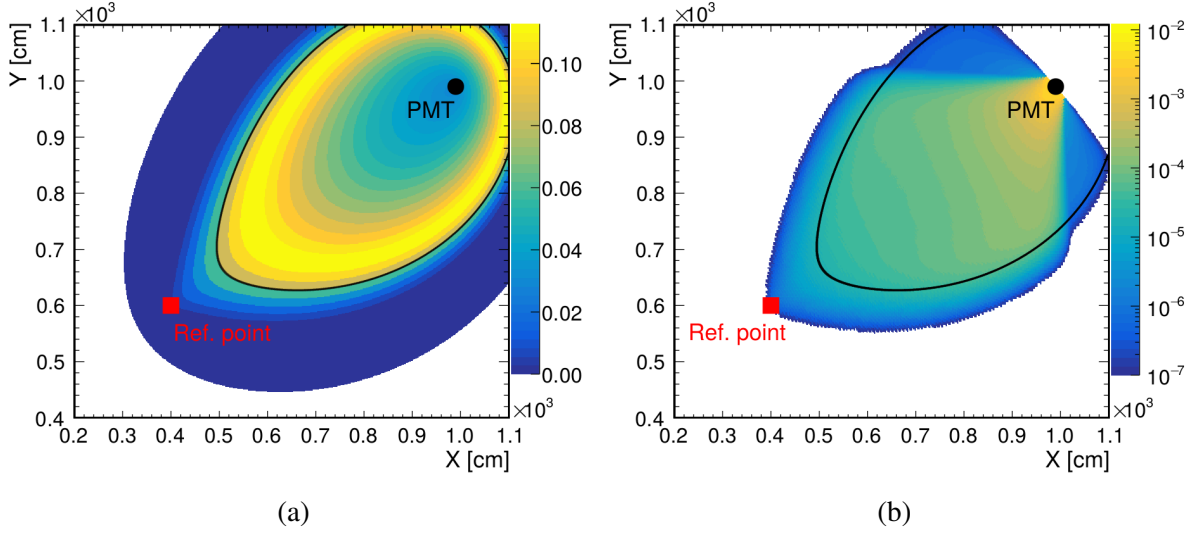


Figure 6.2: 2D projection of the solution for the *basic idea*. In both the position of the reference point (red) is marked and a PMT, which detected a photon. In (a) the black line marks the solution for equation (6.1), without other effects. These are the positions \vec{x} for a 2D slice, which result in the same signal time t_i as would be measured by the PMT, when the *basic idea* describes the problem correctly. Perpendicular on this is the time distribution (6.2), which is indicated by probability from the color gradient of the z -axis. In (b) the same can be seen with the additions of light propagation effects from equation (6.3). [34]

this normalization, the p.d.f $P_i(\vec{x})$ can be given as

$$P_i(\vec{x}) = \frac{p_i(\vec{x})}{\iiint_{\mathcal{V}} p_i(\vec{x}) d\vec{x}} = \frac{D(t_i(\vec{x})) \cdot E_{\text{det}}(\vec{x})}{\iiint_{\mathcal{V}} D(t_i(\vec{x})) \cdot E_{\text{det}}(\vec{x}) d\vec{x}}. \quad (6.5)$$

This is very complicated to solve analytical. Therefore, this may be approximated by a finite amount of voxels, which determine the relative likelihood for a small volume around them. Because the function (6.3) is continuous in space, this is a well defined approximation for infinitesimal small volumes. This enables one to transform the volume integral into a finite sum of measured points for the normalization

$$P_i(\vec{x}) = \frac{p_i(\vec{x})}{\sum_{\vec{x} \in \mathcal{V}} p_i(\vec{x})} = \frac{D(t_i(\vec{x})) \cdot E_{\text{det}}(\vec{x})}{\sum_{\vec{x} \in \mathcal{V}} D(t_i(\vec{x})) \cdot E_{\text{det}}(\vec{x})}. \quad (6.6)$$

This way one can obtain the normalized probability density inside the detector for one photon. But to take into account all light information from an event, this has to be done for every photon detected. Because we do not know, which photon has been emitted from where, we have to consider the signals as independent. Hence, to obtain the 3D topological distribution of an event, the p.d.f.s $P_i(\vec{x})$ have to be summed up

$$P(\vec{x}) = \sum_i P_i(\vec{x}) = \sum_i \frac{p_i(\vec{x})}{\sum_{\vec{x} \in \mathcal{V}} p_i(\vec{x})}. \quad (6.7)$$

Doing this for the whole detector volume results in the 3D topological map of photon detection. But to determine the energy deposition we need the emitted amount of photons at every position inside the detector. To obtain this we need the total local detection efficiency $\sum_k E_{\text{det},k}(\vec{x})$ for every point \vec{x} that was measured. The total local detection efficiency at point \vec{x} is the sum of all local detection efficiencies from every PMT k . Then the emitted amount of photons N_{emit} can be calculated by

$$N_{\text{emit}}(\vec{x}) = \frac{P(\vec{x})}{\sum_k E_{\text{det},k}(\vec{x})}. \quad (6.8)$$

After this step the topological reconstruction of the event is complete, but due to the width of the time distribution it may have a very smeared out look. To further sharpen the result one could use this as a weight in an iterative process. The rational behind this will be discussed in the next section.

6.2 Iteration process

Actually, the photon signals are not completely independent, because they are emitted due to the same event and are connected by its topology. This can be used to constrain the p.d.f for each individual signal from equation (6.3). Hereby, the topology is inferred with a weight, which describes the likelihood of an examined point \vec{x} to be part of the event topology. The distribution of weights for all points \vec{x} in the detector target can be called probability mask $P_{\text{mask}}(\vec{x})$. Then the equation (6.6) can be rewritten to

$$P_i(\vec{x}) = \frac{D(t_i(\vec{x})) \cdot E_{\text{det}}(\vec{x}) \cdot P_{\text{mask}}(\vec{x})}{\sum_{\vec{x} \in v} D(t_i(\vec{x})) \cdot E_{\text{det}}(\vec{x}) \cdot P_{\text{mask}}(\vec{x})}. \quad (6.9)$$

Of course, the probability mask has to hold true for normalization condition

$$\iiint_v P_{\text{mask}}(\vec{x}) d\vec{x} \stackrel{!}{=} 1, \quad (6.10)$$

for each signal. The concept of this probability mask means prior knowledge of the event should be necessary, but obtaining the event topology is the very purpose of this reconstruction. Therefore, this is not feasible, unless done in an iterative manner to converge with the real event topology. This has been done by utilizing the previous reconstruction result, as topology input, to link information between the signals. This can be done several times, and in turn this creates an iterative process, to converge on the true event topology. The process itself can be summarized as follows:

- (0) Provide event photon information and reference point to reconstruction.
- (1) Calculate p.d.f for each signal with (6.3).
- (2) Normalize signals first iteration with formula (6.6) later iterations (6.9).
- (3) Obtain emitted light with equation (6.8).

- (4) Use result to calculate a new probability mask.
- (5) Repeat from step (1) with probability mask.

With the probability mask the region of interest can be more confined for the overall event topology and at a small scale it will emphasize the details of the event topology. As an example it will increase the number of photons emitted due to a shower. This unlocks the determination of energy deposition per unit length. An example for the power of the iteration process can be seen in figure 6.3. The result for the reconstruction at different iteration steps can be seen. The XY-projections are on the left side and on the right are the XZ-projections of the same event. The top two are the result of the first iteration, in the middle the 9th iteration and at the bottom the 22nd iteration. The yellow and blue color in the background is the result and indicates the light emission probability. Overlaid in red is the true muon track, with secondary particle tracks indicated by black lines. One can observe how the reconstruction result becomes much more confined between the first and 9th iteration. Later, in the 22nd iteration the increased energy deposition due to secondaries is clearly visible. Additionally, the voxels are divided into smaller volumes between the iterations, which can enhance the resolution and starting with larger volumes reduces the amount of computations that are necessary.

6.3 Further development

To discuss the major contributions to the TTR, the initial status has to be described and the goals for this work have to be laid out.

The development for the currently used version began in 2016 and the first experiment that it was developed for is LENA. Because LENA ultimately was not built, it had only been tested on the LENA simulation. With this data it has been tested for mostly contained electron and muon events in an energy range from 0-10 GeV. The results of this development stage are discussed in great detail in paper [4].

Because the TTR has initially been developed for LENA, it was later adapted for JUNO. This has been done and the detailed process is discussed in [63]. Some developments during this work have been done in parallel and were merged after the adaptation for JUNO.

This work set out to make this reconstruction applicable to events in the GeV range, or in other words, the reconstruction of spatially extended events. Even though, the TTR was already tested for contained 10 GeV muon events in LENA, this only has limited use for real world events in JUNO. The expected mean energy of muons passing through the detector is about 200 GeV, which implies an increased amount of information that needs processing. Why we care about the reconstruction of these muon events has already been discussed in chapter 3 and 4, but in short: the reduction of cosmogenic backgrounds and therefore the reduction of dead volume may greatly be reduced, if the TTR can be applied to reconstruct muon bundle events and showers. If data for potential events in veto regions is recorded as well, it may be possible to perform this reconstruction later, during analysis efforts. To be most effective and reduce

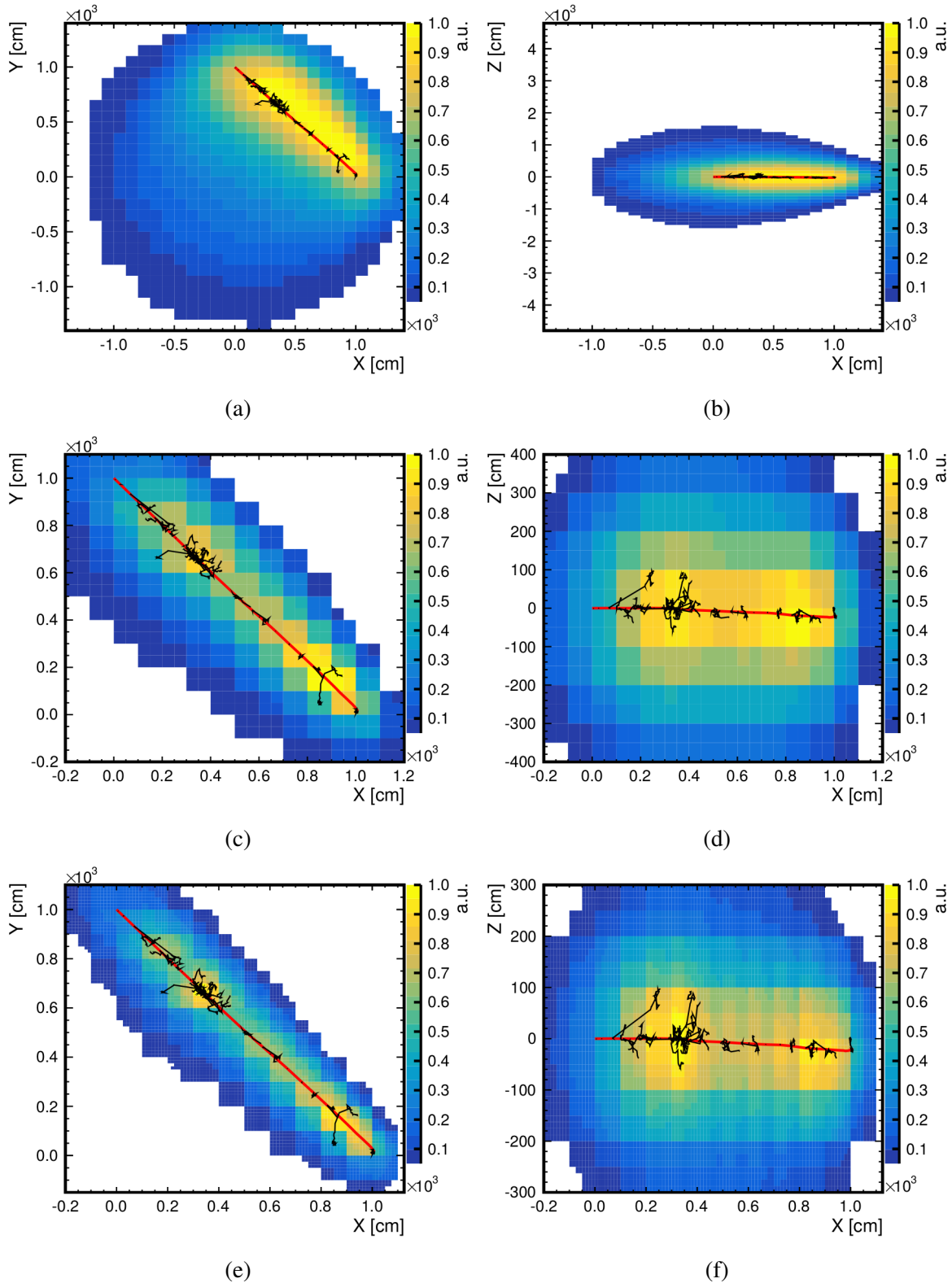


Figure 6.3: The iteration process of the TTR. A 3 GeV muon event was reconstructed. 6 projections can be seen, with XY-projections on the left and XZ-Projections on the right. The Monte Carlo truth of the muon track is shown in red, with secondaries indicated by black lines. The resulting probability density function is color coded from yellow to blue. (a) and (b) show the result for the first iteration, (c) and (d) show the 9th iteration and (e) and (f) hold the result for the 22nd iteration. This example result was performed in LENA [34]

storage requirements, it should be performed on live data. Therefore, it is important to speed up this reconstruction approach to a rate that can keep up with new events, because in the initial state it was much slower than the expected 3.4 ± 0.7 Hz of single muon events in JUNO. To summarize, the main focus is on reconstruction of realistic muon events in JUNO, especially identification of showers and reconstruction of muon bundle events and the acceleration of the reconstruction process. Additionally, a quantitative analysis of energy deposition per volume would be desirable.

With these goals in mind the TTR has been further developed. The next section will discuss modifications during this work in regards to robustness and versatility for spatially extended muon events in JUNO. This is followed by a section about information reduction and reconstruction acceleration. Finally, this chapter will close with the outlook on future developments and the motivation for a similar reconstruction approach in chapter 7.

6.3.1 Robustness & versatility

New features have been added to expand the capabilities of the TTR. The results are presented as slices of the emission probability. As before, the muon track is marked by a red line and secondaries are indicated by black lines. Additionally, the Monte Carlo vertex is marked with a red plus, the reference point used by the TTR is marked with a gray circle and uncharged particles are marked in cyan.

Raw reconstruction This is a simplification of equation (6.3), by not considering the local detection efficiency, which results in:

$$p_i(\vec{x}) = D(t_i(\vec{x})). \quad (6.11)$$

For a single photon the difference can be seen in figure 6.2 (a), where only the time effects of TTS and scintillation time are considered. It is the main motivation for the raw reconstruction to reduce emission probability in front of the PMTs for the first iteration, when no event topology is known, yet. This helps to constrain the event location much faster, otherwise more iterations would be needed. The raw reconstruction can also reduce artifacts near the edge of the detector, which in extreme cases can break the iterative reconstruction process. Additionally, it runs a bit faster, because the local detection efficiency does not need to be calculated or read from a look up table. How this impacts the first iteration of the total photon reconstruction can be seen in figure 6.4. The event is a 4 GeV muon in JUNO, with a projection slice depth of 2 m. Here, the projection of only detected light in the first iteration is shown. In (a) one can see that the topology of the event is much broader, because the local detection efficiency *drags* the probability towards the PMTs and no probability mask, to confine the topology, exists yet. This can be harmful for later iterations, when the topology is not well defined. In figure 6.4 (b) the topology is much more confined to the actual event track. The main contribution of the raw reconstruction is to restrict the event topology early on in the reconstruction, which

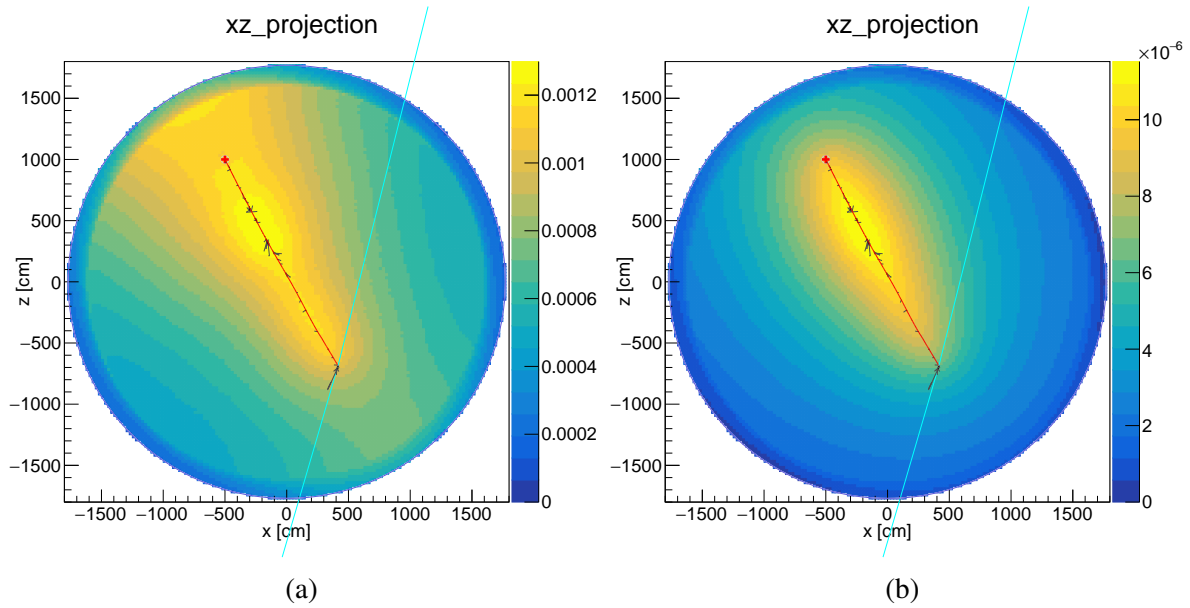


Figure 6.4: Impact of the raw reconstruction for a 4 GeV muon event. In (a) the XZ-projection result of first iteration detected light, with a measurement point distance of 25 cm over the whole JUNO detector target and a slice thickness of 2 meters. In (b) the same, but using the raw reconstruction mode.

results in a much more robust iteration process. Additionally, it is possible to exclude more volume with no event information after the first iteration and in the following iterations only perform calculations at the volume where the event is located. This has the additional benefit of reducing the overall amount of calculations during reconstruction without decreasing event topology detail.

Freedom of the reference point The reference point in time and space was initially implemented as the vertex of the interaction, but sometimes this is not obtainable. An example would be through-going muons that have their creation point high up in the atmosphere. Additionally, it may not always be possible to determine the initial interaction point for spatially extended events right away, even if they are confined in the detector target. Therefore, it is possible to adjust the *basic idea* to work for any point on a track, which is done by allowing the reference time t_{ref} to correspond to any time that fits to a point on the track and allow for reconstruction forwards and backwards in time. This changes the *basic idea* to:

$$t_i(\vec{x}) = t_{\text{ref}} \pm \frac{|\vec{x} - \vec{r}|}{c_0} + \frac{|\vec{x} - \vec{d}|}{c_v}. \quad (6.12)$$

One can see the addition of the negative travel direction along the particle track and t_{ref} needs to satisfy the time at a provided reference point \vec{r} on the track. One can see the backwards in time reconstruction from the end point of a muon in figure 6.5 (a) and the reconstruction in forward and backward direction at the same time in 6.5 (b), which uses a point in the middle of the track. The backward in time reconstruction quality is enough to determine where the muon track is,

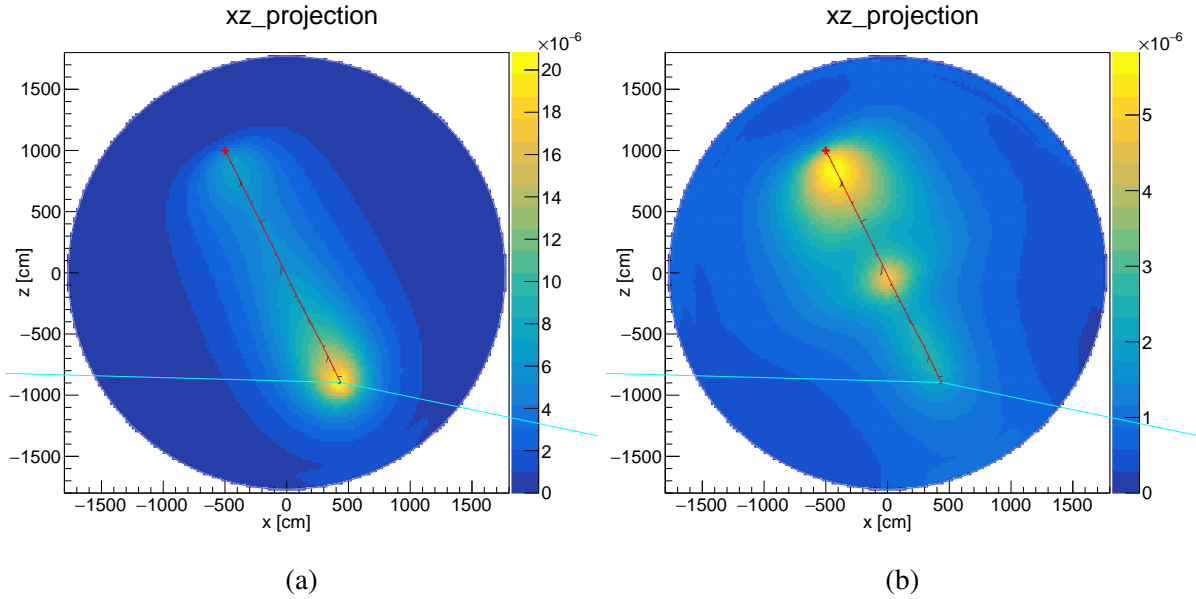


Figure 6.5: TTR using the backward in time reconstruction in (a) and using the backward and forward in time reconstruction at the same time, in (b). A 4 GeV muon is reconstructed and the third iteration is shown. For this reconstruction 25 cm binning is used over the whole JUNO detector. The reference point for backwards (a) is (438,-7,-895) cm and the time is 72 ns. The reference point for both directions (b) is (-5,10,-12) cm and the time is 38 ns.

but energy depositions are not well reconstructed. It is to note that this event did not have many secondary particles. Additionally, the area near the end of the track is exaggerated, which is probably due to delayed light. Reconstructing in both directions at the same time results in an emphasized emission point around (-5,10,-12) cm, which is the reference point that was used for this reconstruction and the backward reconstruction part contributes the an exaggerated Monte Carlo vertex, which again is probably due to delayed light. These findings indicate that the normalization may need additional work to handle this case correctly, which will be investigate in the future. Nevertheless, this enables the TTR to be applied to basically any event where a point on the track is known, with the corresponding time for that point. This is a much less stringent requirement than before.

Dynamic signal function The signal function in the TTR is the point where the time distribution effects of TTS and scintillation time are taken into account. Initially, this was set up as a histogram with nanosecond binning, from the start of the event until 500 ns later. This implies a time cut, which is appropriate because after that amount of time basically all light reaching PMTs will contribute *bad* information, due to scattering, re-emission or reflection. More importantly the nanosecond binning means a resolution of about 20 cm. Therefore, the dynamic signal function was introduced to enable a binning always corresponding to the anticipated resolution. This enables the reconstruction to be more detailed than 20 cm and a reduction of bins for iterations with less resolution. Hence, the dynamic signal function makes the TTR more precise and can reduce the amount of calculations needed.

Oversaturation For high energy muon events passing through the detector, the PMTs near the entry and exit point always have a lot of charge. This can result in a light per PMT distribute, where there are very few PMTs with lots of hits and a large amount of PMTs with a medium amount of hits. Because a lot of charge means a lot of weight during the TTR the result can lose topological detail, to a degree that it basically reassembles the local detection efficiency for the entry and exit point of the track. The result of a passing 209 GeV muon with this effect can be seen in figure 6.6 (a). One can see that there is a very high probability at the entry

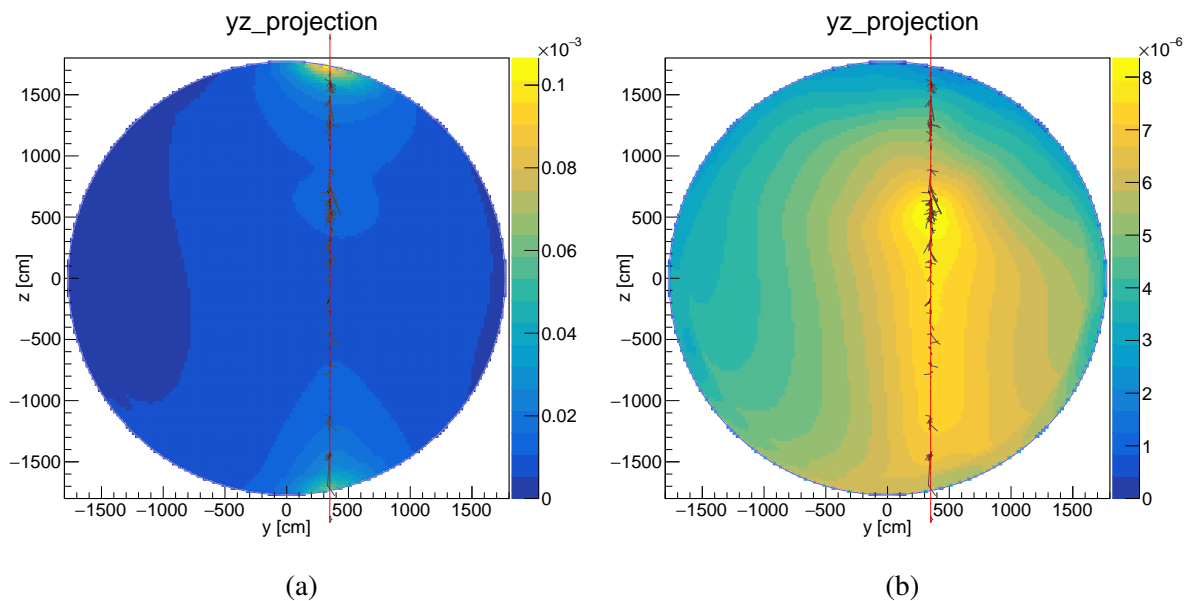


Figure 6.6: Impact of PMTs with very much hit data for a 209 GeV muon. In (a) the YZ-projection for the first iteration, showing emitted light, using a point distance of 25 cm for the whole JUNO detector target and a slice thickness of 2 meters. In (b) the same, but with enabled over saturation criteria.

and exit point of the track and very little detail is preserved from the track. This is the first iteration over the whole detector with 25 cm binning. It is a simple solution to dismiss any PMTs with too much charge, which prevents them from outshining contributions from other PMTs. This simple solution has been applied for figure 6.6 (b). Here, the top 20 % of PMTs with the most hits are excluded from the reconstruction. Some of the detail could be returned, but the probability at the top of the track is still missing. Overall a more sophisticated solution, which prevents too much contribution from the local detection efficiency, is of the essence. The current information used for the reconstruction does not consider PMT saturation, which may be beneficial for the solution of this problem.

6.3.2 Acceleration

In the previous section the addition of features that improved robustness and versatility have been discussed. Some of these already reduced the amount of time needed for the reconstruction process, but this section will be about features specifically added to reduce the amount of calculations needed and that have an impact on the speed up of the reconstruction process.

In its initial state the TTR was not applicable to events with lots of light information. This is mainly due to the approach itself, because information from everywhere inside the detector volume is initially needed and all the provided light information is used. Hence, the reconstruction of a single high energy muon event can take several hours. This is nowhere near the anticipated rate of muon events in JUNO, which is about 4.1 ± 0.9 Hz.

Measurement points Because only the volume taken up by the event itself is of interest, one can reduce the calculations of the TTR significantly by only evaluating the volume close to the event itself. The original reconstruction had something like this in place, where the volume was reduce to only contain the region of interest after some iterations. But this was only possible in a block structure, which means that the initial so called mesh for a detector like JUNO was the size of a cube with edge length 35.4 m. For smaller events this could be quickly reduced to smaller cuboids, but for the worst case scenario of a track passing diagonally through the mesh structure the volume would need to stay the size of the initial cube with edge length 35.4 m. This is why a new mesh structure was introduced, which is based on measurement points. These points can be distributed in any shape or form inside the detector and the reconstruction is only performed on these points. To be able to produce the same results as the previous implementation, the first implementation for the distributions of points was chosen to be the same grid like structure as before. The difference now though is, that any point can be dismissed each iteration just based of the value obtained for this point. Therefore, the point structure can reassemble the event topology much closer than before. Even the previously stated worst case scenario of a muon passing diagonally through the detector has a very similar amount of measurement points, compared to a muon which is following the grid structure perfectly. The time saved highly depends on the travel direction.

Random PMT selection One way to minimize the time the TTR needs to reconstruct an event is to reduce the amount information used. This can be done with the random PMT selection. It does this by calculating how many photons are needed to be able to reconstruct an event with a given resolution. The best statistical possible resolution can be approximated with following equation:

$$\sigma = \tau v_{\text{eff}} \sqrt{\frac{3}{\omega \cdot N_{\gamma}}} \quad (6.13)$$

by rearranging the needed amount of photons can be determined with:

$$N_{\gamma} = \frac{3}{\omega_1} \left(\frac{\tau_1}{\sigma} v_{\text{eff}} \right)^2, \quad (6.14)$$

where N_{γ} is the number of photons needed for this resolution, ω_1 is the ratio of photons emitted with the fast scintillation component, τ_1 is the mean lifetime of the first scintillation component, v_{eff} is the mean group velocity for the involved wavelengths.

Because we are handling spatially extended events this resolution needs to be reached at every

point along the track. This can be achieved by calculating how long the track can maximally be and then dividing it by the anticipated resolution. The distance traveled depends on the particle energy and how much energy is deposited along its way. Of the particles that are of interest, a minimum ionizing particle has the chance of depositing the least amount of energy along its way and therefore can travel the furthest. Therefore, the maximum distance L can be evaluated with:

$$L = \frac{E}{\Delta p}, \quad (6.15)$$

where Δp is the most probable energy loss from equation (2.3). Ignoring PMT saturation the, the energy E of a contained event can be estimated with:

$$E = \frac{\gamma_{\text{emit}}}{\gamma_{\text{yield}} R_{\text{cover}} E_{\text{PMT}}}. \quad (6.16)$$

The light yield γ_{yield} of the scintillator is used to convert photons into energy. This means the energy can be determined when it is known how many photons have been emitted. But a significant amount of photons is lost and needs to be accounted for with the ratio of coverage R_{cover} and detection efficiency E_{PMT} of the PMTs. Another approximation can be used to determine the emitted photons γ_{emit} by weighting the charge of each PMT and reevaluating it with the local detection efficiency under the assumption that all photons have been emitted from the charged barycenter of the event. A pretty rough estimate is enough, because only a maximum energy estimate is needed to determine a maximum travel distance, which itself gauges how many photons are minimally needed to reconstruct the event.

By combining the amount of photons needed with the estimated maximum track length, the total amount of photons can be approximated:

$$N_{\text{total}} = N_{\gamma} \frac{L}{\sigma} f_{\text{clean}}, \quad (6.17)$$

where the additional factor f_{clean} assures a minimum amount of clean photon information without effects like scattering, absorption and reflection. For a high energy muon event in JUNO about $\frac{1}{3}$ of photon information is *clean*. Therefore, a reasonable value for this factor is three. This yields the total number of photons needed for an anticipated resolution σ . In principle there could be a random photon selection, but it is not necessarily the case that single photons can be separated within a PMT. Additionally, the code base made it much simpler to select random PMTs with a given amount of photons instead.

A result with this random PMT selection enabled can be seen in figure 6.7 (b). For reference, the same reconstruction with full photon information was performed in figure 6.7 (a). One can see that the results look visually very similar. It is important to point out the difference in probability, where the overall emission probability is much less for the event reconstructed with the random PMT selection. This is due to the reduced amount of photons used, but can be accounted for by scaling with the amount of actual photons compared to the amount used. Other selection methods than the random selection have been explored, but these introduced biases

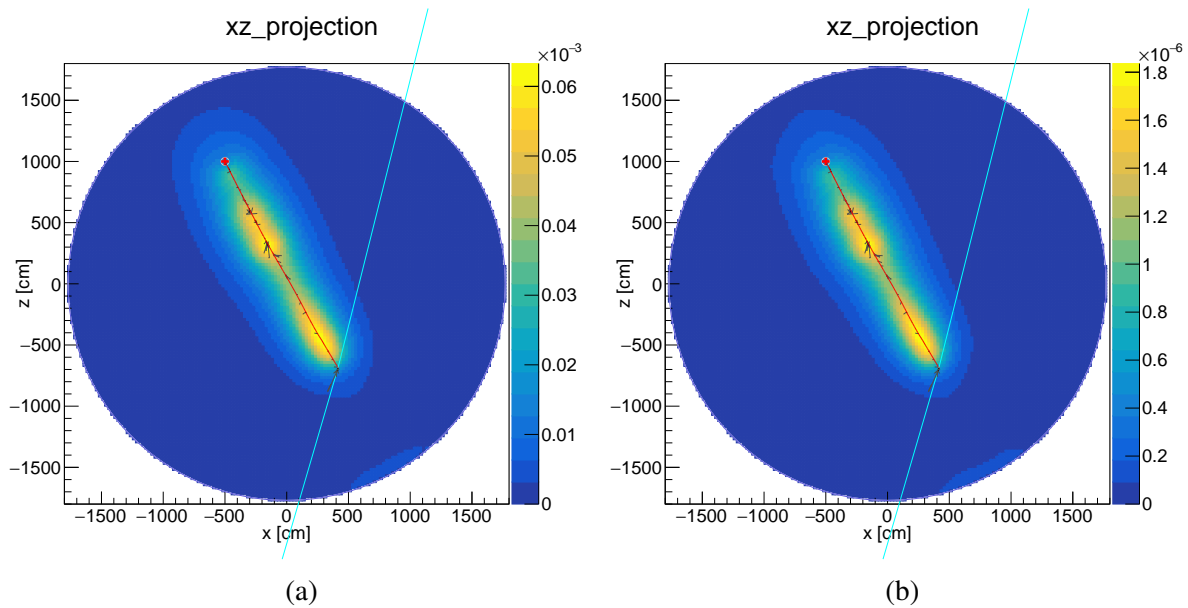


Figure 6.7: Impact of the random PMT selection, for a 4 GeV muon event in JUNO. In (a) the XZ-projection of the 10th iteration, showing emitted light, over the whole JUNO detector target, with a point distance of 25 cm and a slice thickness of 2 m. In (b) the same, but utilizing the random PMT selection.

and therefore the random selection was chosen. With this random PMT selection the time used to reconstruct an event can be reduced by about 30%, but this number heavily depends on the anticipated resolution.

Refactoring & Gprof Sometimes in development decisions are made that heavily impact the performance of a program. To get an idea of which parts of the program are executed more than others and how some of the calculations could maybe be replaced with static data, one can use code analysis tools. One of these tool is Gprof, which is a simple to use, linux based, call-graph profile tool, which was used to analyze the reconstruction code. With the help of this tool, it could be determined that the position of sub cells in the original mesh was recalculated every time it was needed. By calculating this once and saving this information into an array, it was possible to reduce the execution time by about 20%. Because this does not actually change anything about the way the reconstruction behaves, this does not effect the results. This was done at the beginning of this work and the later replacement of the mesh with the measurement points made this change obsolete and further improved the execution time. Nevertheless, it revealed the possible potential for optimization. Another point of attack was the consideration of charge. Originally the TTR had to handle every photon by itself, but this was optimized to process photons, from one PMT with the same time, at the same time. This basically is the charge, but in quantized steps. The result is the same as before, but less calculations are performed. The speed up from this change greatly depends of the amount of photons that have the same hit time at a PMT. For a high energy event, with a great amount of hits, it is more likely to have a time saving effect.

CPU parallelization Parallel to the development of features in this work, the CPU parallelization of the TTR was achieved by another group member and the detailed implementation is discussed in [97]. The CPU parallelization alone can achieve a speed up of the reconstruction by about 90 % with the computing hardware used, which is a Intel Xeon CPU E5-2640 v4 running at 2.40 GHz with 20 physical cores and hyper threading. Like the refactoring this does not change the results of the TTR. To enable the use and time saving of features in this work, the CPU parallelization was merged with this existing code base, during this work. This created a new universally adapted version of the TTR.

6.4 Summary & Outlook

The addition of these features made the TTR more robust and enables it to be applied to a wider range of events. Nevertheless, further development is still needed. For example, important issues that have not been addressed yet, are that the reconstruction does not account for PMT saturation or that it runs in a mode that expects single photon information, even though this may not be obtainable for high energy events. Additionally, there seems to be some issues with muon events that have an energy greater than a few GeV, which can be seen in figure 6.6 (a). The main reason for this is the uneven amount of light distribution over the PMTs for these types of events. This means a usable result is still in there, but it cannot be seen, because some PMTs contribute much more probability. They do this in such a way so that only their contribution is visible. These are points that have to be addressed to enable the use of the TTR for muon events in JUNO. Additionally, the time constraint of a muon reconstruction every second could not be achieved yet, even with the time saving measures implemented during this work. To not undermine the effort put into the reduction of reconstruction time one can see in figure 6.8 that the features introduced already reduced the time needed significantly. The reconstruction time for a 3 GeV muon is stated. Initially, a typical reconstruction for this event took 1 hour and 27.5 minutes, but with the code review this has been reduced to 1 hour and 10 minutes. With the addition of random PMT selection and CPU parallelization it was possible to further reduce this to just 3 minutes and 14 seconds. This is still too slow run live, but it still may be possible to reach this goal with GPU parallelization. To take full advantage of this approach, the current code base should be rewritten with GPU parallelization in mind.

Because it is currently not possible to use the TTR for very high energy muon events in JUNO and the reconstruction time is too slow to be applied to live data, a simplified version of the TTR has been explored, which will be discussed in the next chapter.

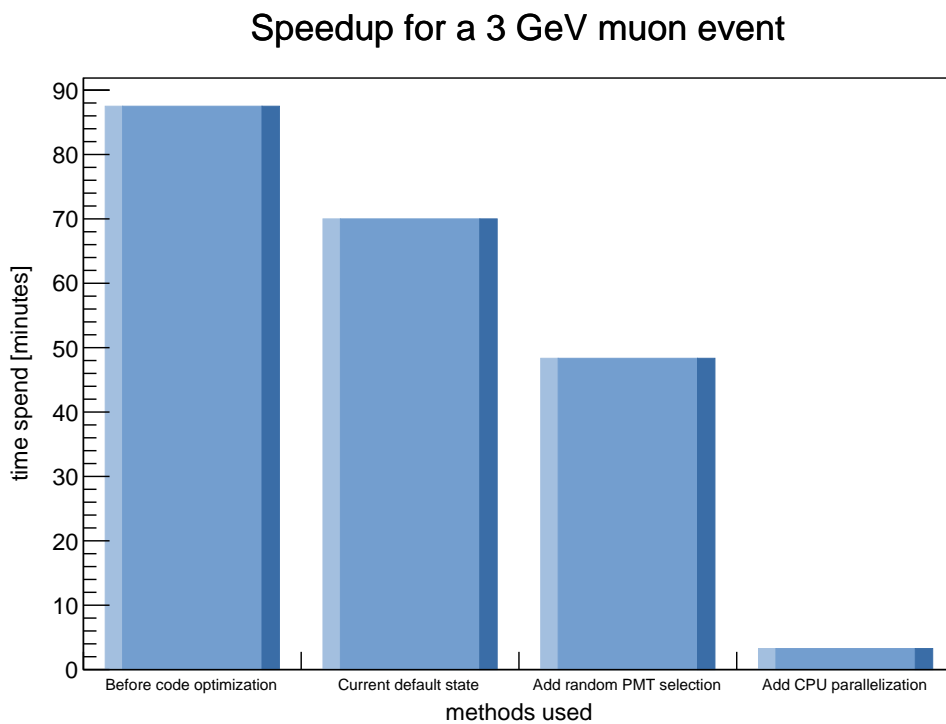


Figure 6.8: Reconstruction time reduction achieved during this work, for an example 3 GeV muon. From left to right: Initial status, then after code review, after enabling the random PMT selection and then with the addition of CPU parallelization.

Chapter 7

Quadratic Reconstruction

Based on the *basic idea* 6.1.1 of the TTR it is possible to create a much simpler and faster version. This chapter will introduce a reconstruction concept, which henceforward will be referred to as Quadratic Reconstruction (QR), because the core concept utilizes a solution method for quadratic equations. The following section presents the mathematics, continued by a section about the estimated applicability of the QR.

7.1 The *basic idea* as a quadratic equation

For more details about the *basic idea* look into 6.1.1. Similar to the TTR some prior knowledge of the event is needed. The main application case for this approach is along muon tracks, which are passing through a liquid scintillator detector. Hence, the prior knowledge can be adjusted accordingly:

- Instead of any reference point, the entry point into the detector is needed \vec{r} .
- Similarly, the corresponding reference time is necessary.
- The particle roughly follows a straight line.
- The speed of this particle is close to the speed of light in vacuum.
- **Additionally, an exit point or direction is needed.**

For high energy muons it is a valid approximation to assume that they are traveling in a straight line and close to the speed of light in vacuum. Because JUNO has a very high coverage of photo sensors it is also likely that a through-going muon will hit a photo sensor while it is entering the central detector and also when it is exiting. These two PMTs will report to see much more light than any other, which can make it simple to provide a reference point and time as well as an exit point or direction. Otherwise, there is still the possibility for traditional algorithms to determine the needed information, as well as the muon veto outside the central detector. The additional requirement of a direction or exit point is the main difference to the TTR approach and the main reason why the simplification and speed up is possible. This enables one to only perform a

reconstruction along the muon track instead of the whole detector. A simplified version of a hypothetical photon emission and detection can be seen in figure 7.1.

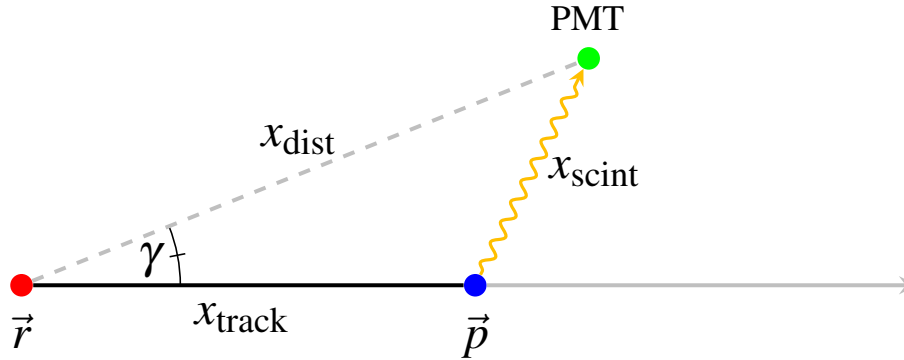


Figure 7.1: Recap of the *basic idea* in section 6.1.1, where a particle is assumed to travel along a straight track, with a reference point \vec{r} (red) and induces scintillation passing point \vec{p} (blue). A photon is emitted and in this example it travels through the scintillator until it is detected at a PMT (green). In contrast to the *basic idea* of the TTR the track direction is known and indicated by angle γ .

Similar to the TTR, it is the goal of the QR to determine where along a track scintillation photons have been emitted. A solution to this problem lies in a comparison between the measured hit time t_i and the calculated time along a track part and scintillation path assumption. This can be written as

$$t_{\text{track}} + t_{\text{scint}} - t_i = 0, \quad (7.1)$$

where t_{track} is the assumed time on a track part and t_{scint} is the time a photon would need from point \vec{p} to a PMT. This approach ignores time differences because of electronics, scintillation processes and photon travel effects, but these may be added in post. This crude analysis already yields promising results for the dE/dx structure, as will be described in chapter 8, with much fewer calculations needed than in the TTR. This is due to only performing this reconstruction along the track and further reducing calculations needed by implementing an analytic solution for quadratic equations, which will be discussed next. We can rewrite equation (7.1) as

$$\frac{1}{c}x_{\text{track}} + \frac{1}{v_{\text{eff}}}x_{\text{scint}} - t_i = 0. \quad (7.2)$$

This replaces the time with a combination of distance and speed. For the first part t_{track} the assumption of the particle travelling with the speed of light in vacuum is reasonable, because the intended use case is $\sim 200\text{ GeV}$ through-going muons. For the second part t_{scint} the speed actually depends on the group velocity for the photons specific wavelength, which is not obtainable during reconstruction. Instead of the real effective velocity, an average velocity has been chosen for simplicity. Hence forward, v_{eff} will be only referred to as v .

Currently unknown during reconstruction are x_{track} and x_{scint} . As one can see in figure 7.1, the problem can be reduced to a triangle. Therefore, x_{scint} can be described with the law of

cosines, as

$$x_{\text{scint}}^2 = x_{\text{dist}}^2 + x_{\text{track}}^2 - 2x_{\text{dist}}x_{\text{track}}\cos(\gamma). \quad (7.3)$$

By utilising this, formula (7.2) becomes

$$\frac{1}{c}x_{\text{track}} + \frac{1}{v}\sqrt{x_{\text{dist}}^2 + x_{\text{track}}^2 - 2x_{\text{dist}}x_{\text{track}}\cos(\gamma)} - t_i = 0. \quad (7.4)$$

To apply the quadratic formula its turned into canonical form,

$$x_{\text{track}}^2 + \frac{2x_{\text{dist}}\cos(\gamma) - 2\frac{v^2}{c}t_i}{\left(\frac{v}{c}\right)^2 - 1}x_{\text{track}} + \frac{t_i^2v^2 - x_{\text{dist}}^2}{\left(\frac{v}{c}\right)^2 - 1} = 0. \quad (7.5)$$

This is now solvable by the quadratic formula [98] . If this is a perfect description one would expect a solution for each zero of this function, but as will be discussed in the next section will results in three possible cases.

7.2 Quadratic Reconstruction concept

The goal of this reconstruction is to identify the points of photon emission along a track. To utilize the concept of QR it has to be put in context with the real application case. In reality, a particle enters the detector or is emitted from an interaction at point \vec{r} and traverses the detector until it stops or exits. A photon is emitted at point \vec{p} . In a perfect case deploying the QR will yield two possible points¹ for photon emission on an infinite track. Only one of them is realized, but there is no distinction possible if only time is considered. However, it can be restricted by the reference point \vec{r} and the dimension of the detector target, resulting in the following two cases for an idealized event.

In the first case, both of the solutions are inside this range. Currently, there are no further restrictions reasonable, therefore both should be weighted equally, even though only one of the points is realized. Hence, an emission probability of 0.5 is given to each, which reflects the total emission of one photon.

In the second case, only one of the solutions is inside the limits, which are constructed and tightened by the detector target size and the reference point. Then this solution found the point where the photon was emitted and a probability of 1.0 is assigned. Only allowing this case results in a perfect dE/dx reconstruction for an idealized test event.

A third case is possible during the real scenario, where larger time differences exist due to electronics, scintillation processes and photon travel effects. Then the solutions can also be imaginary numbers or both solutions are outside the specified range. Since these hits do not advance the reconstruction, they are currently ignored. Some of these hits could still hold usable information. For short hit times, one could argue that these originate from direct light and fast emission, which could hint to Cherenkov light. These hits could improve the dE/dx

¹It is also possible that both points are the same, which is automatically treated correctly by the case identification. Hence, this is not further explained.

reconstruction. To gain information on their emission point a second algorithm could be applied, which determines the shortest distance x_{scint} possible, by reducing the hit time in iterations, until the quadratic formula cannot be solved anymore. This corresponds to a quadratic function, which has been moved above the x-axis so that there is no zero spot. Hit times too large to fit the defined track range maybe delayed, due to scattering, reflection and/or absorption and re-emission. These hits are currently ignored as well, but can be tagged. Running the TTR with tagged photon data could increase robustness and its resolution.

Additionally, the JUNO detector not only has liquid scintillator, on the photon path from the target to a PMT, but also the acrylic sphere and ultra pure water. To not complicate the simplistic nature of this approach, the acrylic sphere is neglected completely and the effect of water on the photon speed is only approximated by adjusting the PMT time for the photons. This means a time offset is calculated for the photon's PMT time by calculating the additional time that would be needed if the water part was liquid scintillator. The refraction at the acrylic sphere will have an effect on the reconstruction, which is currently not considered. To describe refraction more accurately, it is possible to do a second iteration, when photons have already been placed on the track and to calculate a time offset due to refraction from the determined position to the PMT, but this has not been implemented yet.

Chapter 8

Results of the Quadratic Reconstruction

The JUNO detector is not completely built at time of writing. Hence, for JUNO there is only the possibility of testing the QR with simulated data. It can be tested with data from other liquid scintillator detectors and this is planned for the future, but the results presented in this chapter are purely based on simulations. The next section 8.1 will go over the data structure that contains the results, followed by an example of how this data can be presented in a form that is simple to interpret. The next section 8.2 will go into detail about realistic cases and robustness. Then in section 8.3 a quantitative study is explored, which will test the QR on capabilities such as determining the start point and the maximum of a shower. These are important requirements for the veto strategies explored in chapter 4 and will enable one to evaluate if the QR can be used for these veto approaches. Finally, this reconstruction will be compared to the TTR in section 8.5 and it will be discussed what advantages it can provide as a pre-reconstruction.

8.1 Data structure representation

The QR aims to determine the location of photon emission along a track. The simplest representation for this is a coordinate along the track for every photon that has been detected. But the QR has a very simple underlying principle and in reality only about 8 % of photons are reconstructable in this way. Additionally, this approach may reconstruct two points of emission, due to its quadratic nature. Hence, as discussed in section 7.2 there is a probability attached to a possible photon emission point, which is either 1.0 or 0.5. The emission coordinates along a track can be presented as a density distribution. A simple histogram representation can achieve this, with the added bonus of quantifying the number of photons per point. Hence, this has been done for the result representation and an example can be seen in figure 8.1 (a), but it is to note here that the actual result of the QR are the emission coordinates along the track, with its probability for every photon that could be reconstructed. In histogram (a), one can see the summed up probabilities for every reconstructed photon along a muon track, where the muon is entering the simulated JUNO target from the top center and exiting it on the bottom side. The muon energy is 209 GeV and it deposits about 7.2 GeV in the detector target. The target starts at about 2.3 m and ends at 37.7 m. The histogram bin size is 10 cm. One can already see a large

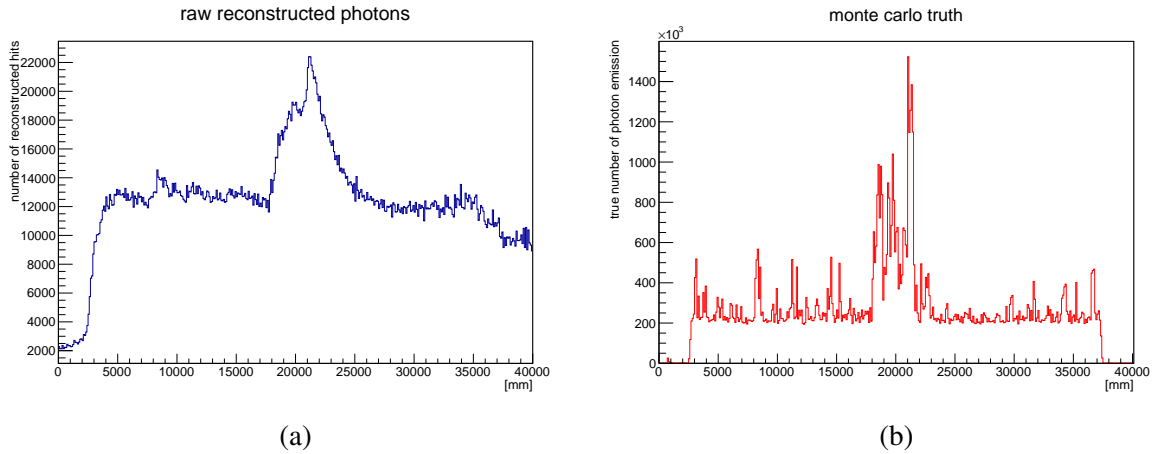


Figure 8.1: Example result representation for QR of a 209 GeV muon, starting at (0,3.5,20) m and traveling in negative Z-direction. In (a) one can see the raw result of the amount of reconstructed detected photons along a muon track. In (b) the Monte Carlo truths of photon emission along the same muon track is shown.

amount of photons have been emitted, during the shower, in the center and there could be some smaller showers, around 9 m and 12 m. The same event can also be seen in (b), but here the actual number of emitted photons has been saved during the simulation. When comparing these two histograms, one can see that the amount of photons reconstructed is much smaller than the actual emitted amount. The QR models perfect information and in turn expects direct timings. This means photons that take an unexpected longer time, shorter time or different path, will not be reconstructed correctly or not reconstructed at all. Reasons for this can be:

- The Photon stems from the Cherenkov effect and does not have scintillation delay.
- It is a scintillation photon, but deviates too much from the mean scintillation time.
- A photon is scattered on its way to the PMT and hence has a delay and an unexpected path.
- A photon is absorbed and is re-emitted, which introduces a delay and an unexpected path.
- The photon is reflected and takes an unexpected path.
- The QR does not include refraction at the acrylic sphere in detail.

One or more of these reasons can lead to an unexpected time, which leads to no solution with the quadratic approach and then this photon can not be reconstructed. This means less statistics, but it has the advantage that the amount of photons with unexpected information is greatly reduced. Unexpected information in this context is anything that can not be simply accounted for and applied on a per-photon basis. For example, a point where a photon scatters or is reflected. If these would be reconstructed, the information gained would be detrimental for the result. Even if not all photons can be used for the reconstruction, it is still possible to reconstruct the actual amount of emitted photons from this raw result, which will be done in the next paragraph.

Determine emitted photon numbers As established, the amount of reconstructed photons is much less than the actual emitted amount of photons and it is desired that the emitted amount of photons correctly estimates the energy deposited in a region. There are some effects that can be accounted for and some that can be reconstructed. For a simplified version this has been done, to show that the expected amount of photons can be found. Simplified means that in the following example all photons with unexpected information have been removed as well as no TTS is assumed. Therefore, this example does not contain scattered, absorbed, reflected or Cherenkov photons. The matching of raw QR to the Monte Carlo truths can be seen in figure 8.2. In the top left the QR and on the top right the number of emitted photons from Monte Carlo truth can be seen. In the middle left is a lookup table (LUT) that accounts for detection efficiencies, depending on the distance to the center. This LUT was created by simulating muons at different distances from the detector center, which pass through the detector target and have all secondary particles (besides photons) disabled. The generated data contains all the information needed to account for detection effects. When these example muons are then reconstructed by the QR, one can divide the Monte Carlo truth by the results of each position, which yields a number for each position that accounts for none reconstructable photons. In other words, these are the numbers for every point in the detector target that can be multiplied with a QR result, to obtain the emitted number of photons for that point. This has been done and is the blue curve at the bottom. A two dimensional LUT is enough, due to symmetries in JUNO. On the middle right is the scintillation function as an emission probability for one photon that was induced at a time 0, which has the x-axis translated from nanoseconds to millimetres, by multiplying it with the speed of photons in the liquid scintillator. The number of emitted photons along the track from the Monte Carlo truth (top right) can be convoluted with this scintillation function, which has been done and can be seen in the bottom as the red curve.

At the bottom, in figure 8.2, the reconstructed curve (blue) and the Monte Carlo truth with scintillation convolution (red) match up quite nicely. They match not only in position along the x-axis, but also in the amount of photons. This means that the main contribution, in this example, is the scintillation time and that detection effects can be reconstructed with a simple LUT. Additionally, delayed light is always shifted along the track direction, otherwise the scintillation function would not match when not applied symmetrically. Nevertheless, it is important to stress the point that this example only contains perfect light and no TTS, which means effects like scattering, absorption and reflection are not accounted for. It is encouraging though that the original amount of emitted photons has been deduced, but the match is not perfect, which is mainly due to neglect of the refraction at the acrylic sphere. The time difference due to the speed of photons in water compared to scintillator has been approximated, by calculating and adding the time difference for the distance of the PMT to the detector target, which is about 1.65 m. This does not account for refraction, but considers that at least that minimum distance was made with the speed of light in water.

There are two important remarks left for this example of determining the emitted photon number along a muon track. Firstly, it is not that simple to obtain a LUT in the real experiment

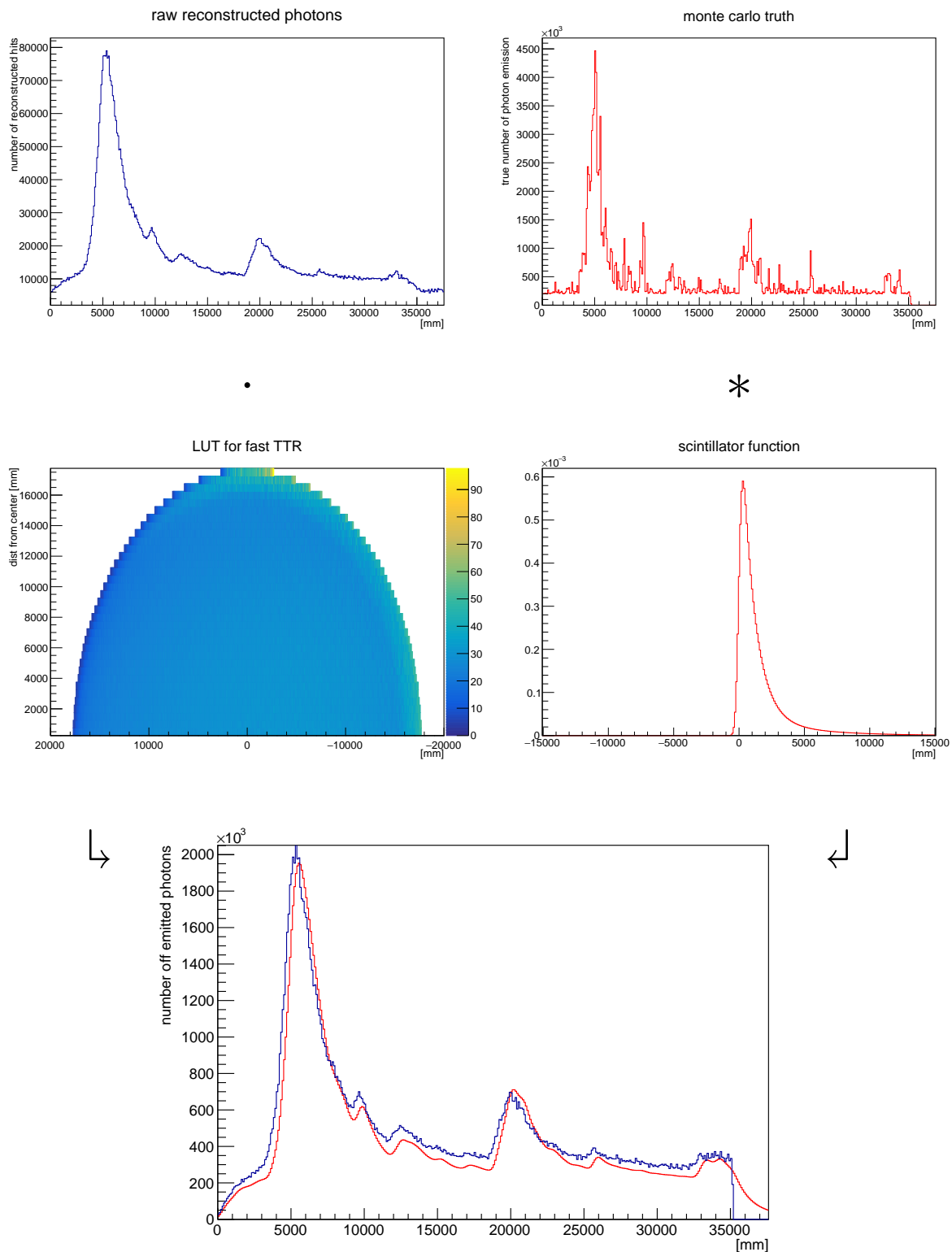


Figure 8.2: Determining emitted photons with the QR. A 209 GeV muon starting at (0,-2,17.6) m and traveling in negative Z-direction. At the top left (blue) the raw reconstruction result of detected photons along a muon track. The top right (red) the Monte Carlo truths of photon emission along the same muon track. In the middle left is the lookup table generated with simulations. At the middle right (red) the scintillation function considers PMT TTS and scintillation decay times. In the bottom center the combination plot of the photon emission along a muon track (blue) and the convoluted Monte Carlo truths (red) for the same event. This example does not contain scattered, absorbed, reflected or Cherenkov photons.

as it is in this example, but something similar can be done. If the JUNO simulation describes reality well enough, a generated LUT from it can be adapted. One can use it as a starting point and additionally measure through-going muons in JUNO, of which there will be about 5.4 per second. About 85 % of these muons are expected not to shower. A muon without secondary particles can give a base number of photons emitted along a muon track and with enough statistics this can be used to adjust the LUT. Secondly, the comparison made here was with the convolution of the scintillation function with the actual number of emitted photons. Ideally, it would be the case that the exact amount of photons emitted along a muon track can be determined. Maybe a deconvolution could be performed to properly account for the delay due to scintillation time and TTS, but this has not been done yet. Hence, in the following sections the QR result will always be compared to the Monte Carlo truth convoluted with the scintillation function. As shown, this is sufficient for now, because any deconvolution applied to both would result in similar differences, as without. To attempt a deconvolution is something for future development, but even if a deconvolution should prove to be unfeasible, one could also attempt to deploy machine learning methods for this problem. Now, the question remains how the QR will fair against imperfect photon data, which will be discussed in the next section.

8.2 Realism & robustness

In the previous section, the QR was performed on perfect data, now realism needs to be added. Going back to the event from figure 8.1 and multiplying with the correction LUT one can obtain the result seen in figure 8.3 (a), in blue. The Monte Carlo truths convoluted with the scintillation

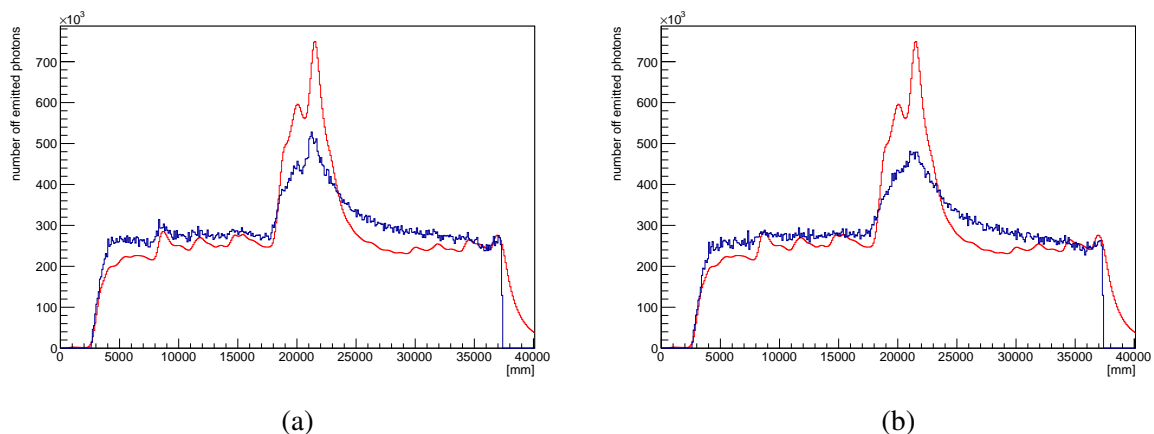


Figure 8.3: Reconstruction result for QR with imperfect data for the same 209 GeV muon, starting at (0,3.5,20) m and traveling in negative Z-direction, as in figure 8.1. In (a) with scattered, absorbed, reflected and Cherenkov photons. The same in (b), but PMT times smeared with PMT type corresponding TTS.

function was also added (red). This 209 GeV muon event already has effects like scattering, absorption and reflection enabled. One can see that the amount of photons match with the expected amount seen in the Monte Carlo truths, but the main shower peak height does not reach

the predicted height. This is caused by none perfect light information, because all the light that has been delayed, due to scattering, reflection and absorption with re-emission, is found to be later along the track by the reconstruction. This means determining the end of a shower as well as its energy is not that simple. Additionally, smaller showering events can be drowned out in the wake of a larger shower, which can make them invisible to the reconstruction. This can be seen when one compares a small shower from around 12 m with a similar shower at around 35 m. Additionally, in figure 8.3 (b) the TTS effect is approximated by randomly smearing photon times with a Gaussian distribution that has a sigma of 1.274 ns for Hamamatsu PMTs, 5.096 ns for NNVT PMTs and 1.911 ns for HZC PMTs. This worsens the reconstruction overall and features clearly visible without TTS can become unrecognizable. Nevertheless, the main shower, that deposits about 5 MeV/cm, can be clearly identified even with the TTS. Performing the reconstruction with only Hamamatsu PMTs creates a similar result, even though they have a lower TTS. This indicates, that there may be a balance between the added information and quality of information from PMTs with a larger TTS. Therefore, it may be possible to reduce the amount of PMTs used, to the PMTs with small TTS, which implies less computation and comparable results.

As expected for high energy muon events with a large amount of light, adding 20 kHz dark noise to all PMTs has no visible effect on the result, because the result looks exactly like figure 8.3 (a), this additional plot was omitted. This is expected, because the amount of dark hits during the time span of a muon event is much smaller than the amount of light produced by the muon and as long as the dark hit time does not match to a point on the muon track it will not be reconstructed. This can be seen as a feature of the QR, which will filter out wrong information.

Robustness wise, one can argue that the effects introduced by no perfect photon paths and TTS as well as dark noise always apply, but these do not make the set goals impossible to reach. Instead, they just limit the performance at which precision the light emission can be reconstructed. To use this reconstruction approach, one can not forget that there are initial parameters needed for the muon track. As a recap, the prior knowledge needed to apply this type of reconstruction is as follows:

- A reference time, which acts as an event start time.
- The start point of a track or entrance point into the target.
- A direction or the end point of the muon track.

The error on this parameters can significantly impact the results of the QR. Until this point it has been assumed that this initial data is perfect. What happens with none perfect initial event data and if these parameters are obtainable will be discussed next.

Firstly, one can look into a none perfect reference times. A time offset of 5 ns for all photon hits can be see in figure 8.4. This effects all hits in the same way and translate into a shift of the entire dE/dx profile. In figure (a) a negative reference time offset of -5 ns was applied and one can see that it moves the event profile to the start, while also impacting the first and the

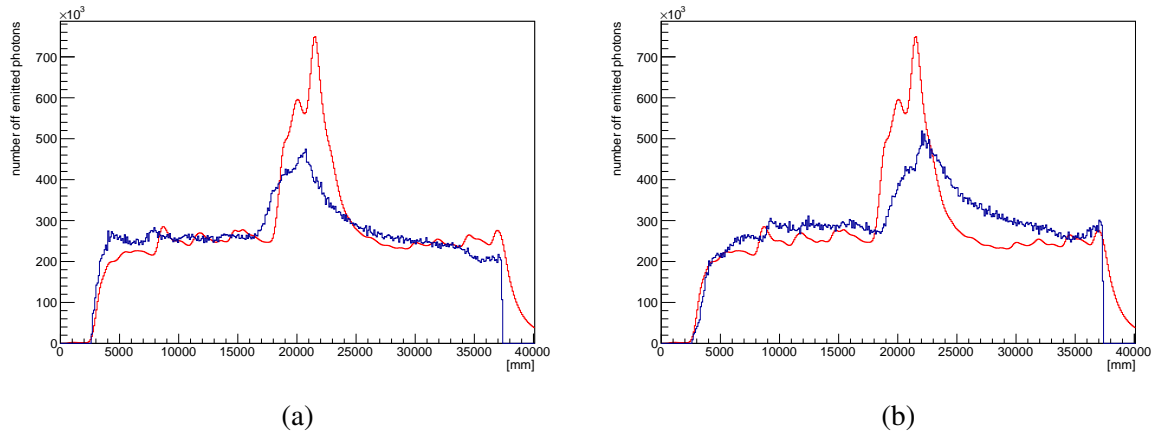


Figure 8.4: QR result for a wrong reference time, for the same 209 GeV muon, starting at (0,3.5,20) m and traveling in negative Z-direction, as in figure 8.1. In (a) the reference time is offset by -5 ns and a shift to the start for the photon emission profile can be seen. In (b) the same event and reconstruction but with a reference time offset by +5 ns and again a shift can be seen, but towards the end of the track.

last 2.5 m of the distribution significantly. The same shift can be seen in (b) for the expected opposite direction of +5 ns. This is detrimental to the reconstruction of shower positions and in this example translates into an offset of about $\pm 5 \text{ ns} \cdot 0.2 \frac{\text{m}}{\text{ns}} = \pm 1 \text{ m}$, but a wrong reference time of $\pm 5 \text{ ns}$ is large compared to a more realistic value of about $\pm 0.33 \text{ ns}$, which is expected to be reachable by reconstructions that can provide a reference time [99].

Secondly, in figure 8.5, the reference start (a) and end point (b) of a muon track has been shifted parallel to the actual simulated muon track. In (a) one can observe that a parallel shift

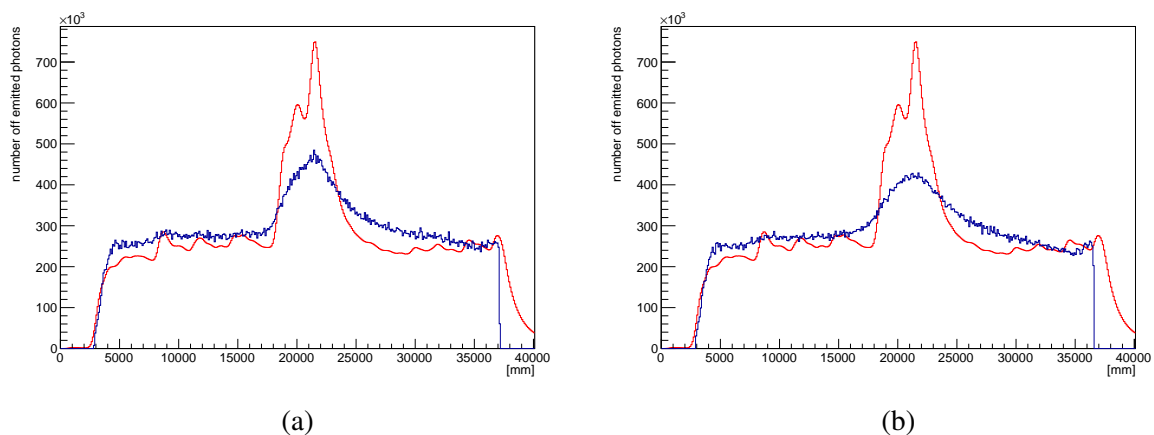


Figure 8.5: QR result with wrong reference information, for the same 209 GeV muon, starting at (0,3.5,20) m and traveling in negative Z-direction, as in figure 8.1. In (a) the reference point is offset by 1 m. In (b) instead the track direction is offset by about 3 degrees.

of 1 m of the reference start point makes small features like the double main peak and the $\sim 2 \text{ MeV/cm}$ peak at 10 m almost invisible. A mismatch of the reference start point along the track axis is expected to have a similar effect on the reconstruction as a reference start time

shift. A combination of these two effects has to be expected for a realistic scenario. But even an offset of 1 m leaves the main feature intact, which is an indicator for the robustness of the QR. A realistic reference point offset can be simulated with a Gaussian distribution with a sigma of about 20 cm, since this is a resolution that is deemed reachable for a provided reference start point. For figure 8.5 (b) the reference end point has been shifted parallel to the track direction by 2 m. This offset corresponds to a direction mismatch of about 3 degrees for this example. This is a relatively large offset when using an entry and exit 20" PMT to determine the direction of a track, where the offset is probably less than $\arctan(0.5[m]/35.4[m]) \approx 0.8$ degrees. This implies that reconstruction is very sensitive to the direction or end point. It is to note here that no TTS is used in this example. A reference start and end point, for through-going muons, can be found by looking for PMTs with the highest photon counts. This is the case, since PMTs through which the muon passed will almost always have reached more than saturation level. The physical size of a large PMT in JUNO is about 25 cm radius, hence a point found will have an offset much smaller than a meter. This is not possible for muons that do not pass through PMTs, but other reconstruction algorithms could provide starting parameters in this case.

As a final word on robustness, the QR is very sensitive to the initial input parameters of the muon track and worse parameters will make the identification of small features harder, as well as the corresponding shower energy reconstruction more complex. Hence, the initial parameters provided to the QR should be selected with great care.

8.3 Quantitative analysis

The performance of the QR has been examined with 976 muon events. For more information on the data sample look into chapter 5.2. The reconstructions in this section considers scattering, reflection, absorption with re-emission, and TTS. Additionally, the event reference time has been smeared with a 1 ns sigma Gaussian distribution and the start position as well as the end position have been randomly shifted with a Gaussian distribution of sigma ~ 20 cm, which corresponds to about 1 ns in photon travel time in scintillator. This will approximate more realistic conditions for the application of this reconstruction approach in JUNO. PMT saturation is not considered and is expected to mostly have an impact on shower energy resolution, which has not been tackled yet.

The shower position analysis was performed. For this, the showers position needs to be determined, as well as a shower matching between the QR results and the Monte Carlo truths needs to be performed. With figure 8.6 the method of peak finding and matching will be explained. In (a) the Monte Carlo truths and corrected QR result with a binning of 1 cm can be seen. To obtain a coherent definition of showers in this figure, both the Monte Carlo truths as well as the corrected QR result have been smoothed, by convolution with a Gaussian distribution with sigma 1 m. This may limit the identification of small energy depositions not only in the reconstruction, but also for the Monte Carlo truth, but when studying figure 8.6 (a) one can see that the resolution of the reconstruction is only around a meter and it seems reasonable to

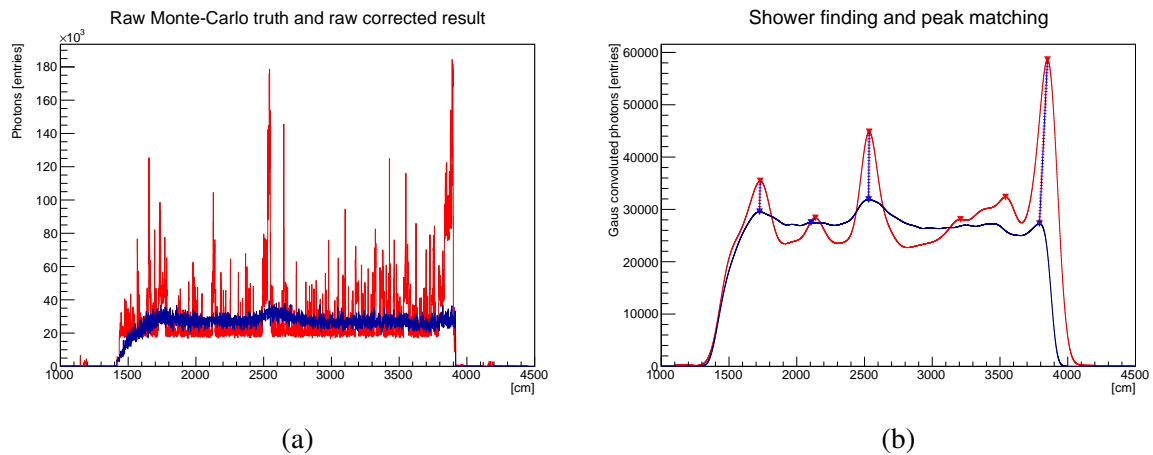


Figure 8.6: A 156 GeV muon has been reconstructed. In (a) the QR emission result and Monte Carlo truths with very fine binning can be seen and in (b) shower finding and peak matching is shown. Monte Carlo truths is marked in red and the corresponding reconstruction result is marked in blue. In (b) small triangles mark identified peaks in the emission profiles and peaks that are connected by dotted lines have been associated with each other.

match what is actually identifiable by the reconstruction, instead of trying to match every small energy deposition that would not be definable or reconstructable. It is to note here that very small energy depositions can not be identified in the Monte Carlo truth due to the convolution with the aforementioned Gaussian distribution. The integral stays the same with this kind of smoothing, but even more importantly the position of the peak stays the same, which is not the case when a convolution with the scintillation function is done. This also means the result of the QR is inherently shifted by a set amount, because of the scintillation time that inevitably contributes during photon emission. Therefore, the corrected QR result is shifted by -38.6 cm in this analysis, to compensate the mismatch in peak positions. This shift was determined rather arbitrarily after the peak positions statistically did not match up by this amount. The result of this processing can be seen in 8.6 (b). The muon in this example has an initial kinetic energy of 156 GeV and 3 main showers, which deposit about 0.3 GeV, 0.4 GeV and 0.7 GeV respectively. Even more than these 3 peaks are marked by the peak finding algorithm, for the Monte Carlo truths as well as the reconstruction result. The criteria for the peak finding are set as follows:

- The derivation at that point needs to be zero
- Moving to the left or right of this point needs to have negative derivation.
- The energy deposition needs to be greater than 2.2 MeV/cm, which is a bit more than the expected base deposition of the muon.
- A new peak must be presided by a valley that has at least 50 keV/cm less energy deposition than the new peak.

The first two points are just a simple definition of a local maximum. The third point makes sure the peak is actually a peak and not just the deposition of the muon. The final point prevents

small random fluctuations to be identified as a shower. Points that qualified under these criteria are marked by a triangle in figure 8.6 (b). Red triangles are used for the Monte Carlo truths and blue triangles mark peaks in the reconstruction result. The matching between the identified showers has its own criteria, which are as follows:

- The peaks have to be in a range of ± 1.4 m (along the track direction) to each other.
- In a linear fashion, both peaks get a likeliness value assigned the closer they are.
- They count as a match when both peaks choose each other as most likely.

One can see that the 3 main showers have been matched up and even a very small shower, which deposits only 100 MeV, has been found at around 21 m. The small showers around 35 m could not be reconstructed in a way that is detectable by these criteria. It is noteworthy that showers in the first 2 m as well as the last 2 m are under represented by the QR method and therefore are only inconsistently found. Some reasons for this might be edge effects, due to the total reflection zone and refraction as well as a large contribution of the photon path being in water and not scintillator. There is no shower at the start of this example, but even if there was a shower it would probably not be detected and the photons would contribute to the shower around 17 m. The shower at the end, around 39 m, has been found, but was identified as being much smaller than the other showers, even though it is supposed to be the largest one in this example. This indicates that it may be necessary to use a fiducial volume cut or a default veto for the beginning and the end of a track.

After the definition of shower finding and matching, a quantitative analysis for 976 muons¹ has been performed and the results can be seen in figure 8.7 (a). For the match up of 2555

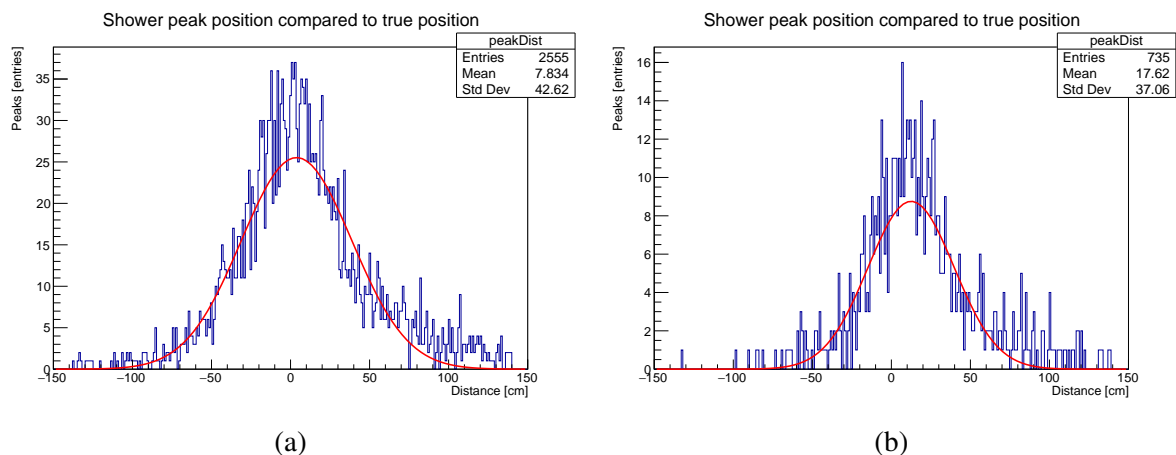


Figure 8.7: QR peak finding and matching of 976 muon tracks, with 2555 shower peaks in (a). In (b) the same analysis for 735 peaks, which deposited more than 500 MeV. It is to note that in both cases the whole distribution is shifted by -38.6 cm and a Gaussian fit (red) has been performed.

shower peaks, the distance of reconstructed shower position minus the true shower position is

¹This amount is explained in chapter 5.2.

marked in (a). The distribution roughly follows a Gaussian distribution, which is why a fit can be performed, which has a sigma of 35 cm. In (b) the same analysis has been done, but only for 735 showers, which deposit more than 500 MeV each. The fit reveals a sigma of 27 cm, which could mean that high energy showers match better to the Monte Carlo truth positions. The same shift of -38.6 cm was used for both reconstruction parts. In (b) the distribution is about 10 cm more shifted to the right, which means that high energy showers are on average reconstructed after the Monte Carlo truth peak. This may hint that higher energy peaks are bound to be found later along the track as they actually are. The reason for this could be an energy dependency, which is not considered. That the mean position is around zero does not matter much in this analysis, due to the shift used and it can be adjusted by shifting the reconstruction profile, but this should be investigated in the future as well as a possible energy dependency.

Interesting follow up questions are: How many shower peaks have been identified from the total and how much energy does a shower need to be identified? To answer this the deposited shower energy has been determined for every shower identified in the Monte Carlo truths and the result can be seen in figure 8.8. The deposited shower energy was determined by fitting a

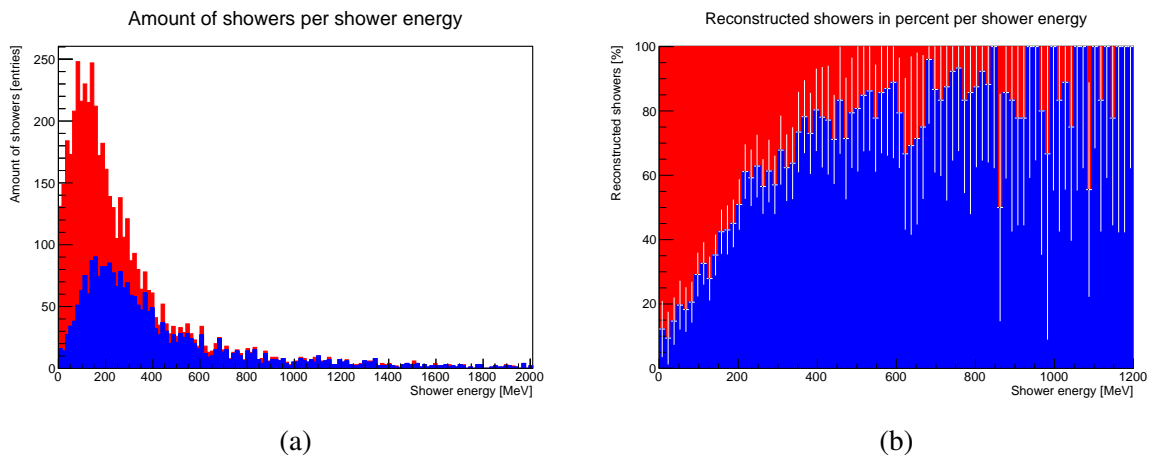


Figure 8.8: Accumulative plot for number of shower peaks matched between Monte Carlo truths and QR, per deposited shower energy, for 976 muon tracks, with 2555 shower peaks. In red are marked the number of unmatched showers and in blue the amount of showers that could be matched. In (a) the total accumulative number of showers per deposited energy is shown and in (b) the ratio of matched to unmatched showers is explored.

Gaussian distribution to the peak position of the convoluted Monte Carlo truths, then the integral of this Gaussian corresponds to the emitted amount of photons, from which the energy deposition can be calculated. But one needs to consider that there is a base contribution of photons emitted from the muon. To account for this the Gaussian fit can be shifted down by the expected amount of photons, which are emitted by the passing muon alone. The integral of this Gaussian fit can be determined and it corresponds to the amount of photons emitted. The energy deposition can be approximated with the relation that about 10 k photons correspond to one MeV in the JUNO simulation. The integration is valid, because it stayed the same under the proposed convolution. As mentioned before, it is not straight forward to obtain a coherent

shower definition as well as shower beginning and end. This approach evades this problem entirely and is reasonable when considering the shower profile processing from before. It is only accurate to about $\pm 10\%$, which was determined by examining and evaluating individual raw shower profiles and comparing them to the found shower energy. A different option would have been to set a threshold, which feels rather arbitrary when considering the continuous exponential decay in figure 8.8 (a). An even more different option would be to look into the detailed Monte Carlo truths and group all particles and daughter particles that have been created from an interaction with the muon into a shower, but how would one define a start or end when two or more of these showers overlap? This is not simple to interpret and it is doubtful that any reconstruction for JUNO will be able to resolve the individual tracks.

In figure 8.8 (a) one can see the total accumulated amount of peaks for their respective shower energy. The showers marked in blue have been found and the ones marked in red could not be determined. It is to note that there is a maximum around 100 MeV, which is only there because small energy depositions are only inconsistently identified with the methods used here². In reality this distribution is similar to an exponential decay and there are a lot of small energy depositions³, but these are not responsible for the creation of ⁹Li and ⁸He and therefore this difference can be neglected⁴. In figure 8.8 (b) the percentage of successfully reconstructed showers is plotted. Starting at around 400 MeV shower energy deposition, the ratio of reconstructed showers reaches more than 80%. Due to the sample size the error becomes quite large beyond 600 MeV. The main reasons why low energy showers may not be identified are:

1. Not enough energy deposition to be above the 50 keV fluctuation limit
2. Being drowned in the wake of a bigger shower
3. Bad input parameters of time and/or track
4. Being at the edge of the detector target

It is unlikely that a shower with less than 50 keV energy deposition contains harmful isotopes. The second point is an issue with this reconstruction approach, as delayed light always collects behind high energy showers, but it may be possible to improve the reconstruction performance by carefully studying the wake of such showers or performing a deconvolution in future developments. Point three is outside the scope of this approach and really depends on the reconstruction providing these parameters. The input parameters assumed for this section are reasonable and therefore there is probably nothing that can be done about this. There are issues at the start and end of a track due to reflection, refraction and water instead of scintillator at the edge of the detector target. To compensate for this issue it may be necessary to completely veto the edge

²Of course, the photons are recorded in the Monte Carlo truth, but the resolution of the QR and the convolution with a Gaussian suppresses the low energy peaks.

³If these small energy depositions qualify as showers is questionable.

⁴The creation of ⁹Li starts at around 1 GeV shower energy deposition.

of the detector target near the entrance and exit point of muon tracks. It may be possible to describe these regions in more detail, because currently there is only a very rough approximation for the surrounding water in place. As already explained at the end of section 7.2, an iterative approach could be used to describe refraction more precisely. A similar story unfolds for the missing high energy showers, but only point three and four are applicable. Why a particular shower was not found will almost always be a combination of these points.

The showers in this sample are almost all electromagnetic and so far there is no way to differentiate these from hadronic showers with the topological approach. Therefore, it makes no difference in reconstruction capabilities, but it makes a difference for cosmogenic isotope production, because only hadronic showers will produce ${}^9\text{Li}$ and ${}^8\text{He}$. Hence, special measures have been taken to evaluate the performance with hadronic showers. This sample of 976 muon only produced 59 hadronic showers, of these 43 have been reconstructed successfully. Of the hadronic showers that have not been found, 7 showers had a very small energy deposition of below 20 MeV and 8 were in the wake of a larger electromagnetic shower. The last missing shower was produced at the very end of a track, which was stopping inside the detector target. None of these showers produced any ${}^9\text{Li}$ or ${}^8\text{He}$ and it is very unlikely for missing showers with very low energy deposition to produce any. As for the other 8 showers, there would be a veto already for the large electromagnetic shower in front of these. Hence, if any cosmogenic isotopes would have been produced, they would be inside a veto region anyway. This leaves one hadronic shower from the stopping muon as unaccounted and this probably coincides with the efficiency that can be expected from the QR.

As for a shower start point definition, which would be of interest for the cone veto from chapter 4, there has been no universally applicable definition found, but just using the maximum instead delivers comparable results. Therefore, developing and evaluating the shower beginning determination capabilities will be a task for the future.

Shower energy reconstruction is something that is of interest, but currently will deliver underwhelming results, which is why it needs to be further explored in the future. It is inconclusive, because no deconvolution or ridge correction has been set up to counter the shower profile distortion from delayed photon information. It may be possible to fit the scintillation function convoluted with the TTS to the corrected QR results and do a linear correction based on the Monte Carlo truth, but this has not been done yet. Additionally, PMT saturation is not simulated yet and will likely complicate this matter even more.

8.4 Multi muon bundle events

It is also possible to have photon information from more than one muon at the same time. This will happen in JUNO, with a rate of 0.69 Hz for muon bundle events, when multiple muons pass through the detector at the same time. These tracks are pretty parallel and their mean distance is expected to be around 10 m [1]. The probability for uncorrelated muons striking the detector at the same time is low. Hence, some example reconstructions with parallel muon tracks have been

performed and the results can be seen in figure 8.9 (b) and 8.10 (b). In 8.9 (a) one can see the

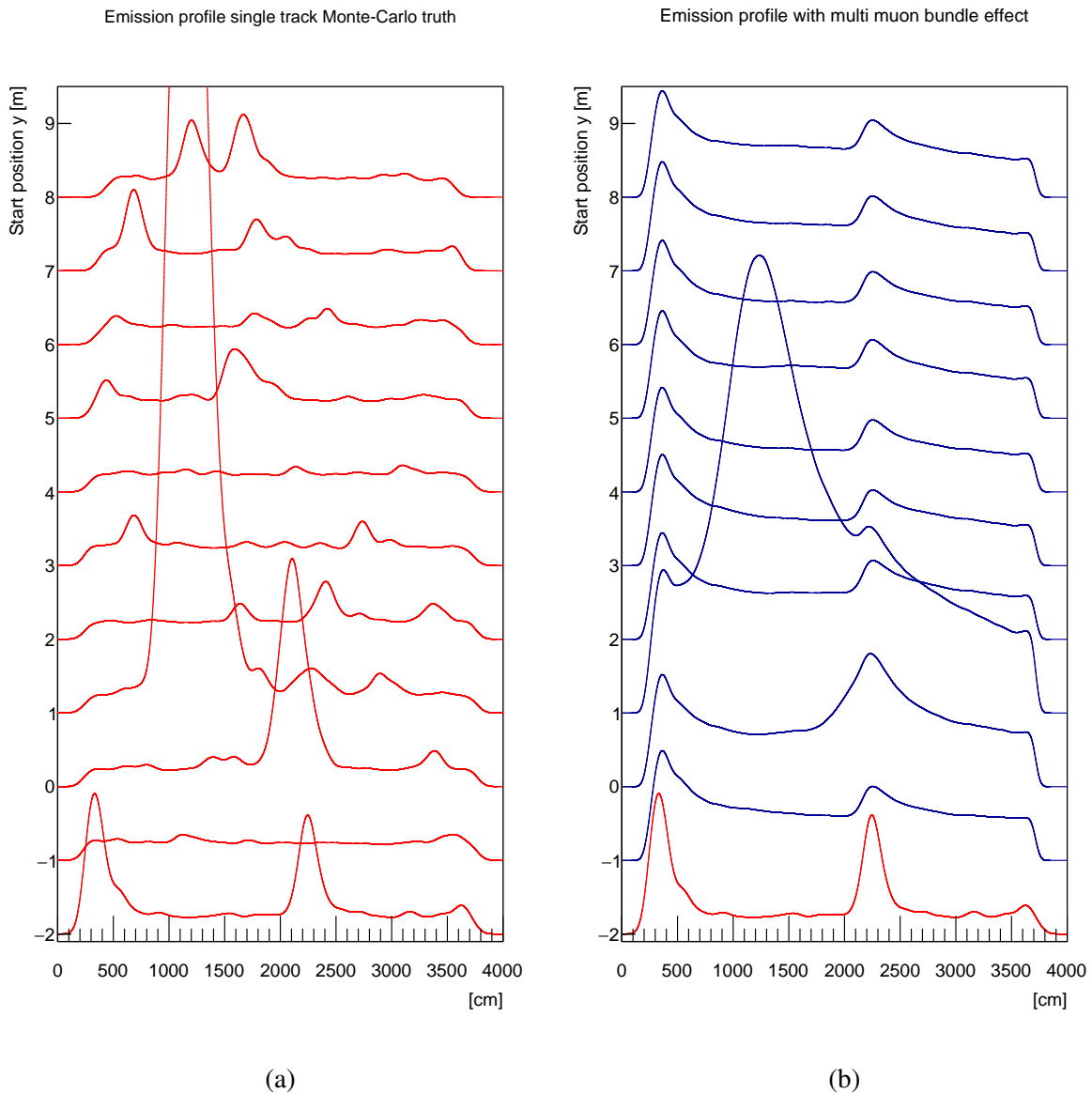


Figure 8.9: Spatially parallel muon track reconstruction for 215 GeV muon tracks. All muons travel in the negative Z-direction and are simulated 1 m apart in Y-Direction. The profiles in (a) show the Monte Carlo truth for each track. In (b) the bottom profile in red shows the Monte Carlo truth for the muon that should be reconstructed and in blue are the results for this muon, but the light from one of the other parallel tracks in (a) has been added as noise.

Monte Carlo truth of the emission profile for eleven 215 GeV muons, which have been simulated spatially parallel and are spaced out 1 m apart from each other. These emission profiles will be used to qualitatively examine multi muon bundle events. The muon start positions are (1, 2 to 8, 20) m. To separate the results and make them more readable, they have been spaced out and the y-axis labels only show the y-position in the detector and not the photon emissions. Additionally, both the Monte Carlo truth as well as the QR result have been smoothed by a convolution with a Gaussian distribution. This is the same method that was already used, in the

previous section, during the quantitative analysis. This was done because the shower position was deemed more important than the shape. A variety of showers can be seen in figure 8.9 (a). The maximum shower deposits more than 50 GeV inside the detector and the bottom shower profile, which will be used for the bundle reconstruction comparison, has two showers. The first one at 4 m deposits ~ 4.6 GeV and the second at 23 m deposits ~ 3.3 GeV. For the multi muon case one can assume an event where 2 of these muons pass through the JUNO target at the same time. The muon with the profile starting at (1,-2,20) m will be reconstructed 10 times, with light contributing as noise from one of the other muons. The results of this can be seen in figure 8.9 (b). The same spacing and offset as before is used. Basically, the emission profile from (a) acts as noise for the reconstruction of muon (1, -2, 20) m in (b). It is interesting to see that, despite the noise of other muons, the two main peaks can be recognized in every reconstruction in figure 8.9 (b). Of course, this depends on the position and energy of these features, as well as the position and energy of the noise features. From this example one can take, that the peak finding capabilities are probably not affected when the noise features are similar or smaller in size and the distance between the two muons is more than 4 m.

The reverse, the reconstruction of the muons (1,-1 to 8, 20) m with the muon starting at (1, -2, 20) m contributing as noise, has been done as well and the results can be seen in figure 8.10 (b). For comparison the QR for all muons has been performed and the resulting shower profiles can be seen in figure 8.10 (a). Here, all muons are treated as if they pass alone through the detector target. In figure 8.10 (b), when the distance gets down to 6 m one can see features appear from the noise of muon (1, -2, 20) m and by closing this distance further these features gradually starts to dominate the photon emission profile more and more, until the event at (1, -1, 20) m basically looks like the noise event. This is especially visible with muon event (1, -1, 20) m, because it has no significant showers. Interestingly, even though the muon event (1, 0, 20) m and noise muon are only 2 m apart, the highest point of the peak at position 21 m, where about 7 GeV are deposited, is unaffected. The reconstruction of muon event (1, 0, 20) m shows a pretty significant fake peak, from the noise at 4 m. It may be possible to identify which peak belongs to which muon for these close events by studying which muon supposedly emitted more photons at the peak position in the reconstruction. Then again, it does not really matter when the muons are so close together, because a veto applied to both in the same way will only increase the dead volume slightly.

The energy reconstruction for bundle muon events will be more complex, as there currently is no simple muon light assignment. It might be possible by carefully evaluating both profiles and comparing them to each other, to gain useful information on the shower energy. Machine learning methods could probably handle this, but this has not been investigate yet.

Only the multi muon case for 2 muons at the same time has been examined and more muons are possible but much less likely. For the case that atleast 1 muon in a bundle strikes the detector, the rate for a two muon bundle is expected to be 0.43 Hz, the rate for a three muon bundle it is 0.13 Hz and for more than three is 0.13 Hz again. This is the rate over the whole detector volume including the water veto and not just the target. The rate for 2 muons at the same time in

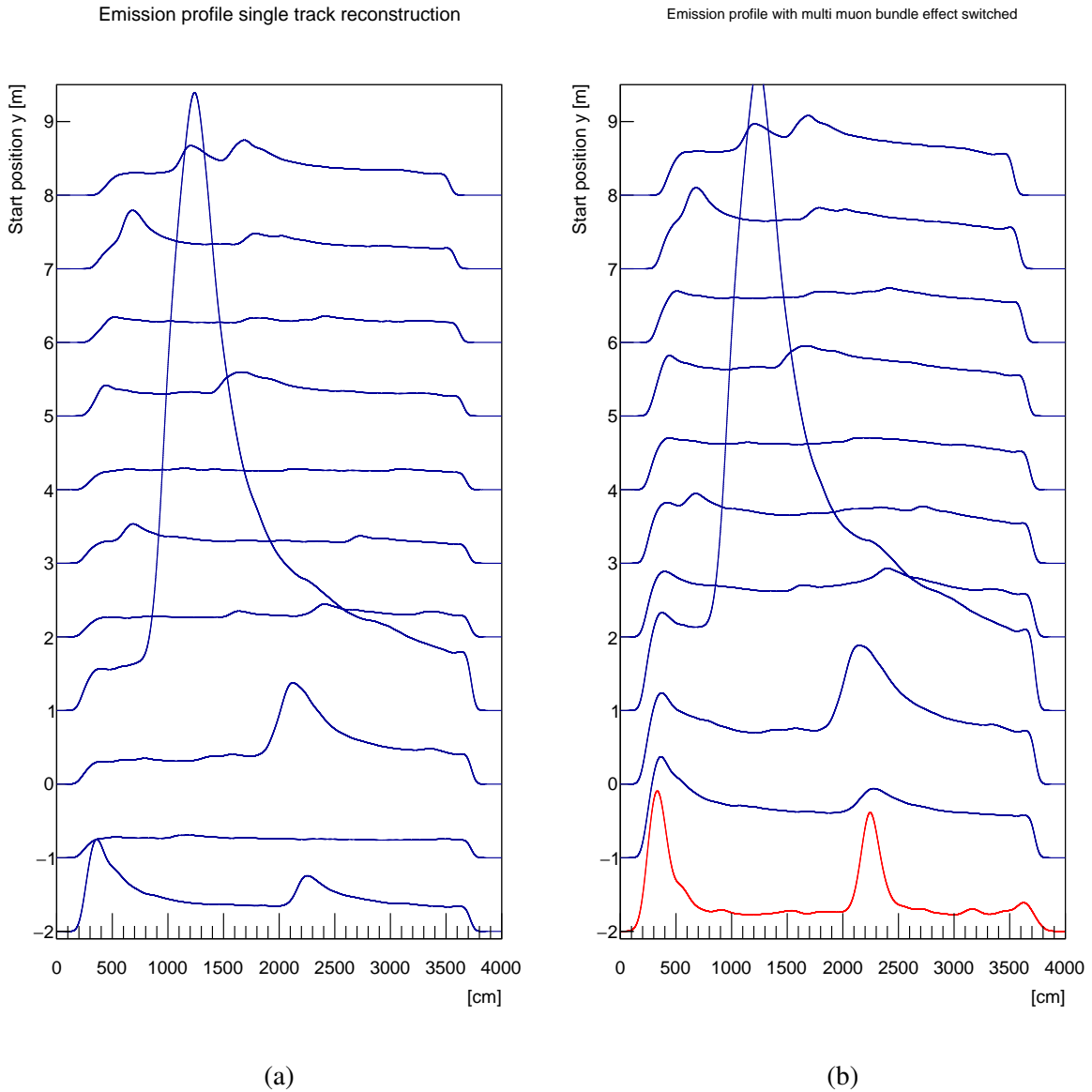


Figure 8.10: Revers parallel muon track reconstruction, where the 215 GeV muon at the bottom was added as noise. In (a) the QR results for each of the muon tracks is shown, as if they would be single muon event. In (b) the red profile this time marks the noise, which was added to each of the reconstructed muon tracks above.

the detector target is expected to be 0.22 Hz [1]. Additionally, these are parallel events and even though the probability for none parallel muon events is low, it is not impossible. The impact of none parallel muon events has not been studied yet. Nevertheless, the results discussed in this chapter show astounding robustness even for the muon bundle case and because the average distance of muons passing at the same time is expected to be ~ 10 m, the QR algorithm should perform well enough. When another reconstruction is able to provide the input parameters for each muon, it is possible to reconstruct their photon emission, one by one. The reconstruction assumed perfect input parameters, but considers TTS, for this multi muon bundle analysis. PMT saturation was not simulated and is believed to impact energy shower reconstruction, but not shower position determination capabilities. It is expected to flatten the features that can be determined by the QR and the effects probably can be compensated by accounting for too few reconstructed photons at peak energy depositions along a muon track, but this has to be investigated in the future.

8.5 Reconstruction comparison & synergy

The QR uses a topological approach, similar to the TTR, which makes a comparison possible. Some aspects of both reconstructions are collected in table 8.1, with a focus on important differences. Both approaches have their place, but there are some types of event where both can

Table 8.1: Comparison between TTR and QR approach, highlighting some differences. The same 200 GeV event and hardware was used for the runtime analysis. The result of the reconstruction is what the approach aspires to determine, but is not necessarily what it can determine currently, at this stage of development.

	Topological Track Reconstruction	Quadratic-reconstruction
Prerequisites:	-Reference time -Reference point	-Target entering time -Track in target
Applicability:	Any type of event	Events with a straight track
Runtime:	~ 20 min	~ 0.6 sec
Result:	Emission probability density for whole detector	Emission profile along track

be applied, namely the case for events with a straight track, which muons most of the time satisfy. It is a bit more difficult to determine the prerequisites for the quadratic approach, because it does not only need a start point but also a direction or end point. They do not necessarily need to be bound by the detector target and more confined tracks will improve the results. Only a reference point and time is needed for the TTR, which is less information that needs to be obtained and it can also be anywhere on an event track. When only the positions of showers are needed, the QR can deliver these much faster than the TTR and has an accuracy of $\sigma = 35$ cm, but if the event consists of more than one straight track, the TTR should be able to deliver a

more comprehensive result. At the time of writing, the TTR has some problems with muon events above 20 GeV. For the time being, the quadratic approach is the only option for higher energy muon events. But the TTR may be able to obtain some useful information, when the QR is used to clean the input data.

This brings us to the reconstruction synergy options. The QR naturally filters out photons that can not be solved with the quadratic relation. This means that a great deal of photons, that can potentially harm the topological reconstruction approach, are ignored. Hence, the QR can determine which is the most valuable information to be used with other reconstruction approaches. Additionally, it is reasonably fast and therefore it can be run as a pre-reconstruction. This has been done as an example. The results, of combining the TTR and QR, can be seen in figure 8.11. By feeding only photons, which have been determined by the QR to be good,

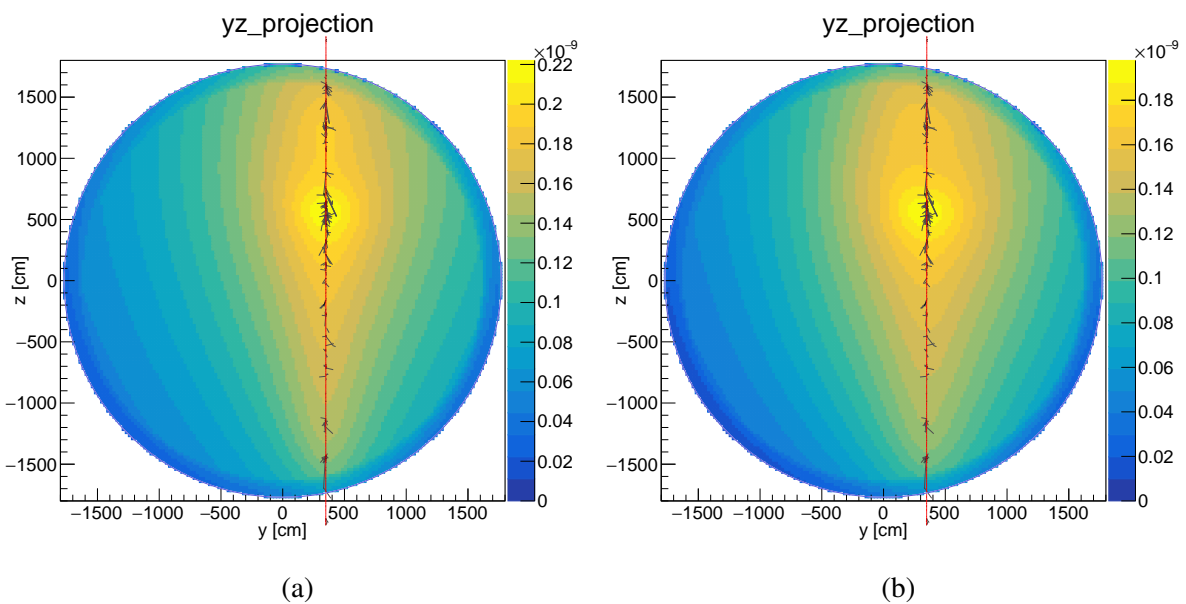


Figure 8.11: Demonstrating filtering effect of QR for the TTR. In (a) one can see the first iteration of a 209 GeV muon event, with all light contributing. In (b) the same muon is reconstructed, but only light that was selected by the QR was used. The same 25 cm binning over the whole JUNO detector and raw reconstruction was applied.

into the TTR the result in figure 8.11 (b) was obtained. Figure 8.11 (a) contains the result for the same event without the preselection of photons. One can see two very similar results, which indicates that both reconstruction approaches can deal with delayed light information to a certain degree. Because less information was used during the synergy run, the reconstruction time of the TTR was also reduced from 28 minutes to 23 minutes and the overall emitted light was determined to be less, which needs to be accounted for if this becomes a regular application case. This is a first promising result for the combination of the QR with other approaches, more reconstructions should be tested for synergy in the future.

Some additional benefits are conceivable and for the multi muon bundle case it may be possible to match information to different tracks and subsequently treat these tracks as single muon events with other reconstructions. It is also possible to determine which volume is important for

an event and this could bring great benefits for the TTR. This drastically reduces reconstruction times by the TTR, because less volume needs to be considered during reconstruction.

A disfavoured synergy could be to determine the direction of a track with the TTR, when it is not able to deliver a satisfactory result on the energy deposition. But this would hugely offset the speed at which the QR can deliver the emission profile and there are other reconstructions that should be able to deliver the needed prerequisites much faster. Hence, this is possible but will probably not be done.

8.6 Summary

During this chapter it was shown that, the QR is able to obtain the shower profiles of muon tracks and the reconstruction time for these kinds of events, on the same hardware as the TTR, is about 0.6 seconds per event. Additionally, it has some inherit features that come with the method, which not only bring robustness but also the ability of filtering out harmful photon information. With some further development of a deconvolution it may even be possible to obtain the original photon emission along a track. For now, it is able to determine the shower positions along a track, with an accuracy of $\sigma = 35$ cm and more than 80 % of showers are found when they deposit more than 400 MeV energy. The main reasons why some showers cannot be found are a bad initial start time and/or track parameters, which need to be provided to the QR from other reconstructions. When these parameters are provided for every muon in a multi muon bundle event, it is also possible to reconstruct these with the QR. A qualitative analysis in this chapter has shown, that the shower tracking capabilities are mostly unaffected for two muons, traversing the detector target at the same time, with a spacing greater than 4 m and it is still possible to extract useful shower information from both tracks even if they are just 2 m apart. Finally, the possibility to use the event information filtering capabilities of the QR has been explored and it is possible to run it as a pre-reconstruction to improve the results as well as runtime of the TTR.

Further development will have to focus on the problems with the reconstruction at the beginning and end of a track, as well as shower energy reconstruction. Additionally, this approach also expects single photon information, which has to be addressed in the future. The development of a deconvolution, for the corrected QR result, should increase the capabilities to a point where the energy reconstruction and shower finding will match up with the raw Monte Carlo truth results.

The veto strategies discussed in chapter 4 could be used in tandem with the QR. Especially, the double cone approach can simply use the shower positions, which are found by the QR. One has to bear in mind that the efficiency of these vetoes will suffer due to the shower position accuracy of $\sigma = 35$ cm, but it is possible to avoid this by enlarging the veto. However, this has the effect that the dead volume produced by these vetoes will be larger and it is less likely to reach the mentioned 12.8 %. Nevertheless, a total active volume increase of around 10 % for JUNO seems reachable.

Chapter 9

Conclusion and Summary

The neutrino is still a fascinating particle, which needs to be further explored and quantified. The observation of neutrino oscillations really opened up the possibility for particle physics to further explore physics beyond the Standard Model and in the coming decade it will enable us to determine the neutrino MO. JUNO and other liquid scintillator experiments will play an important role during this endeavor. The research done during this thesis focuses on high energy events, even though liquid scintillator experiments are more focused on low energy neutrino interactions. However, it is still an important part to study high energy interactions in these types of detectors, because only effective background suppression enables the measurement of aforementioned neutrinos and the main background are isotope, which are generated in showers of throughgoing high energy muons. The determination of energy deposition along high energy muon tracks will enable significantly more effective veto strategies and improve the statistics for JUNO and other liquid scintillator experiments.

During this thesis the default muon veto strategy of JUNO has been examined and it was successfully demonstrated that a more detailed veto approach can reduce the dead volume by roughly 3.5 times. This translates into an increase of total active volume by about 12.8 %, which enables JUNO to reach the same confidence level, for the MO, in only 8.72 years, instead of 10 years.

Three different veto volumes for muon showers and one adaptive cylinder for showering muons have been discussed. A schematic of these custom vetos can be seen in figure 4.13. Additionally, the height of these vetoes can be adapted depending on the deposited shower energy, which can further reduce dead volume. The most promising approach is a veto, which uses a cone in track direction, with 4.7 m radius and 14.3 m height around a shower and a cylinder around a muon track, with radius 1.55 m for muon tracks without a shower.

For this custom muon veto strategy it is necessary to determine energy depositions along muon tracks, which is a task that is currently under development in the JUNO collaboration. This has also been done during this thesis, two topological track reconstructions have been developed and examined for this task.

The first approach is the Topological Track Reconstruction (TTR), which was already examined for muons, with energies up to 10 GeV, in LENA [4]. Testing the same algorithm with

JUNO and muon energies around 200 GeV, which is near the expected mean muon energy, yielded underwhelming results. This can mostly be attributed to the large amount of photon hits that have distorted path information, due to scattering, absorption with re-emission and reflection. The TTR does account for this by weighting the light information with a survival probability, but all detected light is treated as direct. This implies that distorted light information will contribute to the result. A distorted light detection algorithm is currently in development for the TTR, but has not been implemented for JUNO yet. Additionally, a lot of light gathers near the edge of the detector target, which may indicate that the treatment of refraction needs further development. This prompted the expansion of the TTR, during this thesis with features to enhance robustness and versatility. This enabled the reconstruction of contained muon events up to a few GeV and improved the situation with through-going higher energy muon events, but not to a degree where the energy deposition along muon tracks can be extracted reliably. Furthermore, the reconstruction time for such events was around a few hours, which is somewhat expected when considering the large amount of light produced during high energy muon events. Therefore, a lot of time was also invested in the speed up of this reconstruction approach and a time reduction of about 90 % could be achieved, which still means around 15-45 minutes per high energy muon event. It is possible to use this approach during analysis efforts, but this implies that data from veto regions needs to be stored as well. Usage during live data taking in the current state is unlikely, but it may be possible to implement the TTR on GPUs, which would yield a time reduction. Ultimately, further development of the TTR approach is necessary to bring it to its full potential in JUNO.

The second approach, which was developed during this thesis, is the Quadratic Reconstruction (QR). The driving factor was the possible time reduction in reconstruction, by only considering the muon track itself, instead of the whole detector. This implies an additional requirement of a direction or exit point for a muon track. The reconstruction time reduction has been achieved and surpassed expectations by being able to reconstruct the same events more reliably as the TTR and on the same hardware in only 0.6 seconds. The same *basic idea* used for the TTR was adjusted to consider the additional information of a track direction. With this reconstruction it is possible to determine shower positions with an accuracy of $\sigma = 35$ cm and more than 80 % showers can be found when they deposit more than 400 MeV energy. This rate largely depends on the initial track parameters provided to the QR and would further improve if prior knowledge of the track is better than the conservatively assumed 1 ns or $\sigma = 20$ cm, for reference points and time. It could also successfully be demonstrated, that the energy deposition along two parallel muon tracks is reliably obtainable, if said tracks are more than 4 m apart and useful information on shower position can still be extracted if the tracks are only 2 m apart. Additionally, it was shown that the QR has some inherent filtering properties, which enable it to tag light information as likely being distorted or direct. This enables this approach to further enhance the speed of reconstruction and results of the TTR, when used as a light information filter. Of course, the QR is not the be-all and end-all of energy deposition along muon tracks, but has shown very promising results. Therefore, further development is of the essence, where

the focus should be on more detailed treatment of light near the detector target edge and exploration of energy reconstruction capabilities, as well as the development of a deconvolution, which can treat the distortion effect due to scintillation delay and TTS.

The combination of the results presented in this thesis indicate, that it is very likely that a more efficient veto strategy can reduce the dead volume in liquid scintillator detectors significantly. By using the shower position determination capabilities of the QR and the experience gained with the cosmogenic simulation, it should be possible to reduce a 10 year measurement of JUNO to 9 years, or in other words, measure 10 % more signal in 10 years. Additionally, this is not only relevant for JUNO, but also for other experiments, because it is possible to use both of the presented topological reconstruction approaches in any unsegmented liquid scintillator detector.

Appendix A

Addition to the Cosmogenics Simulation

Additional information about the cosmogenic simulation can be found in this chapter. The correct treatment for the initial veto calculation is explained here. The impact is negligible and therefore it was omitted in the original chapter. The initial veto efficiency ε_i of the full detector for every muon can be given by [89]:

$$\varepsilon_i = 1 - e^{-\frac{t}{\tau}}. \quad (\text{A.1})$$

For ${}^9\text{Li}$ the mean decay time τ is ~ 255 ms and the initial veto time $t = 1.5$ ms, this results in efficiency $\varepsilon_f = 0.006$. To obtain the efficiency ε_f , for muons that cannot be tracked, the time t can be set to 1.2 s and an efficiency $\varepsilon_f = 0.991$ is obtained. To calculate the efficiency for the cylinder, one can modify equation (4.7) with the ratio R_r of isotope captured by a cylinder with radius $r=3$ m:

$$\varepsilon_c = \varepsilon_i + (1 - \varepsilon_i) \cdot R_r \cdot (1 - e^{-\frac{t}{\tau}}). \quad (\text{A.2})$$

The ratio $R_{r=3\text{m}}$ can be obtained by fitting figure 4.2 and solving the integral for a radius of 3 m. Assuming the lateral distribution from the simulation is kinematically correct and follows an exponential distribution. The results for a ratio $R_{r=3\text{m}} = 0.995$ of the isotopes being inside the cylinder can be calculated. Therefore, the efficiency of the cylindrical veto is $\varepsilon_c = 0.986$, with $t = 1.2$ s - 1.5 ms. By utilising the same assumption, as in Neutrino Physics with JUNO [36], that 99% of muons are well tracked. The total efficiency is $\varepsilon_t = 99\% \varepsilon_c + 1\% \varepsilon_f = 0.986$.

Some additional plots will help to evaluate the cosmogenic simulation, which follow next.

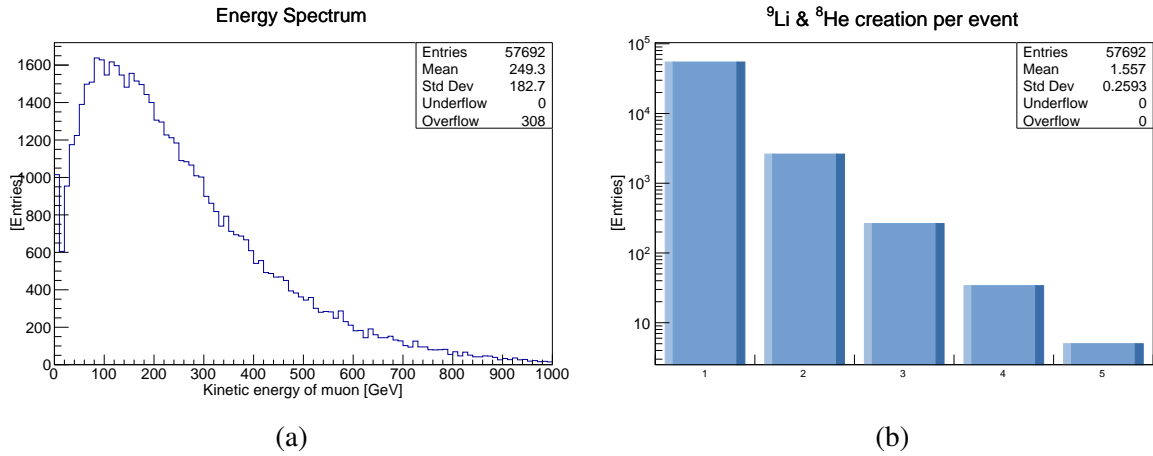


Figure A.1: In (a) initial kinetic energy of the initial muons that produced the isotopes as a total. In (b) the amount of isotopes generated per event.

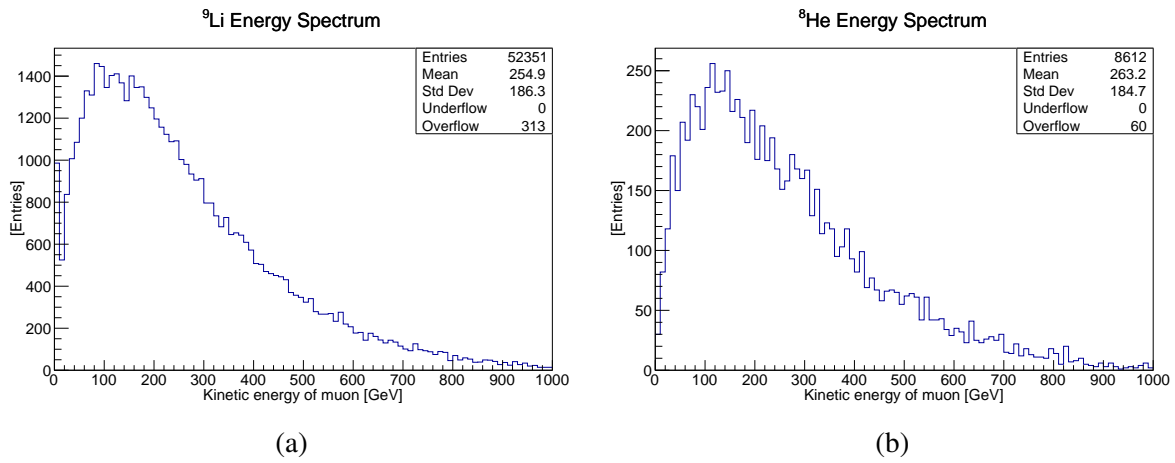


Figure A.2: Initial kinetic energy of the initial muons that produced each isotopes. In (a) the spectrum for ⁹Li and in (b) the spectrum for ⁸He.

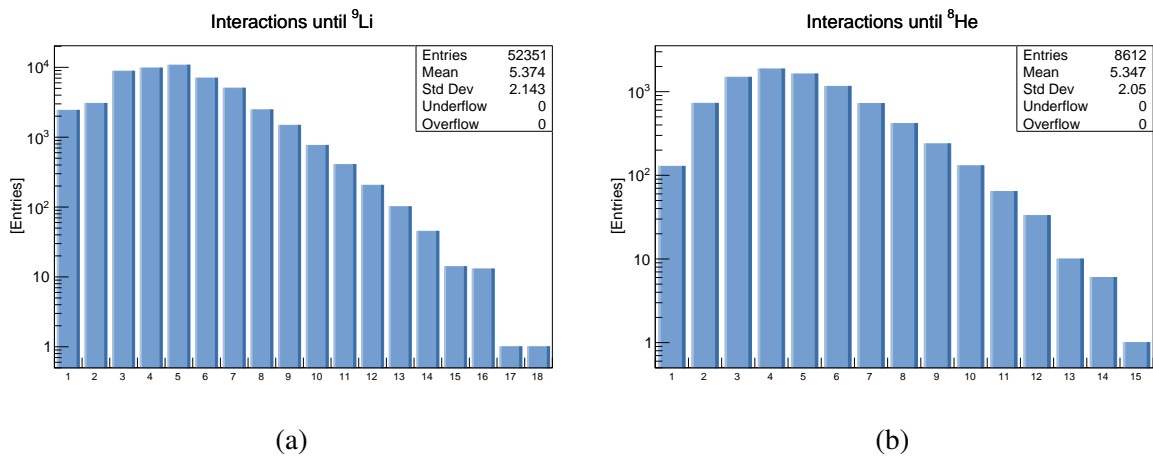


Figure A.3: Counting the interactions from the initial muon, until the isotope has been generated. In (a) for ⁹Li and in (b) for ⁸He. Interactions here mean the number of actual different particles that have been created in a chain, but not necessarily destroyed for the next particle in the chain. The actual number of interactions is much higher, but also irrelevant. This plot may be of interest for the distance definition used.

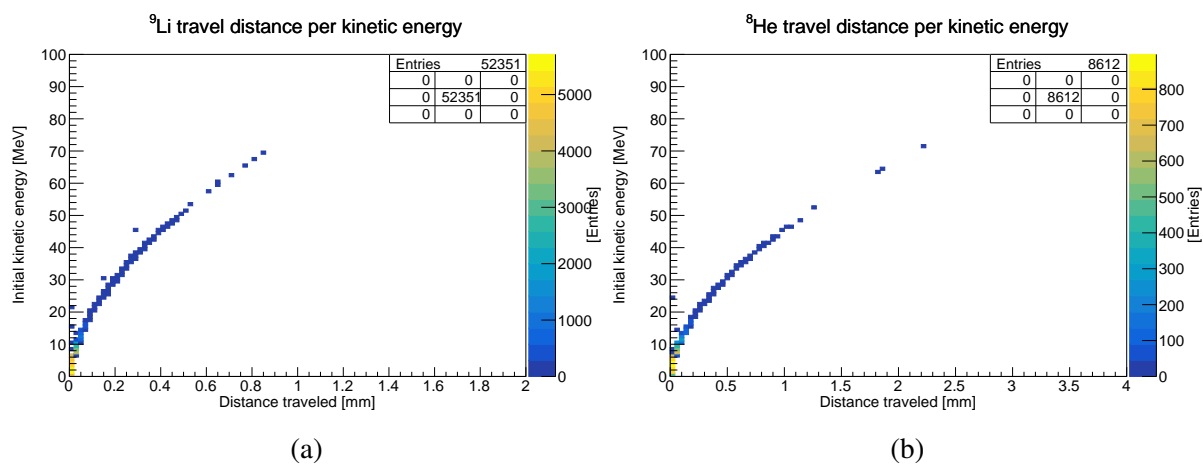


Figure A.4: The travel distance for each isotope correlated with its initial kinetic energy. One can see that the isotopes travel just a few millimeter until they stop. Convection is not included in the cosmogenic simulation, but will probably have more of an impact that the distance shown in this plots. In (a) for ${}^9\text{Li}$ and in (b) for ${}^8\text{He}$.

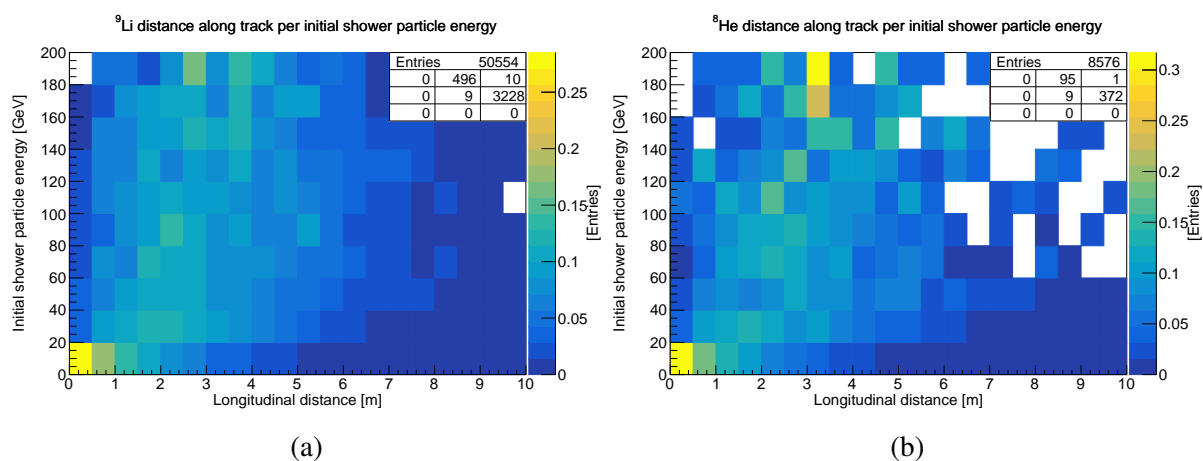


Figure A.5: Distance along track per initial shower particle energy. This shows that the main distance traveled it along the track and the lateral distance is basically independent of energy. Of course, this plot is normalized to one, again for each horizontal bins. In (a) for ${}^9\text{Li}$ and in (b) for ${}^8\text{He}$.

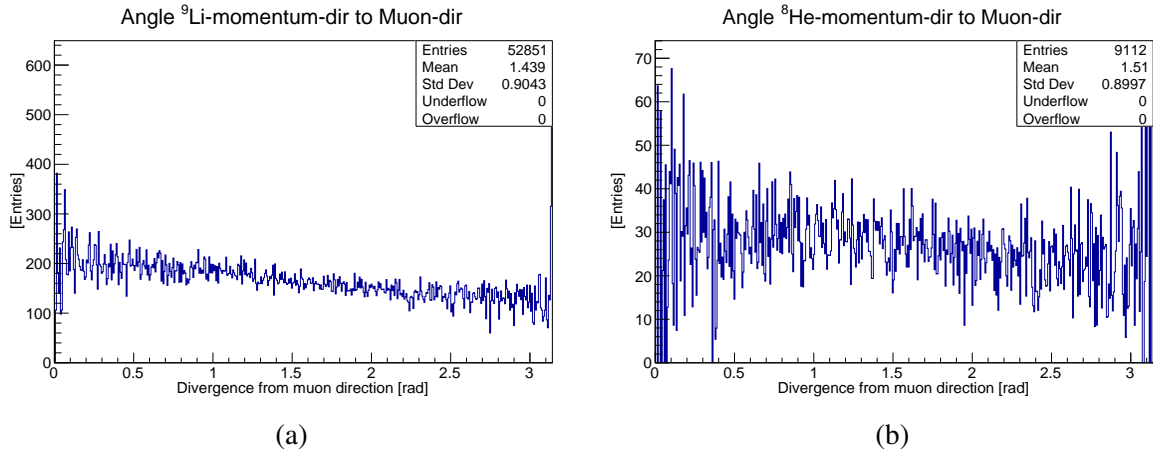


Figure A.6: Angle between isotope direction and muon direction, weighted with the angular element. It is reasonable that slightly more isotopes are traveling in the direction of the muon. In (a) for ${}^9\text{Li}$ and in (b) for ${}^8\text{He}$.

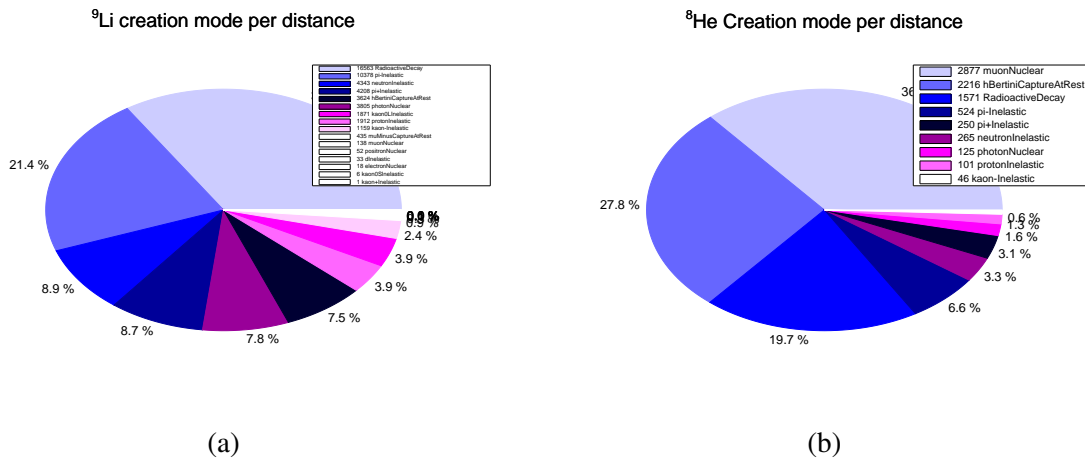


Figure A.7: Creation process of the isotopes from the last particle in the chain before the isotope.

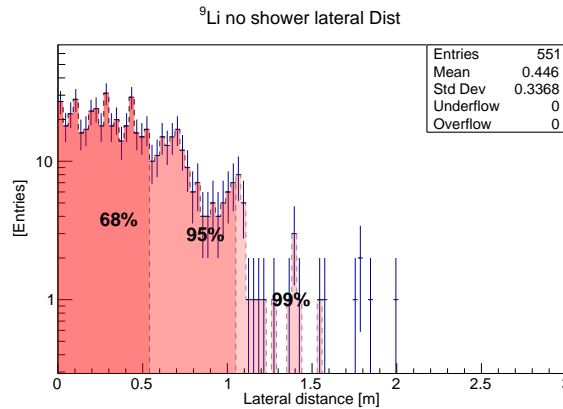


Figure A.8: This plot shows the lateral distance for the case of no shower detection. Only ${}^9\text{Li}$ is shown, because too few data points have been collected for a ${}^8\text{He}$ plot. This indicates that the error on the determined 1.55 m is very large.

List of Figures

1.1	An outline of the Standard Model.	6
1.2	Neutrino flavor mixing.	7
1.3	Survival probability $P_{e \rightarrow e}(E)$ for solar electron neutrinos.	12
1.4	Neutrino mass ordering.	16
2.1	Cross section for gamma energy range.	24
2.2	Example Jablonski diagram for an organic scintillator.	26
2.3	Example liquid scintillator mixture.	27
2.4	Basic scheme for a dynode PMT.	31
2.5	Schematic view of micro channel plate.	32
3.1	A rendering of the JUNO detector, without the top tracker.	36
3.2	Reactor anti-neutrino spectrum.	42
3.3	A simple case of an $\bar{\nu}_e$ interaction.	43
3.4	A positron from the <i>Invers Beta Decay</i> annihilates with an electron.	44
3.5	A neutron capture, where a hydrogen atom becomes deuterium.	44
3.6	Beta decay and branching ratios of ${}^9\text{Li}$ and ${}^8\text{He}$	46
3.7	The expected solar neutrino energy spectra.	51
3.8	The energy neutrino spectrum for ${}^8\text{B}$ neutrinos	51
4.1	A view of the detector for the cosmogenic simulation.	56
4.2	The lateral distance of ${}^9\text{Li}$ and ${}^8\text{He}$	61
4.3	The lateral distance of ${}^9\text{Li}$ and ${}^8\text{He}$ for different energies.	61
4.4	The lateral distance of ${}^9\text{Li}$ in FLUKA.	62
4.5	Muon shower projection.	63
4.6	Projection in yx-plane for isotope creation with distance to initial shower particle	63
4.7	Isotope creation distance for different initial shower particle energies	64
4.8	Isotope creation distance for different shower energies	64
4.9	Isotope creation distance for different shower lengths.	65
4.10	Projection in yx-plane for isotope creation with distance to shower start	66
4.11	Projection in yx-plane for isotope creation with distance to shower maximum.	66
4.12	Average veto volume per muon in cylinder case and radial hit probability.	70

4.13	Different custom veto approaches.	71
4.14	Longitudinal ${}^9\text{Li}$ distance h for 51 batches.	74
5.1	An orthogonal cut view of JUNO.	80
5.2	A 3D wireframe view of JUNO.	80
5.3	Refractive indices and absorbtion lengths in the JUNO simulation.	83
5.4	Wavelength dependent properties of the liquid scintillator in the JUNO simulation.	84
5.5	The event file structure.	87
5.6	The structure of the <i>User-file</i>	88
5.7	Muon energy spectrum, created by generator.	92
5.8	Muon angular altitude distribution.	92
5.9	Muon angular azimuth distribution.	93
6.1	Visual representation of the <i>basic idea</i>	96
6.2	2D projection of the solution for the <i>basic idea</i>	98
6.3	TTR iteration process.	101
6.4	Impact of the raw reconstruction	103
6.5	TTR using the backward in time reconstruction.	104
6.6	Impact of PMTs with very much hit data.	105
6.7	Impact of the random PMT selection.	108
6.8	Reconstruction time reduction achieved during this work.	110
7.1	The <i>basic idea</i> in context of the QR.	112
8.1	Example result representation for QR.	116
8.2	Determining emitted photons with the QR.	118
8.3	Reconstruction result for QR with imperfect data.	119
8.4	QR result for a wrong reference time.	121
8.5	QR result for wrong reference information.	121
8.6	QR result and shower finding and peak matching.	123
8.7	QR peak finding and matching.	124
8.8	Accumulative plot for number of shower peaks matched.	125
8.9	Spatially parallel muon track reconstruction for 215 GeV muon tracks.	128
8.10	Revers parallel muon track reconstruction, with a 215 GeV muon added as noise.	130
8.11	Filtering effect of QR for the TTR	132
A.1	Initial muons energy and amount of isotopes per event.	140
A.2	Kinetic energy of the initial muons that produced each isotopes.	140
A.3	Counting the interactions from the initial muon until the isotope.	140
A.4	The travel distance for each isotope.	141
A.5	Distance along track per initial shower particle energy.	141
A.6	Angle between isotope direction and muon direction.	142

A.7	Creation process of the isotopes	142
A.8	⁹ Li lateral distance for no shower detection.	142

List of Tables

1.1	Neutrino oscillation parameters in 2020	14
2.1	The variables used in the <i>Bethe-Bloch-equation</i>	23
3.1	Radiopurity needed in JUNO for $\bar{\nu}_e$ signal.	38
3.2	JUNO PMT parameter comparison table.	39
3.3	JUNO selection cuts for IBD.	45
3.4	Precision improvement for Δm_{21}^2 , $ \Delta m_{ee}^2 $ and $\sin^2(\theta_{12})$	47
3.5	Supernova channels and event rates in JUNO.	49
4.1	The composition of LAB taken from the JUNO simulation	57
4.2	Number of ${}^9\text{Li}$ created per 1×10^6 muons	58
4.3	The efficiencies for different veto types.	72
4.4	Determination of smallest volume containing 99.2 % of the ${}^9\text{Li}$ isotopes	73
4.5	Results of the minimization algorithm after allowing for individual cone length.	75
4.6	Dead volume for different custom veto types.	76
5.1	Isotope definition for the simulation.	81
5.2	Molecule composition for the simulation.	82
5.3	Information added to the <i>mu-tree</i>	90
8.1	Comparison between TTR and QR approach.	131

List of abbreviations and acronyms

$0\nu\beta\beta$	Neutrinoless double beta decay
BERT	Bertini cascade
BIC	Binary cascade
bis-MSB	1,4-Bis(2-methylstyryl) benzene
CC	Charged current
CCD	Charge-coupled device
CP	Charge Parity
CPU	Central processing unit (computer component)
DNSB	Diffuse supernova neutrino background
ES	Elastic scattering
FLUKA	FLUktuierende KAskade (software)
G4NDL	Geant4 Neutron Data Library
GEANT	Geometry and Tracking (software)
GPU	Graphics processing unit (computer component)
GUT	Grand Unified Theory
HV	High voltage
HZC	Hainan Zhanchuang Photonics
IBD	Inverse beta decay
IO	Inverted ordering
JENDL	Japanese Evaluated Neutron Data Library
JUNO	Jiangmen underground neutrino observatory
LAB	Linear alkylbenzen
LAPPD	Large area picosecond photo detector
MCP	Micro channel plate

MO	Mass ordering
MSW	Mikheyev-Smirnov-Wolfenstein
MUSIC	MUon SIMulation Codes (software)
NC	Neutral current
NNVT	Northern Night Vision Technology
NO	Normal ordering
OSIRIS	Online Scintillator Internal Radioactive Investigation System
PDE	Photon detection efficiency
PE	Photon electron
PMNS	Pontecorvo-Maki-Nakagawa-Sakata
PMT	Photo multiplier tube
PPO	2,5-diphenyloxazole
QE	Quantum efficiency
QGS	Quark-gluon string
QR	Quadratic Reconstruction
SM	Standard model
SNEWS	Supernova early warning system
SNiPER	Software for Non-collider Physics ExpeRiment
SSM	Standard solar model
SiPM	Silicone based photomultiplier
SUSY	Supersymmetry
TAO	Taishan Antineutrino Observatory
TTR	Topological Track Reconstruction
TTS	Transit time spread
WIMP	Weakly interacting massive particle

Bibliography

- [1] M. Grassi, et al., Showering cosmogenic muons in a large liquid scintillator, *Journal of High Energy Physics* 2014 (9) (2014) 49. doi:10.1007/JHEP09(2014)049.
- [2] G. Bellini, et al., Muon and cosmogenic neutron detection in Borexino, *Journal of Instrumentation* 6 (05) (2011) P05005–P05005. doi:10.1088/1748-0221/6/05/p05005.
- [3] Y. Abe, et al., Precision muon reconstruction in Double Chooz, *Nucl. Instrum. and Meth. Phys. Res. A* 764 (2014) 330–339. doi:10.1016/j.nima.2014.07.058.
- [4] B. Wonsak, et al., Topological track reconstruction in unsegmented, large-volume liquid scintillator detectors, *Journal of Instrumentation* 13 (07) (2018) P07005–P07005. doi:10.1088/1748-0221/13/07/p07005.
- [5] F. P. An, et al., Improved Search for a Light Sterile Neutrino with the Full Configuration of the Daya Bay Experiment, *Phys. Rev. Lett.* 117 (2016) 151802. doi:10.1103/PhysRevLett.117.151802.
- [6] J. Ahn, et al., RENO: An Experiment for Neutrino Oscillation Parameter θ_{13} Using Reactor Neutrinos at Yonggwang, (2010). arXiv:1003.1391.
- [7] B. Aharmim, et al., Combined Analysis of all Three Phases of Solar Neutrino Data from the Sudbury Neutrino Observatory, *Phys. Rev. C* 88 (2013) 025501. doi:10.1103/PhysRevC.88.025501.
- [8] E. Fermi, Versuch einer Theorie der β -Strahlen. i, *Zeitschrift für Physik* 88 (3) (1934) 161–177. doi:10.1007/BF01351864.
- [9] The Nobel Foundation, The Nobel Prize in Physics 1995, Press release. NobelPrize.org. URL <https://www.nobelprize.org/prizes/physics/1995/press-release/>
- [10] M. Lubej, ŠTUDIJA MERITVE KRŠITVE SIMETRIJE CP V RAZPADIH $D^0 \rightarrow \pi^0 \pi^0$ Z DETEKTORJEM BELLE II, Master's thesis, University of Ljubljana (Sep. 2014). URL http://www-f9.ijs.si/~lubej/magisterij_lubej_final_v2.pdf
- [11] D. Tong, Line operators in the Standard Model, *Journal of High Energy Physics* 2017 (7). doi:10.1007/jhep07(2017)104.

- [12] J. Davis, Raymond, D. S. Harmer, K. C. Hoffman, Search for neutrinos from the sun, *Phys. Rev. Lett.* 20 (1968) 1205–1209. doi:10.1103/PhysRevLett.20.1205.
- [13] Y. Fukuda, et al., Measurements of the Solar Neutrino Flux from Super-Kamiokande's First 300 Days, *Phys. Rev. Lett.* 81 (1998) 1158–1162. doi:10.1103/PhysRevLett.81.1158.
- [14] A. Bellerive, et al., The Sudbury Neutrino Observatory, *Nuclear Physics B* 908 (2016) 30–51. doi:10.1016/j.nuclphysb.2016.04.035.
- [15] B. Pontecorvo, Neutrino Experiments and the Problem of Conservation of Leptonic Charge, *Soviet Physics JETP* 26 (1968) 984–988.
URL http://www.jetp.ac.ru/cgi-bin/dn/e_026_05_0984.pdf
- [16] A. Y. Smirnov, The MSW effect and Solar Neutrinos, (2003). arXiv:hep-ph/0305106.
- [17] D. G. Michael, et al., Observation of Muon Neutrino Disappearance with the MINOS Detectors in the NuMI Neutrino Beam, *Phys. Rev. Lett.* 97 (2006) 191801. doi:10.1103/PhysRevLett.97.191801.
- [18] L. Wolfenstein, Neutrino oscillations in matter, *Phys. Rev. D* 17 (1978) 2369–2374. doi:10.1103/PhysRevD.17.2369.
- [19] M. Tanabashi, et al., Review of Particle Physics, *Phys. Rev. D* 98 (2018) 030001. doi:10.1103/PhysRevD.98.030001.
- [20] P. C. de Holanda, A. Y. Smirnov, Solar neutrinos: Global analysis with day and night spectra from SNO, *Phys. Rev. D* 66 (11). doi:10.1103/physrevd.66.113005.
- [21] I. Esteban, et al., The fate of hints: updated global analysis of three-flavor neutrino oscillations, (2020). arXiv:2007.14792.
URL <http://www.nu-fit.org/>
- [22] M. Jiang, et al., Atmospheric neutrino oscillation analysis with improved event reconstruction in Super-Kamiokande IV, *Progress of Theoretical and Experimental Physics* 2019 (5). doi:10.1093/ptep/ptz015.
- [23] M. G. Aartsen, et al., Measurement of atmospheric tau neutrino appearance with IceCube DeepCore, *Phys. Rev. D* 99 (2019) 032007. doi:10.1103/PhysRevD.99.032007.
- [24] P. Adamson, et al., Combined Analysis of ν_μ Disappearance and $\nu_\mu \rightarrow \nu_e$ Appearance in MINOS Using Accelerator and Atmospheric Neutrinos, *Phys. Rev. Lett.* 112 (2014) 191801. doi:10.1103/PhysRevLett.112.191801.
- [25] K. Abe, et al., Updated T2K measurements of muon neutrino and antineutrino disappearance using 1.5×10^{21} protons on target, *Phys. Rev. D* 96 (1). doi:10.1103/physrevd.96.011102.

- [26] P. Adamson, et al., Measurement of the neutrino mixing angle θ_{23} in NOvA, Phys. Rev. Lett. 118 (15) (2017) 151802. doi:10.1103/PhysRevLett.118.151802.
- [27] A. Gando, et al., Constraints on θ_{13} from a three-flavor oscillation analysis of reactor antineutrinos at KamLAND, Phys. Rev. D 83 (2011) 052002. doi:10.1103/PhysRevD.83.052002.
- [28] Y. Abe, et al., Measurement of θ_{13} in Double Chooz using neutron captures on hydrogen with novel background rejection techniques, JHEP 01 (2016) 163. doi:10.1007/JHEP01(2016)163.
- [29] F. An, et al., New measurement of θ_{13} via neutron capture on hydrogen at Daya Bay, Phys. Rev. D 93 (7) (2016) 072011. doi:10.1103/PhysRevD.93.072011.
- [30] W. Hampel, et al., GALLEX solar neutrino observations: Results for GALLEX IV, Phys. Lett. B 447 (1999) 127–133. doi:10.1016/S0370-2693(98)01579-2.
- [31] J. Abdurashitov, et al., Measurement of the solar neutrino capture rate with gallium metal. III: Results for the 2002–2007 data-taking period, Phys. Rev. C 80 (2009) 015807. doi:10.1103/PhysRevC.80.015807.
- [32] Y. Nakano, Latest result of solar neutrino analysis in Super-Kamiokande, J. Phys. Conf. Ser. 1468 (1) (2020) 012189. doi:10.1088/1742-6596/1468/1/012189.
- [33] G. Bellini, et al., Final results of Borexino Phase-I on low energy solar neutrino spectroscopy, Phys. Rev. D 89 (11) (2014) 112007. doi:10.1103/PhysRevD.89.112007.
- [34] S. Lorenz, Topological Track Reconstruction in Liquid Scintillator and LENA as a Far-Detector in an LBNO Experiment, Dissertation, Universität Hamburg (Nov. 2016). doi:10.3204/PUBDB-2016-06366.
- [35] A. Dueck, W. Rodejohann, K. Zuber, Neutrinoless double beta decay, the inverted hierarchy, and precision determination of θ_{12} , Physical Review D 83 (11). doi:10.1103/physrevd.83.113010.
- [36] F. An, et al., Neutrino physics with JUNO, Journal of Physics G: Nuclear and Particle Physics 43 (3) (2016) 030401. doi:10.1088/0954-3899/43/3/030401.
- [37] G. G. Raffelt, A. Y. Smirnov, Self-induced spectral splits in supernova neutrino fluxes, Phys. Rev. D 76 (2007) 081301. doi:10.1103/PhysRevD.76.081301.
- [38] M. Frigerio, A. Y. Smirnov, Structure of neutrino mass matrix and CP violation (2002). arXiv:hep-ph/0202247.
- [39] Z. Bai, et al., Standard Model Prediction for Direct CP Violation in $K \rightarrow \pi\pi$ Decay, Phys. Rev. Lett. 115 (2015) 212001. doi:10.1103/PhysRevLett.115.212001.

- [40] S. Bilenky, Neutrinos: Majorana or Dirac?, (2020). arXiv:2008.02110.
- [41] S. Weinberg, Baryon and Lepton Nonconserving Processes, *Phys. Rev. Lett.* 43 (1979) 1566–1570. doi:10.1103/PhysRevLett.43.1566.
- [42] M. Agostini, et al., Probing Majorana neutrinos with double- β decay, *American Association for the Advancement of Science* 365 (2019) 1445–1448. doi:10.1126/science.aav8613.
- [43] A. Gando, et al., Search for Majorana Neutrinos Near the Inverted Mass Hierarchy Region with KamLAND-Zen, *Phys. Rev. Lett.* 117 (2016) 082503. doi:10.1103/PhysRevLett.117.082503.
- [44] J. B. Albert, et al., Search for Neutrinoless Double-Beta Decay with the Upgraded EXO-200 Detector, *Phys. Rev. Lett.* 120 (2018) 072701. doi:10.1103/PhysRevLett.120.072701.
- [45] D. Q. Adams, et al., Improved Limit on Neutrinoless Double-Beta Decay in ^{130}Te with CUORE, *Phys. Rev. Lett.* 124 (2020) 122501. doi:10.1103/PhysRevLett.124.122501.
- [46] O. Azzolini, et al., First Result on the Neutrinoless Double- β Decay of ^{82}Se with CUPID-0, *Phys. Rev. Lett.* 120 (2018) 232502. doi:10.1103/PhysRevLett.120.232502.
- [47] Y. Cai, et al., From the Trees to the Forest: A Review of Radiative Neutrino Mass Models, *Frontiers in Physics* 5. doi:10.3389/fphy.2017.00063.
- [48] R. N. Mohapatra, G. Senjanović, Neutrino Mass and Spontaneous Parity Nonconservation, *Phys. Rev. Lett.* 44 (1980) 912–915. doi:10.1103/PhysRevLett.44.912.
- [49] Y. J. Ko, et al., Sterile Neutrino Search at the NEOS Experiment, *Phys. Rev. Lett.* 118 (2017) 121802. doi:10.1103/PhysRevLett.118.121802.
- [50] A. Aguilar, et al., Evidence for neutrino oscillations from the observation of $\bar{\nu}_e$ appearance in a $\bar{\nu}_\mu$ beam, *Phys. Rev. D* 64 (2001) 112007. doi:10.1103/PhysRevD.64.112007.
- [51] A. A. Aguilar-Arevalo, et al., Improved Search for $\bar{\nu}_\mu \rightarrow \bar{\nu}_e$ Oscillations in the Mini-BooNE Experiment, *Phys. Rev. Lett.* 110 (2013) 161801. doi:10.1103/PhysRevLett.110.161801.
- [52] C. Giunti, et al., Update of short-baseline electron neutrino and antineutrino disappearance, *Phys. Rev. D* 86 (2012) 113014. doi:10.1103/PhysRevD.86.113014.
- [53] M. Agostini, et al., First Direct Experimental Evidence of CNO neutrinos, (2020). arXiv:2006.15115.

- [54] M. Decowski, KamLAND's precision neutrino oscillation measurements, *Nucl. Phys. B* 908 (2016) 52–61. doi:10.1016/j.nuclphysb.2016.04.014.
- [55] JGU Mainz, Status of LENA R&D, Conference talk - NNN at APC Paris, 2014.
URL <https://indico.in2p3.fr/event/10162/contributions/1206/>
- [56] G. Alimonti, et al., Light propagation in a large volume liquid scintillator, *Nucl. Instrum. and Meth. Phys. Res. A* 440 (2) (2000) 360 – 371. doi:[https://doi.org/10.1016/S0168-9002\(99\)00961-4](https://doi.org/10.1016/S0168-9002(99)00961-4).
- [57] M. Wurm, et al., Optical scattering lengths in large liquid-scintillator neutrino detectors, *Review of Scientific Instruments* 81 (5) (2010) 053301. doi:10.1063/1.3397322.
- [58] Hamamatsu Photonics K.K. Editorial Committee, Photomultiplier tubes – basics and applications – (April 2017).
URL https://www.hamamatsu.com/resources/pdf/etd/PMT_handbook_v4E.pdf
- [59] A. Lyashenko, et al., Performance of Large Area Picosecond Photo-Detectors (LAPPD™), *Nucl. Instrum. and Meth. Phys. Res. A* 958 (2020) 162834. doi:10.1016/j.nima.2019.162834.
- [60] J. A. Richardson, L. A. Grant, R. K. Henderson, Low Dark Count Single-Photon Avalanche Diode Structure Compatible With Standard Nanometer Scale CMOS Technology, *IEEE Photonics Technology Letters* 21 (14) (2009) 1020–1022. doi:10.1109/LPT.2009.2022059.
- [61] Y.-F. Li, J. Cao, Y. Wang, L. Zhan, Unambiguous determination of the neutrino mass hierarchy using reactor neutrinos, *Physical Review D* 88 (1). doi:10.1103/physrevd.88.013008.
- [62] T. Adam, et al., JUNO Conceptual Design Report, (2015). arXiv:1508.07166.
- [63] H. Rebber, Event Discrimination with Topological 3D Reconstruction at MeV Energies in the JUNO Experiment, Dissertation, Universität Hamburg (2019).
URL <https://ediss.sub.uni-hamburg.de/volltexte/2020/10347/>
- [64] I. Esteban, et al., Global analysis of three-flavour neutrino oscillations: synergies and tensions in the determination of θ_{23} , δ_{CP} , and the mass ordering, *Journal of High Energy Physics* 2019 (1). doi:10.1007/jhep01(2019)106.
- [65] M. Aker, et al., First operation of the KATRIN experiment with tritium, *The European Physical Journal C* 80 (3). doi:10.1140/epjc/s10052-020-7718-z.
- [66] L. Zhan, et al., Determination of the neutrino mass hierarchy at an intermediate baseline, *Physical Review D* 78 (11). doi:10.1103/physrevd.78.111103.

- [67] A. A. Sonzogni, M. Nino, E. A. McCutchan, Revealing fine structure in the antineutrino spectra from a nuclear reactor, *Physical Review C* 98 (1). doi:10.1103/physrevc.98.014323.
- [68] L. Wei, L. Zhan, J. Cao, W. Wang, Improving the Energy Resolution of the Reactor Antineutrino Energy Reconstruction with Positron Direction, (2020). arXiv:2005.05034.
- [69] A. Abusleme, et al., TAO Conceptual Design Report: A Precision Measurement of the Reactor Antineutrino Spectrum with Sub-percent Energy Resolution, (2020). arXiv:2005.08745.
- [70] H. de Kerret, et al., Yields and production rates of cosmogenic ${}^9\text{Li}$ and ${}^8\text{He}$ measured with the Double Chooz near and far detectors, *Journal of High Energy Physics* 2018 (11). doi:10.1007/jhep11(2018)053.
- [71] M. C. Gonzalez-Garcia, M. Maltoni, T. Schwetz, Updated fit to three neutrino mixing: status of leptonic CP violation, *Journal of High Energy Physics* 2014 (11). doi:10.1007/jhep11(2014)052.
- [72] C. H. Albright, W. Rodejohann, Comparing trimaximal mixing and its variants with deviations from tri-bimaximal mixing, *The European Physical Journal C* 62 (3) (2009) 599–608. doi:10.1140/epjc/s10052-009-1074-3.
- [73] A. Burrows, Colloquium: Perspectives on core-collapse supernova theory, *Reviews of Modern Physics* 85 (1) (2013) 245–261. doi:10.1103/revmodphys.85.245.
- [74] G. Fogli, E. Lisi, A. Marrone, A. Mirizzi, Collective neutrino flavor transitions in supernovae and the role of trajectory averaging, *Journal of Cosmology and Astroparticle Physics* 2007 (12) (2007) 010–010. doi:10.1088/1475-7516/2007/12/010.
- [75] M. Ahlers, P. Mertsch, S. Sarkar, Cosmic ray acceleration in supernova remnants and the FERMI/PAMELA data, *Physical Review D* 80 (12). doi:10.1103/physrevd.80.123017.
- [76] A. Gando, et al., Search for extraterrestrial antineutrino sources with the KamLAND detector, *The Astrophysical Journal* 745 (2) (2012) 193. doi:10.1088/0004-637x/745/2/193.
- [77] R. Möllenberg, et al., Detecting the diffuse supernova neutrino background with LENA, *Physical Review D* 91 (3). doi:10.1103/physrevd.91.032005.
- [78] B. J. Land, Z. Bagdasarian, J. Caravaca, M. Smiley, G. D. O. Gann, MeV-scale performance of water-based and slow liquid scintillators (2020). arXiv:2007.14999.

- [79] M. Aartsen, et al., Combined sensitivity to the neutrino mass ordering with JUNO, the IceCube Upgrade, and PINGU, *Physical Review D* 101 (3). doi:10.1103/physrevd.101.032006.
- [80] M. Fukugita, T. Yanagida, Barygenesis without grand unification, *Physics Letters B* 174 (1) (1986) 45 – 47. doi:https://doi.org/10.1016/0370-2693(86)91126-3.
- [81] S. Davidson, E. Nardi, Y. Nir, Leptogenesis, *Physics Reports* 466 (4-5) (2008) 105–177. doi:10.1016/j.physrep.2008.06.002.
- [82] A. Kusenko, Sterile neutrinos: The dark side of the light fermions, *Physics Reports* 481 (1-2) (2009) 1–28. doi:10.1016/j.physrep.2009.07.004.
- [83] K. Abe, et al., Search for proton decay via $p \rightarrow e^+ \pi^0$ and $p \rightarrow \mu^+ \pi^0$ in 0.31 megaton · years exposure of the Super-Kamiokande water Cherenkov detector, *Phys. Rev. D* 95 (2017) 012004. doi:10.1103/PhysRevD.95.012004.
- [84] Y.-F. Li, Z.-h. Zhao, Tests of Lorentz and CPT Violation in the Medium Baseline Reactor Antineutrino Experiment, *Physical Review D* 90 (11). doi:10.1103/physrevd.90.113014.
- [85] T. Hagner, et al., Muon-induced production of radioactive isotopes in scintillation detectors, *Astroparticle Physics* 14 (1) (2000) 33 – 47. doi:10.1016/S0927-6505(00)00103-1.
- [86] C. Jollet, A. Meregaglia, ^9Li and ^8He decays in GEANT4, *Nucl. Instrum. and Meth. Phys. Res. A* 949 (2020) 162904. doi:10.1016/j.nima.2019.162904.
- [87] Geant4 Collaboration, Geant4—a simulation toolkit, *Physics Reference Manual* (August 2020).
URL <http://geant4-userdoc.web.cern.ch/geant4-userdoc/UsersGuides/PhysicsReferenceManual/fo/PhysicsReferenceManual.pdf>
- [88] Geant4 Collaboration, Geant4—a simulation toolkit, *Book For Application Developers* (August 2020).
URL <http://geant4-userdoc.web.cern.ch/geant4-userdoc/UsersGuides/ForToolkitDeveloper/fo/BookForToolkitDevelopers.pdf>
- [89] M. Grassi, J. Evslin, E. Ciuffoli, X. Zhang, Vetoing cosmogenic muons in a large liquid scintillator, *Journal of High Energy Physics* 2015 (10) (2015) 32. doi:10.1007/JHEP10(2015)032.
- [90] J. H. Zou, et al., SNiPER: an offline software framework for non-collider physics experiments, *Journal of Physics: Conference Series* 664 (7) (2015) 072053. doi:10.1088/1742-6596/664/7/072053.

- [91] S. Agostinelli, et al., Geant4—a simulation toolkit, *Nucl. Instrum. and Meth. Phys. Res. A* 506 (3) (2003) 250 – 303. doi:10.1016/S0168-9002(03)01368-8.
- [92] J. Allison, et al., Geant4 developments and applications, *IEEE Transactions on Nuclear Science* 53 (1) (2006) 270–278. doi:10.1109/TNS.2006.869826.
- [93] R. Brun, F. Rademakers, ROOT — An object oriented data analysis framework, *Nucl. Instrum. and Meth. Phys. Res. A* 389 (1) (1997) 81 – 86. doi:[https://doi.org/10.1016/S0168-9002\(97\)00048-X](https://doi.org/10.1016/S0168-9002(97)00048-X).
URL <http://root.cern.ch/>
- [94] Provided by the JUNO Collaboration.
URL <http://juno.ihep.cas.cn/>
- [95] R. Patterson, et al., The extended-track event reconstruction for MiniBooNE, *Nucl. Instrum. and Meth. Phys. Res. A* 608 (1) (2009) 206 – 224. doi:<https://doi.org/10.1016/j.nima.2009.06.064>.
- [96] T. O'Donnell and the KamLAND Collaboration, Muon tracking for optimized background rejection at KamLAND, *Journal of Physics: Conference Series* 136 (4) (2008) 042013. doi:10.1088/1742-6596/136/4/042013.
- [97] H. O. Schmidt, Parallelization of an algorithm for the topological reconstruction in liquidscintillator detectors, Bachelor's Thesis (2016).
URL https://www.physik.uni-hamburg.de/iexp/gruppe-hagner/pdf/bachelorarbeit_haukeschmidt.pdf
- [98] R. S. Irving, *Beyond the Quadratic Formula*, The Mathematical Association of America, 2013, ISBN 978-0-88385-783-0.
- [99] D. J. Meyhöfer, Vertex reconstruction in large liquid scintillator detectors, Master's thesis, Universität Hamburg (Sep. 2016).
URL <https://www.physik.uni-hamburg.de/iexp/gruppe-hagner/pdf/masterarbeit.pdf>

Acknowledgement

I'm very thankful for this opportunity, given to me by Prof. Dr. Caren Hagner and Dr. Björn Wonsak. I very much enjoyed the freedom I had during the development of this work. The support I received with regard to encouragement, ideas and consultation is greatly appreciated. I'm especially thankful for the excellent supervision provided by Dr. Björn Wonsak. Additionally, I would like to thank Dr. Marco Grassi and Prof. Dr. Cécile Jollet for their support with the cosmogenic simulation and Haoqi Lu as well as Guofu Cao for the insight they gave me into the JUNO simulation. I'm also very grateful to Hauke Schmidt, who enabled the parallelization of the TTR.

Furthermore, the nice atmosphere of the *Arbeitsgruppe Neutrinophysik* always filled me with pleasant anticipation on my way to work. Additionally, Fridays team building opportunities had a great impact on my happiness and reinforced my decision for this research group. This brings me to the main organizer of these events, Dr. Daniel Bick, which I always enjoy talking to, especially about Linux related topics. Furthermore, my sincere thanks is due to Dr. Henning Rebber, Stefan Bieschke and Malte Stender for their support with programming, correction of this work, their knowledge of neutrinos as well as socializing conversations. I would also like to thank Hans-Jürgen "Hajo" Ohmacht for the countless opportunities of *creative problem solving* and the nice chitchat each morning. A special thanks goes to Christian Hellwig for the opportunity of improving my C++ teaching skills. And I would also like to use this opportunity to thank Petra Hinzer for her unprecedented administration skills and the delightful conversations we had. I'm also thanking Dr. Tamer Tolba for his enthusiastic support about any questions I had. In general, I'm very grateful for the socializing and pleasant conversations I had with any past or current group members, especially any Felix that feels addressed as well as Puja and Sofia, which may or may not have had to endure my socializing.

I would also like to thank all the nice people, who I met during JUNO collaboration meetings and especially Haiqiong, who is a very enjoyable character. Also, my neighbors (The *Simrock-Gang*) deserve a thanks, for the distraction and social relief they provided when I was at home. Furthermore, thank you Sascha and Janina for every Friday I could spend with you t., uhm I mean four. And last but not least, I would like to thank my parents, who always believed in me and supported me.

Eidesstattliche Versicherung / Declaration on oath

Hiermit versichere ich an Eides statt, die vorliegende Dissertationsschrift selbst verfasst und keine anderen als die angegebenen Hilfsmittel und Quellen benutzt zu haben.

Die eingereichte schriftliche Fassung entspricht der auf dem elektronischen Speichermedium.

Die Dissertation wurde in der vorgelegten oder einer ähnlichen Form nicht schon einmal in einem früheren Promotionsverfahren angenommen oder als ungenügend beurteilt.

Hamburg, June 1, 2021

(Unterschrift der Doktorandin / des Doktoranden)